UNIVERSITY OF SOUTHAMPTON

Faculty of Engineering and Physical Sciences

Mechanical Engineering Department

Microstructures and Properties of Additively Manufactured Alloys Processed by Severe Plastic Deformation

by

Shahir Yasin bin Mohd Yusuf

Thesis for the degree of Doctor of Philosophy

July 2020

UNIVERSITY OF SOUTHAMPTON

ABSTRACT

Faculty of Engineering and Physical Sciences
Mechanical Engineering Department

Thesis for the degree of Doctor of Philosophy

MICROSTRUCTURES AND PROPERTIES OF ADDITIVELY MANUFACTURED ALLOYS PROCESSED BY SEVERE PLASTIC DEFORMATION

Shahir Yasin bin Mohd Yusuf

For the first time, the microstructure-property relationship of additively manufactured (AM) alloys processed by severe plastic deformation (SPD) was investigated in this PhD project. In this study, experiments were conducted on single-material 316L stainless steel (316L SS) and multi-material 316L SS/nickel 718 (IN 718) superalloy fabricated by selective laser melting (SLM) and then processed by high-pressure torsion (HPT). These include x-ray computed tomography (XCT), Vickers hardness (HV), x-ray diffraction (XRD), nanoindentation, electrochemical and wear tests, as well as optical microscopy (OM), scanning electron microscopy (SEM), and transmission electron microscopy (TEM) observations. This study aims to investigate the influence of ultrafine grains (UFG) and nano-scale grains (NG) obtained by HPT processing on the porosity, hardness, deformation mechanism, and corrosion and wear performances of SLM-fabricated alloys.

316L SS was initially additively manufactured by SLM and then processed by HPT through 1/4 – 10 revolutions at room temperature under 6 GPa of pressure at 1 rpm to produce UFG and NG microstructures. About 89 – 91% reduction of the spherical gas-induced pores is attained even at minimum torsional strain (1/4 HPT revolution) as determined from OM, due to the combined compressive force and extreme HPT-imposed torsional strain. HV measurements indicate significant hardness increase that saturates throughout the disk after 10 revolutions, suggesting the evolution towards microstructural homogeneity with increasing torsional strain. XRD spectra show that the alloy retains its single γ-austenite FCC structure even after extreme HPT straining. XRD line broadening analysis reveal significant decrease in crystallite size, D_c and considerable increase in dislocation density, ρ with larger HPT straining.

TEM and XRD analysis suggest three stages of deformation mechanisms that are related to the microstructural features and the corresponding equivalent strain values, ε_{eq}. Primary twins, dislocations, and twin-matrix lamellae are dominant in stage 1 ($\varepsilon_{eq.}$ = ~ 0 – 10). Shear banding of the twin-matrix lamellae and secondary nanotwins are prevalent in stage 2 ($\varepsilon_{eq.}$ = ~ 10 – 40), while the equiaxed nano-sized grains at stage 3 ($\varepsilon_{eq.}$ > 40) indicate that an equilibrium or saturation stage is achieved. A physical-based model was then established to evaluate the contribution of grain boundaries, dislocations, twins, and solid solution on the hardness increase attained by this alloy. The calculated strain rate sensitivity

(SRS), m and activation volume, V_p^* values from the results of nanoindentation measurements at both constant and varied strain rates were correlated with the microstructural changes from micro- to nano-regime to evaluate the evolution in plasticity and plastic deformation mechanism for all processing conditions. The high m and small V_p^* values calculated for the as-received and HPT-processed disks suggest that reasonably high plasticity level is maintained, and grain boundary (GB)-mediated activities play a major role in the evolution of plastic deformation mechanism.

Electrochemical tests, SEM observations, and energy dispersive x-ray spectroscopy (EDX) analysis indicate improved overall corrosion performance in 3.5% NaCl solution after HPT processing as evidenced by the consistently lower corrosion rates compared to the as-received AM 316L SS. The enhanced corrosion performance is attributed to the substantial porosity elimination, homogeneous distribution of UFG/NG microstructures, and the absence of martensite formation. Dry sliding wear tests demonstrate improved wear performance after HPT processing, as implied by the steady reduction in coefficient of friction (COF), mass loss, m_{loss} and specific wear rate, k_{W} values with increasing HPT torsional strains compared to the as-received AM 316L SS. The improvement in the overall wear resistance could be attributed to the combined grain refinement-induced high hardness and the formation of iron oxides that act as solid lubricant to lower the friction between the contact surfaces. In addition, SEM and EDX analysis suggest that the wear mechanism transitioned from severe abrasive wear for the as-received AM 316L SS to a combination of mild abrasive, adhesive, and tribo-oxidative wear for all HPT processing conditions.

For the multi-material 316L SS/IN 718, about 91% of irregular shaped process-induced pores is eliminated after only 1/4 HPT revolution via the similar pore closure mechanisms from HPT-processed 316L SS as before. HV measurements suggest that hardness saturation is only achieved at the peripheral regions of the disks, as demonstrated by the consistently high HV values at the disk edges compared to the disk centre. XRD analysis shows that the interfacial 316L SS/IN 718 region retains its γ-austenite FCC structure and some (Nb,Ti)C phase throughout all processing conditions. Substantial decrease in D_{c} and remarkable increase in, ρ at the interfacial region are attained with larger HPT straining. TEM, EDX, and XRD analysis, and the physical-based strengthening model suggest that the hardness increase at the periphery of the interfacial region is the result of grain boundaries, dislocations, solid solution, and precipitates, with the additional contribution of nanotwins after 1 and 10 HPT revolutions.

In the future, hip replacement bio-implants and small gas turbine blades are envisaged to be developed by exploiting the advantages of this hybrid AM/SPD approach, particularly the design flexibility of AM and the excellent strength, and superior corrosion and wear performance attained via SPD processing. Finally, the results from the present study show that the primary aim of establishing process-microstructure-property relationships for SPD-processed AM alloys has been achieved.

Table of Contents

Research Thesis: Declaration of Authorship

Print name:	Shahir Yasin bin Mohd Yusuf
Title of thesis:	Microstructures and Properties of Additively Manufactured Alloys Processed by Severe Plastic Deformation

I declare that this thesis and the work presented in it are my own and has been generated by me as the result of my own original research.

I confirm that:

1. This work was done wholly or mainly while in candidature for a research degree at this University;
2. Where any part of this thesis has previously been submitted for a degree or any other qualification at this University or any other institution, this has been clearly stated;
3. Where I have consulted the published work of others, this is always clearly attributed;
4. Where I have quoted from the work of others, the source is always given. With the exception of such quotations, this thesis is entirely my own work;
5. I have acknowledged all main sources of help;
6. Where the thesis is based on work done by myself jointly with others, I have made clear exactly what was done by others and what I have contributed myself;
7. During this PhD study, the following six papers have been published:
    - **S. M. Yusuf**, Y. Chen, R. Boardman, S. Yang, and N. Gao (2017) Investigation on Porosity and Microhardness of 316L Stainless Steel Fabricated by Selective Laser Melting, ***Metals (Basel)***, 7, 1–12.
    - **S.M. Yusuf** and N. Gao (2017) Influence of energy density on metallurgy and properties in metal additive manufacturing, ***Materials Science and Technology***, 33, 1269–1289.
    - **S. M. Yusuf**, M. Nie, Y. Chen, S. Yang, and N. Gao (2018) Microstructure and corrosion performance of 316L stainless steel fabricated by Selective Laser Melting and processed through high-pressure torsion, ***Journal of Alloys and Compounds***, 763, 360–375.
    - **S. M. Yusuf**, Y. Chen, S. Yang, and N. Gao (2019) Microstructural evolution and strengthening of selective laser melted 316L stainless steel processed by high-pressure torsion ***Materials Characterization*** , 159, 110012.
    - **S.M. Yusuf**, S. Cutler, and N. Gao (2019) Review: The impact of metal additive manufacturing on the aerospace industry, ***Metals (Basel)***, 9, 1–35.
    - **S.M. Yusuf**, M. Hoegden, and N. Gao (2020) Effect of sample orientation on the microstructure and microhardness of additively manufactured AlSi10Mg processed by high-pressure torsion, ***The International Journal of Adcanced Manufacturing Technology***, 1–17.
    - **S. M. Yusuf**, Y. Chen, S. Yang, and N. Gao, Micro-mechanical response of additively manufactured 316L stainless steel processed by high-pressure torsion (2020) *Advanced Engineering Materials*, https://doi.org/10.1002/adem.202000052.

Signature: Date:

Acknowledgements

All praises to Allah The Almighty for giving me the strength to face this challenging PhD journey.

I would like to express my sincerest gratitude and appreciation to my main supervisor, Dr. Nong Gao for his excellent supervision and immense patience and guidance throughout my PhD journey at the University of Southampton. I am indeed appreciative of his constructive comments, suggestions, and recommendations that not only helped me to complete this thesis, but also shaped me to become a disciplined researcher. A special mention to my co-supervisor, Professor Shoufeng Yang for his continuous support from Belgium.

I am indebted to the Faculty of Engineering and Physical Sciences, University of Southampton for the studentship provision. I would like to thank Armourers & Braziers' (UK) for their financial support to attend conferences.

I take this opportunity to thank Dr. Ying Chen and Ms. Boqin Lu (Xiamen University of Technology, China) for their assistance in conducting TEM experiments and subsequent discussions. My appreciation is extended to Prof. Indradev Samajdar and Mr. Parvej Raut (Indian Institute of Technology, Bombay, India) for their help on EBSD experiments and analysis. I would like to express my gratitude to Mr. Behrad Mahmoodi (nCATS Research Group, University of Southampton) for his help in carrying out nanoindentation experiments. A huge thanks to Dr. Richard Boardman (μ-Vis X-Ray Imaging Centre, University of Southampton) for his kind help in conducting XCT scans for my samples. A special thanks to Dr. Xiao Zhao for his expertise in helping me to fabricate multi-material AM samples. I am also grateful to Dr. Mengyan Nie (University College London) for the valuable discussion on the corrosion experiments. Many thanks to Aizat Azi and Daryl Lim (both IP students) who assisted me during the corrosion and wear tests.

I sincerely acknowledge all staff and members of the Engineering Materials Research Group, particularly Ms. Marie-Salome Duval-Chaneac, Engineering Design and Manufacturing Centre (EDMC) team, and materials laboratory personnel.

I would like to thank my parents, Mohd Yusuf Husin and Sarminah Samad for their physical and financial supports, love, and prayers to see me succeed in my PhD studies and making this journey possible. I wish to express my eternal gratitude to my amazingly beautiful wife, Nur Farahin Puasa for her love, prayers, emotional support, understanding, and her believe in me even though we are ~ 10000 miles apart, for now. I love you all.

Thank you everyone. God bless!

Abbreviations

2D LPSM - 2-dimensional linear plane strain machining
AM - Additive manufacturing
AMS - Aerospace Material Specification
APB - Anti-phase boundary energy
ASTM - American Society for Testing and Materials
BCC - Body-centred cubic crystal lattice structure
BCT - Body-centred tetragonal crystal lattice structure
BNM - Bulk nanostructured materials
CAD - Computer aided design
CCD - High-speed charged-couple camera
CCGTAW - Continuous current gas tungsten arc welding
CL - Concept Laser company
CM - Conventional manufacturing
COF - Coefficient of friction
CP - Commercially pure
CRSS - Critically resolved shear strees
CTE - Coefficient of thermal expansion
DED - Directed energy deposition
DMD - Direct metal deposition
DMLS - Direct metal laser sintering
DPP - Dry powder printing
DZ - Denudation zone
E-PBF - Electron-beam powder bed fusion
EBM - Electron beam melting
EBSD - Electron backscattered diffraction
EBW - Electron beam welding
ECAP - Equal channel angular pressing
EDM - Electrical discharge machining
EDX - Electron dispersive x-ray spectroscopy
EIS - Electrochemical impedance spectroscopy
FCC - Face-centred cubic crystal lattice structure
FEI - Field electron imaging
FGM - Functionally graded materials
FMRR - Fast multiple rotation rolling
FSP - Friction stir processing
FSW - Friction stir welding

FZ - Fusion zone
GA - Gas atomisation
GB - Grain boundary
GBS - Grain boundary sliding
GMAW - Gas metal arc welding
GND - Geometrically necessary dislocation
GTAW - Gas tungsten arc welding
HAADF - High-angle annular dark field
HAZ - Heat affected zone in welded materials
HCP - Hexagonal close-packed crystal lattice structure
HIP - Hot isostatic pressing
HLS - Heterogeneous lamella-structure
HPT - High-pressure torsion
IFM - Infinite focus microscopy
IGC - Intergranular corrosion
IPF - Inverse pole figure
IR - Infra red
ISO - International Organization for Standardization
L-PBF - Laser powder bed fusion
LBW - Laser beam welding
LC - Laser cladding
LED - Linear energy density
LENS - Laser engineered net shaping
LMD - Laser metal deposition
MAF - Multi-axial forging
MAUD - Materials analysis using diffraction
MHH - Microwave hybrid heating
MMAM - Multi-material additive manufacturing
MMC - Metal matrix composite
MMNC - Metal matrix nanocomposite
MPB - Melt pool boundary
NDT - Non-destructive testing
OCP - Open circuit potential
PBF - Powder bed fusion
PGTAW - Pulsed current gas tungsten arc welding
PM - Powder metallurgy
PP - Potentiodynamic polarisation
PPC - Potentiodynamic polarisation curve

PREN - Pitting resistance equivalent number
PREP - Plasma rotating electrode
RE - Rotary emission
RT - Room temperature
SFE - Stacking fault energy
SLS - Selective laser sintering
SLM - Selective laser melting
SMAT - Surface mechanical attrition treatment
SP - Shot peening
SPD - Severe plastic deformation
SSD - Statistically stored dislocation
ST - Solution treatment
STA - Solution treatment and aging
STL - Standard tessellation language
TCP - Topologically close-packed crystal lattice structure
TTT - Time-temperature-transformation graph
UFG - ultrafine grain
UNSM - Ultrasonic nanocrystalline surface modification
UTS - Ultimate tensile strength
UZ - Unmixed zone
VED - Volumetric energy density
$\mathrm{VED}_{\mathrm{DED}}$ - Volumetric energy density for DED AM techniques
$\mathrm{VED}_{\mathrm{E\text{-}PBF}}$ - Volumetric energy density for E-PBF AM techniques
$\mathrm{VED}_{\mathrm{L\text{-}PBF}}$ - Volumetric energy density for L-PBF AM techniques
WAAM - Wire and arc additive manufacturing
XCT - X-ray computed tomography

Nomenclatures

A - Austenitic phase
A_C - Area of open cylindrical cavity used for electrochemical tests
A_p - Pore area
AF - Austenitic-ferritic phase
at. % - Atomic percentage
B_1 - Cubic crystal lattice structure
$\boldsymbol{b}$ - Burgers vector
C - Circularity factor
C_1 - Material constant
C_{14} - Hexagonal crystal lattice structure
CPE_in - Inner constant phase element applied for EIS simulation
$\mathrm{CPE}_\mathrm{out}$ - Outer constant phase element applied for EIS simulation
c_i - Concentration of i-th alloying element in solid solution strengthening
c/a - ratio of lattice parameter c to lattice parameter a representing lattice distortion
D_L - Diffusion constant
F_comp - Compressive force applied during HPT
D_c - Average crystallite size
$D0_{22}$ - BCT ordered crystal lattice structure
$D0_\mathrm{a}$ - Orthorombic ordered crystal lattice structure
d - Average grain size
d_cell - Average size of cellular structure colonies
d_L - Layer thickness used in PBF AM techniques
$d^{-1/2}$ - Inverse square root of grain size
E - Voltage applied during PP testing
E_corr - Corrosion potential
E_OCP - Reference voltage from OCP obtained after PP testing
E_pit - Pitting potential
EW - Equivalent weight
e - Thickness of twins determined from TEM micrographs
F - Frequency limit for polarisation resistance in PP test
F_DED - Feed rate of wire/powder material used in DED AM techniques
F - Ferritic phase
FA - Ferritic-austenitic phase
f - Fraction of grains with twins
$f_\mathrm{ppt.}$ - Fraction of precipitates and/or secondary phases in the microstructure
G - Shear modulus of a material

G_{L} - Temperature gradient
G_{L}/R - Determinant of solidification microstructure upon cooling
G_{L} x R - Cooling rate
$G(2\theta - 2\theta_1)$ - Gaussian shape function that obeys Pseudo-Voigt function
H - Nanohardness obtained from nanoindentation measurements
$H_{\mathrm{mat.}}$ - Hardness of a material determined from microhardness measurements
HV - Vickers microhardness
h - Displacement during nanoindentation
h_{f} - Final thickness of disk samples after HPT processing
h_{L} - Hatch/scan line spacing used in PBF AM techniques
h_0 - Initial thickness of disk samples before HPT processing
I - Current applied in EBM technique
$I(2\theta)$ - Pseudo-Voigt function
I_{HKL} - Observed relative intensities in XRD
i_{corr} - Corrosion current density
j - Imaginary value used to estimate Z_{CPE}
K_{HP} - Hall-Petch coefficient due to grain boundaries
K_{TW} - Hall-Petch coefficient due to twin boundaries
k - Boltzmann constant
k_{i} - Strengthening coefficient due to the dissolving of i-th alloying element
k_{W} - specific wear rate
L - Liquid phase
$L1_2$ - FCC ordered crystal lattice structure
$L(2\theta - 2\theta_1)$ - Lorentzian shape function that obeys Pseudo-Voigt function
L_{W} - Load applied during wear test
$\bar{l}$ - Average spacing of cellular sub-structure colonies/grain boundaries
M - Taylor factor
M_{f} - Martensite finish temperature
M_{s} - Martensite start temperature
MC - Metal carbide phase
m - Strain rate sensitivity (SRS)
n - Constant for concentration of alloying element in solid solution strengthening
m_{loss} - Mass loss
N - Number of revolutions in HPT processing
N_{ECAP} - Number of ECAP passes
P - Load applied during nanoindentation
P_{ECAP} - Pressure applied during ECAP
P_{HPT} - Pressure applied during HPT processing

P_L - Heat source power used in L-PBF and DED AM techniques
P_p - Perimeter covered by the pores
R_in - Inner charge transfer resistance applied for EIS simulation
R_out - Outer charge transfer resistance applied for EIS simulation
R_p - Polarisation resistance
R_u - Solution resistance of the 3.5% NaCl solution used for electrochemical testing
r - Distance from the centre of the HPT disk samples
$r_\mathrm{ppt.}$ - Distance of precipitates and/or secondary phases from one another
r_C - Radius of circular cavity
S - Sphericity factor
S_W - Sliding distance during wear test
U - Acceleration voltage applied in EBM technique
u - Cladding speed used in DED AM techniques
V - Volume loss during wear test
V_p - Pore volume
V_p^* - Activation volume
v - Scan speed used in PBF AM techniques
vol. % - Volume percentage
wt. % - Weight percentage
Y - Admittance parameter used to estimate Z_CPE
Z - Estimated impedance obtained from EIS testing
Z_CPE - CPE impedance from PP test
Z_im - Imaginary impedance (y-axis of Nyquist plot from EIS simulation results)
Z_mod - Impedance modulus obtained from EIS simulation results
Z_re - Real impedance (x-axis of Nyquist plot from EIS simulation results)
α' - Alpha-martensite phase
α - Alpha-ferrite phase
α_1 - Empirical constant for FCC materials
α_CPE - Exponent of CPE used to estimate Z_CPE
β - Beta phase
γ - Gamma-austenite phase
γ' - Gamma prime phase
γ'' - Gamma double prime phase
γ_shear - Shear strain
$\Delta \mathrm{T}$ - Constitutional undercooling
$\Delta\sigma_\mathrm{GB}$ - Increment in yield strength due to grain boundary strengthening
$\Delta\sigma_\mathrm{SS}$ - Increment in yield strength due to solid solution strengthening
$\Delta\sigma_\mathrm{GB\text{-}TW}$ - Increment in yield strength due to grain boundary and twinning

$\Delta\sigma_{\mathrm{ORO}}$ - Increment in yield strength due to precipitation strengthening

$\Delta\sigma_{\mathrm{TW}}$ - Increment in yield strength due to twinning strengthening

$\Delta\sigma_{\mathrm{\rho}}$ - Increment in yield strength due to dislocation strengthening

$\Delta\tau_{0}$ - Intrinsic CRSS

$\Delta\tau_{\mathrm{tot}}$ - Total CRSS of grains

$\Delta\tau_{\mathrm{\rho}}$ - CRSS contribution by dislocations

$\Delta\tau_{\mathrm{SS}}$ - CRSS contribution by solid solution

δ - Delta-ferrite phase

ε - Epsilon-martensite phase

$\langle\varepsilon^{2}\rangle^{1/2}$ - Lattice microstrain

$\varepsilon_{\mathrm{eq.\text{-}ECAP}}$ - Equivalent von mises strain imposed after ECAP processing

$\varepsilon_{\mathrm{eq.\text{-}HPT}}$ - Equivalent von mises strain imposed after HPT processing

$\dot{\varepsilon}$ - Calculated strain rate

$\dot{\varepsilon}_{i}$ - Indentation strain rate

η - Eta phase

η_{L} - Lorentz fraction

λ - Average twin spacing

$\lambda_{\mathrm{ppt.}}$ - Average spacing of precipitates

ρ - Dislocation density

$\rho_{\mathrm{mat.}}$ - Density of a material

ρ_{Total} - Total dislocation density due to combined GND and SSD from HPT processing

ρ_{XRD} - Dislocation density estimated from XRD

σ - Sigma-phase

σ_{0} - Intrinsic strength

σ_{f}, - Flow stress

σ_{y} - Yield strength of a material

ϕ - Phase angle

Φ - Angle between ECAP channels

χ^{2} - Parameter for circuit simulation in EIS testing

Ψ - Curvature angle of outer arc where ECAP channels intersect

ω - Angular frequency

Chapter 1 Introduction

1.1 Background and motivation

Metal additive manufacturing (AM) is a revolutionary manufacturing technology, in which metallic components are built in a layer-wise (bottom-up), freeform manner without the need of additional tools or moulds. In essence, its operating principle is similar to that of high-energy laser or electron beam fusion welding, i.e. by creating small melt pools to join two base metals together by fusion, often as multiple assemblies of a larger structure. The major difference is the ability of metal AM processes to utilise the high-energy heat source to selectively melt and fuse powder or wire feedstock to build the similar structure as in welding in a single machine operation without any assembly required.

Therefore, metal AM technology allows to build metallic parts with complex shapes and intricate features in a single step, thereby offering a significant time, cost, and waste material reductions. This makes AM very competitive compared to traditional formative manufacturing processes, e.g. welding, casting, forging, and powder metallurgy, and subtractive manufacturing that requires material removal, e.g. milling and machining. So far, metal AM techniques have become the sought-after manufacturing process for highly critical components that require low volume production and mass customisation, particularly in the aerospace, automotive and biomedical industries. For example, turbine blades, race car components, and medical implants have all been successfully fabricated by AM, with the parts having similar or even superior properties compared to those manufactured using traditional processes [1,2]. At present, two classes of metal AM processes are widely studied, including powder bed fusion (PBF) and directed energy deposition (DED), both using either laser or electron beam as heat source. The feedstock materials used in PBF is in powder form, while powder and/or wire are used in DED processes.

Furthermore, it is also possible to tailor the microstructures and properties of AM metallic parts according to desired applications by varying material composition (gradient material delivery) and/or by selecting suitable processing parameters. As a result, comparable or even superior properties have been achieved in AM-fabricated metallic parts with respect to conventionally manufactured (CM) components, e.g. yield and tensile strengths, corrosion and wear resistances, and fatigue performances [3–6]. In addition, the recent development of second-generation multi-material AM (MMAM) facilities have enabled the direct integration of multiple metal materials into complex spatial locations, which previously could not be achieved by any other available manufacturing routes [7–9]. As a result, it offers a promising potential to manufacture novel high-performance functional components with designed compositions, microstructures and properties.

MMAM technology has the capability to improve the mechanical properties and provide extra functionality to the fabricated parts due to its advantage of having different types of material or changing material composition within a single layer [7,10]. This technology will enable the deposition of more than one material from a single machine with tailored properties such as embedded systems, medically compatible implants and in particular, a new class of materials termed Functionally Graded Materials (FGM) [11]. However, the research on process-microstructure-property relationship in metal MMAM processing, particularly for laser powder bed fusion (L-PBF) techniques is still limited [12–14].

Although metal AM offers tremendous advantageous, the as-received parts often suffer from defects such as porosity and cracks. Therefore, numerous post-processing treatments such as hot isostatic pressing (HIP), various heat treatment procedures, surface modification, and shot peening have been applied to improve densification levels up to ≥ 99% [15–17]. Nevertheless, it is well known that grain sizes play a major role in determining the properties of any materials. As a general rule, fine grain sizes are often desirable as they possess several advantages over coarse grain sizes, e.g. higher yield and tensile strengths following the Hall-Petch relationship, superior corrosion and wear resistances, and enhanced creep and fatigue performances, [18]. Decades long of studies in materials science have been devoted on enhancing material properties via the grain refinement route, which has resulted in the development of bulk nanostructured metals (BNM) possessing ultrafine grains (UFG) ranging from 100 nm – 1 µm or nano-scale grains (NG) of < 100 nm [19,20].

To date, one of the approaches that are widely used to produce BNM structures is collectively termed as severe plastic deformation (SPD) processing, which comprises of processes that impose large amounts of strain on bulk metallic materials. Two of the most widely used SPD techniques are high-pressure torsion (HPT) and equal channel angle processing (ECAP) [18,21]. In fact, SPD-processed materials with UFG and NG microstructures often exhibit significantly higher yield and tensile strengths, enhanced fatigue life, and superior corrosion and wear performances compared to the coarse-grained counterparts [22–24]. HPT is more advantageous than ECAP because of its simpler operating mechanism, its effectiveness in obtaining much smaller grains [25–27], and because it can produce a larger amount of grain boundaries with high misorientation angles [28,29].

Although there are many publications for SPD-processed CM materials, there are no literature available in the study of the combination of metal AM and SPD in a single process sequence. Therefore, there are no information on the influence of UFG and NG microstructures attained by SPD processing on the porosity, hardness, and corrosion and wear performances of AM-fabricated alloys.

1.2 Aims and objectives

The main aim of this PhD research project is to investigate the process-microstructure-property relationships in AM metallic parts processed by SPD. In particular, the selective laser melting (SLM) technique from the L-PBF AM category is selected to fabricate the parts, while HPT is chosen to impose extreme torsional strains to attain UFG and NG microstructures. A series of experiments will be carried out to study the influence of HPT processing on the porosity, microstructure, hardness, deformation mechanisms, corrosion resistance, and wear performance of single-material 316L SS fabricated by SLM. In addition, experiments will also be conducted to study the influence of HPT processing on the porosity, microstructure, and hardness of multi-material (MM) 316L SS/IN 718 manufactured by SLM. The properties attained by this hybrid AM/SPD approach are compared with those obtained through SPD processing of CM materials.

Accordingly, the specific objectives of the present research are to investigate the following aspects and compare them before and after HPT processing:

1) To investigate the porosity, microstructural evolution and hardness attained by SLM-fabricated 316L SS processed by HPT.
2) To determine the evolution of deformation mechanisms in SLM-fabricated 316L SS processed by HPT.
3) To analyse the influence of HPT processing on the corrosion performance of SLM-fabricated 316L SS.
4) To evaluate the influence of HPT processing on the wear performance of SLM-fabricated 316L SS.
5) To investigate the porosity, microstructure, and hardness evolution of MM SLM-fabricated 316L SS/IN 718 processed by HPT.
6) To develop a physical-based strengthening model by assessing the contribution of different strengthening mechanisms on the overall hardness increase of SLM-fabricated 316L SS and MM 316L SS/IN 718.
7) To assess the suitability of the hybrid AM/SPD approach for potential commercial applications.

Process-microstructure-property relationships for SPD-processed AM alloys will then be established based on the results from the present study to provide guidance that could be useful to researchers and engineers, particularly to evaluate the strength and corrosion and wear performance of AM materials possessing UFG and/or NG microstructures for various applications in the future.

1.3 Thesis structure

The PhD thesis is structured as follows: The present chapter (Chapter 1) provides the background, motivation, and objectives of the current research. A comprehensive literature review is given in Chapter 2, covering the fundamental concepts, mechanisms, processing aspects, and applications of metal AM and SPD processing, as well as basic information on the studied materials (316L SS and IN 718). Chapter 3 details the material composition and experimental procedures used in the present study. Chapter 4 studies the evolution of porosity in SLM-fabricated 316L SS before and after HPT processing. Chapter 5 describes the microstructure and hardness evolutions, and the physical-based model that explains the contribution of various strengthening mechanisms on the overall strengthening of SLM-fabricated 316L SS obtained through HPT processing. Chapter 6 presents the results of micro-mechanical response obtained by nanoindentation tests to explain the evolution in deformation mechanisms in the as-received and HPT-processed disks. Chapters 7 and 8, respectively investigate the corrosion and wear performances in SLM-fabricated 316L SS before and after HPT processing. The results of porosity, microstructure, hardness and physical-based model used for assessing different strengthening mechanisms at the interfacial region of MM SLM-fabricated 316L SS/IN 718 are presented in Chapter 9. A general discussion on the effectiveness of HPT as a nanostructuring of SLM-fabricated metals and alloys, as well as the suitability of the hybrid AM/SPD approach for commercial applications are presented in Chapter 10. Finally, Chapter 11 summarises the main conclusions from the current research and suggestions for future works.

Chapter 2 Literature Review

2.1 Additive Manufacturing

2.1.1 Background of Additive Manufacturing

Every AM process begins with a digital 3D computer aided design (CAD) model either designed in CAD software or scanned directly into the computer using 3D scanners [30]. A standard tesselation language (.STL) file extension is generated based on the model and then virtually 'sliced' into individual 2D layers, to which any geometrical features requiring extra support are determined automatically or adjusted manually [31]. The required 3D object is built on a substrate by depositing the individual 2D layers, firstly on top of the substrate and then on top of each other. Once completed, further post-processing may be required to enhance the mechanical properties and physical appearance of the fabricated part.

When compared to conventional processing routes, metal AM is better suited for low volume productions, especially for niche components with complex geometries requiring mass customisation [32,33]. The immense potential and benefit of AM, together with continuous R&D of this advanced technology in recent years have attracted widespread applications from various industries. Aerospace, automotive, biomedical and biomaterials, and energy industries are popular commercial sectors which have largely benefited from this technology.

2.1.2 Additive Manufacturing of metals and alloys

There are five AM classifications related to metal AM techniques from the seven described by the ISO/ASTM 52900:2015 standard [34]: (i) powder bed fusion (PBF), (ii) directed energy deposition (DED), (iii) material jetting, (iv) binder jetting, and (v) sheet lamination. Of these five categories, PBF and DED are well-developed and widely used in many industries [15,35–37].

2.1.2.1 Powder Bed Fusion

In PBF processes, metallic powder bed layers are firstly spread on top of a substrate, followed by the spreading of successive powder bed layers on top of each other by using a powder dispensing mechanism. Then, the powder particles within an area in each layer are selectively sintered (partially melted) or completely melted by a laser or electron beam heat source according to the pre-defined CAD design until the build is complete [38–40]. Selective laser sintering (SLS), Selective laser melting (SLM), Direct metal laser sintering (DMLS), and Electron beam melting (EBM) are common PBF techniques. As its name implies, SLS is a laser-based PBF (L-PBF) process that utilises sintering, whereas SLM and DMLS employ complete melting. However, EBM is slightly different because it uses electron beam as heat source instead of laser, thus known as E-PBF [41]. The schematics of L-PBF and E-PBF machines are shown in Fig. 2-1 [40].

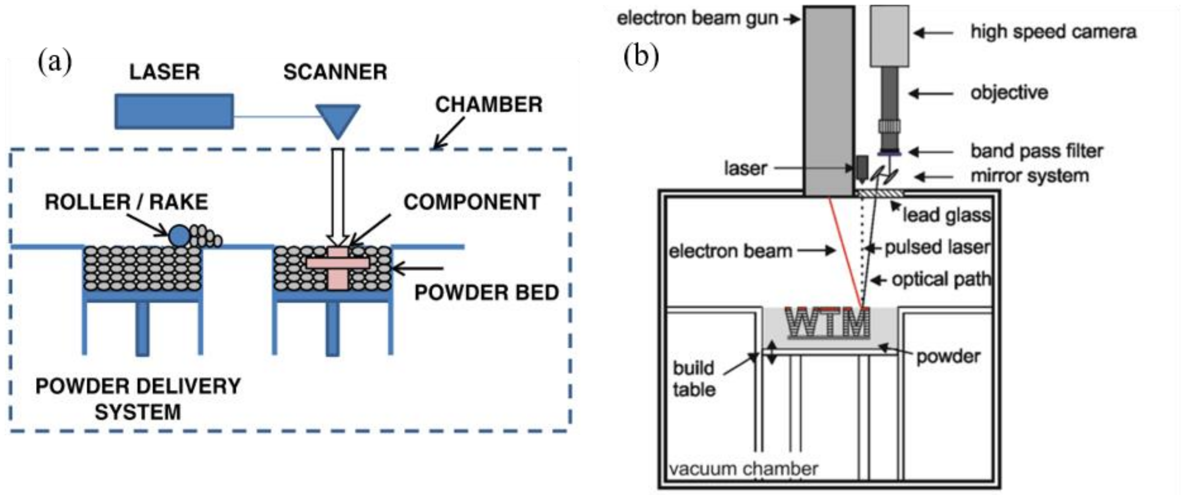

Fig. 2-1 Schematic of a (a) L-PBF and (b) E-PBF machines [40]. Reproduced with permission of the rights holder.

PBF processes are typically conducted in an enclosed chamber with an inert gas environment (L-PBF), e.g. argon and nitrogen, or in a vacuum/near-vacuum condition (E-PBF). This is largely due to the reactive nature of most metals and also to prevent oxidation or other undesired reactions [42,43]. In addition, all PBF processes follow the same operational steps, including machine set-up, raw material processing, powder recovery and finally substrate removal [44,45]. Furthermore, scan strategy and processing parameters govern the operating mechanism of PBF systems. Specific sets of parameters are often required depending on the material being processed, type of machine, and the intended end-application [46].

Earlier development stages of AM in the 1990s have focused on the processing of pure metals via SLS, e.g. commercially pure Ti [47,48] and certain pre-alloyed metals, e.g. Al-Si, W-Cu and CuSnCuCuP [49–51]. On the other hand, PBF processes employing complete melting (SLM, DMLS and EBM) are now typically used to process alloys, e.g. 316L stainless steel (316L SS), Ti6Al4V, AlSi10Mg, and IN 718, metal-matrix composites (MMCs), e.g. TiB, and TiC, as well as alloy-MMC combinations for various niche applications, including TiB_2-316L SS, pure Ti-TiB, TiC-AlSi10Mg, and nano-TiB_2-AlSi10Mg composites. All these materials have been successfully fabricated by SLM for aerospace, and automotive industries [52–56]. The application of high beam power in these techniques compared to SLS enables high densification levels (> 99%) to be achieved [57–60]. PBF has also been applied to fabricate cellular and lattice structures, or compositionally graded structures (either fully dense or controlled porosity) for various applications, e.g. bone implants with controlled porosity and high interconnectivity levels to mimic human body physiology [61] and metal lattice struts for heat exchangers [62]. These requirements could be achieved due to the capability of AM in general, or PBF specifically to fabricate intricate internal features and complex geometrical shapes with controllable porosity levels [63,64].

2.1.2.2 Directed Energy Deposition

In directed energy deposition (DED) techniques, heat source (laser or electron beam) is firstly focused onto a pre-defined area on the substrate to create a small melt pool, to which feedstock material is selectively deposited according to the initial CAD model layer by layer until the whole object is completed [65,66]. The feedstock material may be either in powder (Fig. 2-2(a)) or wire (Fig. 2-2(b)) form [40]. DED processing does not necessarily require an enclosed chamber, depending on the material being processed. Instead, the feedstock material is fed onto the melt pool via a shielded gas flow, similar to conventional welding techniques [67]. Laser engineered net shaping (LENS), developed by Sandia National Laboratories and commercialised by Optomec is an example of powder-based DED technique commonly used in industries [68]. Other DED processes using powder as the raw material include laser metal deposition (LMD), direct metal deposition (DMD), and laser cladding (LC). On the other hand, DED techniques which use wire as the feedstock material are termed wire and arc additive manufacturing (WAAM), which is essentially an expansion of welding technology [69–72]. DED techniques are mostly used to improve wear, impact and corrosion resistance of mechanical components as well as to repair worn-out or damaged high-value components [73]. In addition, DED and WAAM has also been used to fabricate compositionally graded structure for components in service at extreme environments that require localised properties [74]. The substrate of DED machines is typically arranged in one of these two configurations, depending on the application required [15]: (i) 3-axis system which means the substrate is in stationary position, or (ii) 5- or 6-axis system which allows the substrate to rotate while the feedstock is being deposited. The latter configuration enables fabrication of more complex geometries.

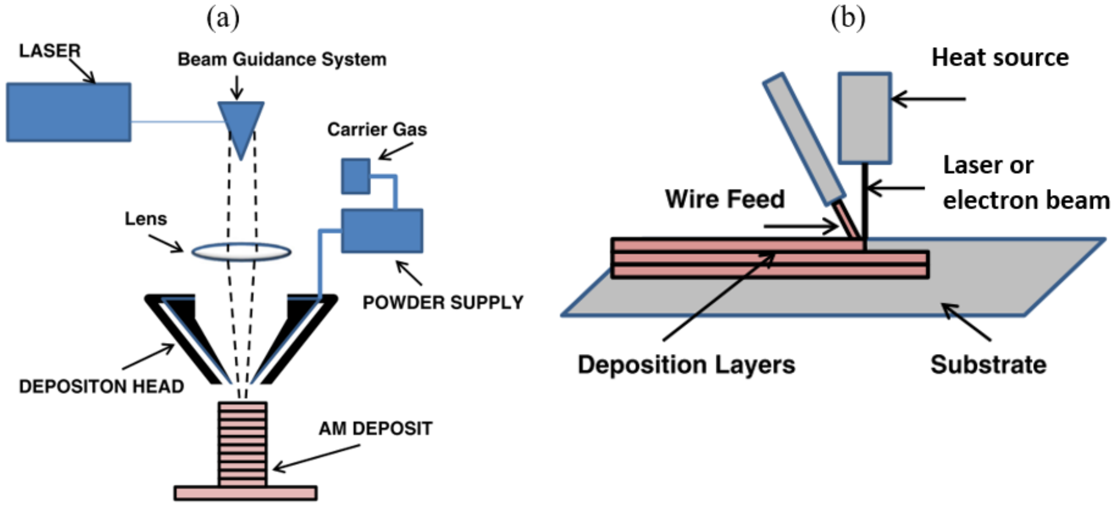

Fig. 2-2 Schematic of (a) powder-fed and (b) wire-fed DED-based technique [40]. Reproduced with permission of the rights holder.

2.1.3 Metal AM processing

2.1.3.1 Material properties and characteristics

The quality of materials (powders and wires) are important in determining the quality of AM-processed parts. Flowability and apparent density are two essential properties that influence the quality of metal powders used in PBF and DED processes, all of which are determined by their size, shape, surface morphology, composition and internal porosity content [75]. Similar to powder metallurgy, the quality of metal powders used in metal AM is also directly influenced by powder production processes. Gas atomisation (GA), plasma rotating electrode (PREP) and rotary emission (RE) are the most common techniques to produce metal powders [76]. However, internal porosity which is commonly present in GA powders due to entrapped inert gas during production results in gas-induced porosity in AM parts. On the other hand, PREP-produced powders do not contain internal porosity and thus have higher quality compared to its GA counterpart [45,77,78].

The flowability and apparent density could be improved by using smooth, spherical powder particles. In addition, a wider range of powder particle size distribution typically results in higher densification levels (> 99%). This is because the finer particles are able to fill the interstitial spaces between larger particles [79]. Furthermore, the combination of deploying smooth and finer powder particles contributes to smoother surface roughness in the final part compared to using irregular shaped particles [80]. However, finer powder particles are usually more expensive compared to the larger ones because typical powder production techniques have higher yield of larger-sized particles [15].

2.1.3.2 Heat transfer and thermal history

AM process for metals is characterised by short interaction time between heat source and feedstock materials. This often leads to non-equilibrium heating/cooling cycle due to the heat transfer and thermal history experienced throughout the process [81]. Heat conduction and convection are two dominant heat transfer modes in PBF and DED processes. In DED processes, heat is conducted from the focal point of the laser beam to the build material as well as the substrate, while heat convection occurs between the heat source and the shielding gas [15]. PBF processes experience similar heat transfer modes, but heat conduction may decrease due to powder bed acting as a thermal insulator in SLM. In addition, heat convection is much less apparent in EBM process because of the near vacuum or vacuum environment due to the nature of electron behaviour. As a result, radiative and conductive losses from the build surface and to the machine respectively become the major heat transfer mechanisms in EBM. Nevertheless, numerous melting/cooling cycles i.e. the thermal history of DED and PBF processes cause complex phase changes, mass transfer and microstructural development [82].

2.1.3.3 Metallurgical phenomena

Three important metallurgical phenomena occur within the melt pools as a consequence of the complex heat transfer and thermal history during metal AM processing, including unmelted powders (unmelts), spatter ejection, and generation of denudation zones (DZ) [44,83]. These phenomena influence part quality, microstructures, and mechanical properties of the fabricated components.

In PBF and powder-based DED processes, the entire powder bed and powder/wire feedstock need to be completely melted to minimise voids and unmelts. One of the reasons for unmelts in PBF processes could be caused by non-uniform powder spreading on the powder bed at the beginning of the process [44]. Material composition also contribute to the formation of unmelts in DED-processed parts. For example, excessive vanadium content in the laser deposition of Ti6Al4V and 316L SS gradient parts results in excess unmelted powder due to insufficient melt pool temperature, indicated by inhomogeneous powder mixing and grain morphology [84].

The unmelts, together with other defects such as porosity are found to have negative impact on the mechanical properties of the fabricated metal parts [68,85–87]. Post-processing, e.g. heat treatment and HIP as well as optimisation of processing parameters are among the efforts that could be taken to minimise or eliminate unmelts [88]. Until now, not many studies have been conducted on elucidating the causes and effects of unmelts in AM-fabricated metallic components [89–91].

Spatter could be observed in both PBF and DED processes and is common in conventional welding techniques. It is manifested in the form of very hot sparks coming off from the build area in contact with the heat source. The resulting high-energy beam during metal AM operation creates localised boiling which causes metal droplets to evaporate from the melt pool [92]. The evaporated metal vapours then exert recoil pressure onto the melt pool, which drives liquid droplets either to the edges or to the centre of the melt pool as shown in Fig. 2-3(a) [93]. The occurrence of this phenomenon is caused by the Marangoni convection that influences the heat flow pattern on the surface of the liquid [94]. Marangoni convection is essentially a convective thermocapillary fluid flow inside the melt pool caused by steep thermal gradients experienced in metal AM processes. The occurrence of this phenomenon depend on the temperature gradient and surface tension caused by the processing parameters, and influences the size and depth of the melt pool generated [49,95,96].

If the recoil pressure exceeds the surface tension in the melt pool, then liquid metal ejection might occur, causing droplet spatter (Fig. 2-3). In addition, the recoil pressure is also found to cause the spattering of raw metal powders (powder spatter) on the powder bed (Fig. 2-3(a)) [93]. A number of recent studies have been dedicated to the occurrence of spatter ejection in metal AM processing. For example, Khairallah et al. [97] modelled the physics of complex melt flow which leading to pore formation, spatter, and denudation zones in L-PBF processes. They studied the mechanisms of each phenomenon by including recoil pressure and Marangoni convection model in the ALE3D commercial multi-physics simulation code.

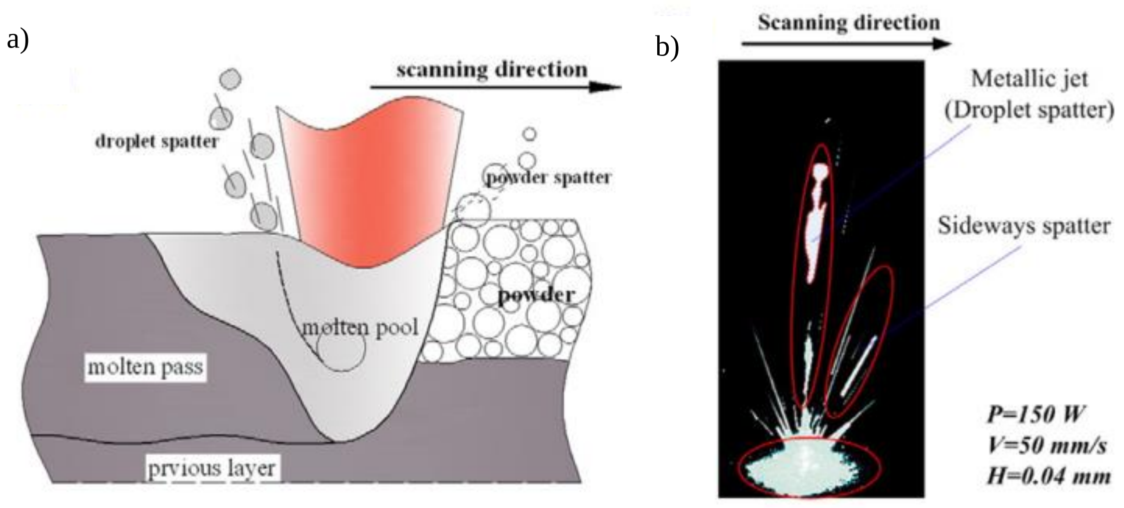

Fig. 2-3 (a) Illustration of spatter ejection mechanism in metal AM processing, (b) Direction of metal droplet spatter (upwards) and that of raw metal powder spatter (sideways) [93]. Reproduced with permission of the rights holder.

Simonelli et al. [95] studied the SLM of 316L SS, AlSi10Mg and Ti6Al4V alloys and found that the spatter ejection contributes to the formation of oxide layers that could deteriorate the mechanical properties of the fabricated samples. Two measures were proposed to reduce spatter ejection and hence improve part quality. The first method initially sintered the powder bed with low energy density before re-melting each layer using higher energy density. This less intense heating mechanism could reduce the generation of plasma plumes due to the difference in absorptivity levels between metallic powders and solid bulk metals [98,99]. Another proposed method was employing pulsed laser instead of continuous wave laser emission to reduce laser power. This allowed the laser power density to be distributed over a longer time period which resulted in better melting of the feedstock materials [99].

One important consequence of the evaporation of metal vapours due to irradiation of high-energy beam is the resulting gas flow, which leads to the formation of ‘denudation zone’ (DZ). DZ is essentially a region of displaced powders driven by the entrainment of particles from the gas flow, which clears the powders along the path of the laser towards the sides of the scan track [100]. Matthews et al. [100] recently investigated the influence of gas pressure and beam power on the formation of DZ, in which two important observations were made. Firstly, at high pressures, the entrapment of powder particles in a shear gas flow due to rapid metal vapour flux could cause either: (i) the powders to be ejected away from the melt pool, or (ii) the powders being pushed towards the region of solidified track, resulting in extra material being consolidated in the melt pool (Fig. 2-4 (a)). At low pressures, the powder particles were driven away from the melt pool due to metal vapour ejection, hence creating a region without any powder particles at the vicinity of the solidified track (Fig. 2-4(b)) [100].

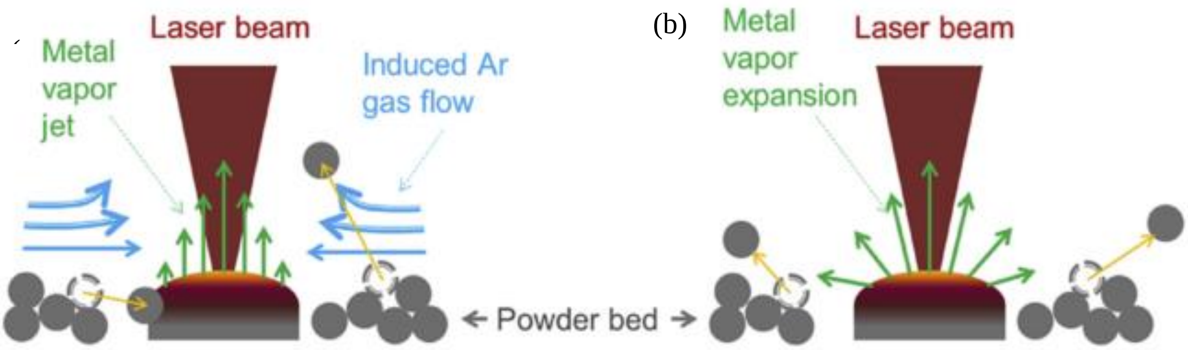

Fig. 2-4 Denudation phenomenon during metal AM processes at (a) high pressure and (b) low pressure [100]. Reproduced with permission of the rights holder.

Kanko et al. [101] revealed that radiation scattering, thermal conduction and capillary phenomenon cause complex particle interactions which contribute to DZ formation adjacent to the melt pool. Yadroitsev et al. [102] explained that the presence of DZ reduces the height of scan tracks after successive scanning, but it could be controlled by varying hatch spacing. Another research on laser deposition AM of nickel superalloys and MMCs conducted by Cooper [103] found that some powders were absorbed into the melt pools due to the denudation phenomenon. This created an area of excess materials at the sides of the scan tracks which actually increased the height of the scan tracks instead of reducing it, similar to the observation made by Matthews et al. [100]. Thus, proper control of pressure and hatch spacing are necessary to avoid the generation of voids and ensure optimum powder consolidation.

2.1.4 Process-microstructure-property relationships

2.1.4.1 Energy density and scan strategy

AM processes follow the progressive line-layer-bulk build philosophy [104]. This process begins with a single line scanning by the heat source, in which heat source power, P_L and scan speed, v are the most important parameters. The quality of resulting scan tracks is assessed by a performance matrix, termed linear energy density (LED), given by [104]:

$$LED = \frac{P_L}{v} \qquad \text{Eqn. 2-1}$$

Once scanning of multiple lines is completed, a single layer is formed, which introduces another important parameter, hatch/scan line spacing, h_L. A suitable layer thickness, d_L needs to be selected so that multiple successive layers could be consolidated to form the bulk component as required. Here, another performance matrix termed volumetric energy density (VED) is often used to evaluate the quality of AM parts, given by [105]:

$$VED_{L-PBF} = \frac{P_L}{v h_L d_L} \qquad \text{Eqn. 2-2}$$

While both LED and DED are common in L- PBF processes, E-PBF and DED-based techniques employ a slightly different energy density relationship. In electron beam based PBF, the acceleration voltage, U and current, I of the electron beam are taken into consideration, thus modifying the VED into [43,106]:

$$VED_{E-PBF} = \frac{4UI}{\pi v s} \qquad \text{Eqn. 2-3}$$

where s is the scan line spacing in this case [43,106]. Meanwhile, the energy density relationship in DED-based processes incorporates material feed rate (powder or wire), F_{DED}, heat source power, P_{L}, and cladding speed, u, which are related by [107]:

$$VED_{DED} = \frac{P_L F_{DED}}{u} \qquad \text{Eqn. 2-4}$$

Based on various studies, high P_{L} and UI, as well as low v and u values, and therefore high energy densities are desired to obtain smooth tracks and solidified layers [83,104,108,109]. These energy density terms are often generalised for most materials that are processed by AM. However, Gibson et al. [10] argued that in some cases for certain materials, energy density alone is not enough to assess the quality of metallic AM parts due to various metallurgical defects and instabilities. They suggested the process mapping approach for specific AM processes and materials to assess the quality of AM-fabricated metallic parts. Yusuf et al. [83] tabulated the processing conditions for particular metallic materials with specific metal AM machines obtained from various literature with the view to aid future process mappings. In addition, Bertoli et al. [110] explained that the VED is unable to include the complex physical phenomena occurring in the melt pool, and hence should not be the only design parameter considered when fabricating metallic parts using AM.

On the other hand, various scan strategies have been developed for PBF-based metal AM processing, including: (i) uni-directional (Fig. 2-5(a)), (ii) bi-directional (Fig. 2-5(b)), (iii) line melting with snaking fill (Fig. 2-5(c)), (iv) island or chessboard (Fig. 2-5(d)), (v) paintbrush (Fig. 2-5(e)), and (vi) spiral (Fig. 2-5(f)) scanning [15,111]. Of these scan strategies, the influence of uni-directional, bi-directional and island scanning on the microstructure and properties of AM-fabricated parts have been widely investigated [112–114]. For example, Thijs et al. [115] investigated the influence of three different scan strategies; uni-directional, alternating (bi-directional), and cross-hatching (rotating the uni-directional scan direction by 90° at every layer) on the microstructural evolution of Ti6Al4V processed by SLM. Different microstructure could be observed in the fabricated parts, following the different scan strategies. A slanting herringbone pattern was obtained for the alternating direction as shown in Fig. 2-6(a), while the herringbone pattern becomes straight when uni-directional scan was used (Fig. 2-6(b)) [115]. However, the microstructure becomes more equiaxed as cross-hatching strategy was applied (Fig. 2-6(c)) [115]. They explained that these variations were caused by the short beam-material interaction, high temperature gradients and the highly localised heating/cooling cycle experienced by metal AM processes.

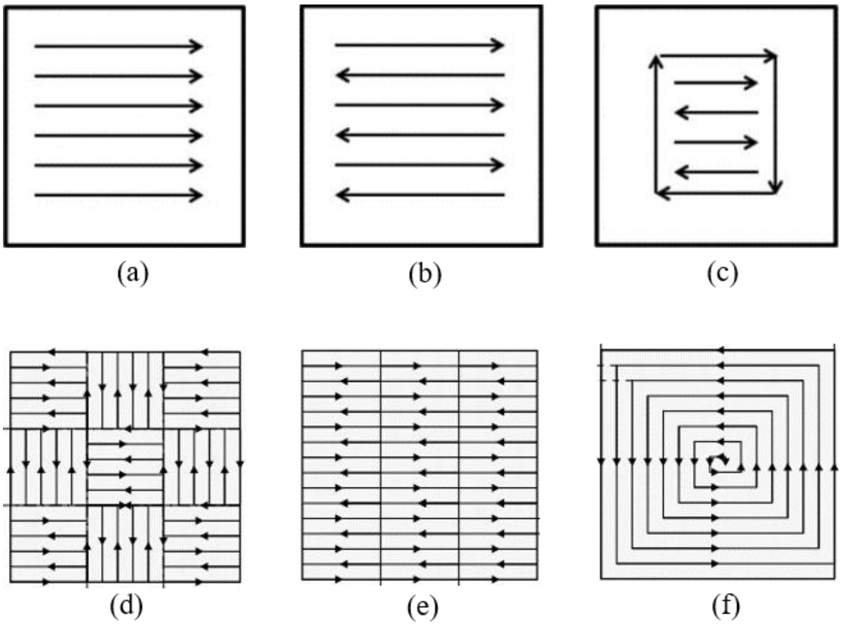

Fig. 2-5 Scan strategies typically used in metal AM processes: (a) unidirectional, (b) bi-directional, (c) line melting with snaking fill [15], (d) island, (e) paintbrush, and (f) spiral [111]. Reproduced with permission of the rights holder.

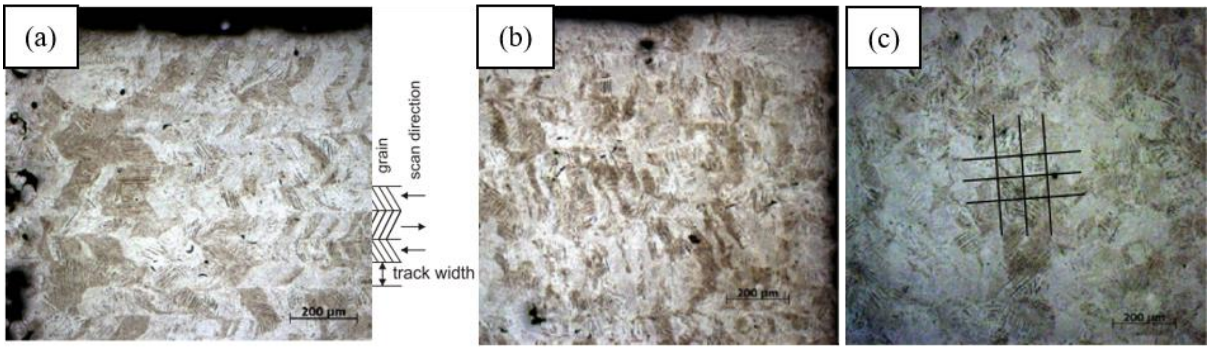

Fig. 2-6 Influence of scan strategies on microstructure of SLM-fabricated Ti6Al4V samples: (a) slanting herringbone for alternating scan direction, (b) straight herringbone for uni-directional scan (b), and (c) equiaxed microstructure for cross-hatch scan strategy [115]. Reproduced with permission of the rights holder.

Lu et al. varied the ‘island’ size (2 x 2 mm^2, 3 x 3 mm^2, 5 x 5 mm^2 and 7 x 7 mm^2) to determine their effect on the microhardness and residual stress of SLM-fabricated IN 718 superalloy [116]. It was revealed that the smallest ‘island’ size (2 x 2 mm^2) corresponded to highest microhardness and lowest residual stress values, while the lowest microhardness value was found at the largest ‘island’ size (7 x 7 mm^2) and the largest residual stress value was obtained when the ‘island’ size was 3 x 3 mm^2. Nevertheless, the application of island/checkerboard scanning strategy has been found to reduce residual stress and deformation in metal AM processes [117–119]. For example, Jhabvala et al. [111] modelled various scanning strategies to determine their impact on the SLM processing of metallic materials. The ‘island’ strategy was found to correspond to homogeneous heating of the feedstock materials compared to other strategies. This is because the area (square) that needs to be heated in one passing is small, allowing temperature homogeneity to be sustained [111].

In addition, the lowering of residual stress and distortion levels in AM metallic parts when using this scan strategy is attributed to the reduction of temperature gradients in the scanned regions, as the heat generated during processing is better distributed throughout the scanned area (x-y plane) [120]. On the other hand, the movement of either the feedstock material feeding system or the substrate limits the scan strategies that can be used in DED processes [15].

2.1.4.2 Melting and solidification microstructures

In PBF and DED processes, small melt pools that can be regarded as small castings are created via melting of the powder bed upon interaction with the laser source. The dimensions of these melt pools are dictated by the surface tension induced by fluid flow, i.e. Marangoni convection, which in turn is controlled by the processing parameters. Since melt pools are the starting point of solidification microstructures in the fabricated parts, their morphologies need to be controlled via careful selection of processing parameters to attain the desired microstructures.

Typically, three types of melt pools could be obtained, which largely depend on the heat source power (P_L for L-PBF and DED; UI for E-PBF) and scan speed (v for L-PBF and E-PBF; u for DED) used during processing [121]: (i) balled, (ii) discontinuous and fragmented, and (iii) smooth and continuous. Ideally, smooth and continuous melt pools are desired to achieve desirable solidification microstructures, which correspond to high P_L or UI and low v or u values, i.e. high LED and VED values.

The solidification morphology of laser melted metals and alloys is largely dependent on the temperature gradient (G_L), the solidification (growth) rate (R) at the solid-liquid interface, and the extent of constitutional undercooling (ΔT) in the localised melt pool, resulting in microstructural variation. The formation of microstructures in solidified structures is described by the following equation [122,123]:

$$\frac{G_L}{R} < \frac{\Delta T}{D_L} \text{ for plane and equiaxed microstructure} \qquad \text{Eqn. 2-5}$$

$$\frac{G_L}{R} > \frac{\Delta T}{D_L} \text{ for cellular and dendritic microstructure} \qquad \text{Eqn. 2-6}$$

where D_L is the diffusion constant. Based on these equations, it follows that planar, cellular, and dendritic (columnar and equiaxed) are expected to be obtained from high to low G_L/R values consecutively. In addition, the size of these solidification structures (microstructures) is determined by the cooling rate (G_L x R) and is strongly influenced by the type of process used to fabricate the desired materials. Generally, finer microstructures will be obtained at high cooling rates and vice versa. The type and size of the microstructure obtained from various extents of constitutional undercooling and cooling rates can be generalised based on the solidification map shown in Fig. 2-7 [124].

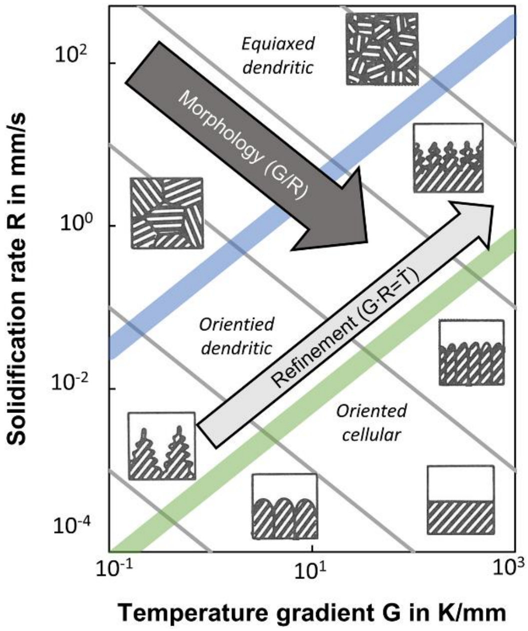

Fig. 2-7 Solidification map portraying the resulting microstructures obtained as a function of temperature gradient (G_L), growth rate (R), G_L/R and G_L x R [124]. Reproduced with permission of the rights holder.

Based on Fig. 2-7, planar solidification mode is obtained at high G_L and low R, cellular structure at low to moderate G_L and R values, while dendrites are formed at low to medium G_L and medium to high R values. For example, conventional casting process of 316L SS typically experience lower undercooling and cooling rates, hence yielding coarse-grained columnar microstructures (20 – 60 μm) [125]. Higher undercooling and cooling rates in welding process of the same material results in finer columnar grains, roughly half the grain size obtained during casting [126].

Metal AM processes normally experience high constitutional undercooling and cooling rates (up to 10^5 – 10^7 K s^{-1}), which is similar to or higher than that of laser or electron beam treated materials, due to repeated localised rapid melting and cooling compared to cast and welded parts, thus yielding much smaller grain sizes as reported in various literature [127–130]. In addition, the continuous re-melting of previously solidified powder layers due to the layer-wise manner of AM processes promote a strong epitaxial growth trend between successive layers. The strong epitaxial growth encourages the formation of columnar grains in AM materials, similar to those obtained via conventional directional solidification (DS) process [131].

2.1.4.3 Microstructural evolution and mechanical properties

The mechanical properties of AM metallic parts are highly dependent on the microstructure obtained upon solidification, which in turn, is influenced by the processing parameters. The repeated rapid heating/cooling cycle and high cooling rates ($10^3 – 10^8$ K s^{-1}) during metal AM processing, or in other laser-based processes lead to fast solidification and produce unique microstructures. As a general guideline, the microstructures of AM metallic parts typically consist of: (i) melt pools made up of individual solidified scan tracks with patterns corresponding to the scan strategy, (ii) cellular sub-structures growing within and across the melt pools, (iii) columnar and/or equiaxed grains depending on the cross-section studied, and (iv) equilibrium or non-equilibrium phases [132–134]. Gu et al. [104] outlined four characteristics for AM metallic parts:

(i) Grain refinement and fine microstructures are often expected as there is insufficient time for grain development and grain growth in the final parts.
(ii) The rapid solidification in metal AM processes is a non-steady state process due to the occurrence of Marangoni convection in the melt pool as a result of surface tension and temperature gradients.
(iii) AM metallic parts often exhibit anisotropic behaviour at different planes and directions due to the layer-wise build manner, which causes kinetic limitation in crystal growth.
(iv) The difference in microstructures observed at different cross-sections is attributed to the change in heat flux direction i.e. different thermal histories within a single layer and across successive layers.

Various studies have been carried out to determine the influence of processing parameters on the microstructures and hence, mechanical properties of metallic parts fabricated by AM [117,135–139]. For example, Han et al. [140] found the set of optimum energy density value to obtain high relative densities (> 99.95%) and high microhardness values (> 377 HV) when processing Ti6Al4V by SLM. Such high densification level and HV values are attributed to the decreased width and spacing of the acicular martensites inside the columnar prior β grains within an optimum energy density range (120 J mm^{-3} to 250 J mm^{-3}). Jue et al. [141] revealed that the mechanical properties of SLM-built Al-Al_2O_3 could be optimised when reducing scan speed from 750 mm s^{-1} to 550 mm s^{-1} at a constant laser power (130 W). This is achieved by homogeneously dispersing Al_2O_3 particles in the melt pool at this scan speed, resulting in the removal of defects such as interfacial microcracks and shrinkage porosity. Another study on the SLM fabrication of beta-solidifying titanium aluminide (TNM-B1) obtained a nearly lamellar β microstructure [142]. This microstructure is usually associated with high strength, high creep strength, and moderate ductility at room temperature. On the other hand, as the scan speed is increased to 200 m s^{-1}, the β phase transforms into a martensitic α' structure. Zhang et al. [143] observed the evolution of dendrite grains to equiaxed grains under high temperature gradients when producing Mg-9%Al by SLM. As scan speeds increase, these equiaxed grains are further refined (Fig. 2-8).

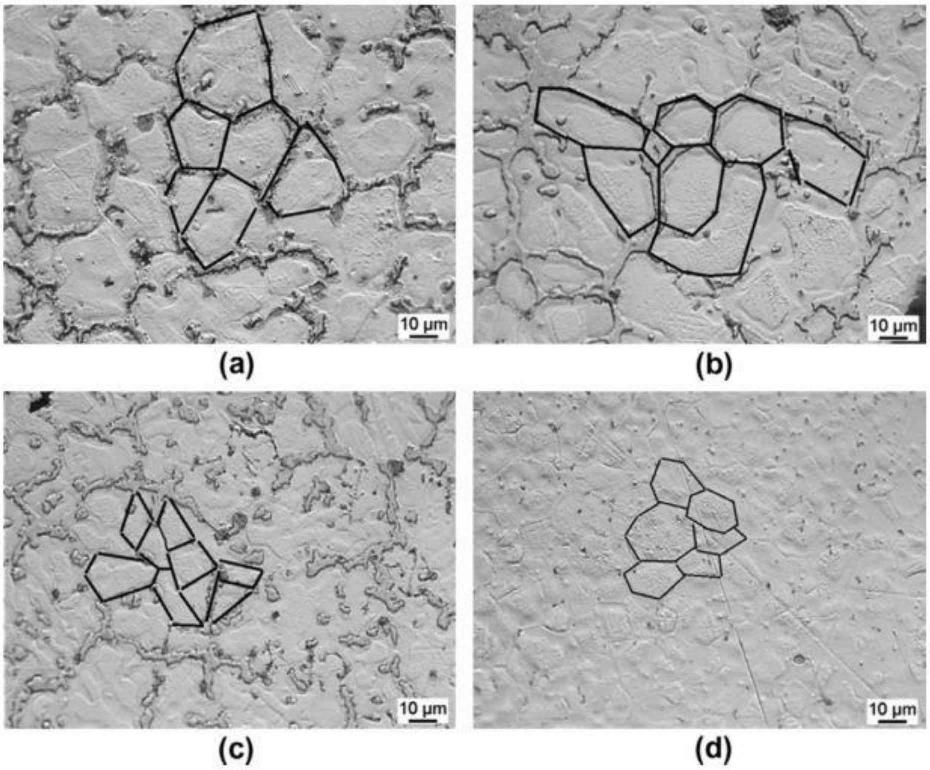

(a) (b) (c) (d)

Fig. 2-8 Optical micrographs showing microstructural characteristics of etched Mg-9%Al samples processed by SLM with different parameters: (a) 10 W, 0.01 m s^{-1}; (b) 15 W, 0.02 m s^{-1}; (c) 20 W, 0.04 m s^{-1}; (d) 15 W, 0.04 m s^{-1} [143]. Reproduced with permission of the rights holder.

The mechanical properties of AM metallic parts are generally assessed by their static properties, e.g. yield and tensile strengths, microhardness and dynamic properties, e.g. creep and fatigue behaviours. However, metal AM processes are subjected to anisotropy, which causes variations in mechanical properties at different part orientation and build direction [144–148]. Such anisotropy is caused by the layer-wise build manner and the rapid heating/cooling cycle experienced throughout AM processing, resulting in directional variation, heterogeneous distribution of grain structures and structural discontinuities [146,149].

Anisotropy in metallic AM metallic parts is normally obtained when they are built in different directions, which contributes to the variation in mechanical properties [150–153]. In some cases, the yield and tensile strengths of AM-fabricated parts are close to if not superior than conventionally manufactured bulk components e.g. cast and wrought, which are often attributed to the finer microstructures obtained via AM [68,154]. On the other hand, studies have also shown that the yield and tensile strengths of two similar AM metallic parts built in different directions can be different although the same processing parameters and scan strategy are used [155,156]. Such anisotropy is largely influenced by the content of porosity and other defects, residual stress levels, and crystallographic orientation of the as-built parts [157–159]. Post-processing such as heat treatment and HIP could improve the yield and tensile strengths, but they could cause dimensional shrinkage and reduce part quality and structural integrity [160].

On the other hand, microhardness values are observed to be typically higher in the scan direction (x-y plane) than that at the build direction (z-axis), which is due to the finer, more equiaxed grains attained at the x-y plane compared to the mostly larger columnar grains that grow epitaxially along the z-axis [161–163]. Recent experiments have shown higher microhardness values in AM metallic parts compared to those manufactured by conventional techniques. For example, relatively higher microhardness values were observed in AM 316L SS parts (265 – 270 HV) compared to their cast counterparts (< 200 HV) [156]. This is largely due to the mix of fine equiaxed and columnar grains obtained as the result of the rapid solidification and high cooling rates in metal AM processes.

Many researches on the mechanical properties of AM metallic parts have focused on static properties from static loading, e.g. hardness, yield strength, and tensile strength. However, studies on cyclic loading, particularly creep and fatigue behaviours are still limited, despite its importance especially in the aerospace and automotive industries [88,164,165]. Moreover, studies on these properties are currently only limited to some materials, e.g. stainless steel, AlSi10Mg and Ti6Al4V. For example, Gong et al. [166] and Seifi et al. [167] investigated the influence of defect distribution on the fracture resistance and fatigue behaviour of Ti6Al4V processed by SLM and EBM, respectively. They found that the presence of porosity and other defects significantly lowers the fatigue limits and fracture toughness of the as-fabricated parts. Spierings et al. [168] found that the fatigue behaviour and endurance limit of both SLM-built 316L and 15-5 PH stainless steel were worse than their CM counterparts. In addition, Brandl et al. [169] demonstrated that post-processing heat treatment had a larger impact on the fatigue behaviour of SLM-fabricated AlSi10Mg compared to build direction.

Furthermore, the microstructures and properties of AM metallic parts are not only controlled by processing parameters but also by the metal AM technique used. Hence, a single material fabricated by two different metal AM techniques may result in different microstructure and mechanical properties [170]. For example, Zhao et al. [171] reported that processing Ti6Al4V by SLM resulted in fine α' martensites, while $\alpha + \beta$ grains were obtained from the same material but fabricated by EBM. The finer α' martensites were responsible for the higher tensile strength but lower ductility for the SLM material compared to its EBM counterpart. Marchese et al. [172] studied the fabrication of IN 625 superalloy by SLM and LMD and found that even though the build rate is higher in DMD, the geometrical accuracy and the microhardness are lower than SLM-built parts. Ma et al. [170] attributed the higher tensile strength in SLM 316L SS compared to that of LC counterparts due to the much finer columnar grains obtained via SLM.

2.1.4.4 Defects in AM metallic parts

Porosity, balling, cracking, and delamination are all common defects in AM metallic parts. Porosity in the as-built parts could be manifested as gas-induced, process-induced, or keyhole mode as shown in Fig. 2-9 [15,90].

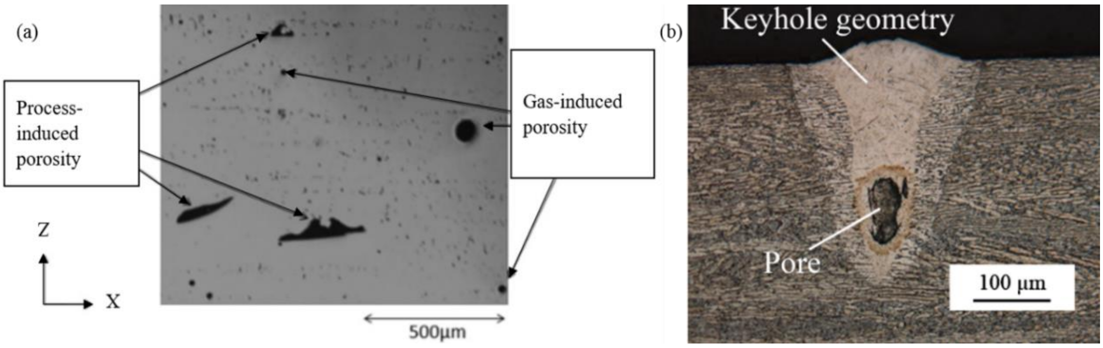

Fig. 2-9 Examples of (a) Process- and gas-induced porosity [15] and (b) keyhole porosity [90]. Reproduced with permission of the rights holder.

Spherical gas-induced porosity is caused by internal porosity resulting from gas entrapment during metal powder production. In contrast, non-optimum processing parameters used in AM contribute to process-induced porosity that is often characterised by irregular-shaped pores (Fig. 2-9(a) [15]. Insufficient power applied to powder bed could result in unmelted powder layers causing lack-of-fusion regions in the completed parts. Meanwhile, spatter ejection caused by excessive power could also result in another type of process-induced porosity called shrinkage porosity [44]. Some powder particles that evaporate due to spatter ejection leave regions of melt pool with incomplete powder solidification causing formation of pores in the solidified structure. In addition, ‘keyhole’ porosity could also be another consequence of spatter ejection, in which powder and/or metal vapour are ejected out of a melt pool, creating a region of void inside the melt pool (Fig. 2-9 (b)) [90].

Fig. 2-10(a) exhibit balling in AM metallic parts, often manifested as either the formation of coarse ellipsoidal balls with diameter ~ 500 µm (type I), or that of fine spherical balls of ~ 10 µm in diameter (type II) [173]. Balling type I is associated with poor melt wettability arising from low laser power applied during processing, which results in limited liquid formation and low degree of undercooling of the melt [108,173]. This increases the viscosity of the liquid-solid mixture considerably, impeding liquid flow and particle rearrangement, causing aggregation of the molten powder particles as coarsened balls roughly the size of the laser spot diameter [108]. On the other hand, while increasing the laser power enables adequate melting of the powder to form stable and continuous cylindrical scan tracks, further increase in scan speeds gradually decreases the scan track width and the working temperature, thus significantly increasing the capillary instability of the melt pool [173]. This results in liquid droplet splashing from the molten scan track surface due to surface energy reduction, forming fine spherical balls upon solidification [108]. In particular for stainless steel powder, oxidation of Cr occurs due to its reactivity with oxygen to form an oxide layer on the surface of the substrate or the melt pool, resulting in poor wettability that causes the liquid metal to wet the oxide layer and preferentially minimising surface area by balling instead [108]. Balling is detrimental to AM metallic parts because it increases surface roughness, impede deposition of fresh powders on previously solidified layers, and induces pore formation at the discontinuities where solidified material is absent, which ultimately degrade material properties, as well as dimensional and structural integrity [108,173]. So far, efforts to minimise balling in AM metallic parts include optimising processing parameters by applying high laser power and low scan speed within a particular processing window, i.e. optimising LED, and reducing oxygen content in the processing chamber to ~ 0.1% [15,108,173–176].

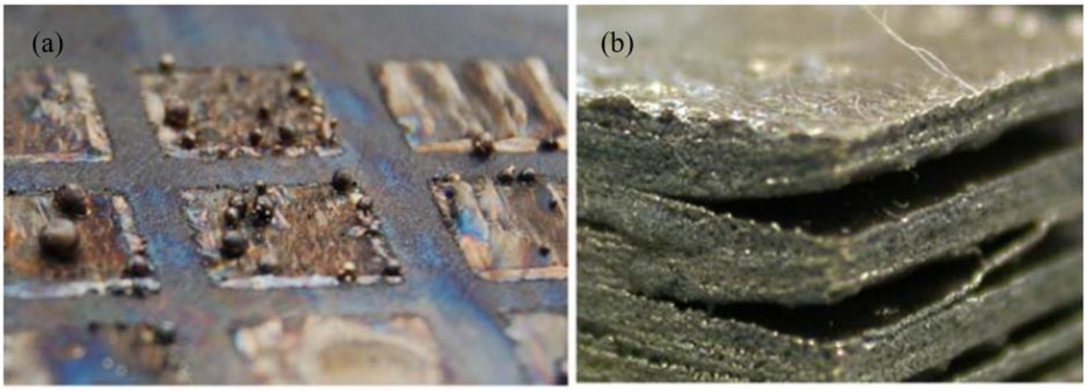

Fig. 2-10 (a) Melt balls formed due to balling, (b) Delamination between solidified layers caused by macrocracks, both in EBM-fabricated stainless steels [177]. Reproduced with permission of the rights holder.

Macroscopic and microscopic cracks are common defects in AM metallic parts, which are process and material dependent, and are significantly influenced by thermal history. Macroscopic cracks are typically caused by process-induced porosity and are visible to the naked eyes. Individual macroscopic cracks in solidified parts may lead to delamination i.e. separation of successive solidified layers due to either incomplete powder melting or insufficient re-melting of previously solidified layers (Fig. 2-10 (b)) [177]. Such cracks are not localised like balling and porosity and hence cannot be remedied by various post-processing methods such as HIP and annealing. On the other hand, microscopic cracks (microcracks) are categorised as solidification cracking and grain boundary cracking (Fig. 2-11 [178]). Solidification cracking is caused by thermal stress in the melt pool induced by the thermal gradients that exist between the cooler solidified layers and the yet to be solidified layers which have higher temperatures [118]. Higher thermal gradients resulting from higher energy densities result in higher thermal stress and increased susceptibility to solidification cracking [15]. On the other hand, grain boundary cracking develops along the grain boundaries of the as-fabricated parts depending on the precipitates formed and the grain boundary morphology [118].

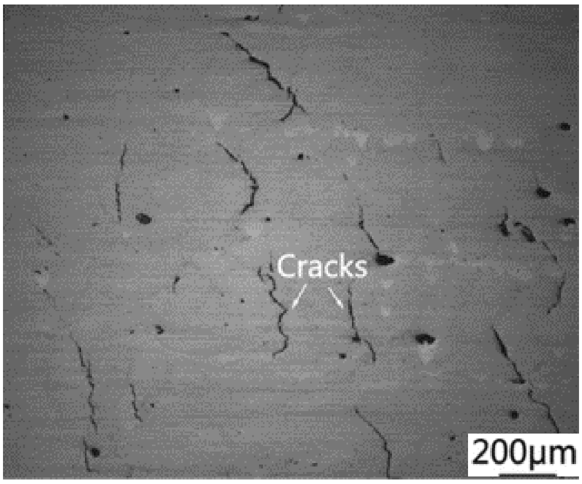

Fig. 2-11 Microcracks in metallic AM parts [178]. Reproduced with permission of the rights holder.

2.1.4.5 Post-processing

A multitude of post-processing steps are required to prepare AM metallic parts for end-use, including removal of excess powder, removal of parts from substrate, heat treatment procedures to improve mechanical properties, and surface finish treatments to attain the finishing and geometrical tolerance as required. In particular, thermal post-processing of AM metallic parts is of significant interest to relieve residual stress, minimise porosity and internal cracks, improve the mechanical performance, and tailor the microstructures to achieve the desired properties according to service requirements. Typical thermal post-processing approaches include stress relief, annealing, HIP, solution treatment (ST), and aging.

Annealing is often carried out on meal AM parts to remove residual stress and provide stress relief. As a guide, annealing for stress relief should be carried out at temperatures high enough to provide atomic diffusion from high to low stress regions and relieve internal strain energy, but for a period short enough to suppress grain growth and recrystallisation [15]. For example, Ti6Al4V is annealed for 2 hours at 700 – 730°C [179], and 30 minutes at 982°C or 90 minutes at 1065 ± 15°C [180] for IN 718. However, recrystallisation and grain growth are sometimes desired to encourage the growth of equiaxed grains from the columnar grains typically obtained from metal AM processing. For example, recrystallisation was observed in the microstructure of SLM-fabricated iron [181] driven by the thermal residual stress existing in the fabricated part. Amato et al. [180] observed the partial rcrystallisation in SLM-fabricated IN 718 due to stress relief annealing, which resulted in an inhomogeneous grain structure distribution.

On the other hand, HIP is typically conducted on AM metallic parts to close internal pores and cracks [118]. The combined of relatively high temperature and pressure in HIP, e.g. at 900°C and 900 MPa for 2 hours [182], and at 1120°C and 200 MPa for 4 hours [15], both for Ti6Al4V are able to close the internal pores and cracks by the recrystallisation of grains surrounding the pores and cracks. However, pores and cracks existing on the surface of the fabricated parts due to manufacturing defects, i.e. open pores and cracks may not be resolved by HIP since they might penetrate deeper into the material upon the continuous heat and pressure applied in HIP cycles, thus causing more damage rather than improvement. Furthermore, typical HIP cycles often cause grain growth, thus yielding large grains, resulting in loss of strength in AM metallic parts [183].

Moreover, solution treatment (ST) and/or aging are often carried out for precipitation-strengthened materials, e.g. IN 718. ST dissolves undesired secondary phases, while aging promotes the growth of precipitates that strengthen the material. Sometimes, ST and aging are combined in a single process sequence, referred to as STA, e.g. for IN 718 [184]: ST at 720°C for 8 hours, followed by cooling at 620°C and holding on to the temperature for 18 hours.

2.1.5 Mutlti-material AM

2.1.5.1 Limitations of single-material AM

In general, metal AM technology draws parallel to conventional welding in terms of the material joining principle; i.e. through solidification of melt pools created by melting the feedstock material. Furthermore, in particular for PBF and DED techniques, the starting raw powder material is similar to those used for the well-established powder metallurgy process. Thus, Gorsse et al. [127] outlined two characteristics of metallic materials that can be processed by metal AM processes: (i) the materials need to possess good weldability to avoid cracks upon solidification for all metal AM processing categories, and (ii) the raw powders used for PBF and DED processes needs to be spherical in the range of 1 – 10 µm to ensure good packing density and to achieve homogeneous powder deposition. Therefore, materials such as Al (AlSi10Mg, AlSi12), Ti (commercially pure Ti, Ti6Al4V), stainless steel (304L and 316L) and Ni (IN 625, IN 718) alloys have received significant attention in first generation metal AM (since the 1990s). This is because they have matured in terms of research and have been widely used in various welding and powder metallurgy industries, thereby readily available and technologically compatible with metal AM processes [127].

However, rapid evolution in technology may increase the demand for more advanced materials with complex structures. Examples of such applications include bimetallic structures, graded material compositions, or tailored properties within different sections of a single component to suit specific requirements. For example, Ni-Ti structures are popular in the biomedical industry. The combined unique superelasticity, biocompatibility, shape memory effect and superior corrosion resistance properties are utilised in manufacturing vascular stents and devices to replace bones and tissues in human bodies [185]. In addition, the graded composition of IN 625 that has high strength and corrosion resistance at elevated temperatures and 304L SS which has lower cost and mass are often used in high performance engine valve stems for the automotive industry [186].

Unfortunately, single-material AM systems are not able to deliver these unique outputs due to limitations in machine design and architecture. Hence, multi-material AM (MMAM) becomes a viable solution to address the restriction of single-material AM in MM processing of functional materials with tailored properties [7,187–189]. In this respect, current researches have focused and progressed more on DED processes compared to their PBF counterpart. The architecture of DED-based AM machines such as LENS, LMD and DMD are modified to enhance their capabilities of processing multiple metallicc materials and/or produce graded material compositions. For example, LENS has been used to successfully fabricate compositionally graded stainless steel-Ti by building compositionally graded 316L SS and Ti6Al4V with a NiCr interlayer [190]. Similarly, porous and functionally graded structures of Ni-Ti for load bearing implants, e.g. hip bone replacement were produced by LENS [191]. In addition, Ti6Al4V bone implants were coated by graded Co-Cr-Mo to improve its wear resistance using the same technology [192].

2.1.5.2 Multi-material deposition strategies

In single-material metal AM, scan strategies (PBF) and powder deposition aspects (DED) play important roles in determining the success of layer solidification to form the final structure. Similarly, material deposition strategies are also important in multi-material processing and in producing of functionally graded materials (FGM) by MMAM. For example, Suresh et al. [193] divided the build method for FGM components into two stages: (1) addition of whole layers which consist of different materials at different layers, and (2) creation of a gradient material composition by diffusion or mass transport. However, in general, there are three key configurations to which multiple materials could be incorporated in a single build of a MMAM system as shown in Fig. 2-12: (1) discrete material change between whole layers, (2) gradual material change within layers, and (3) gradual material change between and within layers [7]. Discrete material change involves the joining of two or more dissimilar materials with a defined border or sharp interface between the materials, whereas a smooth transition area between the dissimilar materials are observed in the gradual material change concept [194].

Fig. 2-12 Material deposition methods in MMAM fabrication [7]. Reproduced with permission of the rights holder.

2.1.5.3 Current state of MMAM research

Ongoing research on MMAM primarily focus on DED techniques which include the combination of one of the three forms of feedstock materials: (i) powder-powder [67], (ii) wire-wire [188], and (iii) powder-wire [195]. Some examples of discrete metal material combinations that have been fabricated using DED are Inconel-Ti [196], Inconel-steel [197–200], Ti-steel [84,190,201], and Ti-Al alloys

[202], while compositionally graded single materials include steel [203,204], IN 718 [205] and Ti6Al4V [206,207]. This is because DED systems have more flexible machine control compared to PBF systems, e.g. easier incorporation of multiple powder deposition nozzles or hoppers [84,190,199]. These studies show that the three key configurations of material deposition methods for MMAM fabrication described previously are accomplishable and have been successfully applied to build FGM parts for various applications. Applications that require such level of complexity include thermal conductivity for cooling channels, high temperature, corrosion and fatigue resistance in different sections along an engine turbine, and nuclear power generation components that needs to have high resistance towards hot cracking and stress during service [7,199].

However, DED-manufactured parts typically have lower resolution and thus higher surface roughness compared to those produced by PBF techniques [15]. Additionally, typical DED-fabricated structures are relatively large and hence limit this technique from fabricating much more complex and intricate geometries compared to the PBF-built components. Although it is possible to produce FGM components via PBF techniques by creating ‘designed’ porosity, MM processing is a complicated process [13]. This is mainly due to the problem of cross-contamination of two different metal powders and the difficulty in controlling powder delivery for PBF systems. Recent studies on MMAM using PBF systems are mostly limited to discrete change of materials.

For example, Chen et al. [14] produced 316L SS/CuSn10 bimetallic structures via SLM. Liu et al. [12] and Sing et al. [13] used SLM to build 316L SS/C18400 copper (Fig. 2-13) and AlSi10Mg/C18400 copper parts, respectively. Terrazas et al. [208] and Hinojos et al. [209] respectively fabricated Ti6Al4V/Cu (Fig. 2-14) and IN 718/316L SS specimens using EBM. Tan et al. manufactured Ti6Al4V graded structures via EBM. Al-Jamal et al. [210] made Cu/H13 tool steel parts by incorporating a multiple nozzle system for powder delivery in their prototype multi-material (MM) SLM system, which selectively dispenses different materials using a rotating disc as shown in Fig. 2-15 [210].

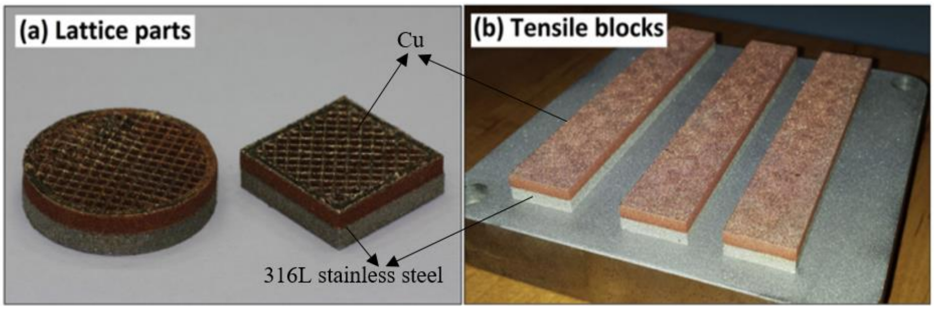

Fig. 2-13 316L SS/C18400 samples built via ‘discrete material change’ MMAM configuration using conventional SLM machine [12]. Reproduced with permission of the rights holder.

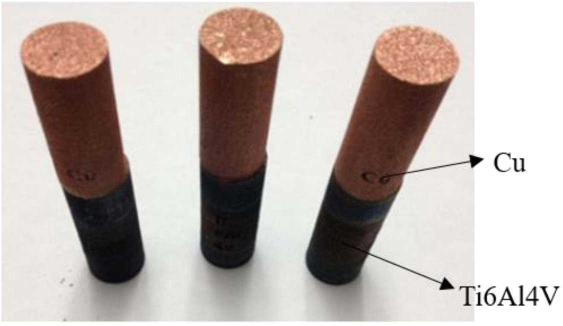

Fig. 2-14 Ti6Al4V/Cu specimens built via 'discrete material change' MMAM configuration using conventional EBM machine [208]. Reproduced with permission of the rights holder.

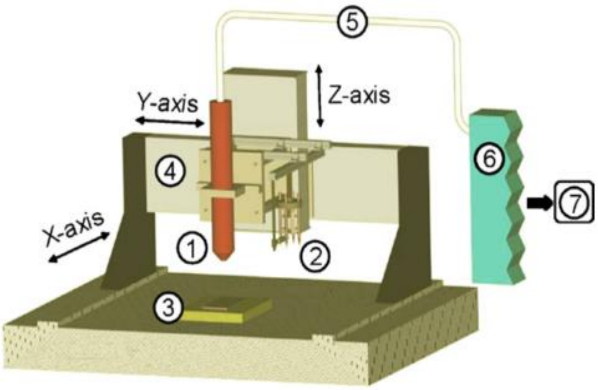

Fig. 2-15 Schematic of prototype MM-SLM system by Al Jamal et al. (1) laser nozzle; (2) feeder system; (3) build area; (4) CNC rig; (5) fibre optic cable; (6) Nd:YAG laser; (7) PC controller [210]. Reproduced with permission of the rights holder.

However, some breakthroughs in the past few years has seen the development of PBF systems, capable of achieving gradient material change especially for MMAM processing. In 2014, Chianrabutra et al. [211] developed a novel dry powder printing (DPP) technique which regulates powder flow via control of piezoelectric transducer input. The development of this ultrasonic dispensing device enables high quality multi-material pattern layers to be built, hence achieving the fabrication of MMAM parts via gradual material change deposition. In 2016, Chivel [212] introduced a system capable of precisely distributing discrete powder of different materials with a range of particle sizes using a special algorithm for re-coating the powder layers. He also proposed a novel platform cleaning and optical monitoring systems, enabling efficient separation of excess powders to be re-used. Very recently in 2018, Wei et al. [9] successfully developed a novel multi-material SLM system that is able to fuse multi-material powders within a single layer and across different layers at discrete locations. This was achieved by incorporating powder bed spreading, multiple point-by-point nozzles, ultrasonic dry powder delivery, and point-by-point single layer powder removal in a single SLM machine architecture (Fig. 2-16(a)). Using this system, they successfully fabricated 316L SS/IN 718 and 316L SS/Cu10Sn multi-material structures (Fig. 2-17(b)). Such significant advancements will undoubtedly open a new research paradigm, capable of filling the knowledge gap that currently exists in the MMAM of metals by using PBF techniques.

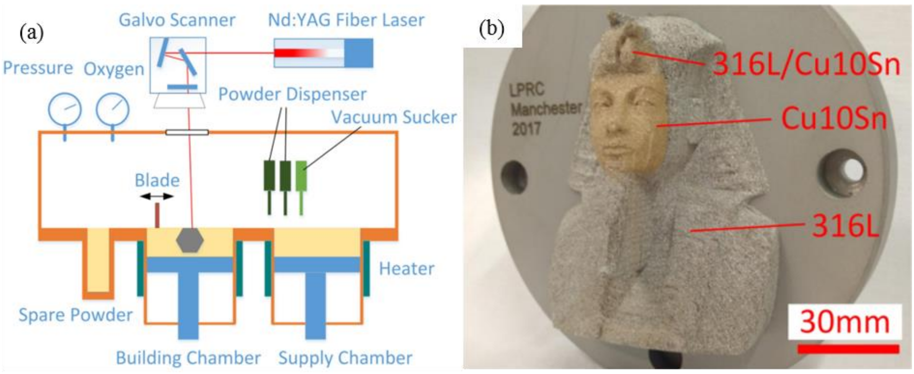

Fig. 2-16 (a) Schematic of a novel MM-SLM machine architecture by Wei et al. [9], (b) example of MM structure made by the novel system. Reproduced with permission of the rights holder.

2.1.6 Process monitoring and control

Despite the vast improvements that have been made in metal AM machine architecture, software, and hardware during the last 10 years, a number of issues encountered during the early stages of metal AM now still exist, including porosity, balling, and thermal management issues [213]. While significant experimental and modelling/simulation efforts have focused on optimising processing parameters, the lack of quality assurance during metal AM processing on-site, especially for high-value components with zero-failure tolerance also hinders its widespread industrial applications [213]. Nevertheless, the continuous development of various process control mechanisms has improved the surface quality, mechanical properties and geometrical accuracy of AM metallic parts.

To date, various thermographic- and visual-based monitoring instruments have been installed inside metal AM machines for both PBF and DED-based processes, such as high-speed camera, infrared (IR) camera, high-speed charged-couple camera (CCD), CMOS-camera, thermocouple, dual-colour pyrometer, inline coherent imaging facility, and photo-detector [213]. These equipment are used to detect defects and discontinuities in AM metallic parts during manufacturing, including porosity, balling, unmelts, and cracks. On the other hand, several non-destructive testing techniques (NDT) have been used to monitor and evaluate the defects inside bulk AM metallic, particularly laser ultrasound [214] and x-ray computed tomography (XCT) [215]. These NDT methods enable the detection and evaluation of defects such as porosity and cracks within the bulk material without sectioning into 2D samples and undergoing typical metallographic analysis.

For example, Cai et al. [216] used XCT to characterise the internal structure of SLM-fabricated AlSi10Mg and determined the influence of processing parameters on internal porosity. By applying this NDT, the pore characteristics and porosity levels could be evaluated, and the results obtained were in agreement with that obtained using conventional Archimedes method and optical microscopy measurements. Similarly, Cunnigham et al. [217] investigated the influence of processing parameters on the size and distribution of gas porosity in SLM-built Ti6Al4V samples using synchrotron x-ray microtomography (minimum feature size 1.5 µm).

XCT has been increasingly used as a vision-based solution for defect characterisation and dimensional metrology in AM metallic parts both in academia and in industries [213,215]. However, there are still persisting challenges that prevent the wide adoption of XCT scanning in large-scale manufacturing industries, including high cost and time limitation trade-off in order to obtain high quality imaging with fine feature size for XCT scanning [154]. Furthermore, to be accepted as an industrial norm to address the quality control, assessment, and assurance issues for AM metallic parts, the XCT technology needs to be able to characterise relatively large areas of 3D structures, e.g. up to the region of cm^2 or even m^2 with very high accuracy and spatial resolution [213]. Moreover, such metrology solutions need to be fast and technologically compatible with the production environment to meet the standards, qualifications and certifications of AM set by various organisations such as ASTM, Federal Aviation Administration (FAA), and National Institute of Standards and Technology (NIST) [218,219]. These could be promising research areas in the future, and if solutions could be found for these persisting issues, then the use of XCT can be incorporated in an industrial scale for defect and metrology measurements as part of quality control, assessment, and assurance for AM metallic parts.

2.2 Severe Plastic Deformation

2.2.1 Ultrafine-grained and nano-structured metallic materials

It is well known that grain size is a key microstructural feature in determining critical properties of polycrystalline metallic materials. Metallic structures with fine grain sizes are often desired, compared to their coarse-grained counterparts as they often lead to improvements in various physical and mechanical properties, as explained by the Hall-Petch relationship [220]. In the early 20th century, alloying, age-hardening, and various heat treatment methods have been utilised to improve the strength of metals and alloys [220]. However, further efforts on microstructural refinement have led to the development of bulk nanostructured materials (BNM) that are obtained via the nanostructuring route [20,221].

Nanostructured materials are generally defined as polycrystalline structures with average grain sizes ≤ 1 µm, which are further divided into (i) ultra-fine grained (UFG) materials with grain sizes in the sub-micrometer range (100 nm to 1000 nm), and (ii) true nanostructured materials having grain sizes < 100 nm (NG) [24,221]. Additionally, to be considered as BNM or as having bulk UFG/NG microstructures, the material must be composed of fully homogeneous and equiaxed microstructures, with most of the grain boundaries having high misorientation angles [24].

For the last 20 years, nanostructuring has emerged as a novel route to produce BNM with enhanced properties for advanced structural and functional applications [19,222,223]. The "bottom-up" and "top-down" procedures have been established as suitable methods to produce nanostructured materials. In the "bottom-up" approach, bulk structures are produced by consolidating individual atoms or nanoparticles, in which inert gas condensation, electrodeposition, and ball milling of metallic powders with subsequent consolidation are common methods [221]. However, despite the capability of obtaining exceptionally fine grain sizes, these methods are deemed disadvantageous as they could only fabricate small parts, with some levels of unavoidable contamination and defects. On the other hand, the "top-down" approach involves extreme grain refinement of coarse-grained materials until the microstructures reach at least the sub-micron range, which is able to eliminate the contaminants and defects. To date, all processing routes in this category impose heavy strains that result in the generation of large amount of dislocation densities and numerous UFG/NG microstructures, hence introducing the term severe plastic deformation (SPD) [221].

UFG and NG materials have been found to exhibit superior strength in various metals and alloys according to the Hall-Petch relationship [224,225]. For example, in pure metals, the average grain sizes processed by various SPD processes often lie within ~ 150 – 300 nm, whereas these values may be even smaller in alloys [22,225]. Another study by Valiev et al. [226] revealed increased ultimate tensile strength (UTS) value from 724 MPa to 1240 MPa for commercially pure (CP) Ti undergoing ECAP and then swaging as well as drawing. Ivanisenko et al. [227] obtained an exceptionally high hardness (10 GPa) for carbon steels processed by HPT, which was superior than that of quenched steel with similar composition. Nevertheless, numerous studies have reported the benefits of having UFG and/or NG microstructures in enhancing corrosion performance [228,229], improving wear resistance [230], and increasing strain rate sensitivity [231] in SPD-processed metals and alloys. Furthermore, other studies have shown that the extreme strain levels imparted during SPD processes is able to close internal pores existing in metals and alloys [232–235]. Such remarkable properties are attributed to the complex structural features obtained via SPD processing, which are [236–238]: (i) non-equilibrium grain boundaries with high extrinsic dislocations and vacancies, (ii) severe lattice distortions and localised phase composition change, and (iii) in-situ crystallisation. Furthermore, there has also been efforts to improve the ductility of SPD-processed metallic materials via grain boundary (GB) engineering, e.g. by introducing bi-modal grain size distribution within the bulk material [239–241].

2.2.2 Classification and principles of severe plastic deformation

Severe plastic deformation (SPD) refers to any metal forming process which exerts a large amount of strain on a bulk solid material to achieve extreme grain refinement down to the UFG/NG regime, without significant changes in the original structural dimensions [24]. The exceptional grain refinement occurs due to the restriction in material flow via special tooling used in SPD machines, thus introducing a large amount of lattice dislocations. At present, there are several SPD processing techniques, but equal-channel angular processing (ECAP) and high-pressure torsion (HPT) are the two prominent processes that have been used to produce BNM.

2.2.2.1 Equal-channel angular processing

The schematic of ECAP processing principle is depicted in Fig. 2-17 [242]. An ECAP machine consists of: (i) a die with two channels having identical cross-sections, intersecting at an abrupt angle in the die, and (ii) a plunger. The plunger presses ECAP samples (rods or bars) under an applied pressure, P_{ECAP}. The channels intersect each other at an angle near or exactly 90° to ensure shearing without any cross-sectional dimensional changes as the sample passes through the channels [243].

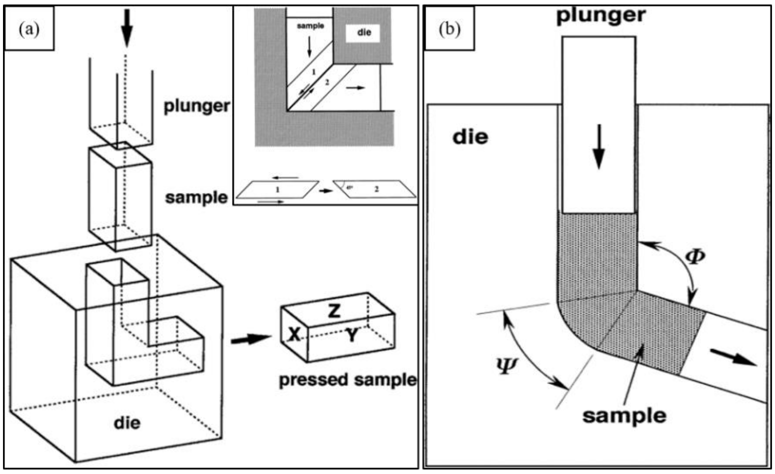

Fig. 2-17 (a) Schematic of ECAP process, with illustration of shearing effect shown inset of (a), and (b) a cross-section of an ECAP die showing two important internal angles, Φ and Ψ (b) [242]. Reproduced with permission of the rights holder.

As a result, multiple passes of the sample through the die is possible to obtain very high accumulative strain levels. Hence, four processing routes were developed to enable multiple-passes for ECAP, namely route A, B_A, B_C and C, with the possibility of initiating different slip systems (Fig. 2-18) [244,245].

For route A, subsequent passes for the samples are carried out without any rotation, whereas routes B_A and B_C involve repetitive rotations of 90° in an alternating or in the same direction, while in route C, the sample is rotated 180° between successive passes [242]. As the sample goes through the die, the accumulated von Mises equivalent strain, $\varepsilon_{\mathrm{eq.\text{-}ECAP}}$ can be calculated by the following equation [24]:

$$\varepsilon_{eq.-ECAP} = \left(\frac{N_{ECAP}}{\sqrt{3}}\right)\left[2\cot\left\{\left(\frac{\Phi}{2}\right)+\left(\frac{\Psi}{2}\right)\right\}+\Psi\csc\left\{\left(\frac{\Phi}{2}\right)+\left(\frac{\Psi}{2}\right)\right\}\right] \qquad \text{Eqn. 2-7}$$

where N_{ECAP} is the number of passes through the die, Φ is the angle between the channels, and Ψ is the curvature angle of the outer arc where the channels intersect.

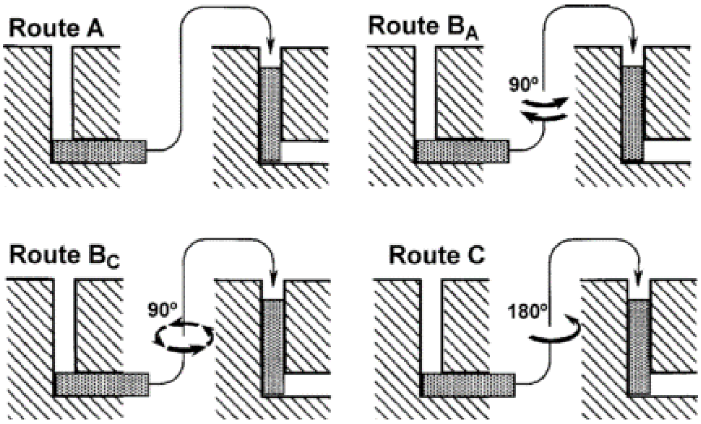

Fig. 2-18 The four processing routes of ECAP process [245]. Reproduced with permission of the rights holder.

2.2.2.2 High-pressure torsion

The schematic of HPT processing principle is shown in Fig. 2-19 [246]. A HPT machine consists of the upper and lower anvils, each having a circular depression (cavity) with a diameter of 10 mm and a depth of 0.25 mm, which are machined from the centre of the anvils.

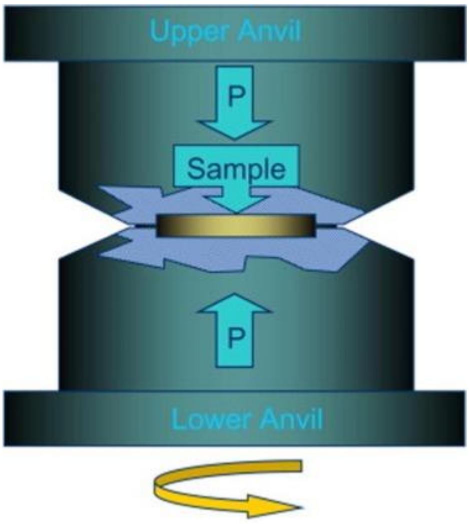

Fig. 2-19 Schematic of HPT process in a quasi-hydrostatic machine setup [246]. Reproduced with permission of the rights holder.

A thin disk sample with corresponding dimensions to the depressions is first placed inside the depression on the lower anvil. The lower anvil is then raised upwards until the remaining exposed area of the disk fits inside the depression on the upper anvil. HPT technique is a two-fold process; firstly, a compressive force, F_{comp}, is applied by the pressing of the two anvils and secondly, torsional strain is introduced by rotating the lower anvil. Deformation of the sample occurs as the result of friction-induced shear between the sample and the anvils under a quasi-hydrostatic pressure [221]. Most HPT processing are carried out under quasi-constrained conditions to restrict outward plastic flow during torsional straining and to maintain the cross-sectional dimension of the original sample [247]. The shear strain, γ_{shear} exerted on the sample during HPT is given by [24]:

$$\gamma_{shear} = \frac{2\pi Nr}{h_0} \qquad \text{Eqn. 2-8}$$

Where N is the number of HPT revolutions of the lower anvil to provide torsional strain, r is the distance from the centre of the disk, and h_0 is the initial thickness of the sample. The equivalent von Mises strain, $\varepsilon_{\text{eq.-HPT}}$ is thus [24]:

$$\varepsilon_{eq.-HPT} = \frac{\gamma_{shear}}{\sqrt{3}} \qquad \text{Eqn. 2-9}$$

However, according to Zhilyaev et al., Eqn. 2-9 is limited for small strain values only, and for higher strain values, i.e. $\gamma_{\text{shear}} \geq 0.8$ $\varepsilon_{\text{eq.-HPT}}$ is given by [25]:

$$\varepsilon_{eq.-HPT} = \left(\frac{2}{\sqrt{3}}\right) \ln\left[\sqrt{1 + \frac{\gamma_{shear}{}^2}{4}} + \frac{\gamma_{shear}}{2}\right] \qquad \text{Eqn. 2-10}$$

They also developed another equation to account for the reduction in thickness of the disk samples due to the applied pressure, P_{HPT} and the torsional strain. The relationship is given by:

$$\varepsilon_{eq.-HPT} = \ln\sqrt{\left[1 + \left(\frac{2\pi Nr}{h_0}\right)^2\right]} + \ln\left(\frac{h_0}{h}\right) \qquad \text{Eqn. 2-11}$$

Where h_0 and h_f are the initial and final thicknesses, respectively. However, the use of the so-called ‘logarithmic equations’ in Eqns. 2-10 and 2-11 is deemed unsuitable to describe the equivalent strain imposed during HPT because of [248,249]: (i) inadequate work conjugacy between the logarithmic shear stress/strain curves, (ii) issues when testing at constant logarithmic strain rates, and (iii) history dependence related to accumulation of prior strain. Hence, the von Mises equivalent strain will be used throughout this study.

Nevertheless, HPT has two major advantages compared to ECAP process [25,26]: (i) the grain sizes obtained via HPT are much smaller than those processed by ECAP, and (ii) HPT-processed samples have larger amount of grain boundaries with high angles of misorientation. However, ECAP has been scaled-up and used in some commercial applications, [243], but HPT is restricted to small thin disk samples and only limited efforts have been made to extend HPT to larger cylinders [247,250].

2.2.3 Microstructural evolution and homogeneity in HPT-processed materials

Based on Eqn. 2-8, the strain imposed by HPT on the processed material is expected to increase linearly with distance from the centre of the disk, resulting in inhomogeneous microstructures at the centre and at the peripheries. Such inhomogeneity is typically assessed by hardness tests, which are usually carried out along the diameter of the HPT-processed samples, together with observation of grain size distribution via TEM. There are cases in which hardness values are lower at the centre and higher at the peripheries, which remain so even after large amounts of strain are imposed with increasing number of HPT revolutions. Examples of such materials include commercial purity Ni (Fig. 2-20(a)) [251], 316L SS (Fig. 2-20(b)) [252], and Al-Mg-Sc alloy (Fig. 2-20(c)) [253], all processed under a constant pressure, P_{HPT} of 6 GPa.

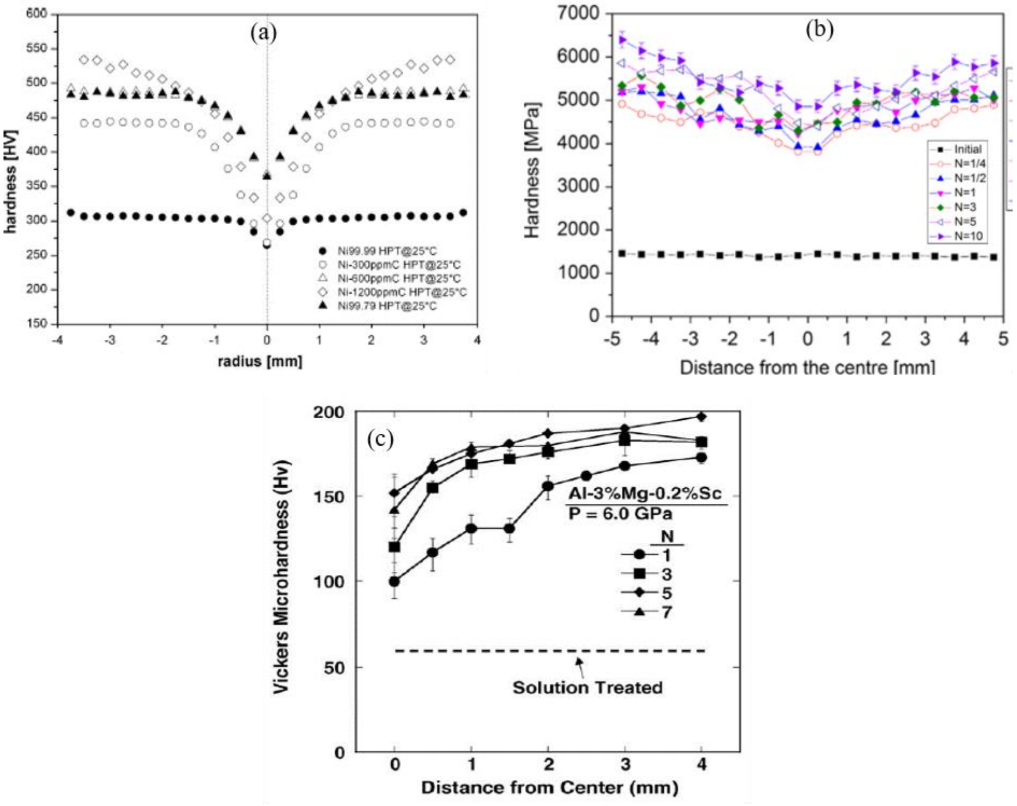

Fig. 2-20 Hardness variations across diameter of HPT-processed (a) commercial purity Ni [251], (b) 316L SS [252], and (c) that across the radius of HPT-processed Al-Mg-Sc alloy [253]. Reproduced with permission of the rights holder.

However, hardness tests have also shown saturation, i.e. closeness to uniform hardness values across the diameter of the samples at higher $\varepsilon_{\mathrm{eq.-HPT}}$ values as the number of HPT revolutions increase. In such cases, rapid dynamic recovery initially occurs in the periphery of the HPT-processed disks at lower number of revolutions. The hardness values then gradually saturate throughout the disk, i.e. achieve relatively uniform hardness distribution across the disk diameter with increasing HPT revolutions [254]. The uniform hardness distribution typically indicates microstructural homogeneity in HPT-processed materials. For example, Loucif et al. [255] initially observed hardness inhomogeneity across the radius of Al 6061 alloys processed by HPT under a constant pressure of 6 GPa at room temperature (RT) at lower number of HPT revolutions (1/2 to 1). However, the hardness values gradually became relatively uniform after 5 HPT revolutions, indicating a saturation level, and hence microstructural homogeneity has been achieved (Fig. 2-21(a)).

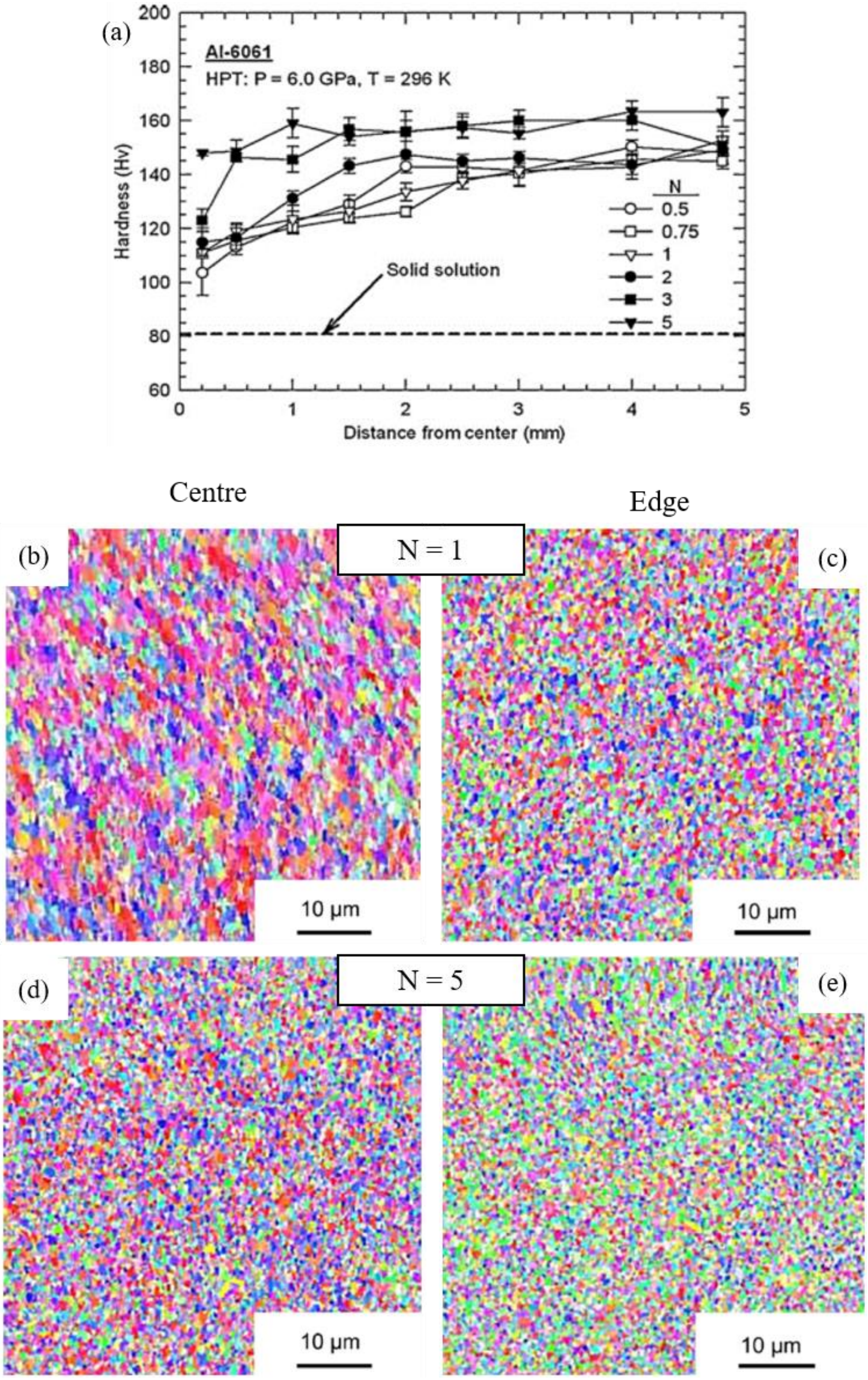

Fig. 2-21 (a) Variation of hardness across the radius of HPT-processed Al 6061, EBSD maps showing grain size distribution at the centre and periphery after (b) and (c) 1 revolution, and (d) and (e) after 5 revolutions [255]. Reproduced with permission of the rights holder.

This finding is supported by the accompanying electron backscattered diffraction (EBSD) maps, which compared the grain sizes at the centre and edges of the HPT-processed disks for 1 and 5 revolutions (Figs. 2-21(b) to 2-21(e)). A distinct grain size distribution could be observed at the centre and edges after 1 revolution (Figs. 2-21(b) and 2-21(c))), whereas the disk processed by 5 HPT revolutions yields a similar grain size distribution both at the centre and edges (Figs. 2-21(d) and 2-21(e)). This confirms that the hardness values across the diameter of the disks could be used as an indicator of microstructural homogeneity in HPT-processed materials. Various factors have been found to influence the hardness and microstructural homogeneity in HPT-processed materials, including applied load, pressure, strain, and temperature (process parameters), stacking fault energy (material property), and grain sizes obtained after HPT [247,256–259].

The typical hardness evolution in HPT-processed materials could be represented by three different models when hardness values are plotted against equivalent strain, as shown in Fig. 2-23 [260]. The first model (Fig. 2-22(a)) depicts a general model that shows no material recovery, i.e. increasing hardness with number of HPT revolutions before saturation at large strain levels, which occurs in most HPT-processed materials [261–263]. The second model (Fig. 2-22(b)) shows a curved peak formed at low equivalent strain values due to hardening, followed by softening and saturation as the number of revolutions increase. This behaviour has been found to occur in materials having very high stacking fault energies [254], e.g. high purity Al, Mg, and Zn, causing easy cross-slip and rapid material recovery [264–266]. The third model (Fig. 2-22(c)) shows decreasing hardness values with increasing imposed strains, i.e. material weakening, and has been reported in HPT-processed pure metals e.g. Pb, Sn, and In [266], and in alloys such as Zn-Al and eutectic Pb-62%Sn [267,268].

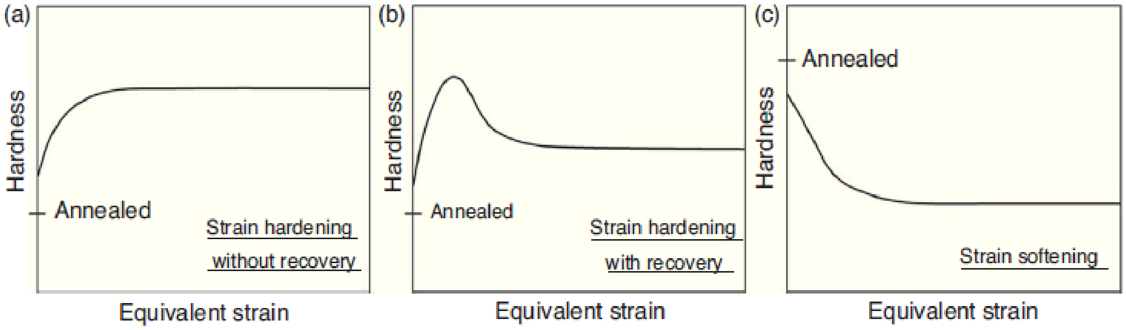

Fig. 2-22 Variation of hardness with equivalent strain in HPT-processed metals: (a) strain hardening without recovery, (b) strain hardening with recovery, and (c) strain softening or weakening [260]. Reproduced with permission of the rights holder.

2.3 316L stainless steel

2.3.1 Background

316L SS is a variant of austenitic stainless steel that consist of the γ-austenite FCC crystal lattice structure. It has been widely used in various applications and industries including construction, orthopaedic implants, petrochemical, pharmaceutical, and nuclear power plants, owing to its excellent corrosion resistance, low neutron radiation absorption rate, and superior mechanical properties e.g. exceptional strength and fracture toughness, and good ductility [269–272]. The main alloying elements of this alloy are Cr, Ni, and Mo. Cr inhibits uniform corrosion, while Ni promotes toughness and ductility. Furthermore, Ni is also an austenite stabiliser that stabilises the FCC structure at room temperature. The addition of Mo enhances resistance to localised uniform and pitting corrosion [273], and improves the corrosion resistance in chloride environments [274,275]. The typical composition ranges of alloying elements in 316L SS are shown in Table 2-1.

Table 2-1 Typical composition ranges of various alloying elements in 316L SS (wt. %).

Cr	Ni	Mo	C	Mn	P	S	Si	N	Fe
16-18	10-14	2-3	< 0.03	< 2	< 0.045	< 0.03	< 0.75	< 0.1	***Bal.***

The ductile nature of FCC crystal lattice structure compared to the BCC crystal lattice structure of pure iron gives this alloy its high toughness property. The low C content in this alloy, < 0.03 wt. % (thus designated L for low carbon) reduces its susceptibility to sensitisation, precipitation of Cr-rich carbides, and intermetallic phases that could deteriorate its corrosion resistance and mechanical properties [276]. However, unlike other stainless steels, 316L SS could not be strengthened or hardened via heat treatment due to its low C content, but can only be strengthened by cold working to introduce the work hardening effect [117,127,170,277–279].

2.3.2 Solidification microstructures

The classic equilibrium Fe-Cr phase diagram is often used to describe the stability of phases in this alloy [280]. Complete solubility of Cr in Fe could be observed at high temperatures (> 1500°C), while a circular ‘gamma loop’ is obtained at ≤ 15 wt. % of Cr within the 912 – 1394°C range, separating the austenite and ferrite regions. Distinct α and α’ at relatively low temperatures (~ 200 – 500°C and at low and high Cr levels (< 10 wt. % and > 90 wt. %), respectively. A $\alpha+\delta$ region could also be found between approximately 12 – 13 wt. % of Cr. On the other hand, an intermetallic σ-phase consisting of FeCr compounds could be formed in Fe-Cr alloys at temperatures < 812°C, which has been found to reduce their ductility and corrosion resistance [281].

However, the pseudo-binary Fe-Cr-Ni phase diagram proposed by Lippold and Savage [282] is a more suitable representation for 316L SS as it captures the three main constituents of this alloy. This pseudo-binary phase diagram details four different solid-state phase transformation (solidification microstructures) are possible; austenitic (A), austenitic-ferritic (AF), ferritic-austenitic (FA), and ferritic (F) phases. These transformations are related to the Cr_{eq}/Ni_{eq} ratio by the following equations [283]:

$$Cr_{eq} = \%Cr + \%Mo + 0.5\%Nb + 1.5\%Si \qquad \text{Eqn. 2-12}$$

$$Ni_{eq} = \%Ni + 30\%C + 0.5\%Mn + 25\%N \text{ (if N is present)} \qquad \text{Eqn. 2-13}$$

All the element concentrations are in wt. %. Increase in the $Cr_{eq.}/Ni_{eq.}$ ratio results in the transformation sequence from A→ AF → FA→ F.

Similarly, the Schaeffler diagram that was developed based on laser welding processes could also be used to estimate the phases formed in austenitic stainless steels from the $Cr_{eq.}$ and $Ni_{eq.}$ values, which can be calculated using the corresponding Eqns. 2-12 and 2-13 [284]. However, the rapid solidification and high cooling rates in metal AM processes could have some influence on the composition and kinetics of the processed materials during solidification. Hence, the pseudo-binary Fe-Cr-Ni phase diagram and Schaeffler diagram mentioned previously may not accurately predict the type of solidification morphologies and microstructures obtained through metal AM processing [285–287]. Nevertheless, they could be a good starting point to estimate the solidification behaviour in metal AM processes.

2.3.3 Current research on 316L SS

To date, various processing routes have been used to fabricate bulk 316L SS structures; from conventional processes such as casting, forging, and extrusion that possess relatively limited degrees of freedom [277], to novel techniques such as additive manufacturing (AM) capable of producing complex geometries [35], and severe plastic deformation (SPD to achieve extreme grain refinement and significantly improves mechanical and functional properties [18].

So far, numerous studies have shown that AM-fabricated 316L SS can achieve better mechanical properties, e.g. yield and tensile strength, improved corrosion and performance, enhanced fatigue and creep life in, compared to their CM counterparts [117,127,170,277–279]. It is also possible to tailor the microstructures and grain sizes by fine-tuning the processing parameters and selecting proper scan strategies [288–291]. Nevertheless, defects such as porosity, cracks and residual stress still exist in AM-fabricated parts, which deteriorate the performance of this material. Thus, in addition to optimising processing parameters, post-processing approaches, e.g. stress relief, heat treatment, shot peening, and HIP are often necessary to minimise these defects and improve the corrosion performance and fatigue life, two of the key performance aspects of 316L SS significantly affected by defects [6,16,292–295]. Interestingly, although it is well known that traditionally 316L SS could not be strengthened or hardened via heat treatment due to its low carbon content, recent studies have shown that the presence of Cr-based nano-silicates can increase the yield strength of AM-fabricated 316L SS compared to their CM counterparts [126,277,296–299]. In fact, Chen et al. [299] found that annealing at 400°C resulted in 10% increase in yield strength of SLM-fabricated 316L SS, and explained that the increased volume percentage of the nano-silicates after annealing strengthened the alloy via the Orowan looping mechanism.

On the other hand, research has shown that the UFG microstructures produced by SPD processing, e.g. by HPT are able to strengthen cast, wrought, and weld 316L SS and other austenitic SS [252,300–304]. These SPD-processed materials are typically strengthened by grain boundary strengthening due to the ultrafine or nano-scale grain sizes and dislocation hardening as the result of generation and multiplication of dislocations via extreme strain levels [221], and through phase transformation from austenite to martensite in some cases [305–307].

2.4 Inconel 718

2.4.1 Background

IN 718 is a Nb-bearing precipitation-strengthened Ni-based superalloy developed by the International Nickel Company in 1959 [308]. Due to its good weldability, good corrosion, oxidation and creep resistances, and excellent high-temperature properties (up to 650°C) [128]. IN 718 is able to maintain structural integrity and mechanical performance and withstand extreme environments. In addition to these excellent properties, the competitive cost of IN 718 due to the respectively low and high Co and Fe contents makes it highly attractive and is widely used in the aerospace industry, particularly for the gas turbine components (including blades, discs, and rear frame) of commercial aeroplanes and other aircrafts [309]. At present, IN 718 is the most commonly used superalloy in terms of tonnage, accounting for ~ 35% of the total production of superalloys [310], and representing ~ 50% of the superalloy content in some jet engines [308].

2.4.2 Metallurgy of Inconel 718

IN 718 consists of the γ-austenite FCC Ni base matrix. The strength and unique characteristics of IN 718 superalloys are derived by the addition of various alloying elements to achieve the required properties. Solid-solution strengthening is provided via the addition of Cr, Fe, and Mo. Precipitation hardening is attained by adding Nb to form gamma double prime, γ'' secondary phase precipitates that strengthen the Ni matrix. These precipitates have the chemical formula Ni_3Nb, and are formed upon applying certain heat treatment procedures [311–313]. Al and Ti, are sometimes added in small contents to provide additional strength via the formation of gamma prime, γ'-$Ni_3(Al,Ti)$ precipitates. Appropriate C content within the γ matrix can provide limited strengthening either via dispersion hardening or grain boundary strengthening by forming (Nb,Ti)C that impede impurity segregation and improve cohesive strength [314–316]. Table 2-2 shows the typical composition ranges of alloying elements in IN 718.

Table 2-2 Typical composition ranges of various alloying elements in IN 718 (wt. %).

Ni	Cr	Fe	Nb	Mo	Ti	Al	Co	Cu	C	Si	Mn
50-55	17-21	***Bal.***	4.7-5.5	2.8-3.3	0.65-1.15	0-2-0.8	< 1.0	< 0.3	< 0.08	< 0.35	< 0.35

The γ''precipitates have a body centred tetragonal (BCT) crystal lattice structure that is coherent with the γ matrix and is the major strengthening phase for IN 718.They appear as coherent disks on the (100) planes with average diameter of ~ 60 nm and thickness of ~ 5 – 9 nm. The superior high temperature properties of IN 718 is attributed to the considerable coherency strain, i.e. lattice mismatch between the γ''precipitates and γ matrix due to the tetragonal lattice distortion ($c/a = 2.04$) [317,318]. The lattice mismatch between $\gamma''$and γ is reported to be relatively high, ~ 3% (3:1 ratio) [318]. Therefore, although both γ' and γ'' phases may exist concurrently in IN 718, the principal strengthening phase of this superalloy is ascribed to γ''rather than γ'as a result of its larger volume fraction and the higher lattice mismatch with the γ matrix.

On the other hand, $\gamma''$is a metastable phase and could transform into the thermodynamically stable δ phase upon thermal exposure beyond 650°C. It has an orthorhombic crystal lattice structure with the same chemical composition as γ'' (Ni_3Nb), but is incoherent with the γ matrix and do not provide additional strength [319]. In fact, IN 718 loses some of its strength and plasticity when δ phase is present in large amounts [320]. This is because the precipitation of δphase is associated with the loss of the γ''precipitates, which reduces the significant coherent γ''/γ lattice mismatch that may decrease the strength of IN 718. [319,321]. This phase forms along the grain boundaries and may appear as either acicular (needle-like) shape or as globular particles at temperatures ranging from 800 – 1150°C. The phase transition from γ'' to δ is often associated with reduced creep resistance and ductility because the acicular morphology acts as stress raisers at high temperatures [322,323]. However, reports have shown that the globular shaped δ precipitates are able to retard the intergranular crack propagation, thus improving stress to rupture and creep resistance [324–326]. Moreover, small amounts of δ precipitates can control and refine grain sizes to improve notch sensitivity and tensile properties, and can maintain the structural integrity of wrought IN 718 [322,327].

The Nb content in IN 718 is susceptible to heavy segregation during solidification and considerably influences the favourable distribution and volume fraction of strengthening precipitates in the γ matrix. However, this also means that some undesirable secondary phases such as MC carbides, (Nb,Ti)C, and Laves phase $(Ni,Fe)_2(Nb,Ti,Mo)$ might also form upon solidification. Precipitation of MC carbides and Laves phase in large amounts consume a large amount of Nb, which reduces the γ'' strengthening precipitates and can reduce tensile ductility as well as fatigue and creep properties [328,329].

MC carbides are formed via a eutectic reaction with the γ matrix upon solidification, e.g. $L \rightarrow \gamma + NbC$. They have a FCC crystal lattice structure and appear as globules that are inhomogeneously distributed within the grains (intragranular) and/or along the grain boundaries (intergranular) [316,330]. Although small contents of MC carbides in IN 718 may provide minimal strengthening, their presence in large amounts are undesirable as they could be detrimental to the mechanical properties during service. For example, NbC causes liquation cracking at the heat affected zone (HAZ) of weld IN 718 due to liquid penetration along the HAZ grain boundaries [322]. Intergranular MC carbides transitions the fracture mechanism from transgranular to intergranular mode at RT [330]. MC carbides precipitated intragranularly on the surface of a component may undergo cracking or oxidisation under thermal stress, resulting in the notch effect and poor fatigue life [319].

Laves phase is a brittle intermetallic compound with a hexagonally closed packed (HCP) crystal lattice structure. It appears as near-spherical globules, or as platelets upon exposure to high temperatures. It forms due to the strong segregation of Nb, Si, and Mo from the dendrites into the interdendrites during solidification [331,332]. The higher Fe and Cr contents in IN 718 have also been found to promote the formation of Laves phase [333]. Due to its brittle nature, Laves phase typically results in poor ductility, toughness, and creep properties [332,334]. Furthermore, Laves phase is also able to deplete a large amount of Nb necessary for the formation of the principal strengthening γ'' phase (Ni_3Nb) in IN 718 [335]. Examples of the secondary phase precipitates that are typically present in IN 718 are shown in Fig. 2-23.

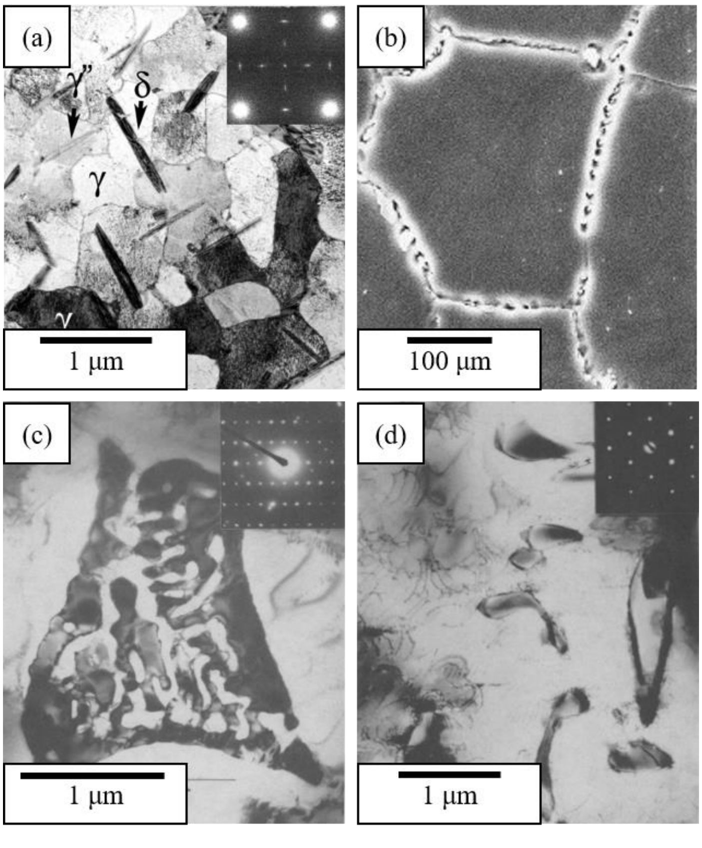

Fig. 2-23 (a) γ'', needle-like δ, and γ matrix (regions A and B) [311], (b) globular shaped δ [321], (c) MC carbide [336], and (d) Laves phase [336]. Reproduced with permission of the rights holder.

Overall, phase transformations do not occur in IN 718 at any temperature range, therefore any deterioration in the high-temperature properties is associated with the dissolution of the strengthening γ'' precipitates, and/or the formation of detrimental phases such as Laves phase. Furthermore, the base Ni matrix remains austenite in the solid solution from the point of solidification down to absolute zero temperature. Hence, IN 718 can be used for service at both elevated and cryogenic temperatures, or for applications that have a broad range of service temperature [78,337,338].

2.4.3 Solidification microstructures

The segregation of alloying elements in IN 718 superalloy is expected during solidification because of their different partitioning behaviour. In particular, cast IN 718 is heavily segregated with Fe, Cr, and Ni typically remain in the dendrites, while Nb, Mo, and Si are segregated into the interdendrites [331]. In addition, the relatively larger volume fraction of Nb compared to Al and Ti promote higher percentages of γ'' phase, thus becoming the primary strengthening phase of IN 718 superalloy compared to the γ' phase in other superalloys. However, such high Nb content also makes IN 718 susceptible to the formation of NbC (MC carbide) and Laves phase upon solidification, which are detrimental to its mechanical properties. Hence, when considering the Nb content and the resulting NbC and Laves phase, the solidification of IN 718 superalloy involves a three-step sequence, as summarised in Fig. 2-24 [336].

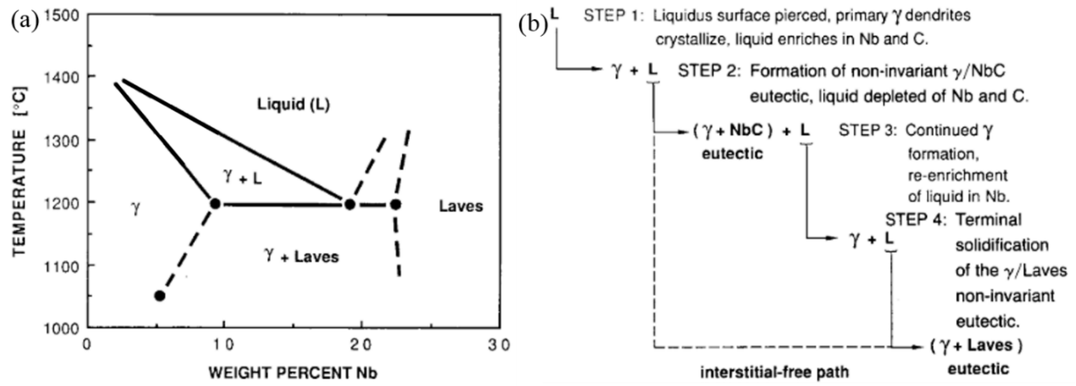

Fig. 2-24 (a) Phase diagram, and (b) solidification path for IN 718 [336]. Reproduced with permission of the rights holder.

The solidification process begins by the piercing of liquidus surface to form primary dendrites through the reaction of L → γ (Fig. 2-24 (a) and step 1 in Fig. 2-24 (b)). Here, the segregation of Nb and C occurs continuously and enrich the liquid phase. As the growth of γ dendrites continues, the compositions of Nb and C allow for the eutectic reaction L → γ + NbC to occur and form eutectic γ/NbC (step 2 in Fig. 2-24 (b)). A significant percentage of Nb and C has been consumed due to this reaction, returning the remaining liquid phase to to the composition of γ that favours the L → γ reaction again (step 3 in Fig. 2-24 (b)). As the temperature decreases upon further cooling, the further growth of γ dendrites and segregation of Nb in the remaining liquid phase cause the formation of eutectic γ/Laves through the reaction L → γ + Laves (step 4 in Fig. 2-24(b), before the solidification of IN 718 is terminated. At this point, the C content is no longer sufficient for the reaction of L → γ + NbC.

However, the solidification path for IN 718 described here is particularly for those fabricated via processes with low to intermediate cooling rates of < 10^1 K s^{-1}, e.g. casting [339]. For processes that utilise higher cooling rates, e.g. > 10^3 K s^{-1} such as welding or laser treatment, the solidification process terminates with the reaction $L \rightarrow \gamma + NbC$ [339]. Kwon et al. [340] reported that the presence of Laves phase in cast IN 718 is much higher compared to other manufacturing processes. Moreover, rapid solidification at higher cooling rates may reduce the size of Laves phase since there is less time for the segregation of Nb into the liquid. However, Chlebus et al. [341] explained that the dendritic growth during rapid solidification processes may cause micro-segregations and forms non-equilibrium Laves phase at the interdendritic regions, along grain boundaries, and on the surface of the solidified parts.

Overall, careful selection of heat treatment procedures is necessary to dissolve the carbides and Laves phase as much as possible in the γ matrix, thus releasing more Nb atoms to be precipitated as the γ'' phase and provide the required strengthening. [128,312,341–344]. Typical heat treatment procedures for IN 718 involve a three-step process, starting with homogenisation, followed by solution annealing, and finally aging [128,312,341–344]. Homogenisation is carried out to dissolve the Laves phase and remove compositional segregation. Solution annealing further homogenises the remaining segregated microstructure and precipitates small quantities of δ phase as necessary. Precipitation of the γ' and γ'' strengthening phases occurs at the aging stage. In 1986,Thompson et al. proposed a time-temperature-transformation (TTT) graph for weld IN 718 that could serve as a guideline in selecting the best heat treatment procedures for other fast cooling processes, e.g. metal AM to produce the desired microstructures or phases according to the intended applications [345].

2.4.4 Current research on IN 718

Conventional wrought and casting techniques have been the preferred choice to manufacture components from IN 718 for various high-temperature applications in the aerospace and energy industries at the early stages of this material five decades ago. For example, complex-shaped turbine rotor disc, thin-walled hollow blade, and high-pressure parts have been fabricated by the combined vacuum-induced melting and investment pattern precision casting techniques [346]. In wrought IN 718, the cast billet or ingot is mechanically worked on several times at high temperatures to achieve the desired shape, often resulting in more homogeneous microstructures and much finer grain sizes compared to the wrought counterpart [347,348].

Later, powder metallurgy (PM) and welding techniques have also been used to fabricate many engineering components from IN 718. For example, PM was utilised to manufacture IN 718 turbine rotors for space vehicles to withstand extreme temperatures and high stress conditions [335]. Near-net-shape parts with fine grains and more uniform properties are able to be obtained using this approach [347,348]. Since IN 718 possesses good weldabiltiy, it has been employed intensively in the welding of disks, frames, and blades of gas turbines and aero engines through gas tungsten arc welding (GTAW) and electron beam welding (EBW) [336,339,349]. However, liquation cracking in the heat affected zones (HAZ) of weld IN 718 due to the liquefaction of Laves phase and NbC along the grain boundaries remains an issue that needs to be resolved [322,349,350].

The development of metal AM techniques, particularly in the PBF category, e.g. SLM and EBM have seen their adoption in the manufacturing of many IN 718 engineering components. AM techniques offer many advantages, including design flexibility, intricate and complex structures. In addition, the low material wastage also makes AM very attractive in terms of cost savings, particularly for manufacturing repair patches for turbine parts, and in rapid prototyping of IN 718 components [15,40,104]. The vast data available on the welding of IN 718 is often used as a starting point to study the fundamentals of metal AM processing of this material due to the similarity between welding and metal AM, in which heat power input, speed, and energy density are important aspects in both manufacturing methods.

To date, research on AM of IN 718 has mainly focused on fine-tuning process parameters and scan strategies to achieve the highest densification level with the lowest defect content [45,351–353]. In addition, various heat treatment procedures involving homogenisation, solution annealing, and aging, have also been explored to achieve the desired microstructures, secondary phases and precipitates that contribute to the strengthening and structural integrity of the parts, e.g. γ'' and adequate δ precipitates, and at the same time to minimise detrimental phases, e.g. Laves and NbC as possible [313,354,355]. On the other hand, although there are currently no literature available SPD-processed IN 718, the SPD processing of pure Ni by ECAP and HPT processes have been studied comprehensively. These include the microstructural evolution, deformation mechanisms, and thermal stability of UFG/NG pure Ni studied by microscopy and calorimetry techniques [27,356–362], investigations on the mechanical properties such as hardness, tensile strength, ductility, and fracture toughness [240,363–366], and studies on the influence of heat and ultrasonic treatments on the evolution of microstructure and strength [367–370].

2.5 Summary

Overall, this chapter provides a comprehensive review on metal AM technology, including classification, various processing aspects, process-microstructure-property relationships, and the current progress in single- and multi-material AM as well as process monitoring efforts. In addition, SPD processing as the most effective processing route to produce UFG/NG microstructures have also been described, focusing on the main SPD techniques, as well as the process-microstructure-property relationships for SPD-processed CM materials. In particular, current research on AM fabrication and SPD processing of 316L SS and IN 718 are presented. These materials are chosen because they are widely used for various applications, particularly those requiring exceptional corrosion and wear resistance, and reasonable strength and ductility, such as in the petrochemical, aviation, and power industries. Furthermore, they have also been widely researched in the context of conventional manufacturing, thus numerous baseline data and information have been established as a starting point for comparison and/or further research for their AM counterparts.

It is revealed that as-received AM metals and alloys possess unique microstructures, comprising of melt pools following the shape of the scan strategy, numerous sub-micron cellular (equiaxed and columnar) sub-structures, and a mix of coarse and fine grains growing, with the cells and grains growing across multiple melt pools. In some cases, fine sub-micron secondary phase particles such as oxides (AlSi10Mg), acicular martensites (Ti6Al4V), and Laves phase (IN 718) are also formed upon solidification. These microstructures are in contrast with as-received conventional cast and wrought materials that typically have relatively coarser equiaxed grains and secondary phase particles. Such finer microstructures are attributed to the rapid heating/cooling cycles during AM fabrication, and generally result in improved properties of AM materials compared to those of their CM counterparts.

In particular, AM 316L SS has been reported to possess higher yield and tensile strengths while maintaining good ductility, as well as superior corrosion and wear performance compared to CM 316L SS due to the much finer grain sizes and unique microstructural features such as dense dislocation networks, micron-sized twins and spherical Cr-based nano-silicates [127,278,299]. Similarly, in addition to producing refined microstructures, the short heat source-material interaction time of AM processes has been found to prevent macrosegregation of Nb into the grain boundaries of IN 718, thus significantly eliminating the brittle Laves phase and δ phase precipitates that could compromise the high-temperature properties of this material [341,371].

Nevertheless, although the finest grain size obtained in AM materials is in the range of 1 – 10 µm, which is smaller than the 30 – 60 µm range often attained in their wrought or cast counterparts [127], they are still not in the UFG/NG regime. Such grain refinement to the UFG and/or NG microstructural scale has been found to significantly enhance the properties of CM materials, particularly yield and tensile strength, as well as corrosion and wear performance compared to those in the micron-grain scale. Thus, it is reasonable to hypothesise that if sub-micron and/or nano-scale grain sizes could be introduced in AM materials, even superior properties could be obtained in comparison to the as-built AM metallic parts.

On the other hand, there is a caveat to these excellent properties obtained by AM compared to CM; as-received parts usually suffer from defects, particularly porosity and cracks, thus compromising their otherwise remarkable properties. In particular, these defects have been found to result in poor corrosion and wear resistances of AM 316L SS [6,292,293] and poor high temperature oxidation resistance of AM IN 718 [371] by obstructing homogeneous microstructural distribution and disrupting the ability to form stable protective oxide layers on the surface of both materials. It is difficult to obtain completely dense (100% of theoretical density) even though the AM processing parameters are optimised. Post-processing methods such as various heat treatment procedures, HIP, and shot peening have been applied to as-built AM metallic parts are able to significantly eliminate substantial amounts of porosity and cracks. However, these are often accompanied with recrystallisation and grain growth that diminishes the initially better properties of the as-built parts. Therefore, if defect-free AM parts could be obtained, the excellent properties of AM materials can be maintained and be consistently superior than those of CM materials.

So far, only SPD processing through HPT has been reported to produce UFG/NG microstructures that enhance the strength and improve other properties, as well as eliminate porosity simultaneously in CM metals and alloys [221,247,372,373]. Thus, HPT processing could be a viable approach to attain UFG/NG microstructures and remove pores in AM metallic parts, thereby producing a defect-free structure with enhanced properties compared to CM materials. This is an interesting avenue that has not been investigated before, which becomes the motivation for the current study. However, there are two main disadvantages associated with HPT processing when it is applied to AM metallic materials, which may not be suitable for practical applications: (i) the extreme HPT-imposed torsional strains will destroy the complex geometries of AM structures, and (ii) HPT facility is limited to process only small thin disk sample. Nevertheless, the study of HPT processing for AM alloys in this study is relevant and justified to achieve the primary aim of establishing process-microstructure-property relationships, particularly in determining the influence of UFG/NG microstructures on the porosity, strength, and corrosion and wear performances of AM alloys (316L SS and IN 718) as described in Section 1.2. The results of this study could be useful to guide the development of future manufacturing processes and post-processing treatments for AM materials upon consideration of the target applications.

Chapter 3 Materials and experimental procedures

3.1 Materials

Spherical gas atomised 316L SS powder (CL 20ES, Concept Laser GmbH, Germany) ranging from 5 – 55 µm (average particle size: ~ 25 µm), shown in Fig. 3-1, and spherical gas atomised IN 718 powder (Batch. No. 18D1550, Sandvik Osprey Ltd., Neath, UK) ranging from 15 – 45 µm (average particle size: ~ 28 µm), shown in Fig. 3-2 were used in this study.

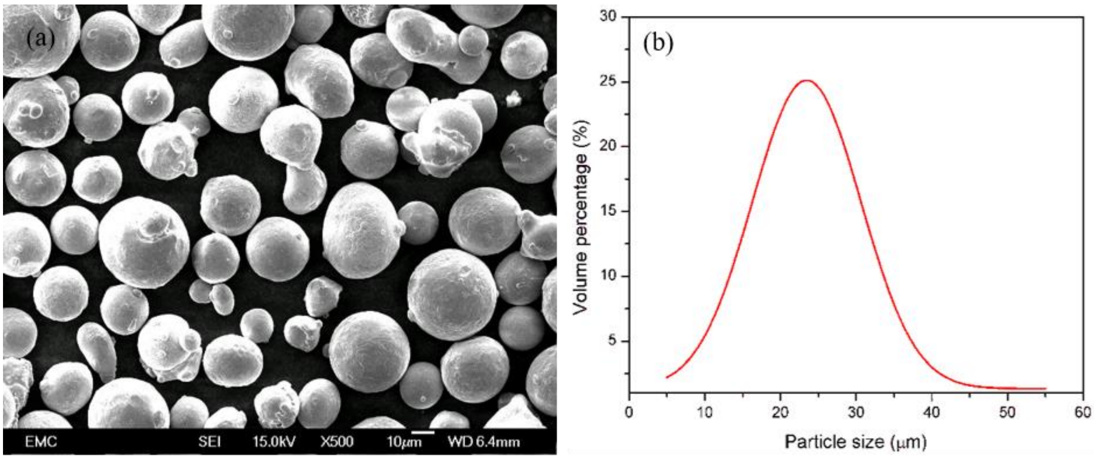

Fig. 3-1 (a) 316L SS powder particle morphology, and (b) particle size distribution determined via SEM and ImageJ analysis [374].

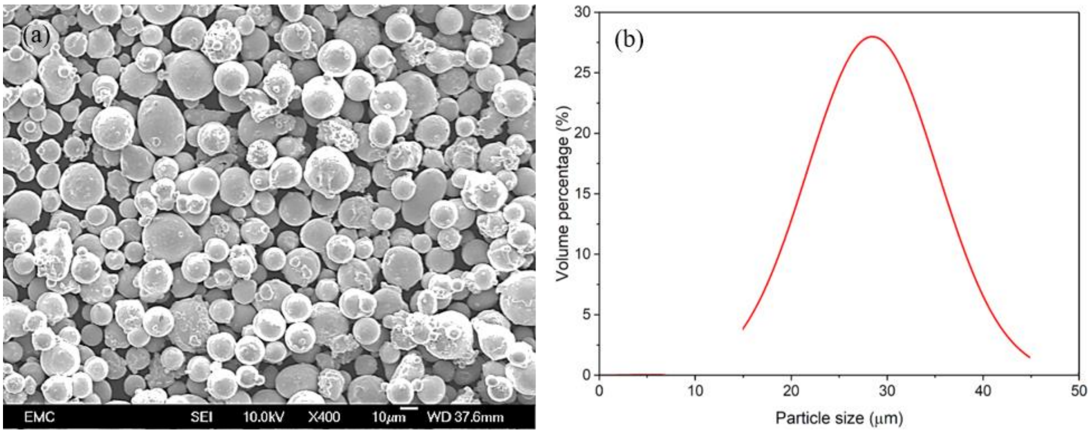

Fig. 3-2 (a) IN 718 powder particle morphology, and (b) particle size distribution determined via SEM and ImageJ analysis.

On the other hand, the chemical composition of the 316L SS and IN 718 powders are shown in Table 3-1. The particle size distribution and chemical composition of both powders were determined via SEM and ImageJ analysis.

Table 3-1 Chemical composition of the 316L SS and IN 718 powders used in this study based on EDX analysis (wt. %).

	316L SS	**IN 718**
Ni	12.2	50.7
Fe	64.3	20.89
Cr	18.43	18.6
Nb	-	5.01
Mo	2.46	3.1
Ti	-	0.89
Al	-	0.52
Si	-	0.09
N	-	0.064
Co	-	0.05
Mn	1.86	0.04
C	-	0.016
P	0.032	0.013
Cu	-	0.01
S	0.01	< 0.003
B	-	< 0.001

3.2 Additive Manufacturing

3.2.1 316L stainless steel

316L SS samples were fabricated by using a Concept Laser M2 ‘Laser Cusing’ SLM machine (Concept Laser GmbH, Germany) shown in Fig. 3-3. The processing parameters used for this machine are shown in Table 3-2.

Fig. 3-3 Concept Laser M2 ‘Laser Cusing’ SLM machine.

Table 3-2 Processing parameters used for fabricating 316L SS samples using Concept Laser M2 SLM machine.

Parameter	**Value/condition**
Build area	X = 250 mm, y = 250 mm, z = 280 mm
Chamber environment	Nitrogen gas
Operating temperature	21°C
Laser focus diameter	50 µm
Laser power (P_L)	200 W fiber laser (Rofin)
Scan speed (v)	1600 mm s^{-1}
Layer thickness (d_L)	30 µm
Scan line spacing (h_L)	150 µm
Scan strategy	Island/checkerboard (5 x 5 mm^2)

Based on these parameters, the VED value used in this study was calculated as ~ 27.8 J mm^{-3}. A 200 mm long rod with a diameter of 10 mm was built vertically upright, parallel to the build direction (z-axis or x-z plane) on a 304L SS substrate. The laser scan direction is parallel to the x-y plane, and perpendicular to the build direction. The schematic of the build is shown in Fig. 3-4.

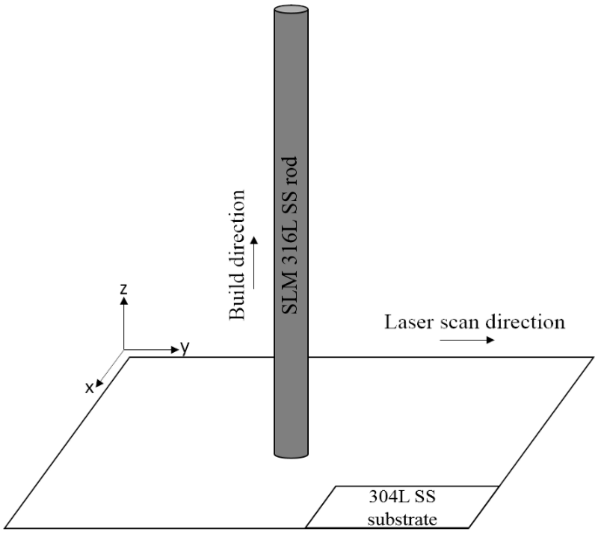

Fig. 3-4 Schematic of the 316L SS rod built by SLM in this study.

3.2.2 Multi-material 316L stainless steel/Inconel 718

MM 316L SS/IN 718 samples were fabricated by using an in-house built HK PM250 SLM machine developed at the University of Southampton as shown in Fig. 3-5. This machine is equipped with a multi-powder feeding system and a powder removal and cleaning system. The processing parameters used for this study are given in Table 3-3.

Fig. 3-5 HK PM 250 MM SLM machine developed at the University of Southampton.

Table 3-3 Processing parameters used for fabricating MM 316L SS/IN 718 samples using the HK PM250 SLM machine.

Parameter	**Value/condition**
Build area	X = 250 mm, y = 250 mm, z = 280 mm
Chamber environment	Argon gas
Operating temperature	21°C
Laser focus diameter	100 µm
Laser power (P_L)	300 W continuous fiber laser
Scan speed (v)	900 mm s^{-1}
Layer thickness (d_L)	30 µm
Scan line spacing (h_L)	80 µm
Scan strategy	Uni-directional (rotated 90° between each layer)

Based on these parameters, the VED value used in this study was calculated as 138.8 J mm^{-3}. Using this machine, a rectangular bar with the dimensions of 10 (L) x 10 (W) x 50 (H) mm was built vertically upright, parallel to the build direction (z-direction or x-z plane) on a 304L SS substrate. The ‘discrete material change between layers’ deposition strategy (Fig. 2-12) was used to fabricate the bar, which started with the deposition, melting, and solidification of successive 316L SS powder layers to obtain a 10 x 10 x 5 mm small bar. Then, the remaining 316L SS powder was removed from the build area using the powder removal and cleaning system equipped with the machine, followed by the deposition, melting, and solidification of successive IN 718 powder layers to obtain another small bar with the same dimensions as that of 316L SS. These steps were repeated until the required rectangular bar with the dimensions of 10 x 10 x 50 mm is completed. In total, five small bars of each material for a total of 10 bars overall were manufactured as shown in Fig. 3-6.

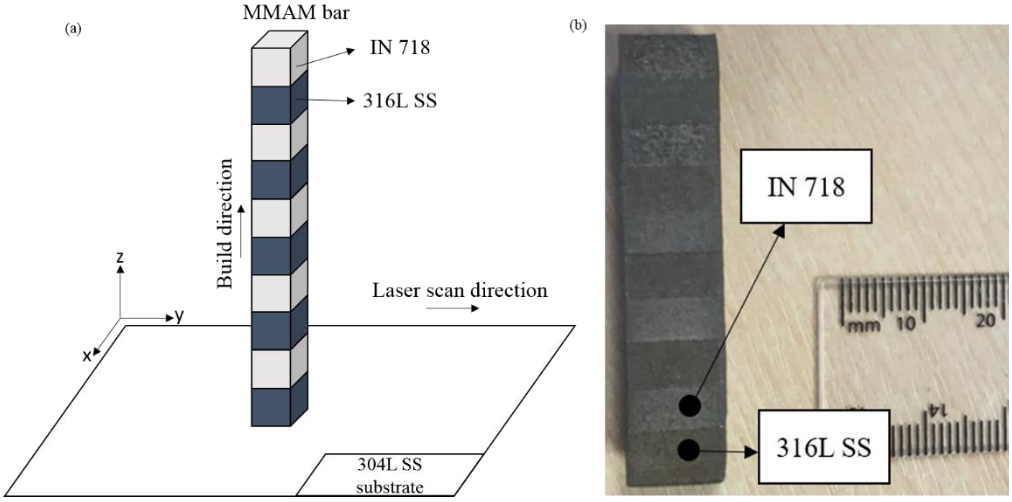

Fig. 3-6 (a) Schematic and (b) as-built MM SLM-fabricated 316L SS/IN 718 bar using the ‘discrete material change between layers’ deposition strategy using the HK PM250 SLM machine.

For the purpose of analysis and discussion of the results throughout this study, the phrase ‘SLM-fabricated’ will be referred to as ‘AM’.

3.3 High-pressure torsion

3.3.1 HPT facility operation

HPT processing was carried out on a HPT facility available at the University at Southampton at RT conditions. The facility consists of an upper and a lower anvil made from high strength tool steel. Both anvils contain flat, circular depressions at their centres with depth and diameter of 0.25 mm and 10 mm, respectively. The upper anvil is fixed in position, while the lower anvil rotates to exert compressive force and then exert torsional strain on the thin disk samples. Different pressures of 1, 3, and 6 GPa can be selected by adjusting the hydraulic pressure settings on the machine. In this study, HPT processing was conducted under quasi-constrained conditions to limit material outflow from the periphery of the disk samples. The ground disks were subjected to a constant pressure of 6 GPa under a constant rotation speed of 1 rpm in an anti-clockwise direction for 1/4, 1/2, 1, 5 and 10 revolutions.

.

3.3.2 HPT sample preparation

The as-received AM 316L SS rod of 200 mm in length was machined to a diameter of 9.8 mm to improve its surface finish and to ensure that the disks fit within the anvils of the HPT machine. The rod was then sliced into a series of thin disks having a thickness of ~ 1 mm using wire electrical discharge machining (EDM). For the MMAM 316L SS/IN 718 bar, a series of thin disks (diameter: 10 mm, thickness: 1 mm) were cut from the bar using wire EDM, such that they were divided equally into 316L SS and IN 718 halves as shown in Fig. 3-7. The disks were then ground with 800 grits SiC abrasive paper to a thickness in the range of 0.81 – 0.86 mm.

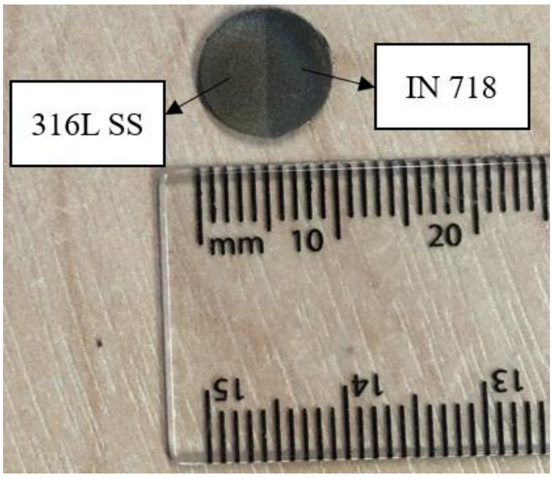

Fig. 3-7 An example of the thin disk divided equally into 316L SS and IN 718 halves for HPT cut from the rectangular bar using wire EDM.

3.4 Microstructural characterisation

3.4.1 Optical and scanning electron microscopy

Prior to microstructural observation, all disks were firstly ground using 120, 800, 1200, and 4000 grits sandpaper, polished using 3 μm and 1μm diamond suspensions, and then etched using Kalling's No. 2 reagent (50 ml HCl, 50 ml ethanol, 2 g copper chloride for 100 ml of etchant). Olympus BX41M-LED optical microscope (OM) and JSM-JEOL 6500 field-emission scanning electron microscope (FE-SEM) were used to observe the porosity and microstructures of the as-received and HPT-processed disks. The average cellular sub-structure sizes, d_{cell} were calculated using the linear intercept method described in Ref. [375]. This method involves the determination of the average spacing of the cell boundaries, $\bar{l}$ by firstly counting the number of intersecting points at grain (or cell) boundaries for a given line drawn on a micrograph. Several lines were drawn, and the total number of intercepts were then averaged to calculate the value of d_{cell} based on more than 200 cells from 20 OM/SEM micrographs for each processing condition.

3.4.2 Transmission electron microscopy

TEM and STEM observations were carried out to examine microstructural features at higher magnifications. Specimens were prepared by mechanically grinding the as-received and HPT-processed disks down to a thickness ~ 80 μm and punching out smaller disks of 3 mm in diameter at a distance of 3 mm from the centre of the larger disks. A dimple grinder (Model 656) and a precision ion polishing system (PIPS, Gatan) were then used to obtain thin films for TEM. A FEI TalosTMF200 machine was used to perform TEM/STEM observations at 200 kV. The average grain sizes, *d* obtained via HPT processing were calculated based on more than 100 grains in 20 TEM micrographs using the intercept method described in Ref. [375]. Selected area diffraction (SAD) patterns were taken with an aperture of 200 nm.

3.4.3 Electron backscattered diffraction

The grain size, morphology, and crystallographic orientation of the as-received and HPT-processed disks were determined by electron backscattered diffraction (EBSD) using a digital HKL Nordlys F++ camera (Oxford Instruments, UK) attached to the JSM-JEOL 6500 FE-SEM machine. Prior to EBSD experiments, the disks were prepared following normal sample preparation procedures described in Section 3.4.1. However, instead of etching with Kalling’s No. 2 reagent, the disks were further polished mechanically using colloidal silica (average particle size: ~ 0.05 µm), followed by electropolishing in an electrolyte composed of 80% methanol and 20% perchloric acid at 16 V and 0.5 A for 18 s. The EBSD images were taken within areas of 100 µm x 100 µm at the central region of the disk (centre to 2 mm from disk centre) with a step size of 0.1 µm covering ~ 100 grains each, and evaluated using Aztec HKL software (Oxford Instruments, UK).

Throughout all microscopy analysis (OM, SEM, and TEM) in this study, the following denotation have been used when referring to the surface of the as-received and HPT-processed disks for consistency and to avoid confusion: (i) if the observed surface is parallel to the build direction (z-axis or x-z plane), it is labelled as surface-parallel, and (ii) if the observed surface is perpendicular to the build direction, or parallel to the scan direction (x-y plane), it is labelled as surface-normal.

3.5 Porosity evolution

3.5.1 Optical microscopy

Porosity is a common defect in AM metallic components. ImageJ analysis software was used to characterise the pores in as-received and HPT-processed disks from the optical micrographs obtained during OM observations. To evaluate the porosity content in this study, 100 thin disks of 1 mm in thickness were extracted from the 200 mm cylinder (30 from either end and 40 at the centre) representing 50% of the overall cylinder, and 10 micrographs were taken for each disk, covering the whole surface area of the disk. The micrographs were initially binarised, i.e. converted into black and white (Fig. 3-8) using a pre-set threshold value, in which black corresponds to porosity while white is the solidified structure. Then, the area fraction (%) of pores was determined by calculating the ratio of black and white pixels. Surface area analysis was also carried out to determine the average pore size in the disks. The pore size is quantified as the Feret diameter, defined as the distance between two parallel planes that restrict any two opposing edges of the pores. This allows a more accurate representation of the pore diameter to be made, particularly for irregular-shaped pores. The porosity distribution was measured on both the surface-normal (x-y plane) and surface-parallel (x-z direction) of the as-received and HPT-processed disks.

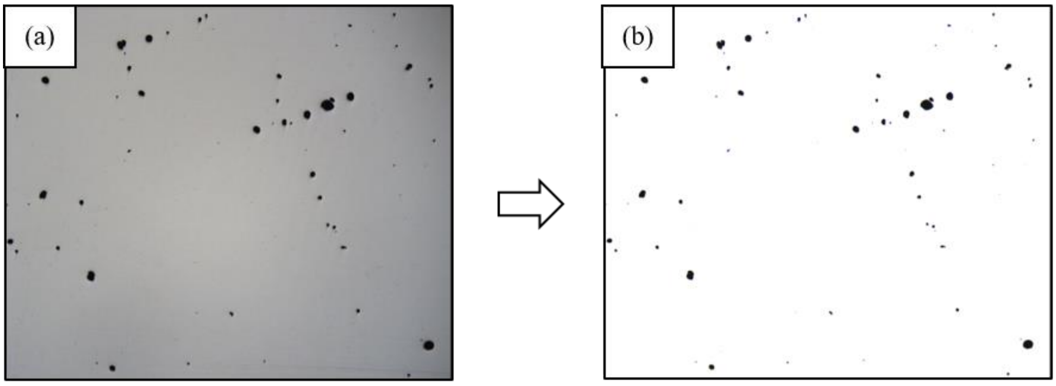

Fig. 3-8 (a) Actual micrograph area, (b) binarised micrograph area ready for analysis.

3.5.2 X-ray computed tomography

X-ray computed tomography (XCT) was employed to obtain a three-dimensional (3D) visualisation of the pores in the as-received disk. A beam energy of 160 kVp at 10 W was used, yielding a flux of 62.5 µA. The beam was filtered with 3.3 mm of calcium fluoride. Over 2000 projections were taken, covering a full 360° for the disk. Each projection was exposed for 25 s. The detector binning was set to 2x, yielding an effective projection size of 1015 x 1015 pixels. Using the 4x objective lens, a resolution of 1.832 µm was achieved. The projection data acquired during the scan were reconstructed using Zeiss Versa XRM-510 Reconstructor, a filtered back projection-based reconstruction software. Then, subsequent analysis was performed based on this volumetric reconstruction. 3D visualisations of the porosity distribution were created from the reconstructed images using VG Studio Max 2.1 software.

3.6 X-ray diffraction

X-ray diffraction (XRD) was carried out using Rigaku SmartLab X-ray Diffractometer to determine the phase composition and evolution of dislocation density, ρ in the as-received and HPT-processed disks. Immediately before XRD measurements, the disks were ground and polished to obtain a flat surface, followed by light etching (~ 3 s) using Kalling's No. 2 reagent to remove residual stress, strain and deformation that might be induced during mechanical grinding. XRD measurements were carried out on the disks through θ/2θ scans in the range of 40° – 110°), with 10 steps per degree and a count time of 1 s per step on the instrument, which was equipped with a graphite monochromatore using CuKα radiation. A slit length of 5 mm was chosen to focus the laser penetration on the disks. The phase composition of the as-received and HPT-processed disks was determined from the resulting XRD peaks and line broadening data using the Materials Analysis Using Diffraction (MAUD) software for profile fitting [376–378].

3.7 Mechanical tests

3.7.1 Microhardness

Vickers microhardness (HV) measurements were carried out on the as-received and HPT-processed disks. Prior to the test, the disks were ground using 800, 1200, and 4000 grits of SiC abrasive papers followed by polishing using 3 µm and 1 µm suspensions to obtain mirror-like surface finish. These provide a good contrast when generating indentations for the microhardness test. HV measurements were conducted using a Future Tech FM-300 microhardness tester under a load of 100 gf with a dwell time of 15 s. Individual HV measurements were taken with set distances across the disk diameter, as illustrated in Fig. 3-9(a) [379]. Each main indentation was spaced 0.3 mm between each other. Four further indentations were made around each main indentation with a uniform distance of 0.15 mm. The HV value at each location was estimated by averaging a total of five indentations. These measurements detail the evolution of HV values across the diameter of the disk. To demonstrate the evolution of hardness homogeneity due to HPT processing, microhardness measurements were also taken throughout the whole surface of the disk in a rectilinear grid pattern, as shown in Fig. 3-9(b) [379]. The hardness profiles were then displayed in colour-coded contour maps based on the HV values measured using the rectilinear grid pattern.

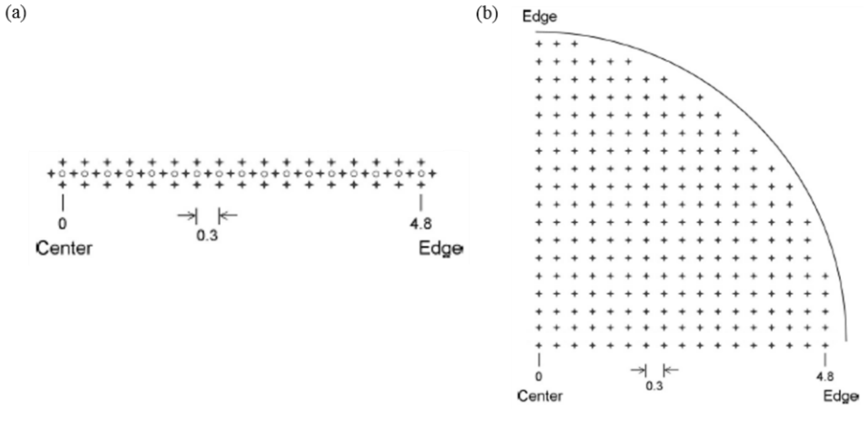

Fig. 3-9 (a) Half of a disk illustrating hardness measurement locations across the diameter of the disk, and (b) A quarter of a disk illustrating the rectilinear grid pattern for hardness measurements throughout the circular section of the disk [379]. Reproduced with permission of the rights holder.

3.7.2 Nanoindentation

The micro-mechanical response, i.e. the evolutions in plastic deformation mechanism due to microstructural changes after HPT processing of AM 316L SS is evaluated using nanoindentation testing. Nanoindentation measurements were taken at the centre and edge (3 mm from centre) of the disks using a nanoindentation facility (NanoTest Vantage System, Micromaterials Ltd., UK) with a three-sided pyramidal Berkovich indenter with a centreline-to-face angle of 65.3° [231]. More than 15 indents were made each at the centre and edge (3 mm from centre) of the disk under a constant peak load, P_{max} 50 mN at various indentation strain rates, $\dot{\varepsilon}_i = h^{-1}(dh/dt)$ of 0.0125, 0.025, 0.05, and 0.1 s^{-1} corresponding to strain rates, $\dot{\varepsilon}$, of 1.25 x 10^{-4}, 2.5 x 10^{-4}, 5.0 x 10^{-4}, and 1.0 x 10^{-3} s^{-1} estimated using an empirical relationship [21,22]. Thermal drift was maintained below 0.1 nm s^{-1} and the indentation results were normalised by correcting the readings upon consideration of the thermal drift.

3.8 Electrochemical tests

To evaluate the corrosion performance of as-received and HPT-processed AM 316L SS disks, three electrochemical tests were conducted in this study, including open circuit potential (OCP), potentiodynamic polarisation (PP), and electrochemical impedance spectroscopy (EIS). An electrochemical test rig consisting of these apparatuses was set up:

- Three-electrode electrochemical cell in 3.5% NaCl electrolyte
    - Custom sample holder (Polyethylene) – working electrode
    - Carbon rod – counter electrode
    - Ag/AgCl reference electrode
- Digitally controlled potentiostat (Gamry Reference 600)
- Gamry Framework and Echem Analysis Software

The disks were housed in a custom-built sample holder so that only one side of the surface area was exposed to the electrolyte. The design of the sample holder resembled a casing made of polyethylene with a cylindrical stainless steel cavity and a holder rod. The polished thin disks were screwed into position inside the cavity. The assembly was made water-tight by closing the casing with an insulating screw cap secured by a rubber o-ring as shown in Fig. 3-10, which is now referred to as the working electrode. When immersing the sample holder into the electrolyte, special care was given to ensure that no air bubbles were trapped inside the exposed surface area as their presence would influence the results of the electrochemical tests.

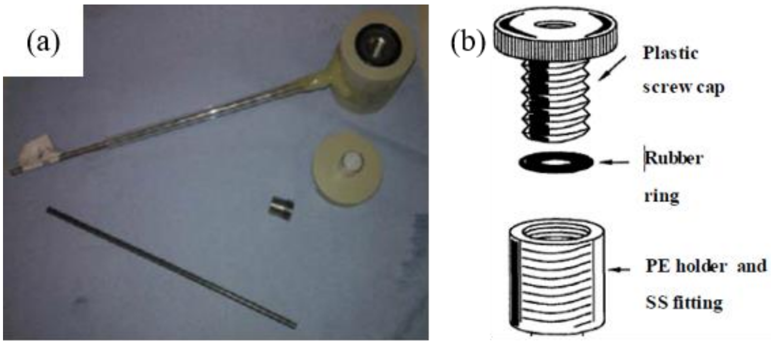

Fig. 3-10 (a) Physical design of the working electrode, (b) illustration of the sample holder.

The counter electrode is used as a secondary conductor to: (i) supply the amount of current required to control the potential of the working electrode, and (ii) ensure current flow inside the electrochemical cell. Thus, it is not involved in measuring the actual potential of the circuit. Counter electrodes are usually inert such that they do not corrode in the test solution, apart from providing a reactive surface for electrochemical reactions involved throughout testing [380]. Hence, carbon was used to prevent ion contamination. The reference electrode becomes a datum which serves as a reference point to which the actual measurement of potential is made at the working electrode. The potential of the reference electrode needs to be stable and reproducible, thus Ag/AgCl was chosen because of the negligible stray current that allows the potential to remain constant throughout the experiment (Fig. 3-11).

Fig. 3-11 Ag/AgCl reference electrode.

The electrochemical cell setup was then connected to the digitally controlled potentiostat, which is a set of software-controlled instrumentations that acts as the source of potential. These instruments are also equipped with current and potential measurement capabilities. Four potentiostat leads were connected to the electrodes (two to the working electrode, and one each to the counter and reference electrodes respectively) based on the schematics described by NACE international. [380].

As their names imply, the working and working sense leads were connected to the working electrode, the reference lead was connected to the reference electrode, and the counter lead was connected to the counter electrode. The floating ground lead was attached to one of the insulating cables available, whereas the counter sense lead was not used. The complete setup of the whole test rig is shown in Fig. 3-12. The experiment was conducted inside a Faraday cage to prevent stray frequencies and noise interference which might influence the results of the electrochemical tests.

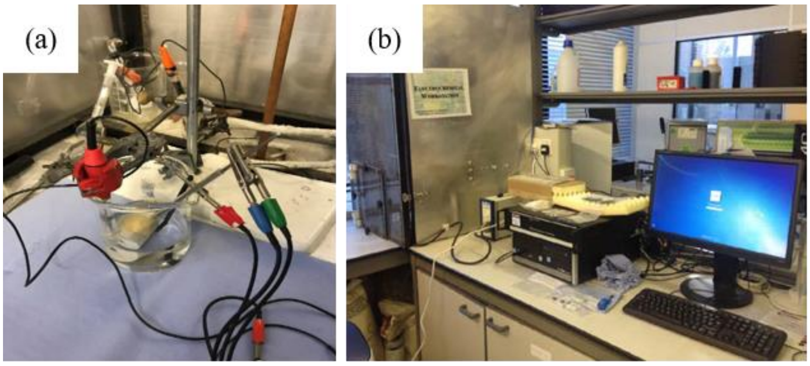

Fig. 3-12 (a) Electrochemical cell setup, (b) Electrochemical test workstation.

3.8.1 Sample preparation

Prior to corrosion testing, the as-received and HPT-processed disks were wet ground with 1200 and 4000 grits of SiC abrasive papers, followed by polishing with 6 μm and 1 μm diamond pasts, degreasing with distilled water and acetone, and finally blown to dry by using compressed air.

3.8.2 Open circuit potential

The open circuit potential (OCP) measures the changes in potential over a set time period in order to determine the thermodynamic tendency of corrosion. It also enables the stability of the test samples to be monitored via fluctuations and steadiness of the OCP values throughout the test period. The parameters used for the OCP test in the Gamry Framework software are shown in Table 3-4.

Table 3-4 Parameters for OCP test in the Gamry Framework software.

Parameter (unit)	Value
Total time (s)	3600
Sample period (s)	2
Sample area (cm^2)	0.2826

A total time of 3600 s was set as the time period for the study, i.e. the total time that the electrochemical test rig setup was immersed in the electrolyte was 1 hour. The time period is sufficient to achieve a quasi-steady OCP value for the test samples. The sample period refers to the time gap between two test points, which translated to collected data being recorded every two seconds. On the other hand, the sample area is determined by the circular surface area of the open cylindrical cavity on the sample holder, A_C ($A_C = \pi r_C^2$), where r_C is the radius of the circular cavity. Since $r_C = 0.3$ cm, hence the sample area was calculated to be 0.2826 cm^2 for all the electrochemical tests. The measured OCP data were plotted against time using Gamry Echem Analyst software to investigate the variation and stability of the potential over time.

3.8.3 Potentiodynamic polarisation

After conducting the potentiodynamic polarisation test, potentiodynamic polarisation curves (PPC) were plotted to determine the anodic and cathodic corrosion current density, i_{corr} and hence to calculate the corrosion rate for the as-received and HPT-processed AM 316L SS disks. The potentiodynamic polarisation (PP) test was conducted over potential values ranging from -500 mV to 2000 mV with respect to the OCP at a scan rate of 0.17 mV s^{-1}. The parameters used for this test are shown in Table 3-5.

Table 3-5 Parameters for potentiodynamic polarisation test in the Gamry Framework software.

Parameter (unit)	Value
Initial E vs E_{OCP} (mV)	-200
Final E vs E_{OCP} (mV)	1500
Scan rate (mV s^{-1})	0.167
Sample period (s)	1
Sample area (cm^2)	0.2826
Density (g cm^{-3})	7.97
Equivalent weight (EW)	2

3.8.4 Electrochemical impedance spectroscopy

The electrochemical impedance spectroscopy (EIS) analysis is used to determine the current and impedance of the potential cell. The potentiostat supplied a sinusoidal voltage (10 mV) against the OCP with frequencies ranging from 10 mHz to 100 kHz, and the values of the resulting current and impedance obtained from the working electrode were measured and recorded. The parameters for EIS test, as entered in the Gamry Framework software are shown in Table 3-6.

Table 3-6 Parameters for EIS test in the Gamry Framework software.

Parameter (unit)	Value
DC voltage vs E_{OCP} (V)	0
Initial frequency (Hz)	100000
Final frequency (Hz)	0.01
Points per decade	10
AC voltage (mV ms)	10
Sample area (cm^2)	0.2826
Estimated impedance, Z (Ω)	100

The ‘DC voltage vs E_{OCP}’ parameter refers to the offset of the constant potential applied to the electrochemical cell throughout testing. The AC voltage refers to the root mean square (RMS) value of the AC signal applied to the electrochemical cell. Initial and final frequency refers to the initial and the last AC signal applied during data collection, respectively. The ‘points per decade’ parameter defines the number of measurements that will be taken within one decade of frequency in the log scale.

All electrochemical tests (OCP, EIS and PP) were repeated at least three times for the as-received and HPT-processed disks to reduce experimental errors as much as possible and maintain a high statistical accuracy for the obtained results.

3.8.5 Characterisation of the corroded disks after electrochemical tests

The JSM-JEOL 6500 FE-SEM machine was used to further characterise the microstructures and surface morphologies of the corroded disks at higher magnifications. Images of microstructures and corroded areas were taken at 100x, 400x, and 1000x magnifications throughout the disk surface. In addition, the information on the chemical compositions of the corroded area were determined via EDX analysis. EDX characterises the elemental composition according to the amount and energy of the x-rays emitted from various elements in the corroded disks, including Fe, Ni, Cr and O. The corrosion test area was at the centre of the thin disks with an area of 6 mm in diameter.

3.9 Wear test

3.9.1 Wear test facility

The TE 77 high frequency friction tribometer is typically used to evaluate the friction and wear properties of materials in either dry or lubricated conditions in a reciprocating (back and forth movements) rolling or sliding contact manner. This wear test rig consists of an eccentric cam which rotates inside a lubrication bath, an upper clamp fixed to an arm connected to the eccentric cam, and a lower clamp that is held onto the base of the rig by a load linkage mechanism. The lower clamp houses the specimen being studied and does not move while the counter surface, i.e. the material used to run the wear test via reciprocating rolling or sliding movements is placed inside the upper clamp. The whole hardware setup is connected to a control unit that comprises of a SLIM 2000 Serial Link Interface Module and a COMPEND 2000 software to manage the test procedure sequence and acquire data on a host computer.

The counter surface inside the upper clamp does reciprocating movements against the material being studied that was placed inside the lower clamp, with the load applied to the counter surface through a spring, a linkage, and a roller cam follower. A geared servomotor and pulley in the eccentric cam serve as actuators for the spring, providing loads up to 1000 N. A piezoelectric transducer with a sensitivity of 45.7 pC N^{-1} within a range of ± 500 N was used to measure the friction force exerted during the wear test. The contact potential and temperature of test materials were measured by respective sensors connected to the control unit.

On the other hand, the surface morphology, topology, and roughness of a material before or after undergoing wear test were measured using the following profilometers: (i) Alicona infinite focus microscopy (IFM) and (ii) TAICAAN XYRIS 2000 TL/CL metrology system. The Alicona IFM is an optical 3D micro-coordinate system that measures the surface morphology of a material by delivering a measurement density of more than 100 million points across the sample, with vertical resolution up to 10 nm. It is capable of measuring small to large areas and volumes. The TAICAAN XYRIS 2000 TL/CL machine is an advanced metrology system equipped with a confocal and triangular laser beams to provide a wide range of measurements. It can measure the topology of the surface roughness by creating 2D or 3D surface profiles. The 2D mode scans the surface of the sample to quantitatively measure and analyse the surface roughness, while the 3D mode offers high-precision measurements of the radii of the rough surfaces.

3.9.2 Rig setup and wear test parameters

To assess the wear performance of as-received and HPT-processed AM 316L SS disks, dry sliding reciprocating wear tests were conducted on a the TE 77 tribometer. The tests were conducted on the as-received and HPT-processed disks in a linear reciprocating pin-on-disk mode. The disks were secured on a mild steel plate using adhesive, which was then fixed onto the lower clamp. The counter surface, i.e. the pin used was an alumina ball with a diameter of 6 mm and a hardness value of 1160 HV, which was fixed inside the upper clamp. During the wear tests, the alumina ball glided on the surface of the disks in a linear back and forth (reciprocating) manner. The complete setup of the wear test rig used in this study is illustrated in Fig. 3-13 [381].

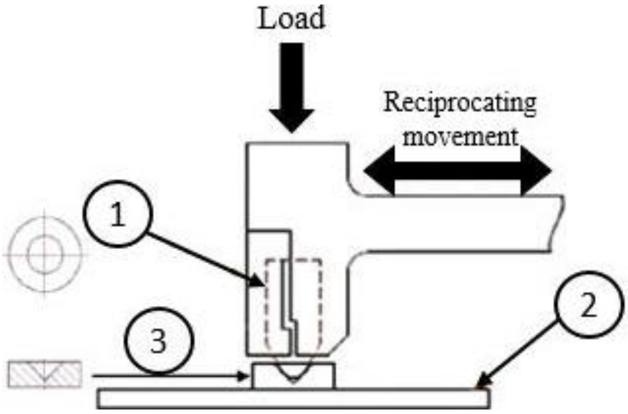

Fig. 3-13 Illustration of wear test setup on TE 77 tribometer [381]. Reproduced with permission of the rights holder.

Prior to test, the as-received and HPT-processed disks were ground using 800, 1200, and 4000 grits SiC paper before polishing down to 3 µm and 1µm diamond suspensions. The disks were subsequently cleaned using isopropanol, dried, and weighed before being glued on to the mild steel plate. After each testing, the adhesive that secures the disk and mild steel plate were removed by using an ultrasonic acetone bath. The disk and mild steel plate were further cleaned in the same bath for 10 minutes to remove any debris or dirt on the surface. Finally, the mass loss, m_{loss} due to material removal during wear test was determined using a Mettler AE240 microbalance (± 0.1 mg). In addition, the alumina ball was replaced after each testing due to slight wear and deformation introduced on the ball after testing to obtain consistent results across all test conditions.

The small-scale dry sliding tests were conducted at the peripheral regions of the as-received and HPT-processed disks under a constant load of 5 N. Hence, the alumina ball (counter surface) glided over the edges of the disks (> 3 mm from the centre) with a stroke length of 2 mm and reciprocating frequency of 1 Hz, giving an average sliding velocity of 4 mm s^{-1}. The temperature and humidity during testing were 21°C and 30.3%, respectively. A total of 8 separate measurements were made at 8 different peripheral locations on the disk to obtain average values when determining the tribological properties as shown in Fig. 3-14 [382].

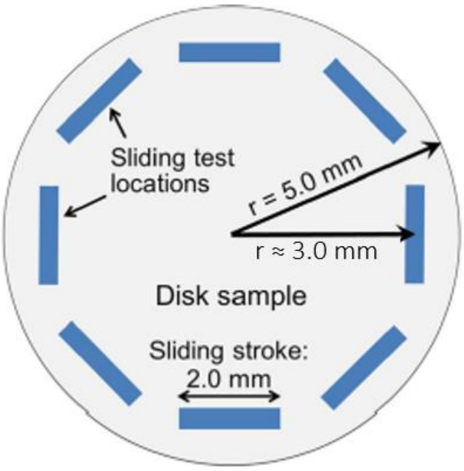

Fig. 3-14 Illustration of wear test locations on the periphery of the disks [382]. Reproduced with permission of the rights holder.

3.9.3 Characterisation of worn disk surface after wear test

For each test. the coefficient of friction (COF) was measured for a total sliding distance of 20 m using the COMPEND 2000 software on the computer after being fed test data from the SLIM 2000 Serial Link Interface Module. Before and after wear tests the surface roughness of the as-received and HPT-processed disks was measured using the Alicona IFM system, while 2D and 3D surface profiles of the surface roughness topology of the disks were created and analysed by using the TAICAAN XYRIS 2000 TL/CL metrology system. The microstructures of the worn surfaces were analysed using SEM and EDX.

Chapter 4 Porosity evolution in AM 316L SS processed by HPT

4.1 Introduction

Despite the tremendous advantages of design flexibility, low material wastage, and cost savings offered by AM processes compared to CM methods, as-built AM metallic parts still suffer from defects such as porosity and cracks that may deteriorate the mechanical properties and reduce its lifespan during service. So far, various post-processing techniques have been applied to AM metallic parts to reduce pores and cracks, as well as to improve surface quality and mechanical properties. Typical post-processing techniques include thermal processes such as HIP and various heat treatment procedures, and non-thermal processes such as surface machining, cold spraying, and shot peening (SP).

Although HIP and heat treatment has been shown to reduce porosity and cracks in AM metallic parts, they are often accompanied by reduced yield and tensile strength [383–386]. In addition, cold spraying and SP can reduce porosity and improve strength on the surface only, therefore such improvements could not be achieved for the bulk material [387–389]. On the other hand, HPT is one of the widely used SPD techniques that imposes simultaneous hydrostatic pressure and extreme torsional strain on bulk metallic materials, resulting in large amounts of accumulated dislocations and significant grain refinement down to the UFG and/or NG regime. Studies on HPT-processed CM metals and alloys have shown the combined hydrostatic pressure, extreme torsional strain, and UFG/NG microstructures are able to completely close pores and improve the yield and tensile strengths of the bulk material [18,221,233,372].

However, SPD processing has never been applied on AM metallic materials. Therefore, this is the first time that HPT processing is applied on 316L SS fabricated by SLM. HPT was conducted under 6 GPa for 1/4, 1/2, 1, 5 and 10 revolutions at RT. The distribution, morphology, and area fraction (%) of the pores in the as-received and HPT-processed disks were analysed by using conventional 2D microscopy approach (OM and SEM) and ImageJ software. In addition, XCT scan was conducted to evaluate the porosity content in 3D for the as-received disk and compared with the results obtained from microscopy analysis. The overall results of porosity evolution were discussed in terms of the hydrostatic pressure, variation in torsional shear strain, and the UFG microstructures. In addition, the porosity evolution in AM 316L SS was also compared with that in other AM metallic materials obtained by various post-processing techniques.

4.2 Results

4.2.1 Porosity and microstructural evolution from microscopy examinations

Fig. 4-1 displays the microstructures and porosity distribution in the as-received disk. The etched OM image taken at the surface-normal, i.e. the x-y plane (perpendicular to build direction) show a mix of coarse and fine equiaxed grains (Fig. 4-1(a)), while elongated grains growing through the numerous semi-circular melt pools are observed at the surface-parallel, i.e. the x-z plane (parallel to build direction) as shown in Fig. 4-1(b). The polished OM images in Figs. 4(c) and (d) exhibit the pores at the surface-normal, taken at the centre and edge of the as-received disk. The pores are arranged in square patterns, indicating that they are concentrated at the boundary of the melt pools. The average pore size is 24.86 ± 18.81 μm, which makes up 0.679 ± 0.051 % of the surface-normal area. The pores at the surface-parallel of the disk (Fig. 4-1(e)) are arranged in a slanting manner upon successively solidified layers with an average size of 23.48 ± 21.25 μm, accounting for 0.564 ± 0.022 %. of the surface-parallel area.

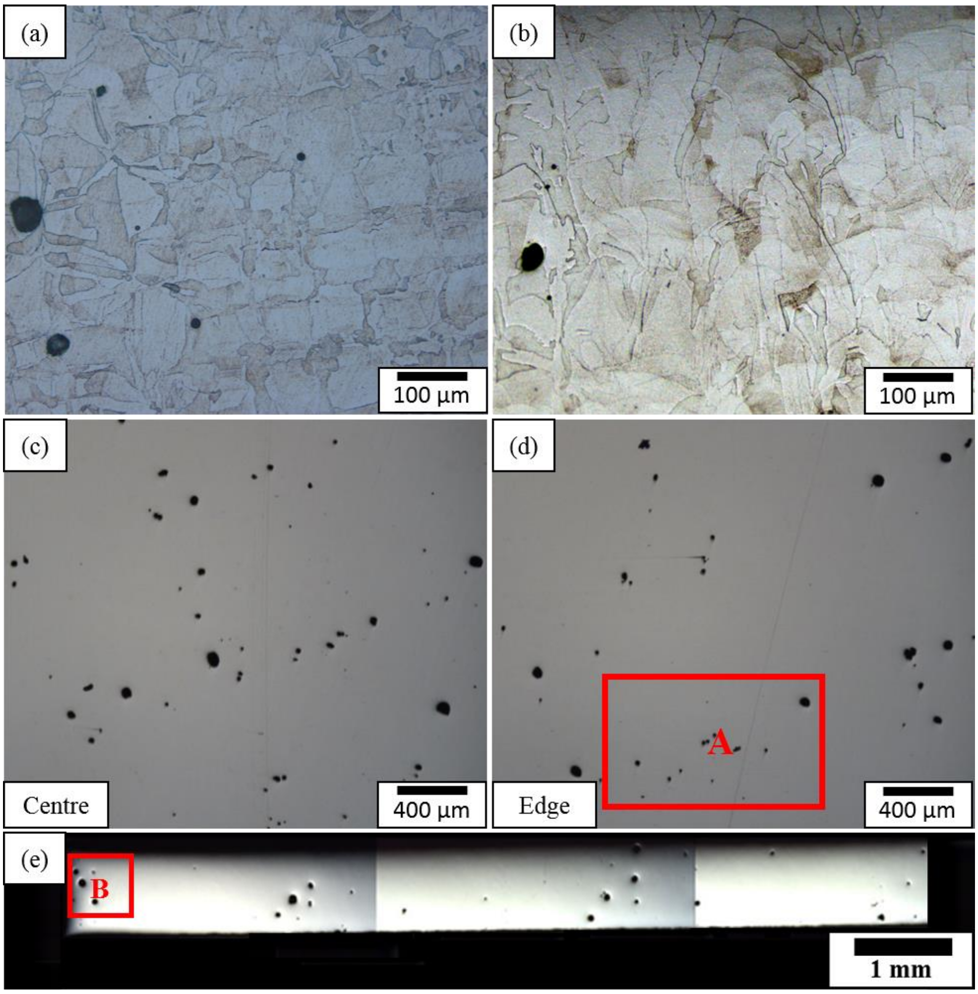

Fig. 4-1 Etched OM images of microstructures at (a) surface-normal – x-y plane and (b) surface-parallel – x-z plane; polished OM images showing porosity distribution at disk (c) centre and (d)

edge of surface-normal, and at (e) surface-parallel. Areas A and B are further investigated after HPT processing. Images are taken from the as-received disk.

Despite the slight discrepancy between the percentage of porosity at the surface-normal and the surface-parallel, they indicate high solidification levels (> 99%) are attained for the as-received AM specimens in this study. Furthermore, the spherical morphology of the pores indicate that they are gas-induced pores, which could be caused by the entrapment of inert gas in the melt pool during the melting of powder or may already exist inside the initial raw powder and then remain in the finished structure [15,45].

Fig. 4-2 exhibits the microstructures and porosity distribution in the disk processed through 1/4 HPT revolution. The torsional strain applied via HPT at this stage ($\varepsilon_{\text{eq.-HPT}}$ = 3.4) results in the melt pools being stretched, while the initially spherical pores become increasingly elongated (red arrow), both rotated in the direction of the torsional strain as shown in Fig. 4-2(a) for the surface-normal. Similarly, the elongated grains observed at the surface-parallel appear distorted and directed to the edge of the disk as displayed in Fig. 4-2(b).

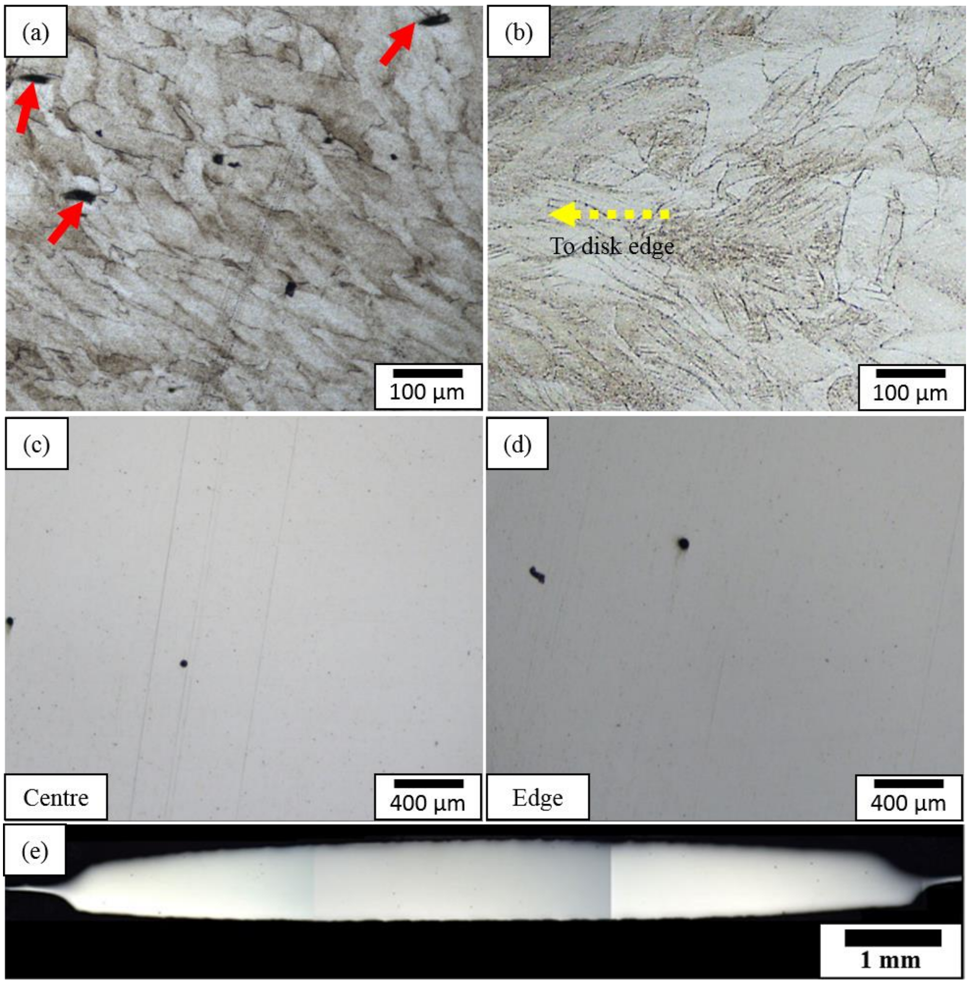

Fig. 4-2 Etched OM image of microstructures at (a) surface-normal – x-y plane and (b) surface-parallel – x-z plane; polished OM images showing porosity distribution at (c) disk centre and (d) disk

edge of surface-normal, and at (e) surface-parallel. Images are taken on the disk after 1/4 HPT revolution.

Figs. 4-2(c) and (d) demonstrate a significant contrast in porosity content between the HPT-processed disk after 1/4 revolution and the as-received counterpart at the centre and peripheral regions of the surface-normal. The average pore size and percentage are considerably decreased to 4.87 ± 4.31 μm and 0.058 ± 0.011 %, respectively, representing a reduction of 91.4%. Likewise, Fig. 4-2(e) shows an almost pore-free structure at the surface-parallel compared to the as-received disk, with the average pore size and percentage diminished to 7.29 ± 3.57 μm and 0.059 ± 0.015 %, respectively, indicating an improvement of 89.5%.

Fig. 4-3 compares the pore size distribution in the as-received disk and in the disk after 1/4 HPT revolution at the surface-normal and at the surface-parallel. The pore size is quantified as the Feret diameter, defined as the distance between two parallel planes that restrict any two opposing edges of the pores. This allows a more accurate representation of the pore diameter to be made, particularly for irregular-shaped pores. The Feret diameter is used instead of normal spherical diameter to provide consistent measurements for all pore morphologies; the spherical and near-spherical pores in the as-received disk and the elongated pores observed after 1/4 HPT revolution.

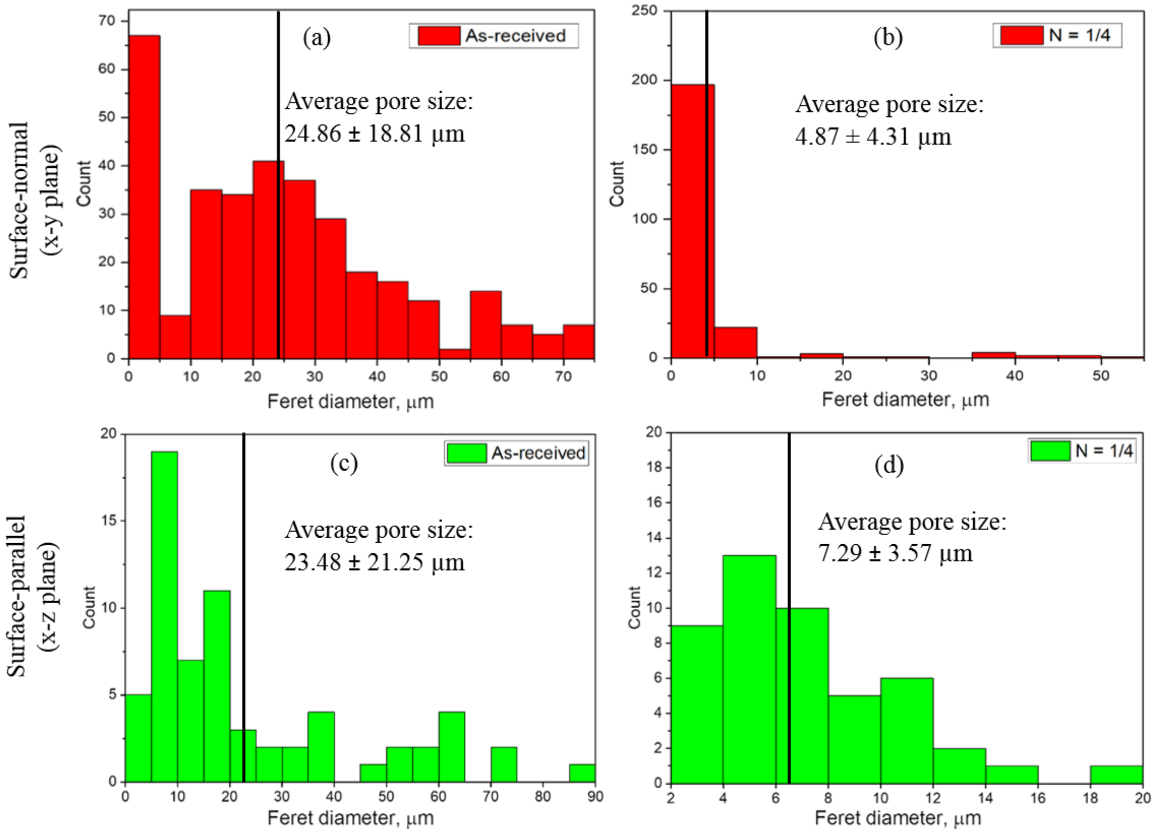

Fig. 4-3 Comparison of pore size distribution for as-received and HPT-processed disks through 1/4 revolution at the (a) and (b) surface-normal (x-y plane), and (c) and (d) surface-parallel (x-z plane).

A wide pore size distribution could be observed in the as-received disk at the surface-normal, ranging from 0 – 75 µm as displayed in (Fig. 4-3(a)). Most of the pores lie in the 10 – 40 µm range. However, the pores with sizes > 50 µm initially observed in the as-received disk are eliminated completely after 1/4 HPT revolution, and most of the larger pores (> 10 µm) are reduced into considerably smaller pores in the 0 – 5 µm range as shown in Fig. 4-3(b). Similarly, the pore sizes in the as-received disk observed at the surface-parallel are also widely distributed, ranging from 0 – 90 µm (Fig. 4-3(c)), whereas they are significantly reduced down to only 2 – 20 µm after only 1/4 HPT revolution (Fig. 4-3(d)). These results suggest that the combination of compressive force and minimal torsional straining at the early stage of HPT ($\varepsilon_{eq.\text{-HPT}} \leq 5$) are already able to 'close' the small pores and significantly reduce the size of the larger pores.

However, the analysed area for pores at the surface-normal is obviously larger compared to that at the surface-parallel, resulting in a discrepancy in the total pore count between these two areas. For the as-received disk, the average total pore count at the surface-normal is 331, while it is only 64 at the surface-parallel. After 1/4 HPT revolution, the average total pore count is 240 at the surface-normal and 47 at the surface-parallel. Therefore, the percentage of porosity is normalised by dividing the pore count for a given size range with the total pore count within the particular surface area being analysed, and the results are shown in Fig. 4-4.

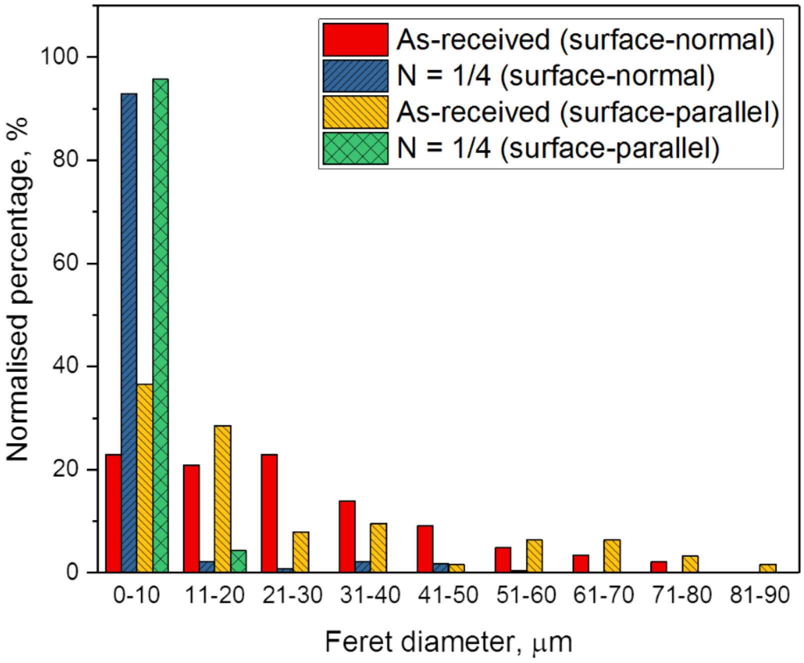

Fig. 4-4 Normalised percentage of pore size distribution for as-received and HPT-processed disks through 1/4 revolution at the surface-normal (x-y plane) and at the surface-parallel (x-z plane).

Based on Fig. 4-4, the majority of pore diameters in the as-received disk lie in the region of 0 – 30 µm and 0 – 20 µm at the surface-normal and surface-parallel, respectively. In both cases, the majority of pores are concentrated in the 0 – 10 µm size range after 1/4 HPT revolution, suggesting a threshold to which pore reduction could be achieved at the early stages of HPT straining. In addition, the circularity factor, *C* is introduced to evaluate the change in pore morphology before HPT processing and after 1/4 HPT revolution by using the following formula [383]:

$$C = 4\pi \frac{A_p}{{P_p}^2} \qquad \text{Eqn. 4-1}$$

where P_p is the perimeter (μm) and A_p is the pore area (μm^2), both determined from ImageJ software. *C* values close to 1 indicate near perfect circular pore, while *C* values close to 0 demonstrate increasingly elongated pore. The results of the calculations are shown in Table 4-1. The average circularity of the pores for the as-received disk at the surface-normal is 0.92 ± 0.08, which is slightly lower than that at the surface-parallel (0.95 ± 0.05). This could be due to the higher pore count at the surface-normal, in which a higher amount of near spherical pores is present compared to that at the surface-parallel, therefore reducing the average circularity. After 1/4 HPT revolution, the average circularity significantly reduces to similar values; 0.26 ± 0.04 at the surface-normal and 0.27 ± 0.03 at the surface-parallel. These values represent ~ 72% elongation in pore sizes, signifying the effectiveness of HPT to minimise porosity even at low torsional strain level.

Table 4-1 Average pore circularity before HPT processing and after 1/4 HPT revolution.

Processing condition	Surface analysed	Average circularity
As-received	surface-normal (x-y plane)	0.92 ± 0.08
	surface-parallel (x-z plane)	0.95 ± 0.05
N = 1/4	surface-normal (x-y plane)	0.26 ± 0.04
	surface-parallel (x-z plane)	0.27 ± 0.03

Upon further HPT straining to 1/2 revolution ($\varepsilon_{\text{eq.-HPT}}$ = 6.8) and 1 revolution ($\varepsilon_{\text{eq.-HPT}}$ = 13.6), the HPT-processed disks are free from pores, as shown by the SEM images for both surface-normal and surface-parallel in Figs. 4-5(a) – (d). In particular, the SEM and TEM images in Fig. 4-5 are taken at areas A and B of the as-received disk shown in Fig. 4-1 after 1/2 and 1 HPT revolutions. It could be observed that the pores are now completely closed as indicated by the sub-micron spherical and near-spherical inward indents (dashed red arrows) and outward bumps (solid black arrows) that appear at the surface-normal and the surface-parallel. The indents and outward bumps are actually internal sub-surfaces that help to close the pores when they collapse upon the application of compressive force and continuous torsional strain as the number of HPT revolutions increase [244,247]. In the present study, the indents and bumps can be confirmed as closed pores because the SEM images in Figs. 4-5(a) – (d) are taken at areas A and B of the as-received disk shown in Fig. 4-1 that initially contain pores. Furthermore, the TEM images taken at area A after 1/2 and HPT revolutions shown in Figs. 4-5(e) and (f), respectively show nano-sized grains (< 100 nm) with dense dislocations obtained grow through the elongated pores and internal sub-surfaces to further close the remaining pores, suggesting that a strong metallic bond is created at the area of the closed pores [372].

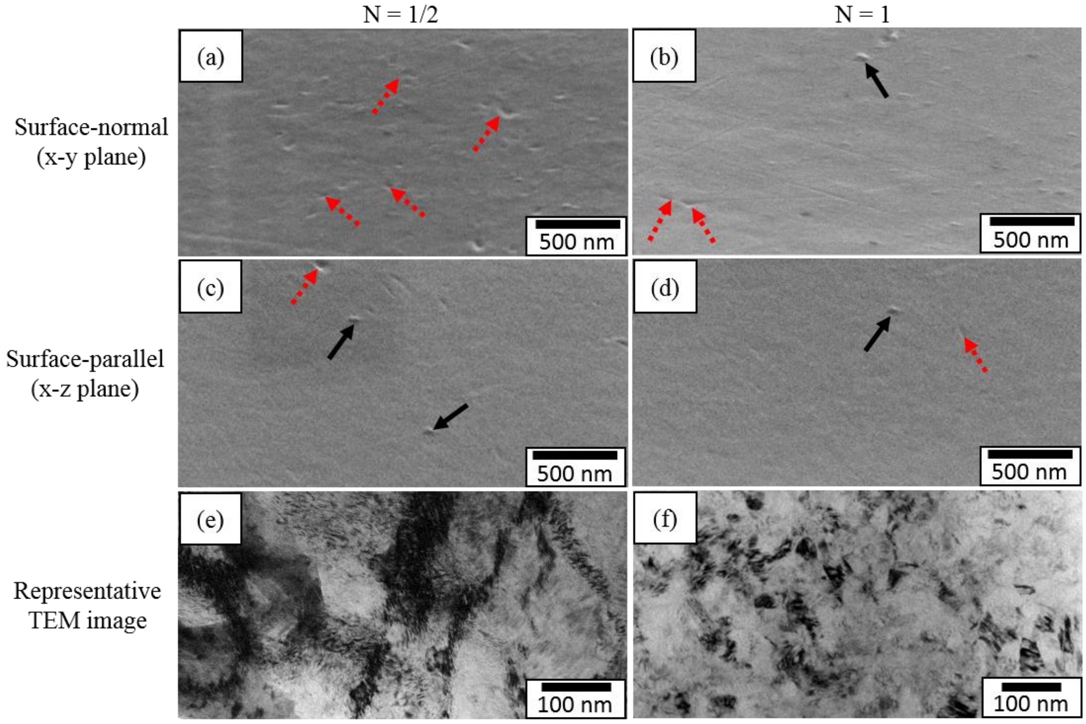

Fig. 4-5 (a), (c), and (e) SEM and TEM images after 1/2 HPT revolution, and (b), (d), and f) SEM and TEM images 1 after 1 HPT revolution. The images are taken at areas A and B of Fig. 4-1 after HPT processing.

4.2.2 Porosity measurement results from x-ray computed tomography

Fig. 4-6 shows examples of representative pores and their corresponding sphericity for the as-received disk based on the reconstructed XCT image stack (> 1000 layers) obtained from VG Studio Max 2.1 software. Sphericity allows for direct 3D visualisation of the pore morphology, and the sphericity factor, *S* is calculated by using the following equation [390]:

$$S = \frac{\pi^{\frac{1}{3}}(6V_p)^{\frac{2}{3}}}{A_p} \qquad \text{Eqn. 4-2}$$

where V_p is the pore volume (μm^3), and $S = 1$ indicates ideal sphere. The completely spherical and near spherical pores indicate that the pores in the as-received disk are indeed gas-induced porosity in the range of 10 – 90 µm, confirming the OM observations in Fig. 4-1.

2D and 3D projections of the reconstructed images are displayed in Fig. 4-7. These images show similar porosity distribution throughout the disk without major variations through the disk thickness (surface-parallel). The surface-normal view (Fig. 4-7(a)) shows that a square-shape outline representing the ‘island’ scan strategy is present in the centre of the XCT scan region, while Fig. 4-7(b) displays the pore distribution at the surface-parallel of the as-received disk. The isometric projection shown in Fig. 4-7(c) clearly reveal spherical and near-spherical pores that are dominant in the as-built AM 316L SS specimen in this study. The average sphericity of the pores for the as-received disk obtained from XCT is 0.83 ± 0.17.

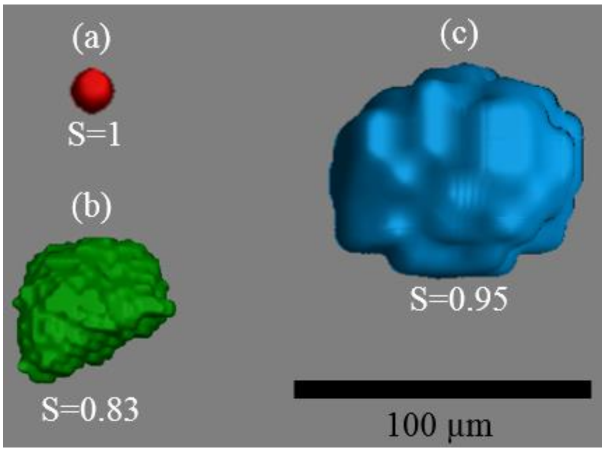

Fig. 4-6 Examples of spherical or near-spherical pores in the as-received disk.

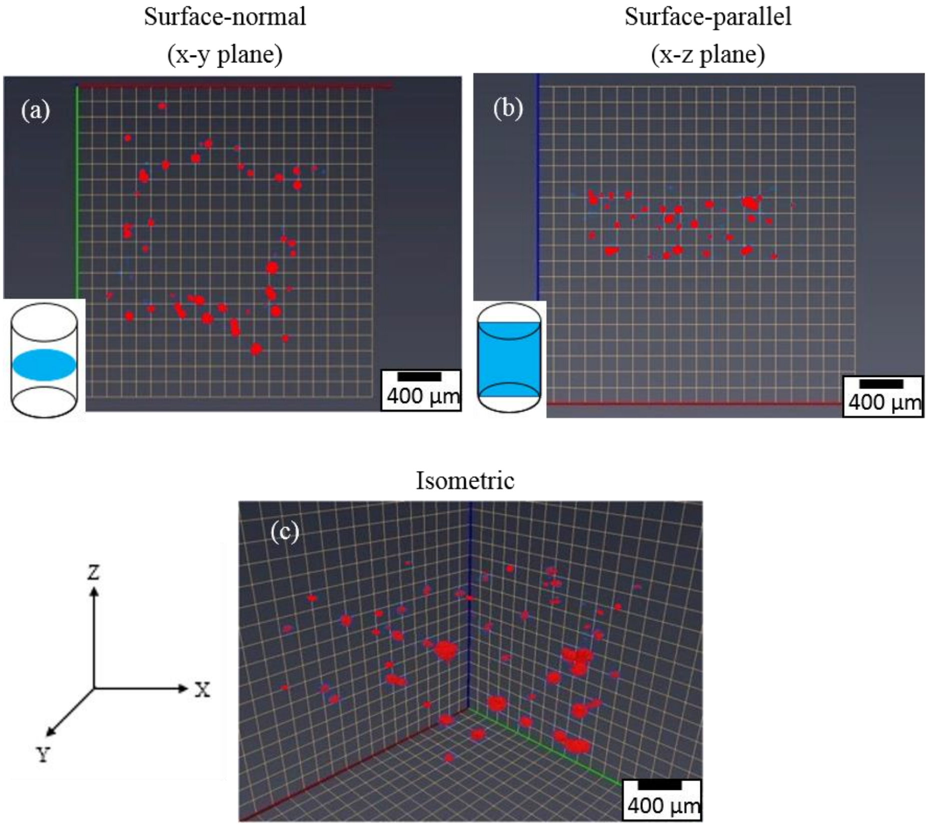

Fig. 4-7 3D visualisation of the XCT scan on the as-received disk at different planes.

On the other hand, Fig. 4-8 shows the comparison between a binarised OM micrograph and a reconstructed XCT image at the surface-normal (x-y plane) of the as-received disk. Upon close inspection, similar pore distribution could be observed, but much smaller pores (< 10 µm) in the OM image indicated by the blue circled areas and arrows in Fig. 4-8(a) are absent in the reconstructed image for XCT (Fig. 4-8(b)).

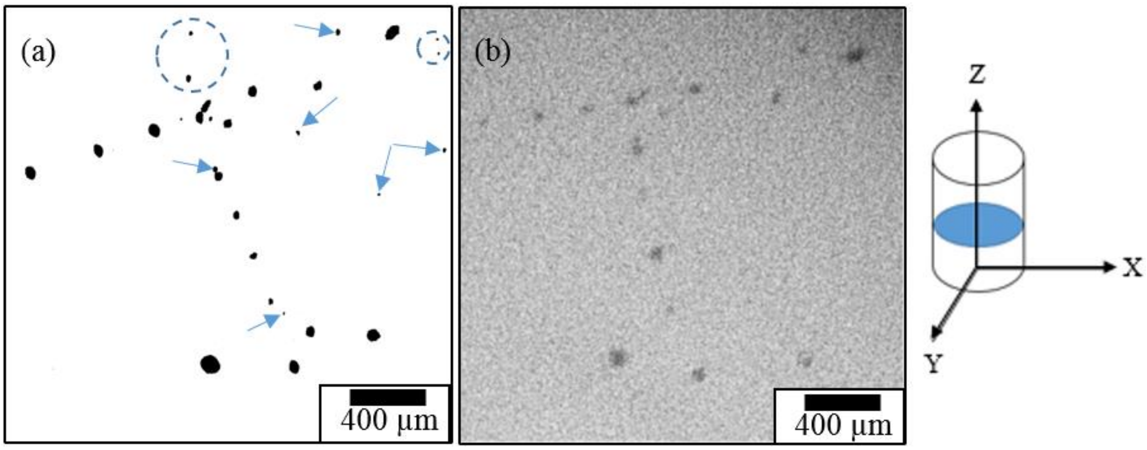

Fig. 4-8 Comparison between (a) binarised OM micrograph, and (b) reconstructed XCT image taken at the surface-normal (x-y plane) of the as-received disk.

When comparing the pore size distribution of the as-received disk obtained from XCT (Fig. 4-9(a)) with that obtained from OM images (Fig. 4-3(a)), it can be seen that the XCT scan yields fewer pores in the 5 – 10 µm region, and no pores between 0 – 5 µm could be detected. Hence, the average pore diameter detected from XCT is relatively higher than that of OM. A total of 294 pores have been detected from the reconstructed XCT image layers compared to 331 detected from OM images. Therefore, the percentage of porosity obtained from XCT images are normalised to provide a direct comparison with that from OM images as shown in Fig. 4-9(b). A similar pore size distribution is observed for both analysis methods, except in the 0 – 10 µm region, in which the percentage of pores obtained from OM is significantly higher than that attained from XCT images (~ 23% compared to only 7%). This could be attributed to the detection limit from the XCT parameter settings such that pores < 5 µm could not be detected during XCT scan.

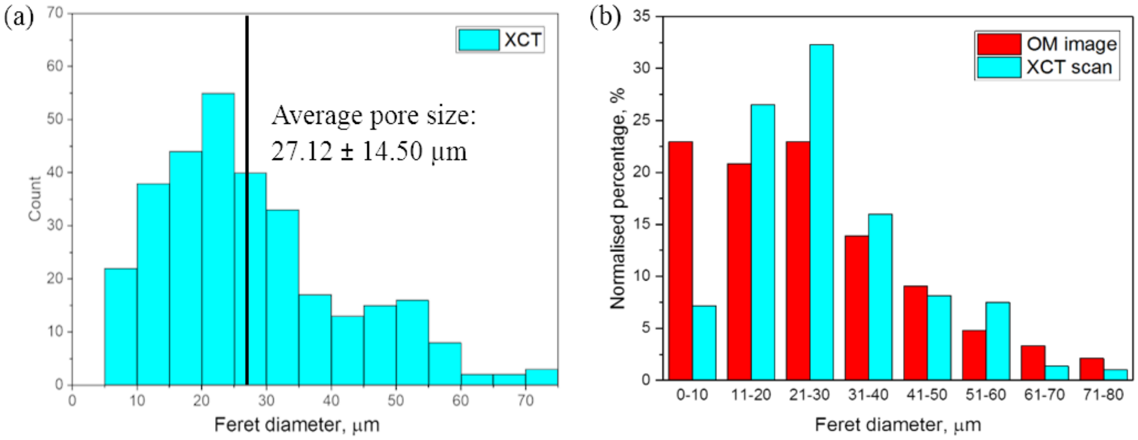

Fig. 4-9 (a) Pore size diameter distribution obtained from XCT and (b) comparison of normalised porosity percentage from XCT and OM images for the as-received disk.

4.3 Discussion

4.3.1 Mechanism of pore formation and closure

The as-received AM 316L SS is found to have a porosity content of 0.679 ± 0.051 % at the surface-normal (x-y plane) and 0.564 ± 0.022 % at the surface-parallel (x-z plane), indicating that high densification level of $\geq$ 99% is achieved in the bulk material. Such high densification and low porosity levels, plus no cracks observed in the final parts are typical of AM materials obtained under optimum processing conditions, e.g. energy density and scan strategy [83,152,351,391]. In addition, no other typical metal AM defects are observed in the as-built structure aside from gas-induced porosity, which is also indicative of optimum selection of processing parameters. For example, Yusuf et al. [154] recently obtained ~ 0.82% porosity level in AM 316L SS when the energy density used was ~ 260 J mm^{-3} using the 'island' scan strategy. Cherry et al. [392] found an optimum porosity level of 0.38% using an energy density of 104.52 J mm^{-3} and bi-directional scan strategy.

However, the pores found in the as-received AM 316L SS in this study are not evenly distributed, with major pore concentration observed at the boundary between each 'island' (for observation at surface-normal) as shown in Figs. 4-1(c) and (d). This is similar to the results obtained by other researchers using the same scan strategy [154,393,394]. In addition, majority of the pores at both surface-normal and surface-parallel are found to be spherical, indicative of gas-induced porosity. Porosity is a defect commonly observed in metal AM processes and they are categorised into gas-induced and process-induced porosity [15]. Gas-induced pores are spherical and are typically formed in the precursor powder during powder production process, e.g. gas-atomisation. Such pores could also be present due to the reaction between C and traces of O found in the build chamber during SLM processing, causing the formation of either CO or CO_2 which are eventually entrapped in the as-built part [395]. The presence of oxide-based inclusions could also become nucleation sites for gas-induced pores [396,397]. On the other hand, non-spherical process-induced pores are attributed to non-optimum processing parameters [398,399], which are not found in this study.

The tendency of the spherical pores to segregate into the 'island' boundaries may be the result of the laser beam displacing the entrapped gas pores in the powder towards the boundaries at the end of each scan. Superheating and expansion of small regions of entrapped gas during subsequent scans could also result in spherical gas pores at this area [400]. Even though no oxygen was found in the precursor powder, and that the atmosphere of the build chamber was predominantly purged with nitrogen prior to SLM processing, traces of oxygen may still exist inside the build chamber. CO and CO_2 formed due to the interactions between carbon and these oxygen traces during SLM processing are speculated to be the reason for the spherical pores observed within the 'islands'.

In addition, a remarkable 91.4% reduction in porosity level is attained after 1/4 HPT revolution, yielding a porosity content of only 0.058 ± 0.011 % for surface-normal, and 0.059 ± 0.015 % for the surface-parallel (reduction of 89.5%). Furthermore, the average pore size significantly decreases from 24.86 ± 18.81 µm to only 4.87 ± 4.31 µm surface-normal and from 23.48 ± 21.25 µm to 7.29 ± 3.57 µm for the surface-parallel. Such exceptional pore size reduction from HPT processing is generally attributed to the coupling of compressive force and severe plastic deformation (straining) of the torsional force employed during the process [401]. The pores are essentially pressed and squashed before being effectively 'closed' as the number of HPT revolutions increase. In this study, the larger pores in the as-received disk (≥ 50 µm) are observed to become elliptical and smaller after 1/4 revolution of HPT processing as shown in Fig. 4-2(a), which contributes to the significant decrease in the pore count for this pore size range (Fig. 4-3), similar to the study carried out by Li et al. [402]. Instead, the pore count for pore sizes ranging from 0 – 10 µm increases, which is expected due to the resulting compressive force and torsional strain applied after 1/4 HPT revolution.

It is widely accepted that the generation and growth of pores in metals mainly depend on large levels of stress triaxiality under hydrostatic tension, either under loading or during processing [403,404]. On the other hand, the application of hydrostatic pressure has been found to be crucial in eliminating porosity. For example, Nakasaki et al. [405] observed that rolling a steel billet in multiple passes via a constant hydrostatic pressure was able to eliminate the centre pores that initially existed in the steel billet. Wang et al. [406] found that the rate of pore closure during hot rolling of steels are influenced by rolling process parameters and the pore location relative to the rolling contact surfaces. In addition to hydrostatic pressure, the application of shear strain also promotes the collapse and closure of pores. This enables a sound bonding to be achieved throughout the pores after they come into close contact atomically due to the combined hydrostatic pressure and shear strain [407,408]. Hydrostatic pressure and shear strain are two main features in severe plastic deformation (SPD) techniques to yield UFG/NG microstructures and promote strong metallic bonding within the processed materials at both atomic and macroscopic scales [244,247].

Furthermore, Qi et al. [372] systematically studied the generation and healing of porosity in HPT-processing of pure Cu and explained the pore elimination mechanism in terms of grain refinement. The pressure from compressive force (from pushing the lower anvil to the upper anvil) and low torsional strain (from rotating the lower anvil) could cause the pores to collapse and stretch their internal sub-surfaces, and generate UFG microstructures. Upon higher torsional strains, sub-micron grains with clear grain boundaries start to form and the pores continuously elongate parallel to the shearing direction. These result in the fragmenting of the pores that create intimate atomic contact within the internal sub-surface of the pores, subsequently closing the pores and hold the bulk material together.

The mechanism of pore closure in this study is illustrated in Fig. 4-10. At the early HPT deformation stage corresponding to $\varepsilon_{\text{eq.-HPT}} = 3.4$ after 1/4 revolution, the combination of hydrostatic pressure and low torsional strain cause the pore to elongate towards the direction of shear strain and push the internal sub-surface upwards to fill the pore area (Fig. 4-10(b)). Upon higher torsional strain values,

$\varepsilon_{eq.\text{-}HPT}$ of 6.8 – 13.6 from 1/2 to 1 HPT revolution, the emergence of nano-sized grains with dense dislocations (Figs. 4-5(e) and (f)) and the existing internal sub-surfaces create a strong metallic bond that is able to completely close the pore by (Fig. 4-10(c)). This is evidenced by the growth of nano-sized grains (< 100 nm) through area A for 1/2 and 1 HPT revolutions (Figs. 4-5(e) and (f), respectively) without any observable discontinuities at the spots that are otherwise pores in the as-received disk. Since the grain sizes at these stages are < 70 nm and grow throughout area A without any discontinuities, it is reasonable to infer that a strong metallic bond is created at the closed pores. Therefore, HPT has been proven as a very effective approach to reduce porosity via the strong metallic bonding that brings together and closes the pores as the result of the combination of hydrostatic pressure and torsional shear strain imposed.

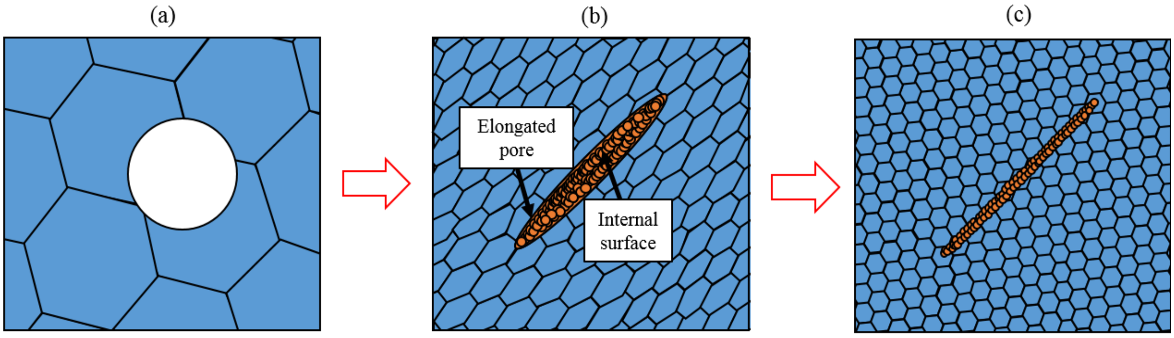

Fig. 4-10 Schematic illustration of pore closure and evolution of microstructure in this study.

4.3.2 Comparison between porosity content analysed by OM and XCT

The distinction in pore size measured by OM and that detected by XCT could be attributed to several factors. Firstly, optical micrographs could be influenced by microscope settings, e.g. light, focus, thresholding and binarisation options, as well as sample preparation techniques, e.g. sectioning and polishing. Secondly, XCT scan results could be affected by one or more of the following [216,409]: (i) image artefacts due to material properties and x-ray scattering, (ii) attained resolution, in which pore sizes lower than the spatial resolution could not be detected, and (iii) thresholding procedure.

In this study, despite the long scan time taken for each disk (21 hours) under a fine resolution of 1.832 μm, the background noise present in the reconstructed XCT image in Fig. 4-8(b) due to high z-value of the material results in the increased minimum pore size (> 5 μm) that can be detected. Thus, a different approach is needed for future works, such as detecting pore sizes < 5 μm, determining measurement uncertainty, and examining pore evolution in HPT-processed disks. For example, longer scan times can be used to improve the background noise by spot scanning on a small area. Nevertheless, the XCT method is expected to be more reliable in analysing porosity compared to cross-sectional analysis in OM for pores > 5 μm as XCT provides multiple slices of images through the thickness of the disk to form a single 3D image, which is impossible from only a single cross-section. Furthermore, XCT is a non-destructive technique (NDT) that does not require any physical sample preparation such as sectioning, grinding, and polishing which may eliminate some of the very fine pores and could compromise the analysis results.

4.3.3 Comparison of HPT and other metal AM post-processing techniques

A significant reduction in porosity level and average pore size could be obtained even with a relatively small range of equivalent strain, $\varepsilon_{\text{eq.-HPT}} \leq 5$ experienced by the material after 1/4 HPT revolution. Upon further straining to 1 revolution ($\varepsilon_{\text{eq.-HPT}} = 13.6$), the pores are completely closed, and the bulk material can be considered pore-free. This indicates the effective of HPT processing in eliminating porosity in AM metallic parts via a combined hydrostatic pressure and extreme shear strains. The nature of pore elimination obtained by HPT processing makes this SPD process very attractive compared to other SPD techniques, particularly ECAP. This is because retained porosity remains an inherent problem in metallic components processed by ECAP [410]. Moreover, since the presence of porosity almost always result in relatively poorer mechanical properties, e.g. hardness and yield and tensile strengths, the significant pore reduction and elimination is expected to result in much better mechanical performance in AM parts.

Pores have been found to become sites for crack initiation and propagation in AM metallic parts, which deteriorate both static properties such as hardness, and yield and tensile strengths [411–413], and dynamic properties such as fatigue life [169,386]. In particular for ductile materials such as 316L SS, porosity usually significantly influences its ductility (strain to failure) and fatigue life compared to the static properties [294,414]. Thus, efforts have been made to minimise porosity in as-fabricated parts as much as possible by various post-processing techniques, including HIP, machining, and various heat treatment procedures.

In this study, HPT processing has been proven to significantly reduce porosity content in AM metallic parts. Thus, Table 4-2 compares the porosity evolution in different AM materials undergoing various thermal post-processing techniques obtained from literature with that in HPT-processed AM 316L SS in this study. It is clear that HIP and heat treatment are effective procedures for eliminating porosity in AM metallic parts with high percentages of reduction (> 30%). In the two studies by Geenen at al. [415] and Rottger et al. [416], porosity could not be eliminated even after post-processing by HIP. It was found that the as-built AM 316L SS contained a large volume of defects, including process-induced pores, cracks, and spheriodised balls originating from Si-rich [415,416]. In fact, the volume fraction of pores and spheriodised balls (balling) worsen after HIP treatment, although the cracks were partially densified. It could be inferred that balling will reduce the effectiveness of heat- and/or pressure-based post-processing approaches in mitigating the overall defects in as-built AM metallic parts. Balling can occur due to contaminated raw powders and improper selection of processing parameters. Therefore, they need be eliminated with strict handling of the raw powders and ensure that optimised processing parameters and scan strategies are selected before conducting AM operation [49,104,108,175].

However, the porosity reduction is often accompanied by reduction in mechanical properties, e.g. decreased yield and tensile strengths as has been shown in various studies [126,383–386,415,417]. Therefore, SP has emerged as a non-thermal post-processing technique for AM by blasting metallic balls on the surface of AM metallic parts to induce surface SPD, reduce porosity, induce UFG microstructures, and increase the microhardness of SP-treated surface [387–389]. However, the benefits of SP are limited only to the surface of the AM parts and this process is highly location-specific, therefore could not be extended to the bulk material. On the other hand, the results in this study clearly indicate that the porosity reduction due to HPT is in fact on the higher end (average: ~ 90%) when compared with other current post-processing techniques. Furthermore, HPT processing is also known to produce UFG and/or NG microstructures with high density of dislocations and significantly enhanced hardness throughout the bulk material, which will be discussed in the following chapters. This could suggest improved yield and tensile strengths in the bulk material, highlighting the advantages of HPT compared to other current post-processing techniques.

Table 4-2 Comparison of initial and final porosity contents in AM metals and alloys undergoing different post-processing techniques.

Material	**Post-processing Technique (PP)**	**Porosity before PP, P_0 (%)**	**Porosity after PP, P_{PP} (%)**	**% difference, increase (+) or decrease (-)**	**Ref.**
316L SS	HPT	0.68	< 0.059	> 91.3 (-)	This study
316L SS	HIP	1.1 – 2.0	4.7	> 76.6 (+)	[415,416]
316L SS	HIP	0.36 – 40.5	0.00 – 13.0	67.9 – 100 (-)	[383]
316L SS	Annealing	1.4	1.4	No difference	[126]
	HIP		0.3	78.6 (-)	
316L SS	Low speed finish machining	1.39	0.25	82 (-)	[418]
	High speed finish machining		0.48	65.5 (-)	
316L SS	Heat treatment	5	2.6	48 (-)	[419]
	Hybrid machining		2.8	44 (-)	
Ti6Al4V	HIP	0.66	0.16-0.18	72.0 – 75.0 (-)	[384]
Ti6Al4V	HIP	~ 0.095	~ 0.067	29.5 (-)	[385]
	HIP + heat treatment		~ 0.044	53.7 (-)	
IN 718	HIP	0.09 – 0.13	0.011 – 0.015	87.7 (-)	[386]
IN 718	HIP	0.09 – 0.2	0.04 – 0.08	55.5 – 60.0 (-)	[417]
	Heat treatment		0.06 – 0.13	33.3 – 35.0 (-)	
	HIP + heat treatment		0.05 – 0.09	44.4 – 55.0 (-)	

4.4 Summary

In this chapter, the evolution of porosity in AM 316L SS processed by HPT through 1/4, 1/2, 1, 5 and 10 revolutions were evaluated by using conventional microscopy technique and XCT method. The main results have been obtained as follow:

1. OM and XCT analysis reveal that the porosity content in the as-received disk is very low (< 1%), indicating that high densification level (> 99%) is attained, which suggests that optimum processing parameters were used during SLM fabrication.
2. HPT-processing is able to significantly reduce porosity content in the as-received disk by ~ 89 – 91%, even at early stages of HPT deformation, i.e. after 1/4 revolution corresponding to $\varepsilon_{\text{eq.-HPT}} = 3.4$.
3. After 1/4 HPT revolution, a large number of pores are effectively ‘closed’, while some of the initially spherical pores become increasingly elongated as indicated by the significantly lower circularity compared to the as-received disk.
4. Pore-free structures are attained after 1/2 and 1 HPT revolution ($\varepsilon_{\text{eq.-HPT}}$ of 6.8 and 13.6). These are the result of combined hydrostatic pressure and extreme torsional strain, which release the internal sub-surfaces and produce NG microstructures to completely close the pores by creating a strong atomic bond to hold the bulk material together.
5. XCT scans on the as-received disk demonstrates high sphericity of the pores, indicating that the pores are gas-induced, and not related to processing parameters.
6. The difference in porosity content in as-received disk analysed by microscopy and XCT techniques is caused by the detection limit of the XCT machine.

Chapter 5 Microstructural evolution and strength of AM 316L SS processed by HPT

5.1 Introduction

316L SS is an austenitic stainless steel that is widely used for applications in various industries such as orthopaedic implants, marine, petrochemical, pharmaceutical, and nuclear power plants, owing to its excellent corrosion resistance, low neutron radiation absorption rate, and superior mechanical properties e.g. exceptional strength and fracture toughness, and good ductility [269–272]. However, the relatively soft γ-FCC phase means that the hardness and ultimate tensile strength (UTS) of 316L SS are relatively lower than steels with BCC structures, which restricts its use for structural applications [301]. However, 316L SS could not be strengthened by conventional heat treatment procedures due to its low carbon content (< 0.03 wt. %) since the formation of the required strengthening carbide precipitates is not possible.

HPT has been shown to be the most effective approach to significantly enhance the mechanical strength of cast and wrought 316L SS via the dislocation hardening and grain boundary strengthening routes as the result of the extreme torsional strain imposed [252,300,305,307,420]. Moreover, the influence of HPT processing on the microstructure, hardness, and strengthening mechanisms of additively manufactured 316L SS is currently not known. Accordingly, in this chapter, the microstructural evolution, hardness, deformation mechanisms, and the factors that contribute to the strengthening of HPT-processed AM 316L SS were investigated by using OM, SEM, TEM, XRD, and microhardness measurements. A physical-based model was derived based on the linear additive theory to predict and explain the increase in strength obtained due to HPT processing.

5.2 Results

5.2.1 Microhardness evolution

Fig. 5-1 (a) shows the Vickers microhardness (HV) against indentation locations, while Fig. 5-1(b) depicts the average HV values vs. equivalent strain, $\varepsilon_{\text{eq.-HPT}}$ for the as-received and HPT-processed disks. From Fig. 5-1(a), it can be seen that the microhardness of HPT-processed disks is much higher than their as-received counterparts, which continues to increase as the number of revolutions increase. The HV values are initially inhomogeneous across the diameter of the disks at lower HPT revolutions (1/4, 1/2 and 1), with higher values at the peripheral region compared to the centre of the disks. This is consistent with the radial dependency of HPT process as described by Eqn. 2-8. As the number of revolutions increase, the difference in HV values tends to decrease and a homogeneous hardness distribution across the diameter of the disk is eventually obtained after 10 revolutions, indicating that a saturation stage is reached at a critical torsional strain value.

In addition, it is evident from Fig. 5-1(b) that significant strain hardening only occurs at lower torsional strain values, and the microhardness is relatively constant upon further straining, in this case, at $\varepsilon_{eq.\text{-}HPT}$ values beyond ~ 40. Such saturation in microhardness beyond a critical strain value is also observed in HPT processing of other FCC materials, e.g. Cu and Cu-Al alloys [421–423]. Furthermore, the inset of Fig. 5-1(b) indicates that the microhardness evolution can be divided into three stages based on the equivalent strain, $\varepsilon_{eq.\text{-}HPT}$ values. The most significant hardening occurs at stage 1 in the range of ($\varepsilon_{eq.\text{-}HPT}$ = ~ 0 – 10), i.e. at early HPT straining, as indicated by the steep gradients of the HV vs $\varepsilon_{eq.\text{-}HPT}$ curve, while the much less steeper gradients in the range of $\varepsilon_{eq.\text{-}HPT}$ = ~ 10 – 40, i.e. stage 2 only exhibit marginal increase in HV values. Thereafter, the HV values remain relatively constant at the later deformation stage 3 for the range of $\varepsilon_{eq.\text{-}HPT} > 40$, i.e. after 10 HPT revolutions, showing further evidence that a saturation stage has been reached.

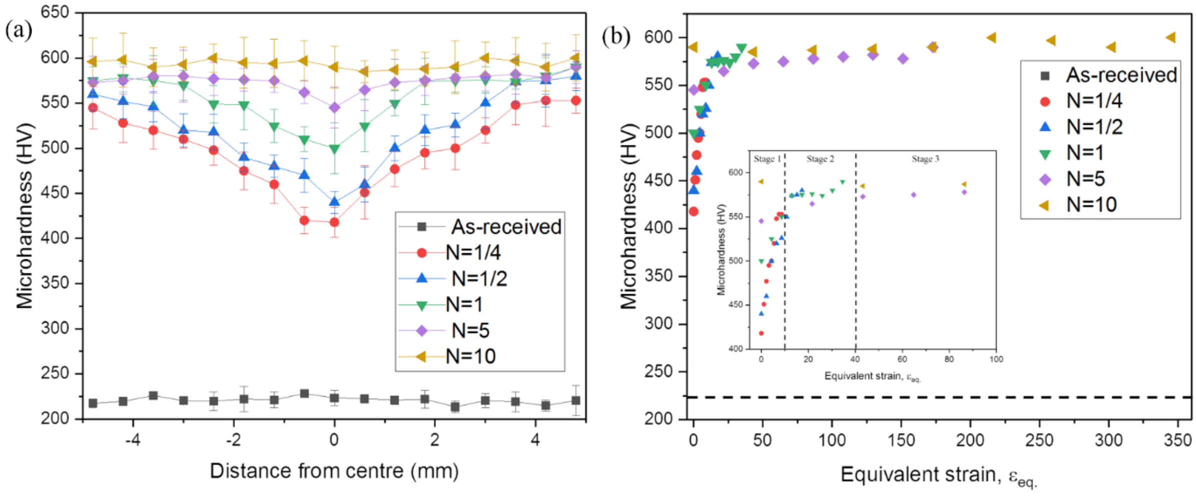

Fig. 5-1 (a) HV distribution across the diameter, and (b) HV vs. equivalent strain, $\varepsilon_{eq.\text{-}HPT}$ for as-received and HPT-processed disks (inset HV vs $\varepsilon_{eq.\text{-}HPT}$ in the range of ~ 0 – 50) [424].

In addition, the HV values for as-received and HPT-processed disks were measured in a rectilinear grid pattern throughout the surface-normal (x-y plane) of the disks and the results are shown as colour-coded contour maps in Fig. 5-2, in which the HV values are indicated in the colour key to the right of the hardness maps. The as-received disk (Fig. 5-2(a)) shows a homogeneous microhardness distribution, (average: 220 HV) that is higher than conventional wrought or cast 316L SS but this value is typical of AM 316L SS [126,296,425]. The microhardness increases inhomogeneously with increasing HPT revolutions from 1/4 to 1 with relatively higher values around the peripheral compared to the central regions of the disks (Figs. 5-2(b) and (c)). Hardness saturation throughout the disk surface is obtained after 10 revolutions observed in Fig. 5-2(d) (average: 600 HV), similar to previous studies on HPT-processed CM 316L SS [252,426]. The rapid increase in HV values after 1/4 and 1 revolution is due to the grain refinement and the presence of appreciable work hardening at early deformation stages, while the low work hardening level at later deformation stages contributes to the hardness saturation at maximum values, i.e. after 10 revolutions in this study. Nevertheless, this behaviour is typical of HPT-processed materials exhibiting strain hardening as reported in various literature [427–429].

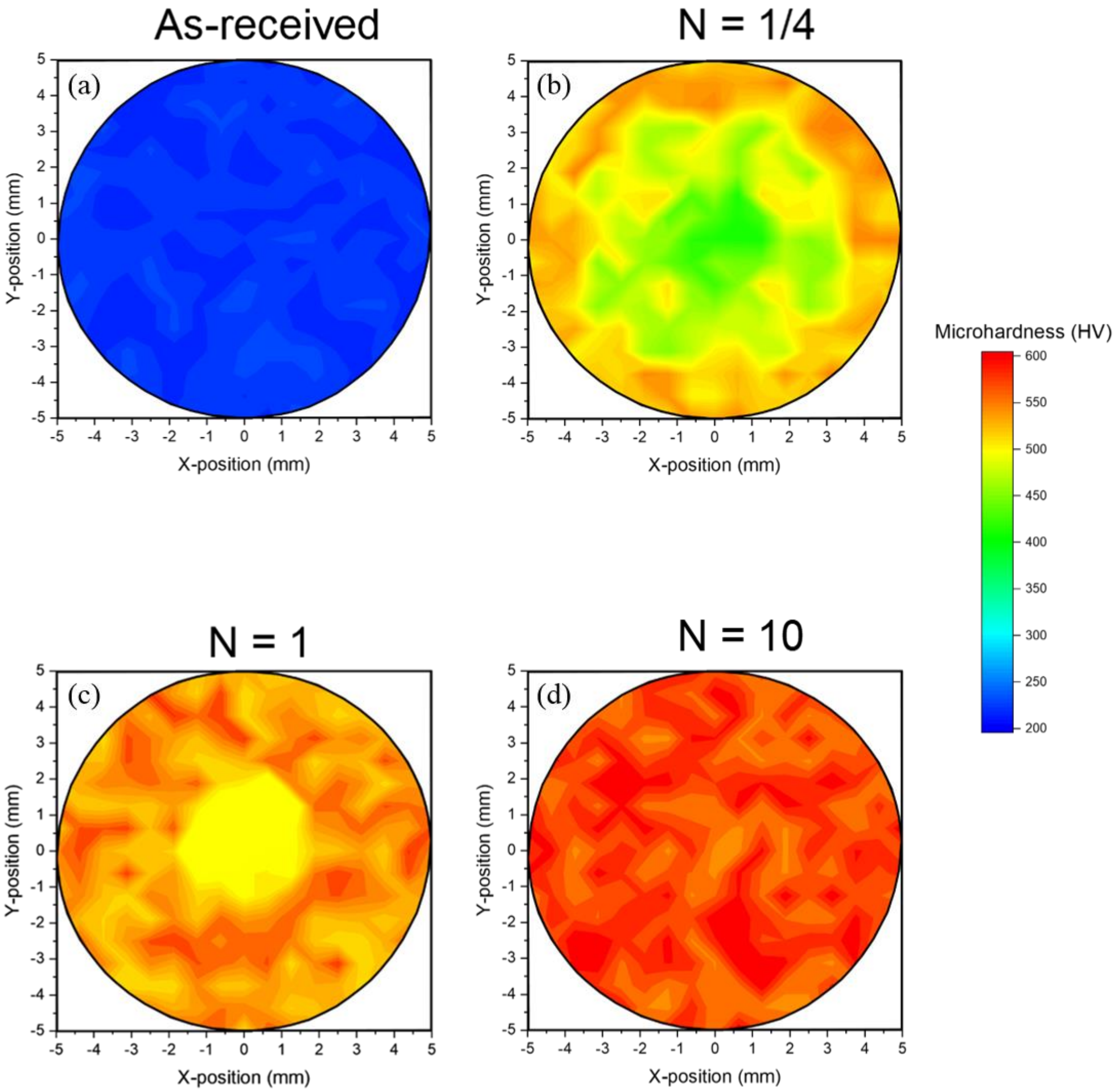

Fig. 5-2 Colour-coded contour maps showing hardness distribution at the surface-normal (x-y plane) for as-received and HPT-processed disks [430].

5.2.2 X-ray diffraction analysis

The XRD patterns for all processing conditions are shown in Fig. 5-3. The peaks for all diffraction patterns are shown to be the FCC γ-austenite phase, indicating that no phase change has occurred to the austenitic 316L SS even though extreme torsional strains were imposed during HPT processing.

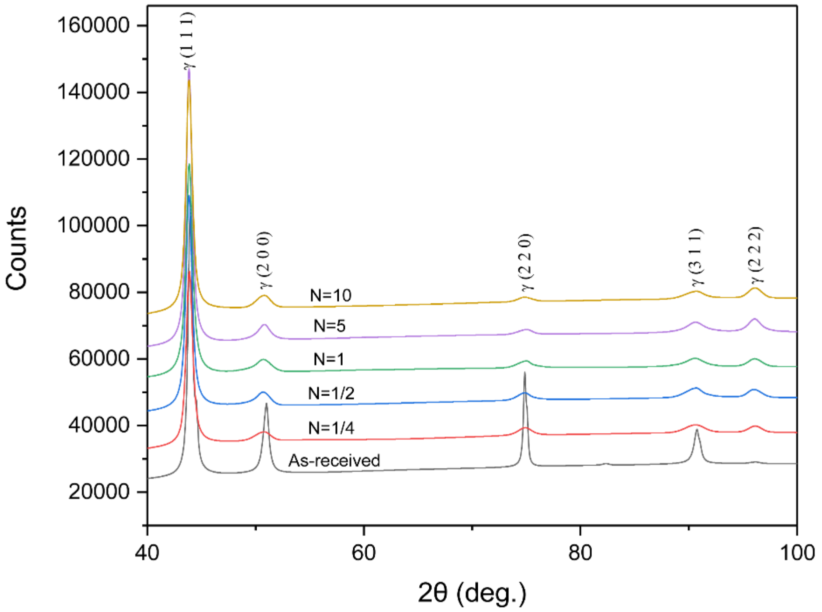

Fig. 5-3 X-ray diffraction patterns of the as-received and HPT-processed disks [424].

However, peak broadening could be observed for the HPT-deformed disks compared to the as-received counterpart. The X-ray line broadening is mainly caused by lattice defects, e.g. small crystallite sizes and internal microstrains, and dislocations induced by HPT processing [431]. Therefore, the dislocation density, ρ can be calculated from the lattice microstrain obtained from the XRD peaks, using the following equation [432,433]:

$$\rho_{XRD} = \frac{2\sqrt{3}\langle\varepsilon^2\rangle^{1/2}}{D_c b} \qquad \text{Eqn. 5-1}$$

where D_c is the average crystallite size, referred to as coherently scattered domains (CSD), and b is the burgers vector (b = 0.25 nm for austenitic stainless steels [304]). The values of $\langle\varepsilon^2\rangle^{1/2}$ and D_c are obtained through the Rietveld refinement method applied in MAUD software.

In this refinement method, all data points of the XRD peaks were fitted to pre-existing structure models by accounting both the effects of the disk samples and the x-ray instrument [376,434] using the MAUD software. The pseudo-voigt mathematical function was used as a theoretical model to approximate and fit the experimental data obtained from the XRD peaks of the as-received and HPT-processed disks, given by [378]:

$$I(2\theta) = I_{HKL}[\eta_L L(2\theta - 2\theta_1) + (1 - \eta_L)G(2\theta - 2\theta_1)] \qquad \text{Eqn. 5-2}$$

where $L(2\theta\text{-}2\theta_1)$ and $G(2\theta\text{-}2\theta_1)$ are Lorentzian and Gaussian functions, respectively, η_L is the Lorentz fraction, and (1- η) is the 'remaining' Lorentz fraction of each peak within an XRD pattern [377]. The least-square calculation method is used to fit the theoretical profile of the pseudo-voigt function with the experimental data obtained from XRD measurement. To minimise the influence of instrumental broadening, asymmetry, and reflection caused by the XRD equipment as much as possible, and improve the reliability of the actual measured results, these parameters were evaluated by comparing the corundum (Al_2O_3) pattern measured from the XRD equipment used in this study with that of the model proposed by Caglioti et al. [435] in MAUD software. A correction factor was then applied to the calculated data automatically in the software, before the estimated final values of the D_c and microstrains were extracted from the Rietveld refinement profile fitting procedure in this study.

The corresponding values of ρ calculated based on Eqn. 5-1 are shown in Fig. 5-4. It is revealed that the dislocation density, ρ significantly increases from ~ 0.69 x 10^{13} m^{-2} for the as-received disk to ~ 8.4 x 10^{14} m^{-2} at lower number of HPT revolutions (1/4 revolution), before further increasing to ~ 1.69 x 10^{15} m^{-2} after 10 revolutions.

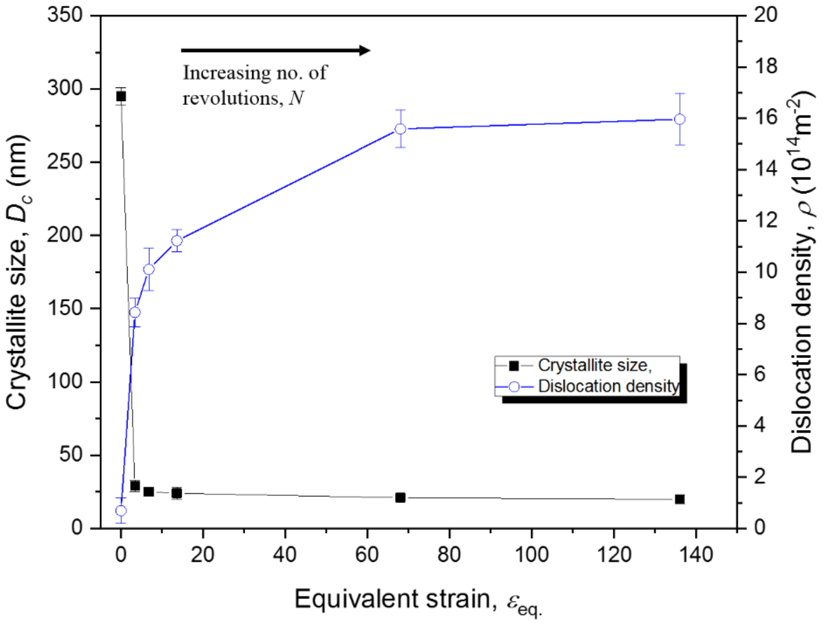

Fig. 5-4 The average crystallite size and average dislocation density evaluated via Rietveld refinement vs equivalent strain, $\varepsilon_{eq.\text{-}HPT}$ plot [424].

5.2.3 Microstructure evolution

5.2.3.1 As-received microstructures

Fig. 5-5 displays OM images of the as-received microstructures obtained from the as-received AM 316L SS, observed at the surface-normal (x-y plane) surface of the disk. It is clear that manufacturing route plays a major role in determining the microstructure of the solidified structure. The typical equiaxed grains with clear grain boundaries commonly attained in wrought 316L SS are not readily observed. Instead, the etched as-received AM 316L SS in Fig. 5-5(a) reveal melt pools represented by small square 'islands' that are formed as the consequence of the 'island' scan strategy. The overlapping of adjacent melt pools indicate successful fusion and good bonding of the laser-melted powder bed within a single layer [277,436].

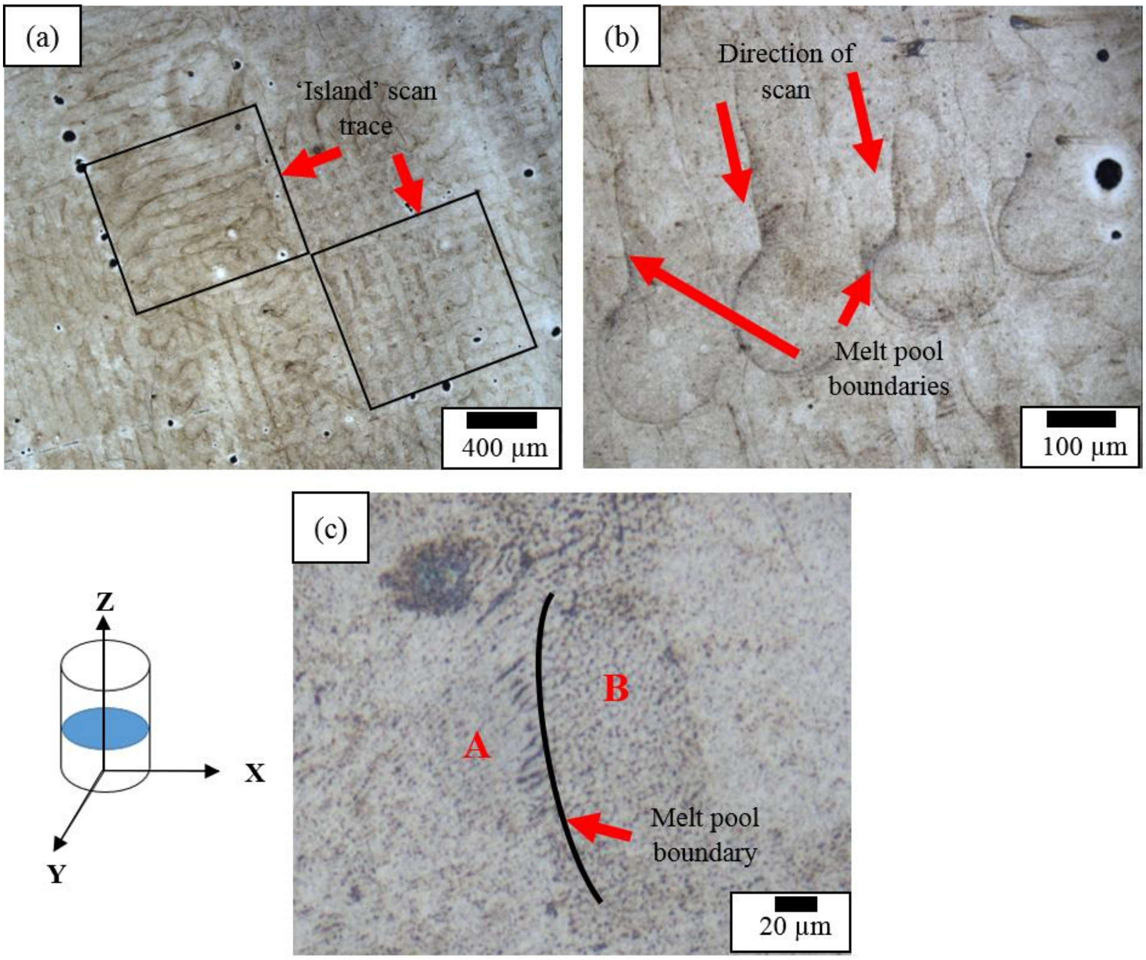

Fig. 5-5 As-received AM 316L SS microstructures obtained from optical microscopy (OM). Blue indicates surface for microstructural observation (surface-normal, x-y plane) [374].

Furthermore, the scan traces within an 'island' are observed to intersect perpendicular to each other, indicating the overlap of individual scan lines due to the laser scanning rotation of 90° after each layer. In addition, only spherical pores could be seen mainly at the edges of the small 'islands', indicating that the pores are produced during powder production and not resulting from the SLM process. Non-spherical pores or cracks are not observed in the as-received disk, which suggest that optimum processing parameters are applied in this study as discussed in Chapter 4.

Fig. 5-5(b) shows that the scan direction begins from the top and ends towards the centre of the OM image. The scan trace becomes wider towards the end of the scan and the melt pool boundary becomes more apparent. In addition, two distinct microstructures are evident at each side of the melt pool boundary, in which fine elongated (area A) and equiaxed (area B) cellular structures could be observed in Fig. 5-5(c), respectively. SEM observations in Figs 5-6(a) and (b) reveal that the cellular structures consist of equiaxed and columnar (elongated) cells with sizes 1 ± 0.5 μm, similar to those obtained by Zhong et al. [297] and Sun et al. [298]. These cells are formed due to the rapid, non-equilibrium heating/cooling cycles experienced during SLM process in the range of $10^3 - 10^8$ K s^{-1} that kinetically favour the cellular solidification morphology [437,438].

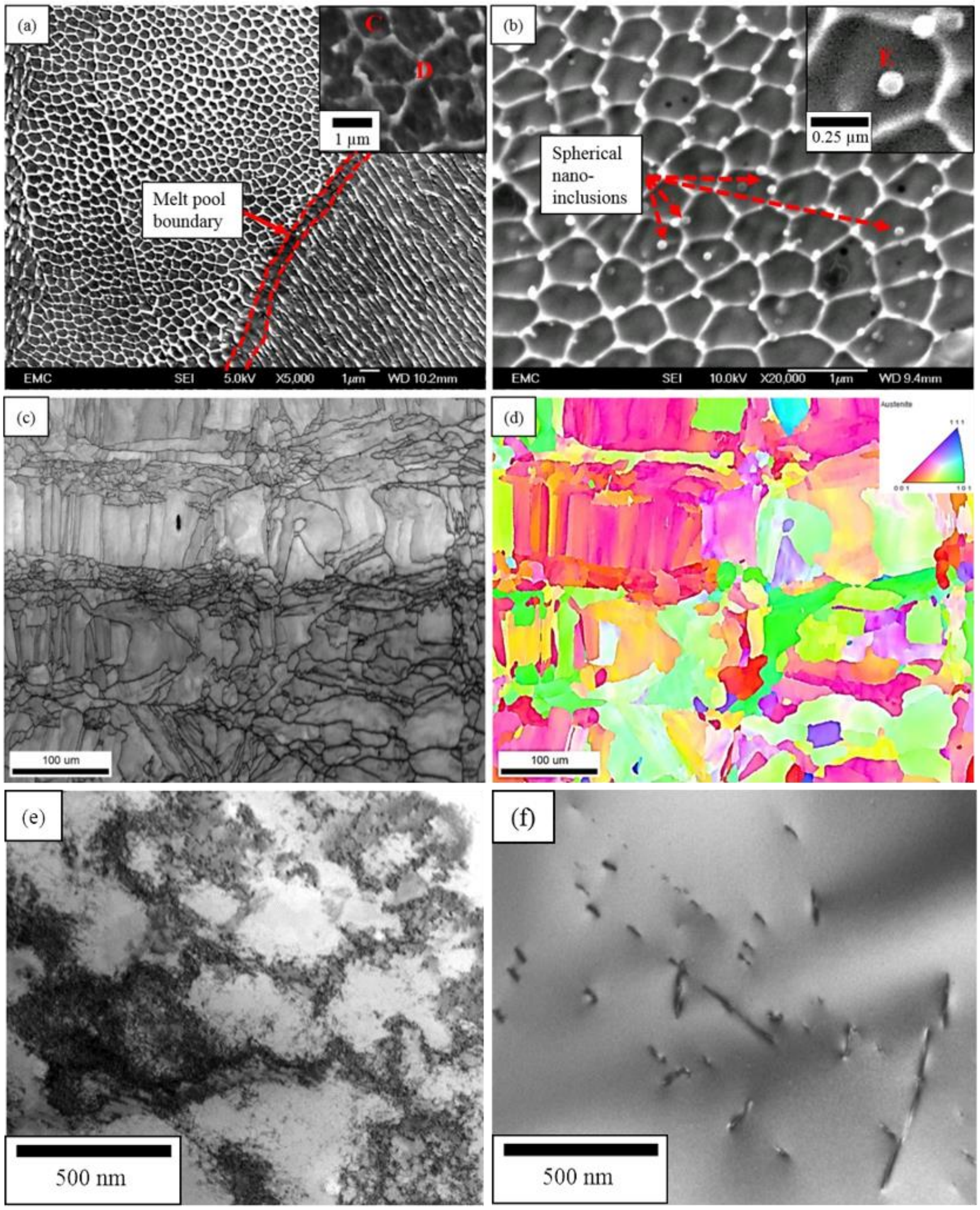

Fig. 5-6 (a) and (b) SEM images of cellular structure network, melt pool boundary, and spherical nano-inclusions, (c) BSE-SEM image revealing grain boundaries, (d) EBSD map and IPF (inset) indicating crystallographic orientation, and (e) bright field TEM image showing dense dislocation network along the cell boundaries and within the cell interior. All images are from the as-received disk. Image (f) is an example of well-annealed rolled 316L SS as comparison [278]. Reproduced with permission of the rights holder.

In addition, Fig. 5-6(a) also demonstrate that the growth of a particular cell morphology stops at the melt pool boundary (MPB), such that equiaxed cells dominate the left side of the MPB and columnar cells to the right of the MPB. This is most likely caused by the change in direction of heat flux from the laser heat source that continuously moves around following the scan strategy to melt the powder bed. As a result, the convective heat transfer and fluid flow are able to alter the growth orientation of the cellular structures in the direction of heat transfer due to the Marangoni effect [277,439]. Since the laser movement changes direction at every MPB, the resulting change in heat flux direction causes the cellular structures to grow in different orientations at either side of the MPB. The cell boundaries appear brighter compared to the interior, which might indicate enrichment by heavier elements [440]. Hence, EDX analysis was performed to distinguish the elemental composition inside each cell (area C within inset of Fig. 5-6(a)), at the cell boundaries (area D within inset of Fig. 5-6(a)), and the whole area of Fig. 5-6(a), as displayed in Table 5-1.

Table 5-1 Chemical composition of marked areas in Fig. 5-6 in wt. % [374].

Area	Cr	Mn	Fe	Ni	Mo	Si	O
C (inside cell)	17.90	1.90	63.69	13.84	2.67	-	-
D (cell boundary)	20.20	1.40	60.17	12.94	5.29	-	-
Whole area of Fig. 5-6(a)	18.83	1.64	64.03	12.78	2.51	0.21	-
E (Spherical nano-inclusion)	31.78	-	-	-	-	1.50	66.72

Table 5-1 reveals Cr and Mo enrichments with slight Ni decrease at the cell boundaries compared to those inside the cells. Upon closer inspection of Figs. 5-6(a) and (b), the cell boundaries are observed to have different thicknesses, which is most likely caused by the high cooling rates of AM processing that results in uneven diffusion of the heavier Mo atoms into the cell boundaries. Such elemental segregations into the cell boundaries have been found to influence the microhardness and corrosion characteristics of AM 316L SS [126,296,441]. On the other hand, when compared with the initial powder composition listed in Table 3-1, Table 5-1 reveals increasing Cr, Ni, and Mo, with decreasing Mn, Fe, and Si (in wt. %). in the as-received structure.

Spherical nano-inclusions ranging from 120 – 20 nm along the intragranular region (cell boundaries) and within the matrix (cell interior) are also revealed by the SEM image in Fig. 5-6(b). EDX analysis of the nano-particles (e.g. spot E inset of Fig. 5-6(b)) indicate that that they are rich in Cr, Si, and O, while Fe and other alloying elements are absent. Therefore, it is reasonable to suggest that these nano-inclusions are actually Cr-based silicates, an oxide phase that have also been observed in other studies on AM 316L SS [126,277,296,297]. Silicate melts are known to form spheres to reduce the high surface tension that exist due to their nature of high viscosity [126]. The high surface tension of the silicate melts also means that they have poor wettability and low solubility in steel, thereby remaining undissolved in the steel matrix [277].

However, the formation of such silicates in SLM is actually unexpected because the oxygen content was removed from the build chamber and nitrogen was purged inside prior to SLM operation. Therefore, it is speculated that residual oxygen may still exist inside the build chamber during SLM processing. Furthermore, according to the supplier (Concept Laser), the 316L SS powder was produced by gas-atomisation in nitrogen and the contamination of oxygen was < 0.05%, i.e. lower than the limit of detection by EDX. Although oxygen is considered negligible, very small oxygen contents might still exist. In addition, the content of Si in the initial powder is very low, 0.75 wt. % as indicated by EDX analysis in Table 3-1. Therefore, the affinity of Si and Cr to react with the residual oxygen in the build chamber and initial powder favours the formation of these spherical nano-inclusions at high temperatures during SLM processing [127,277]. Due to the combined effects of very high cooling rates of SLM process and the low solubility of the silicates in steel as a result of the high surface tension, they could not be dissolved within the steel matrix and remain randomly dispersed within the as-received structure. Furthermore, although other studies have shown that the nano-inclusions to become effective sites to impede dislocation motions and increase the hardness of AM 316L SS, e.g. [126,296,297,299], their overall volume fraction (0.38 ± 0.12 vol. %) observed in this study seems to be too small to have significant influence on the hardening of the current as-received AM 316L SS [277,299].

Backscattered electron SEM (BSE-SEM) image in Fig. 5-6(c) shows overlapping melt pool squares at the surface-normal (x-y plane) formed due to the ‘island’ scanning strategy. The square melt pools comprise of a mix of coarse (~ 40 – 70 µm) and fine grains (~ 10 – 40 µm). Very fine equiaxed grains (~ 1 – 10 µm) are formed at the end/intersection between the melt pools. This is because of the shortest laser-material interaction time at the end of the scan compared to other regions along a single scan track before the laser changes direction to scan a new powder bed region. Therefore, the end of each scan track experiences the highest heat flux and fastest cooling rate, compared to the middle or the beginning of the scan track [293,295,299]. As a result, grain growth and recrystallisation are suppressed and very fine grains are formed at this region [278,342].

Furthermore, the EBSD map in Fig. 5-6(d) demonstrates that the grains grow through the melt pools and the fusion lines, resulting in multiple grains growing within a single melt pool. Such inhomogeneous nucleation of grains are typical of AM microstructures, which is attributed to the competition between heat flux direction due to the convective heat transfer induced by the laser scan pattern path, and the continuous remelting and solidification of successively deposited powder layers [126,127,170,277]. The intercept average grain size is determined as ~ 40 µm. The inverse pole figure (IPF) inset of Fig. 5-6(d) indicate random grain growth without any preferred orientation and therefore no dominant texture [442–447].

The cellular structure morphologies observed in Figs. 5-6(a) and (b) are not revealed by the EBSD map because they have similar crystallographic orientation, thus can only be considered as sub-structures rather than actual grains. However, the bright field TEM image in Fig. 5-6(e) reveals a dense dislocation network concentrated along the equiaxed cell boundaries with some dislocations formed within the cell interior. Furthermore, the TEM image in Fig. 5-6(e) exhibit dense dislocation network within the as-received AM 316L SS microstructure, which is significantly more populated than a typically well-annealed rolled 316L SS observed in literature, e.g. Fig. 5-6(f) [278]. In addition, XRD analysis in Fig. 5-4 estimated the dislocation density, ρ for the as-received AM 316L SS as ~ 0.69 x 10^{13} m^{-2}, significantly higher than those of CM 316L SS, often in the range of 10^{9} – 10^{10} m^{-2} [127]. The high concentration of dislocations can be attributed to the enrichment of heavier alloying element such as Mo that segregate into the cell boundaries due to high stresses induced by the superfast heating and cooling cycles [126,277]. The dislocation pile-up can therefore be effective sites to impede dislocation motions, which could explain the higher hardness of AM 316L SS (average: 220 HV in this study) compared to CM 316L SS (~ 155 HV) [126,127,252].

5.2.3.2 Microstructures after HPT processing

Fig. 5-7 shows the microstructural evolution of the HPT-processed disks through lower number of HPT revolutions (1/4, 1/2, 1), whereas Fig. 5-8 shows that for higher number of HPT revolutions (5 and 10) obtained from OM observations at the at the surface-normal (x-y plane).

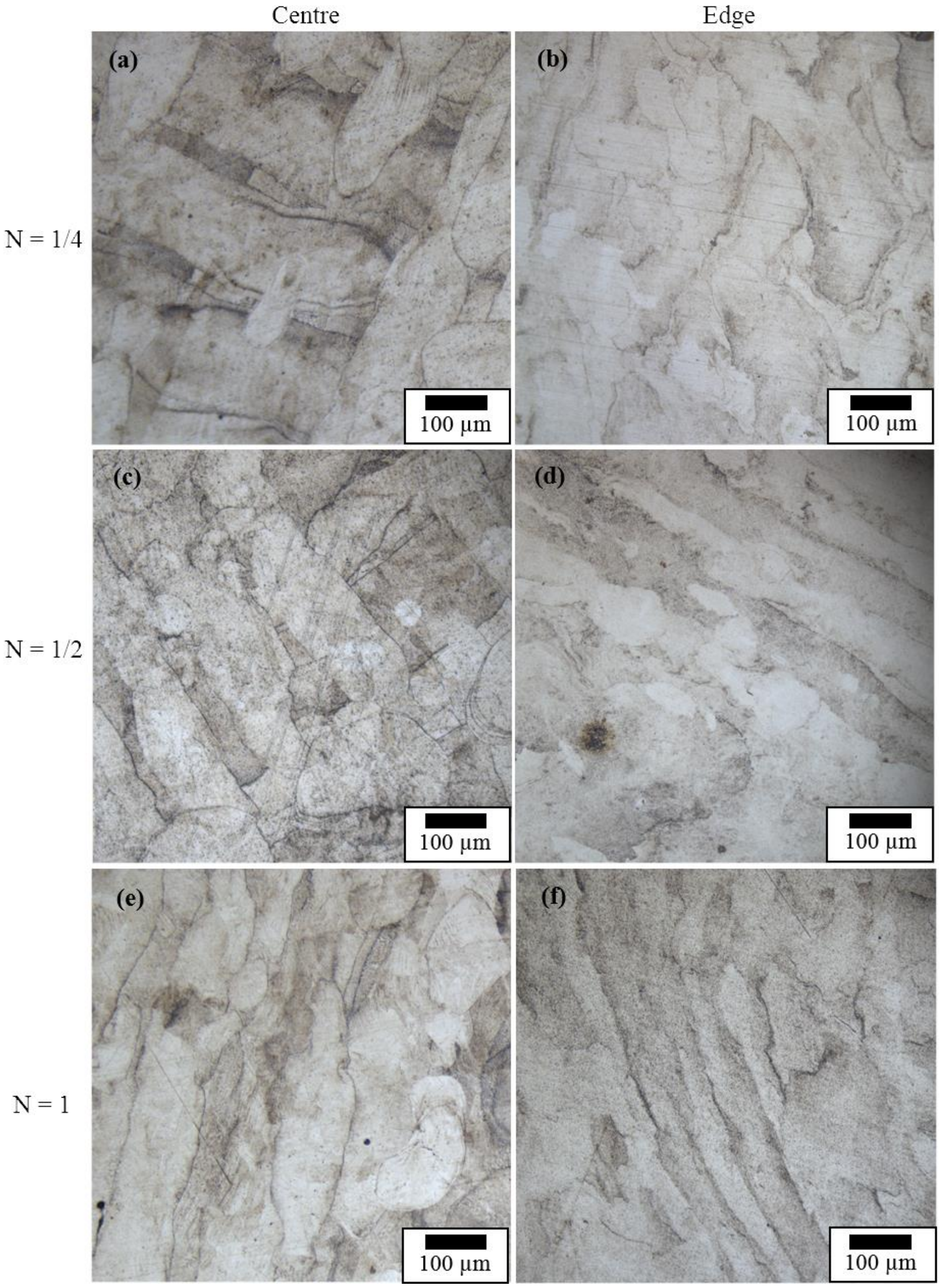

Fig. 5-7 Evolution of ‘island’ scan traces in HPT-processed disks observed from OM after 1/4, 1/2, and 1 revolutions observed at the surface-normal (x-y plane).

Figs. 5-7 and 5-8 show the evolution of the 'island' scan traces (melt pools) at low magnification. At lower number of revolutions (1/4, 1/2, and 1), the 'island' traces become increasingly elongated and disoriented as the number of revolutions increase with the edges being more refined compared to the centre of the disks. These are expected due to the combined impact of compressive force and increasing torsional strains with higher number of HPT revolutions. Not much elongation and distortion of the 'islands' are observed at the centre and periphery of the disk after 1/4 HPT revolution as shown in Figs. 5-7(a) and (b). However, Figs. 5-7(c) – (f) exhibit extremely refined 'islands' at the peripheral areas compared to at the centre of the disks with increasing torsional strains up to 1 HPT revolution. Furthermore, the difference in elongation and distortion of the 'island' traces between the centre and the edge is diminished after 5 HPT revolutions (Figs. 5-8(a) and (b)). The 'island traces disappear completely throughout the disks after 10 HPT revolutions (Figs. 5-8(c) and (d)), suggesting that a reasonable homogeneity and strain saturation have been achieved.

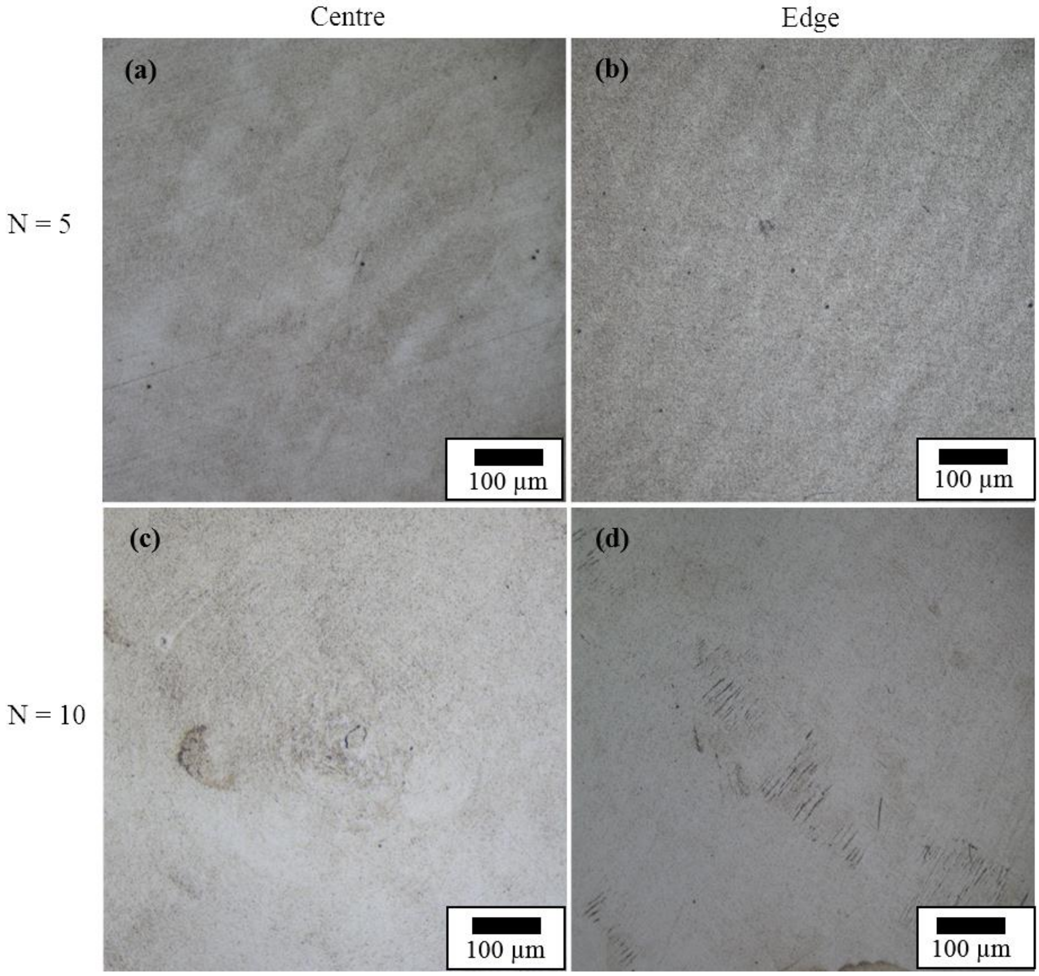

Fig. 5-8 Evolution of 'island' scan traces in HPT-processed disks observed from OM after 5 and 10 revolutions observed at the surface-normal (x-y plane).

The SEM images in Fig. 5-9 show that the deformation of the cells for the disk processed through 1/4 HPT revolution are not obvious and the sizes are still roughly similar to those of the as-received disk. Only a slight elongation of cells could be observed at the edges compared to at the centre of the

HPT-processed disk through 1/4 HPT revolution, which could be attributed to the low equivalent strain imposed, $\varepsilon_{\text{eq.-HPT}} = 3.4$ (Figs. 5-9(a) and (b)). However, as the $\varepsilon_{\text{eq.-HPT}}$ value increases to 6.8 (N = 1/2) and 13.6 (N = 1), more severe cellular distortions are observed at the disk edges compared to the centre due to the radial dependency of HPT-induced torsional strain (Figs. 5-9 (c) – (f)). Even though the cell boundaries become increasingly thinner with higher number of revolutions, EDX measurements do not show any obvious changes to the composition of the heavily segregated Cr and Mo. The Cr content varies between 20.15 ± 1.24 wt. %, while the content of Mo varies in the range of 5.18 ± 1.33 wt. %.

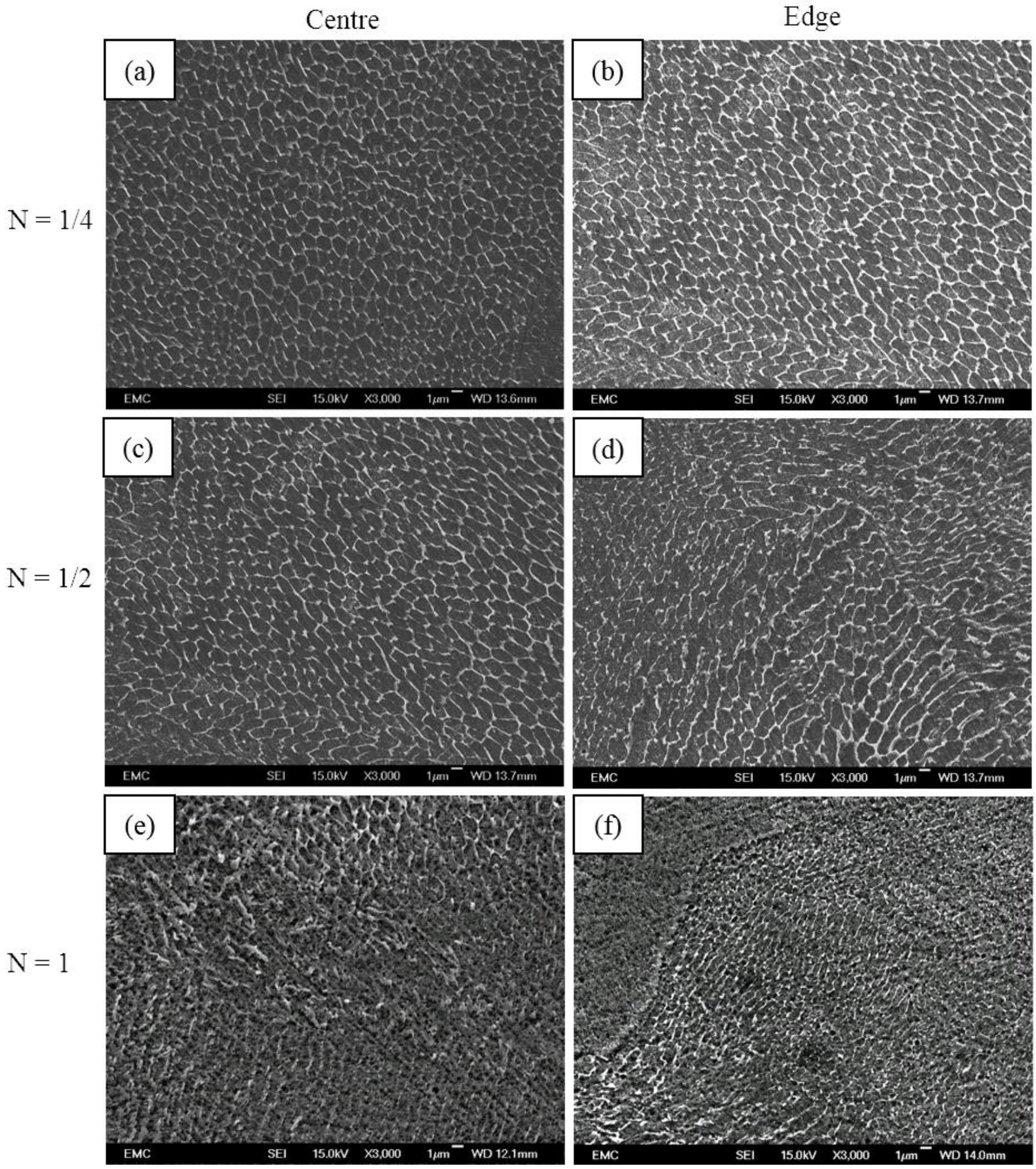

Fig. 5-9 Evolution of cellular structure in HPT-processed disks observed from SEM after 1/4, 1/2, and 1 HPT revolutions observed at the surface-normal (x-y plane).

The trend of cellular refinement and deformation continues as the $\varepsilon_{eq.\text{-}HPT}$ values significantly increase from 68 after 5 HPT revolutions to 136 after 10 HPT revolutions as shown in Fig. 5-10. After 5 HPT revolutions, the cellular structure at the centre of the disk become even more refined (Fig. 5-10(a)), but cellular annihilation is observed at the disk edges (Fig. 5-10(b)). Homogeneous cellular structure annihilation is attained at both disk regions after 10 HPT revolutions, suggesting that a critical torsional strain value is reached that reduces the work hardening effect, $\varepsilon_{eq.\text{-}HPT} = 136$ in this case (Figs. 5-10 (c) and (d)). At this stage, the segregation of heavier elements into the cell boundaries observed earlier is no longer visible. Since it is known that HPT-induced torsional strain results in generation and multiplication of dislocations, it is reasonable to assume that the pre-existing dense dislocation networks contained within the cell boundaries could be dismantled and re-organised by merging with the newly generated dislocations due to HPT processing.

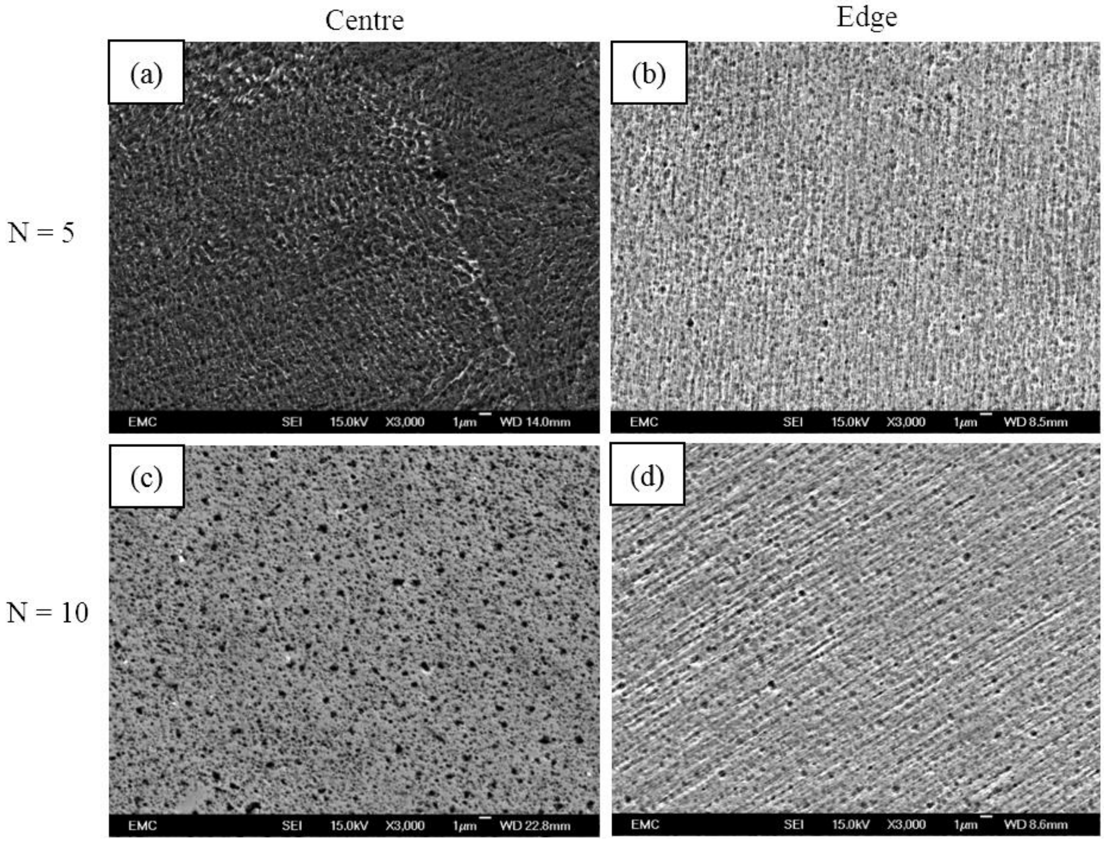

Fig. 5-10 Evolution of cellular structure in HPT-processed disks observed from SEM after 5 and 10 revolutions observed at the surface-normal (x-y plane).

EBSD maps and the accompanying inverse pole figure (IPF) shown in Fig. 5-11 reveal the evolution of grain sizes and crystallographic orientations of the HPT-processed disks at the central region (< 2 mm from the disk centre). After 1/4 HPT revolution, the grains appear elongated and the average intercept grain size is 18 ± 17 µm (Fig. 5-11(a)). After 1 HPT revolution, the fraction of elongated grains reduced, and equiaxed sub-micron grains (UFG microstructure) start to form with an average intercept grain size of 980 ± 500 nm (Fig. 5-11(b)). After 5 HPT revolutions, fully equiaxed UFG microstructures are obtained at the central area of the disk with an average intercept grain size of 400

± 130 nm (Fig. 5-11(c)). However, the grain sizes could not be resolved by EBSD after 10 HPT revolutions, suggesting the formation of nano-scale grains with sizes < 100 nm.

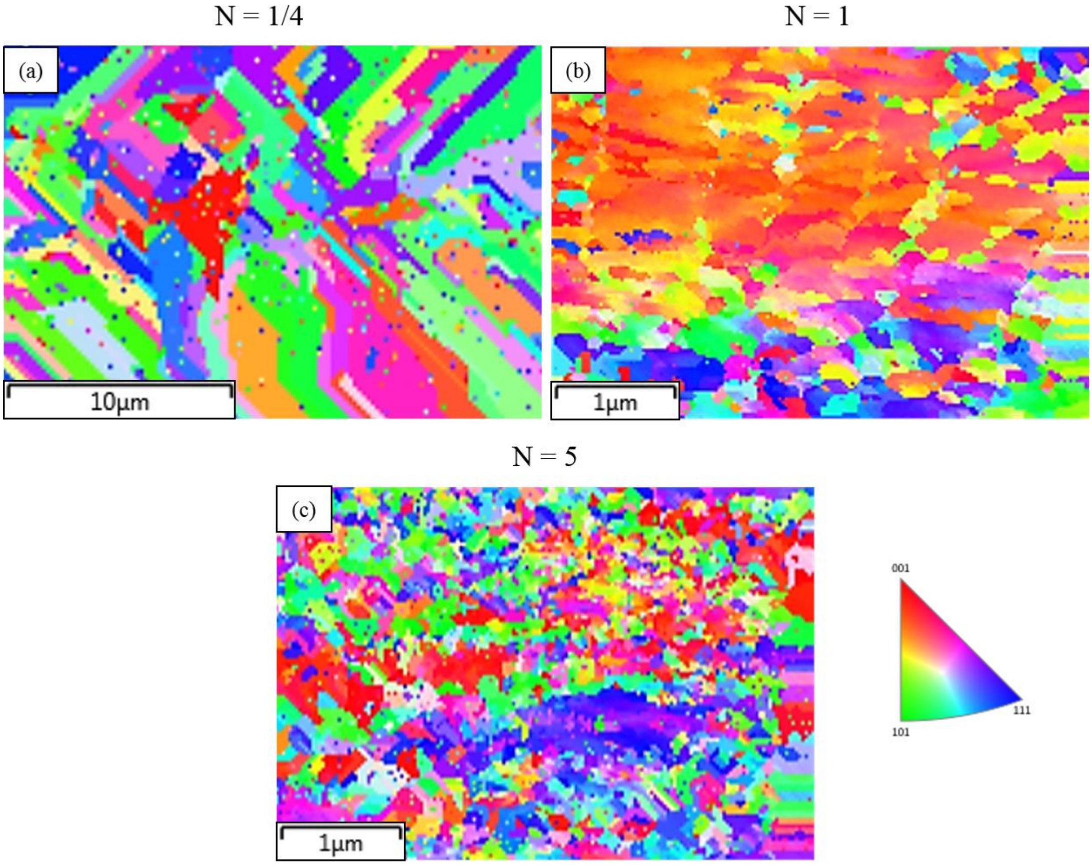

Fig. 5-11 EBSD maps and the accompanying IPF taken at the surface-normal (x-y plane) from the central region of the HPT-processed disks.

On the other hand, Fig. 5-12 shows the grain size distribution at the central region of the as-received and HPT-processed disks (< 2 mm from the centre) evaluated via EBSD analysis. The grain sizes are defined as those having large angle grain boundaries with angle of misorientation ≥ 15° that can be set in the Aztec HKL software. The grain sizes remain in the fine micron region (~1 – 35 µm) despite the refinement after 1/4 HPT revolution (Fig. 5-12(a) but are both in the UFG and fine micron ranges (~ 0.1 – 2 µm) with increased torsional strain to 1 HPT revolution (Fig. 5-12(b)). However, the grain sizes are further refined after 5 HPT revolution and are now fully in the UFG regime (~ 0.1 – 1 µm) as shown in Fig. 5-12(c).

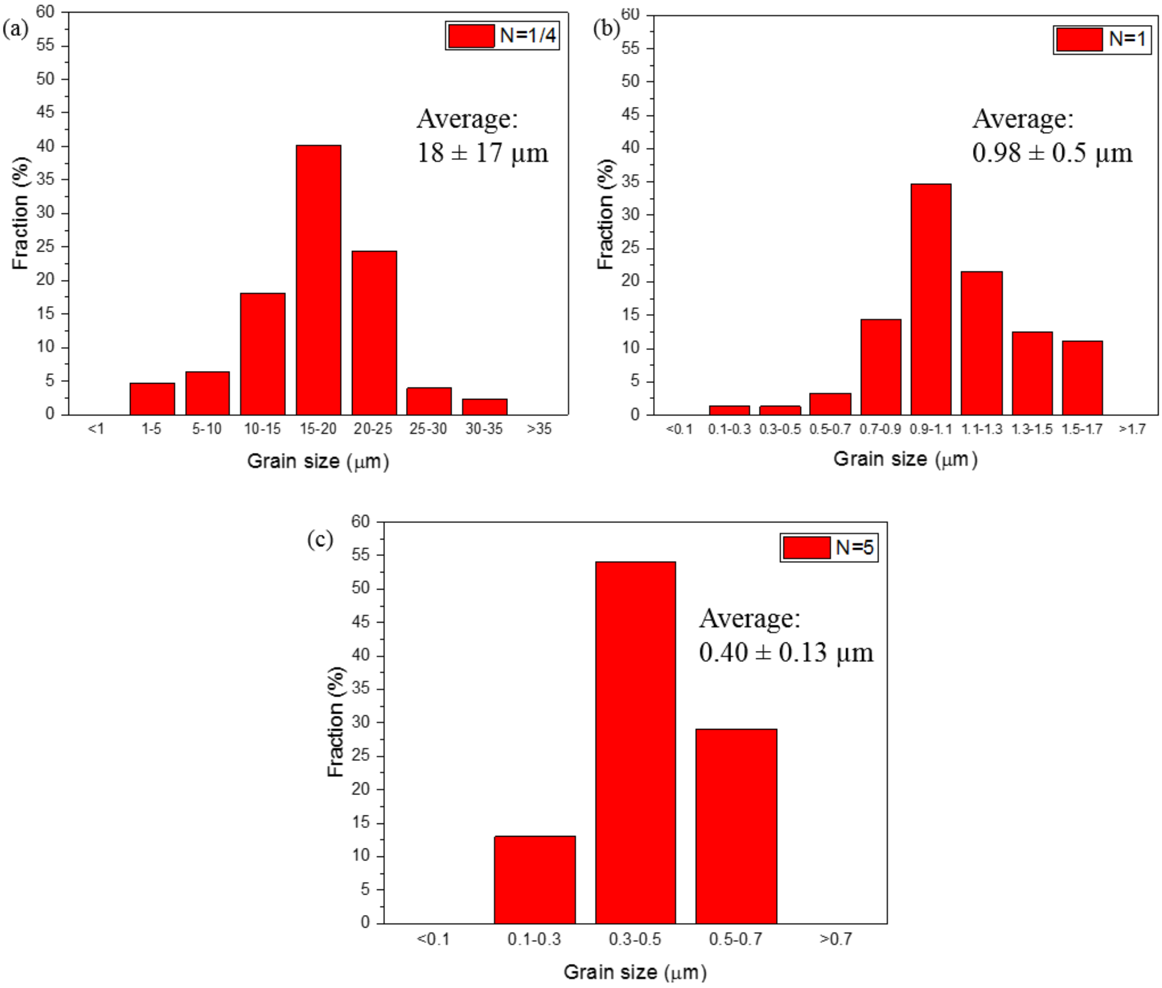

Fig. 5-12 Grain size distribution for as-received and HPT-processed disks at the central disk regions (< 2 mm from the centre) obtained via EBSD analysis.

TEM observations on the microstructural features at the peripheral region of the disks (3 mm from the centre) demonstrate that the severely deformed AM 316L SS can be categorised into three deformation stages, relating to the number of revolutions and the corresponding equivalent strain values, $\varepsilon_{\text{eq.-HPT}}$, as shown in the inset of Fig. 5-1(b) [420,448]. For the initial deformation in stage 1 ($\varepsilon_{\text{eq.-HPT}} = \sim 0 - 10$), the microstructures are mainly deformed by two competing mechanisms; dislocation generation and multiplication, and development of primary twins after 1/4 HPT revolution ($\varepsilon_{\text{eq.-HPT}} = 3.4$), as displayed in Figs. 5-13(a) and (b), respectively. Some elongated sub-micron grains also start to appear as shown in Fig. 5-13(c). This is followed by the formation of twin-matrix lamellae via the intersection of twins, forming rhombic blocks after 1/2 HPT revolution ($\varepsilon_{\text{eq.-HPT}} = 6.8$), as shown by the arrows in Fig. 5-14(a). High density of dislocations is also introduced in the twin-matrix lamellae to accommodate the severe deformation. In addition, examples of sub-micron grains obtained after 1/2 HPT revolution are shown in Fig. 5-14(b). The average intercept grain size is measured as 118 ± 25 nm after 1/4 revolution, which decreases to 95 ± 19 after 1/2 revolution, indicating that UFG microstructures could be obtained even at low torsional strains.

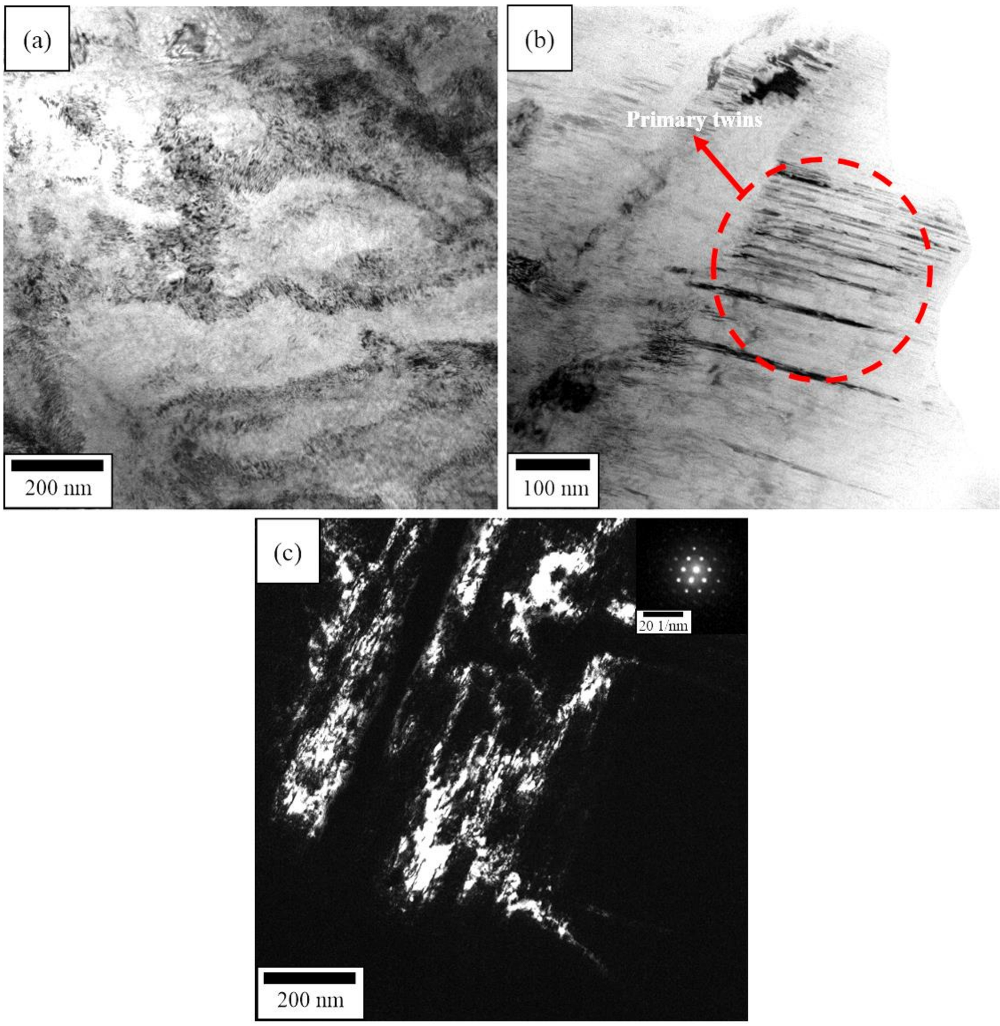

Fig. 5-13 Bright field TEM images of (a) dislocations, (b) primary twins, and (c) dark field TEM image showing ultrafine sub-micron grains (UFG microstructure) with the corresponding SAD pattern (inset). All images are taken after 1/4 HPT revolution ($\varepsilon_{eq.\text{-}HPT} = 3.4$) [424].

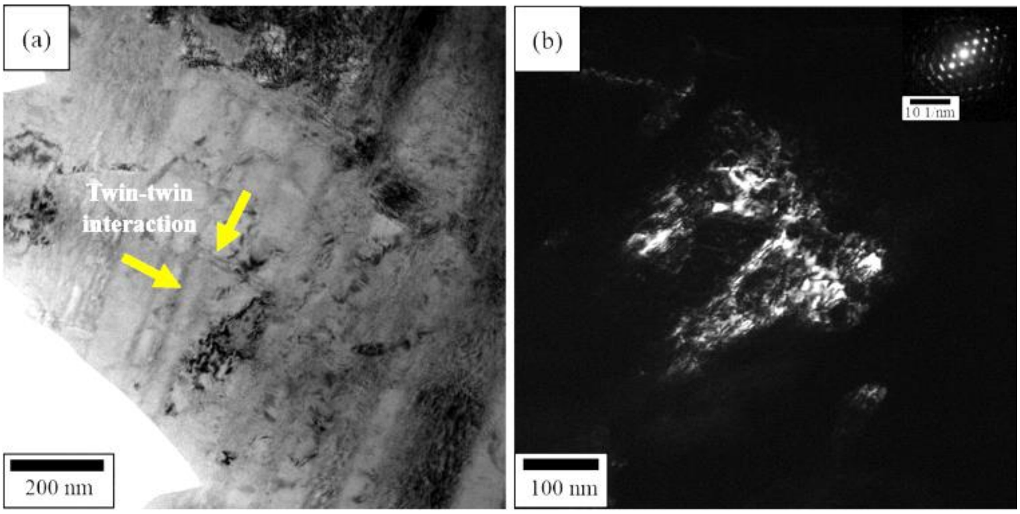

Fig. 5-14 (a) Bright field TEM image of twin-twin interaction and (b) dark field TEM image showing ultrafine sub-micron grains (UFG microstructure) with the corresponding SAD pattern (inset). Both images are taken after 1/2 HPT revolution ($\varepsilon_{eq.\text{-}HPT} = 6.8$) [424].

In the subsequent deformation stage 2 ($\varepsilon_{eq.\text{-HPT}}$ = ~ 10 – 40), grain refinement begins to take place through the shear banding of the twin-matrix lamellae and the formation of secondary nanotwins. Localised deformation takes place in the form of shear banding of the twin-matrix lamellae after 1 HPT revolution ($\varepsilon_{eq.\text{-HPT}}$ = 13.6) as illustrated in Figs. 5-15(a) and (b), in which the twins move through a shear band, while even thinner secondary nanotwins are generated at the edge of the shear band. The shear bands further twist and rotate to generate equiaxed nano-scale shown in Fig. 5-15(c) via dislocation slip and rotation of the cellular sub-structures due to the increased torsional strain at this stage [448]. However, the grain boundaries are not well-defined and appear wavy and diffused at this stage (arrows in Fig. 5-15(c)), which is typical of SPD-processed microstructures that indicate high-energy non-equilibrium boundaries and an excess of extrinsic dislocations [449]. The dark field TEM image in Fig. 5-145d) displays some of the equiaxed nano-scale grains, and the average intercept grain size is measured as 68 ± 15 nm after 1 HPT revolution.

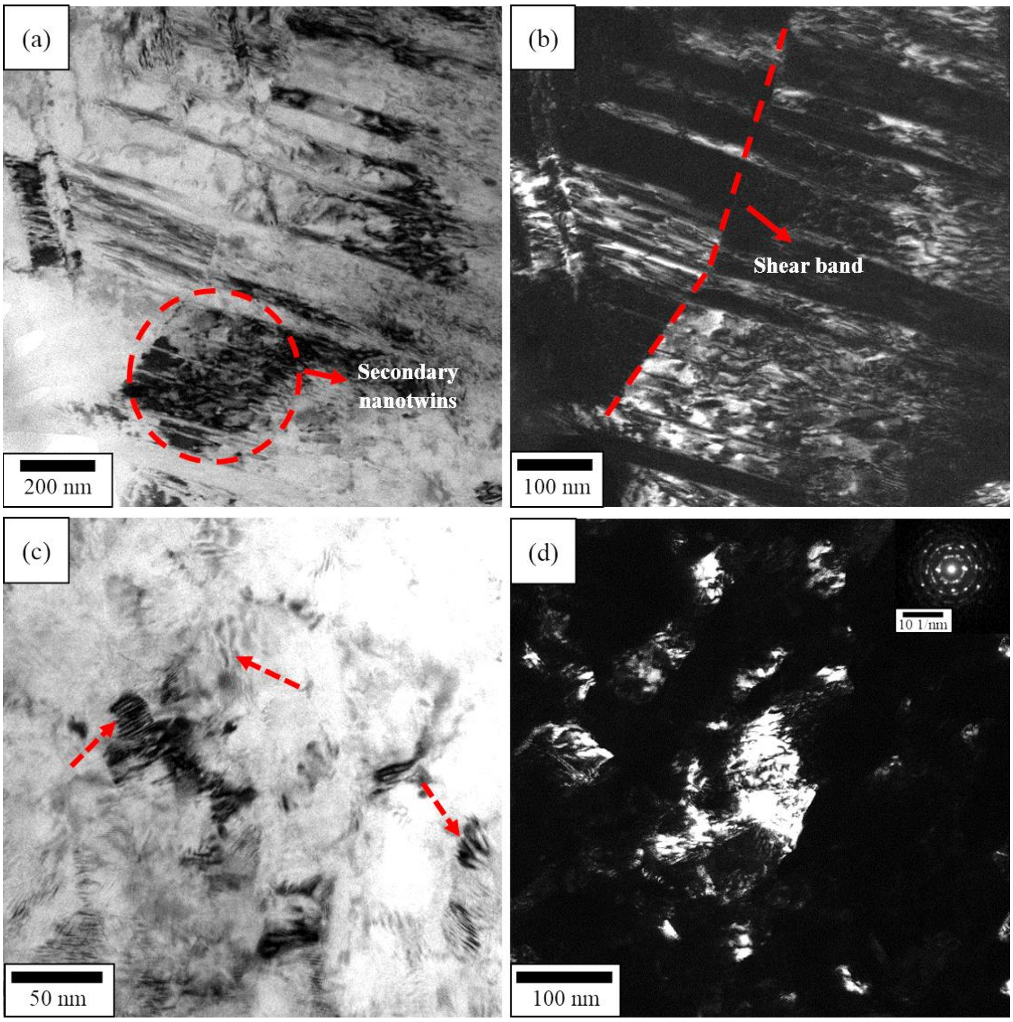

Fig. 5-15 (a) Bright field TEM image indicating secondary nanotwins, (b) dark field TEM image of (a) revealing a clear shear band, (c) nano-scale grains (NG microstructures) with high density of dislocations within the interior and along the boundaries, and (d) dark field TEM image showing nano-scale grains with the corresponding SAD pattern (inset). All images are taken after 1 HPT revolution ($\varepsilon_{eq.\text{-HPT}}$ = 13.6) [424].

In the final deformation stage 3 ($\varepsilon_{\text{eq.-HPT}} > 40$), the microstructure reaches an equilibrium state where equiaxed nano-scale grains with clear grain boundaries are formed after 5 HPT revolutions ($\varepsilon_{\text{eq.-HPT}} = 68$) as shown by the bright-field and dark-field TEM images in Figs 5-16(a) and (b). The bright diffuse ring patterns of the SAD image (inset of Fig. 5-16(b)) indicate very fine grains with random orientation.

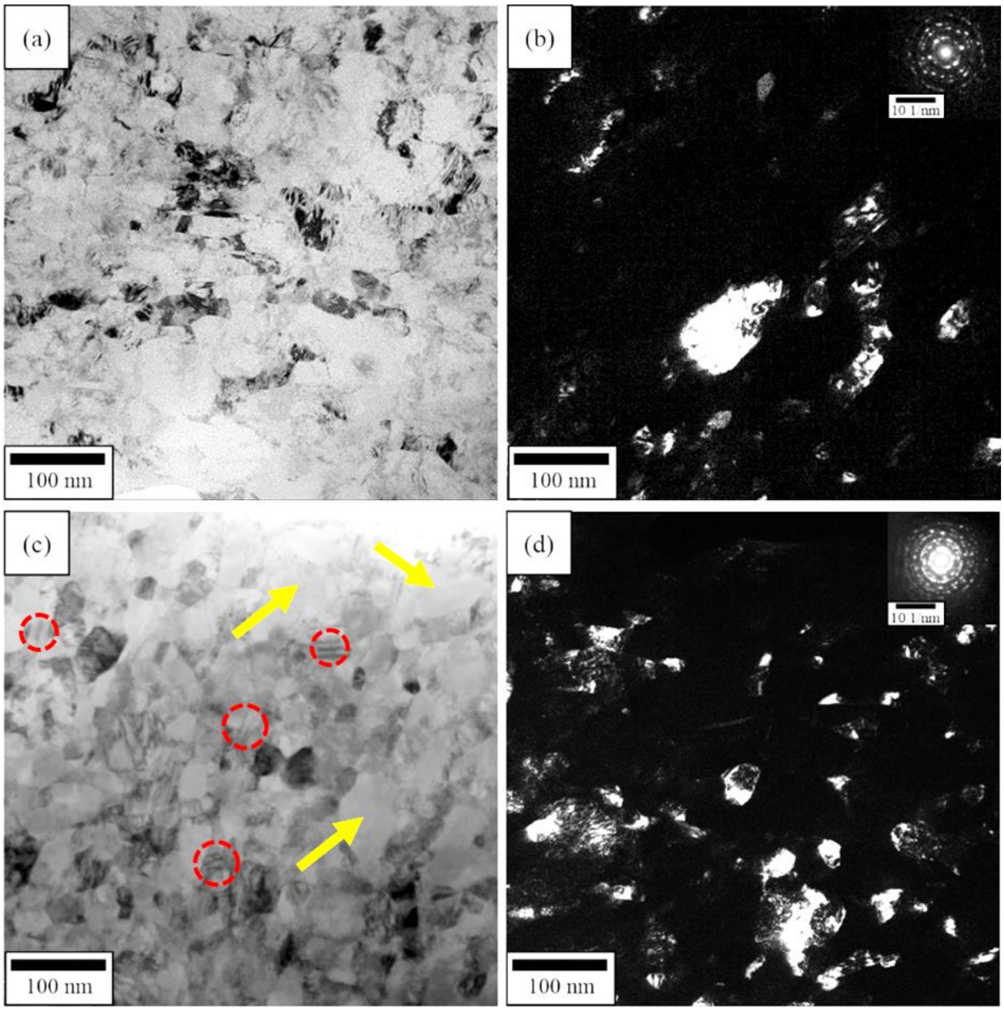

Fig. 5-16 (a) Bright field TEM image, and (b) dark field TEM image showing equiaxed nano-scale grains obtained after 5 HPT revolutions ($\varepsilon_{\text{eq.-HPT}} = 68$), (c) bright field TEM image, and (d) dark field TEM image showing nano-twins, nano-scale grains with clear grain boundaries, and grains without any substructure obtained after 10 HPT revolutions ($\varepsilon_{\text{eq.-HPT}} = 136$) [424].

After 10 HPT revolutions corresponding to $\varepsilon_{\text{eq.-HPT}} = 136$), the grain sizes only show little refinement, indicating a saturation stage has been reached, as shown in Figs. 5-16(c) and (d). In addition, secondary nanotwins could be observed in the grain interior (dashed circles in Fig. 5-16(c)), and grains that are free from any internal sub-structures are also observed at this stage (arrows in Fig. 5-16(c)). The brighter and more diffused ring patterns shown by the SAD image after 10 revolutions (inset of Fig. 5-16(d)) compared to the SAD patterns after 5 revolutions indicate even more finer grains are produced at this stage. Obviously, the final grain size attained at this microstructural saturation stage is determined by the balance between generation and annihilation of dislocations caused by the extreme torsional strain imposed through HPT [450–454]. Nevertheless, the nanotwins, dislocations, and grain boundaries are effective sites for impeding dislocation motions, thus contributing to the increased strength in this HPT-deformed alloy. The average grain size is measured as 48 ± 11 nm after 5 revolutions and it further decreases to 42 ± 10 nm after 10 revolutions. The grain sizes for all HPT-processed disks are always larger than the crystallite size measured via XRD, as the x-ray line broadening analysis measures the crystallite size rather than the actual grain size [426,455].

On the other hand, Fig. 5-17 exhibit the grain size distribution at the peripheral region of the as-received and HPT-processed disks (> 3mm from the centre) evaluated via the line intercept method described in Chapter 3 based on TEM observations. HPT processing is already able to produce ultrafine grains in the range of ~ 90 – 150 nm after 1/4 revolution, which further reduces to the true NG regime (< 100 nm) with increasing HPT revolutions. In addition, the grain size distribution becomes narrower as the number of HPT revolutions increase, and plateaued at ~ 30 – 60 nm upon strain saturation after 5 and 10 HPT revolutions.

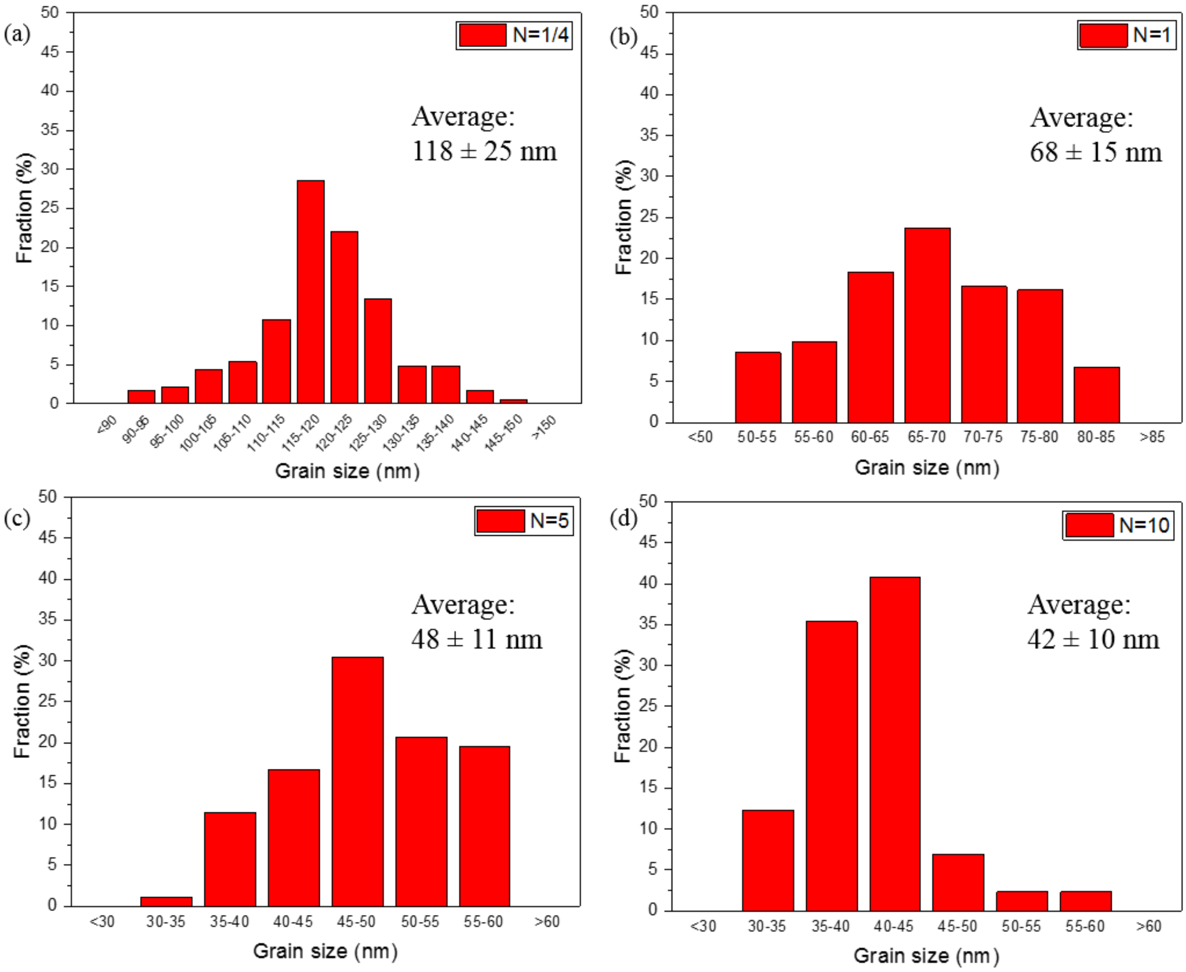

Fig. 5-17 Grain size distribution for as-received and HPT-processed disks at the peripheral disk regions (> 3 mm from the centre) obtained via TEM analysis.

5.3 Discussion

5.3.1 Phase, dislocation density, and grain refinement

XRD measurements and analysis in this study showed that the initial γ-austenite FCC phase in AM 316L SS remains unchanged even after being imposed with extremely large torsional strains through HPT. This indicates that the deformation-induced martensite is not observed in this investigation, though martensite transformation has been observed in heavily deformed CM 316L SS or other CM austenitic SS [305,306,420,426]. This could be explained by considering the stacking fault energy (SFE) of the material, which determines: (i) the prevalent deformation mechanism to accommodate the plastic strain during the SPD process, either by phase transformation, twinning, or dislocation glide [456], and (ii) austenite stability [300].

Deformation is largely controlled by martensitic phase transformation for stainless steels with low SFE (< 20 mJ m^{-2}), twinning in medium SFE (20 – 45 mJ m^{-2}), and dislocation glide and twinning in high SFE (> 45 mJ m^{-2}) [457]. According to conventional dislocation theory, full dislocations in FCC materials, as an energetically favourable process, tend to dissociate into two partial dislocations (Shockley partials) to lower their energies, and the SFE of a material determines the separation of the partial dislocations [458]. Medium/high SFE materials favour dislocation glide because of the small separation between the Shockley partials, which enables them to recombine easily and extend on the cross-slip plane [459]. However, the separation of the Shockley partials is larger in materials with lower SFE, causing difficulty for them to recombine, thus promoting the role of deformation twinning as major carriers of plastic deformation [460–462].

Furthermore, the SFE of a material is largely dependent on its chemical composition (alloying elements) and the deformation temperature [300,463], which significantly influences the propensity of martensite transformation in SPD-processed and heavily strain-deformed CM 316L SS and other CM austenitic SS. For example, austenite-martensite transformation (either into ε-hcp or α'-BCC martensite, or both) were observed in CM 316L SS, 304, and 304H austenitic SS heavily deformed by various SPD techniques, e.g. HPT [252,307,426,464], fast multiple rotation rolling (FMRR) [465], and 2D linear-plane strain machining [466], where the SFE was calculated to be in the range from low to medium values (~ 15 – 57 mJ m^{-2}). In all these cases, the content of Cr was relatively consistent (~ 17 – 18 wt. %), but the Ni content was < 11 wt. %, in which it is known that low Ni content lowers the SFE of austenitic SS [457,467,468].

Within this range of SFE values, twinning and martensitic transformation are found to be the dominant deformation mechanisms, leading to easy formation of stacking faults (SF) on every second {1 1 1} γ-austenite planes through the gliding of the Shockley partial dislocations. As a result, the ABCABC stacking sequence of the FCC lattice is transformed to ABABAB, which is the stacking sequence of ε-HCP martensite [420,426]. Therefore, the ε-HCP bands may become nucleation sites for α'-BCC martensites, which occupy larger volumes than the γ-FCC and ε-HCP phases, respectively [252]. Furthermore, Scheriau et al. [420] observed the transformation from γ-austenite to ε-martensite in wrought 316L SS having relatively high SFE (~ 80 mJ m^{-2}) processed by HPT at low temperature (-196°C – 20°C), but no martensitic transformation was observed at RT or at elevated temperatures (> 450°C). This further indicates that temperature also plays an important role in influencing the SFE of a material, in this case, by lowering the SFE of the HPT-processed wrought 316L SS to favour the formation of HCP martensite.

In other cases where martensite formation was not observed in heavily deformed CM austenitic SS via various SPD techniques, it was found that the SFE values were in the medium to high range (> 60 mJ m^{-2}) with higher Ni content (> 11 wt. %), and the SPD processing was conducted at RT or at higher temperatures [270,301,303,420,456,469–471]. Therefore, it can be inferred that martensite formation can be suppressed in heavily strained austenitic SS if the SFE values are high and the processing is conducted at moderate to high temperatures.

The SFE of the 316L SS powder used for SLM in this study is estimated as ~ 64 mJ m^{-2} (Ni content: 12.2 wt. %) using the formula given in [300] and HPT processing was conducted at RT. In this study, martensite formation is not observed, and the HPT-processed disks remained a single γ-austenite phase even at the saturation stage, i.e. after 10 revolutions. This suggests that the deformation in HPT-processed AM 316L SS, particularly during the earlier stages (1/4 to 1 revolution) is predominantly controlled by the generation and multiplication of dislocations, and twins without any phase transformation. This correlates well with dislocation density measurements based on XRD line broadening data in Figs. 5-3 and 5-4 and TEM observations in Figs. 5-13 to 5-16. Therefore, this indicates that the formation of strain-induced martensites in heavily strain-deformed 316L SS largely depends on the SFE, chemical composition, and deformation temperature, regardless of the fabrication route, either CM or AM.

Interestingly, the dislocation density of as-received AM 316L SS is in the order close to ~ 10^{14} m^{-2} (Fig. 5-4), which is significantly higher than ~ 10^{9} – 10^{10} m^{-2} in conventional cast or wrought 316L SS [127]. The high dislocation density in AM 316L SS is attributed to the numerous fine cellular structure colonies with sizes ~ 1 ± 0.5 µm, formed due to the segregation of heavier elements such as Mo (Figs. 5-6(a) and (b)). They act as additional storage for dislocations that impede dislocation motions, translating to relatively higher HV values compared to CM 316L SS, despite the existence of porosity [126,297,298]. Thus, if porosity could be eliminated or minimised, then the mechanical properties of SLM parts could be further improved and can be more widely applied in various commercial industries, rather than only niche areas at present, e.g. automotive, biomedical, and aerospace due to its design flexibility.

In this study, the significant increase in HV values after HPT processing by ~ 2 – 3 times compared to that of the as-received disk shown in Fig. 5-2 can be attributed to grain refinement, generation and multiplication of dislocations, and twin formation. The grain size measurement results demonstrate rapid grain refinement, in which UFG microstructures (average: 118 ± 25 nm) is achieved even after only 1/4 revolution. True nano-scale grains are attained after 1/2 revolution (average: 95 ± 19 nm) and saturates at 42 ± 10 nm after 10 revolutions. In addition, the estimated dislocation density values in HPT-processed disks increase significantly to the order of 10^{14} m^{-2} after 1/4 revolution and to the order 10^{15} m^{-2} after 5 and 10 revolutions (Fig. 5-4). Thus, it can be reasonably inferred that the refinement and subsequent annihilation of the cellular structure colonies that initially contain pre-existing dislocations could also contribute to the increased dislocation density by combining with the accumulated dislocations generated via HPT processing.

Figs. 5-13 and 5-14 suggests that the development of twin-matrix lamellae and generation and multiplication of dislocations results in the initial hardness increase at the early stages of deformation (stage 1) after 1/4 and 1/2 revolution. At this stage, the UFG microstructures begin to develop, but the grain boundaries are not well-defined. Fig. 5-15 indicates that the shear banding of the twin-matrix lamellae, secondary nanotwins, and equiaxed nano-scale grains (NG microstructures) contribute to hardness increase in deformation stage 2 after 1 revolution. Fig. 5-16 demonstrates that the equilibrium microstructures (equiaxed nano-scale grains, either with or without dislocations and nanotwins embedded in the grain interior) plays an important role towards achieving strain saturation in deformation stage 3, which corresponds to the homogeneous microhardness distribution attained after 10 revolutions. In addition, the effects of dislocation annihilation are indicated by the limited dislocations present inside some of the nano-scale grains as shown by the arrows in Fig. 5-16(c).

Finally, it is worth noting that Figs. 5-12 and 5-17 demonstrate inhomogeneous grain refinement in the HPT-processed disks from 1/4 up to 5 revolutions, as indicated by the different values of average intercept grain sizes at the centre and peripheral regions. Based on the Fig. 5-12, UFG microstructures are only achieved at the centre of the disks after 1 HPT revolution with an average grain size of 980 ± 500 nm, and further reduces to 400 ± 130 nm after 5 HPT revolutions. Since EBSD could not resolve the grain sizes at the disk centre after 10 HPT revolutions, it is reasonable to infer that true nano-scale grains with grain sizes < 100 nm (NG microstructures) are obtained at this region. However, Fig. 5-17 indicates that UFG microstructures are already achieved at the peripheral region of the disks after 1/4 HPT revolution (average: 118 ± 25 nm), and nano-scale grains begin to develop after 1 HPT revolution (average: 68 ± 15 nm) and onwards. These suggest that HPT-processed disks through 1/4, 1/2, and 1 revolutions essentially possess gradient microstructures, i.e. micron-scale grains at the centre and sub-micron grains (UFG) and/or nano-scale grains (NG) at the peripheral regions, with increasing amounts of the UFG and NG microstructures compared to the micron-scale grains as the number of HPT revolutions increases. In addition, although the UFG/NG regime is achieved throughout the disk after 5 HPT revolutions, the wide discrepancy in average intercept grain sizes (400 ± 130 nm at the centre, and 48 ± 11 nm at the peripheral regions) means that the grain size distribution is still considered inhomogeneous. Therefore, homogeneous grain size distribution with fully equiaxed NG is only obtained throughout the whole disk after 10 HPT revolutions.

5.3.2 A physical-based model for multiple strengthening mechanisms

The significant improvement in strength of the HPT-processed AM 316L SS is obviously caused by a number of factors, including solid solution effect, twinning effect, dislocation generation, and grain size effect. These factors account for individual strengthening mechanism representing different obstacles capable of impeding dislocation motions, which contribute to the total yield strength of a given material, σ_y, and can be estimated by the additive theory [472]. Hence, the contribution of different strengthening mechanisms can be analysed as follows [473–476]:

$$\sigma_y = \Delta\sigma_{GB} + M(\Delta\tau_{tot}) \qquad \text{Eqn. 5-3}$$

where $\Delta\sigma_{GB}$ is the increment in yield strength due to grain boundary strengthening, M is the Taylor orientation factor, and $\Delta\tau_{tot}$ is the critically resolved shear stress (CRSS) of the grains. The current model considers three main contributions to the CRSS; the intrinsic CRSS, $\Delta\tau_0$, the contribution due to dislocations, $\Delta\tau_\rho$, and the contribution due to solid solution strengthening, $\Delta\tau_{SS}$. Hence, Eqn. 5-3 can be modified by the superposition of these three contributions as follows [477]:

$$\sigma_y = \sigma_0 + \Delta\sigma_\rho + \Delta\sigma_{SS} + \Delta\sigma_{GB} \qquad \text{Eqn. 5-4}$$

Where σ_0 is the intrinsic strength, or the friction stress of the γ-iron lattice, defined by the Peirelis-Nabarro stress, $\sigma_0 = 2 \times 10^{-4}G$ [478]. G is the shear modulus of the material (G = 77000 MPa for austenitic stainless steels [479]).

In HPT-processed metals, the increment in yield strength is due to high density of dislocations. Thus, the dislocation strengthening, $\Delta\sigma_\rho$, is given by [480,481]:

$$\Delta\sigma_\rho = M\Delta\tau_\rho = M\alpha_1 Gb\sqrt{\rho_{Total}} \qquad \text{Eqn. 5-5}$$

where M for FCC materials is taken as 3.05 [479], α_1 is an empirical constant taken as 0.3 [482], and ρ_{Total} is the total dislocation density, which includes both geometrically necessary dislocations (GNDs) and statistically stored dislocations (SSDs), estimated via XRD analysis through Eqn. 5-1.

The concentration of solute atoms (alloying elements) dissolved in the matrix determines the solid solution strengthening, $\Delta\sigma_{SS}$ of 316L SS, expressed by [483]:

$$\Delta\sigma_{ss} = \sum k_i c_i \qquad \text{Eqn 5-6}$$

where k_i is the strengthening coefficent due to the dissolving of i-th alloying element in the matrix at 1 wt.%, and c_i is the concentration of the i-th alloying element in wt.%.

The contribution of grain boundary strengthening, $\Delta\sigma_{\mathrm{GB}}$ as the result of grain refinement in HPT-processed metals can be estimated by the Hall-Petch relationship, $\Delta\sigma_{\mathrm{GB}} = K_{\mathrm{HP}}d^{-1/2}$, where K_{HP} is the material-dependent Hall-Petch constant, taken as 2.8 MPa $\mathrm{m}^{-1/2}$ for relatively coarse grains (as-received condition) and 0.3 MPa $\mathrm{m}^{-1/2}$ for sub-micron and nano-scale grains (HPT-processed disks) following the assessments in Refs. [252,479], and $d^{-1/2}$ is the inverse square root of the grain size. However, the nanometer twin boundaries (twinning) observed within the grains of the HPT-processed disks in the current study also act as additional grain boundaries, which also contribute to the grain boundary strengthening of the material as has been reported in various literature [303,482,484,485]. Thus the Hall-Petch equation is modified to [303,479]:

$$\Delta\sigma_{GB-TW} = \Delta\sigma_{GB} + \Delta\sigma_{TW}$$

$$= (1-f)k_{HP}d^{-1/2} + fk_{TW}\lambda^{-1/2} \qquad \text{Eqn 5-7}$$

where $\Delta\sigma_{\mathrm{GB}}$ is the contribution to strengthening by grain size, $\Delta\sigma_{\mathrm{TW}}$ is the contribution to strengthening by twinning, f is the fraction of grains with twins, K_{TW} is the Hall-Petch coefficient of twin boundaries, and λ is the average twin spacing. K_{TW} is estimated to be the same as K_{HP}, which equals to 0.3 MPa $\mathrm{m}^{-1/2}$ [479,482], while f can be estimated by the Fullman stereological analysis, given by [486]:

$$\frac{1}{\lambda} = \frac{1}{2e}\frac{f}{1-f} \qquad \text{Eqn. 5-8}$$

where e is the twin thickness, measured from the TEM micrographs.

The linear additive model for strengthening mechanisms expressed by Eqns. 5-3 to 5-7 was applied to predict the yield strength, σ_{y} of the as-received and HPT-processed disks. Data from the current study, e.g. microhardness, XRD, microstructures (TEM) combined with the values of constants and parameters obtained from various literature were used for this model and presented in Table 5-2. The average grain size values for HPT-processed disks were obtained from TEM. Dislocation density values were obtained from the XRD line broadening analysis through MAUD software.

The modelling results showing the predicted yield strength σ_{y} are presented in Fig. 5-18. The estimated yield strength obtained by summing the individual contribution of each strengthening mechanism based on the model is also compared with the HV values measured for the HPT-processed disks in this study. The relationship between hardness and yield strength can be approximated through the empirical correlation [487]:

$$\Delta\sigma_y = \frac{HV}{C_1} \qquad \text{Eqn. 5-9}$$

where HV is the hardness value in MPa, obtained by multiplying the measured HV value with a multiplicative factor of 9.87, and C_1 is a constant, taken as 3 for most FCC materials [488]. This relation could be used as a good approximation to estimate the yield strength of UFG/NG AM 316L

SS obtained through HPT processing [489,490]. The HV values in this study were measured at the distance of ≥ 3 mm from the centre of the disks.

Table 5-2 Parameter values used in calculations for the strengthening mechanism model [424].

Mechanism	Symbol	Value	References
Dislocation strengthening	$\boldsymbol{C_i}$	3	[488]
	$\boldsymbol{M}$	3.05	[479]
	$\boldsymbol{b}$	0.25 nm	[304]
	$\boldsymbol{G}$	77000 GPa	[304]
	$\boldsymbol{\alpha_1}$	0.3	[482]
	$\boldsymbol{\rho_{total}}$	0.69×10^{13} m^{-2}–1.69×10^{15} m^{-2}	This work (XRD)
	$\boldsymbol{D_C}$	300 nm – 20 nm	This work (XRD)
Solid solution strengthening	$\boldsymbol{k_{Cr}}$	1 MPa/wt.% Cr	[491]
	$\boldsymbol{k_{Ni}}$	5 MPa/wt.% Ni	[491]
	$\boldsymbol{k_{Mo}}$	19.4 MPa/wt.% Mo	[491]
	$\boldsymbol{k_{Mn}}$	-1.5 MPa/wt.% Mn	[491]
	$\boldsymbol{k_P}$	6.3 MPa/wt.% P	[492]
	$\boldsymbol{k_{Si}}$	8.7 MPa/wt.% Si	[492]
Grain boundary/twin strengthening	$\boldsymbol{K_{HP}}$	As-received: 2.8 MPa m$^{-1/2}$ HPT-processed: 0.3 MPa m$^{-1/2}$	[479,482]
	$\boldsymbol{K_{TW}}$	0.3 MPa m$^{-1/2}$	[479,482]
	$\boldsymbol{d}$	40 µm – 42 nm	This work (TEM)
	$\boldsymbol{e}$	3.18 nm – 4.8 nm	This work (TEM)
	$\boldsymbol{f}$	0.12 – 0.19	This work (TEM)
	$\boldsymbol{\lambda}$	40 nm – 48 nm	This work (TEM)

The comparison between the predicted strength, σ_y and the measured HV/3 values, both with the units of MPa is shown in Fig. 5-18. Two observations can be made from Fig. 5-18. Firstly, the modelling results broadly captures the trend of increasing hardness or strength of the UFG/NG AM 316L SS obtained from HPT due to various strengthening mechanisms, supporting the present model. Secondly, while the predicted and measured strength values show good correspondence with each other for the as-received and HPT-processed disks up to 1 revolution, the predicted strength values exceed that of the measured values for disks processed through 5 and 10 revolutions by ~ 11%.

This discrepancy could be attributed to the applied K_{TW} values for the highest equivalent strain range ($\varepsilon_{eq.\text{-}HPT} > 40$) i.e. after 5 and 10 HPT revolutions, which may be lower than K_{HP} according to several studies [484,493]. In addition, it could also be caused by the inaccuracy in evaluating some microstructural parameters in the solid solution effect. This is because the present model assumes that the contribution from the solid solution strengthening remain constant for all processing conditions, but it is possible that the extreme torsional strain imposed after 5 and 10 HPT revolutions could alter the concentration of different elements and segregate at the grain boundaries [220,494]. This could reduce the influence of solid solution on the strengthening of the deformed material with higher number of HPT revolutions. However, for simplifying the analysis of strengthening mechanisms, the grain boundary segregation effect is not considered in this study.

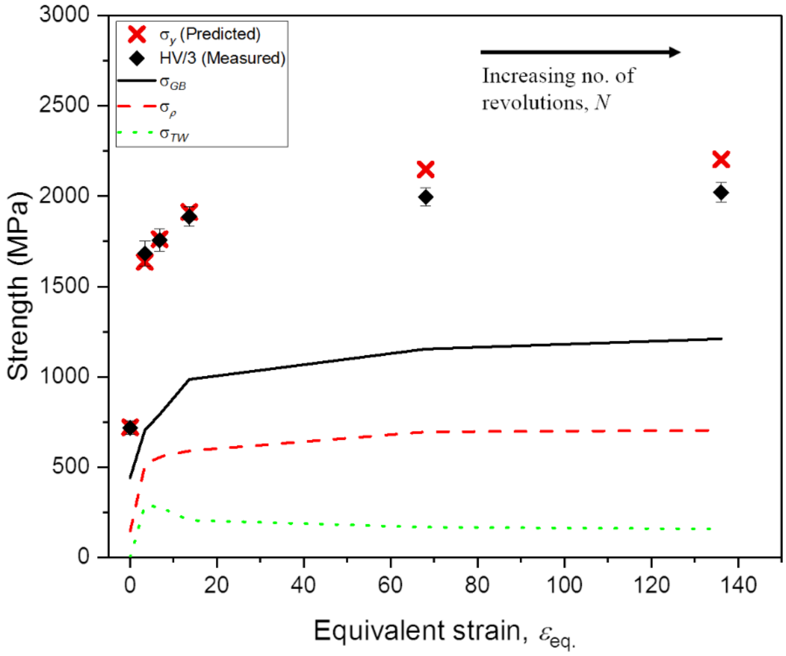

Fig. 5-18 The predicted strength based on the model presented in this study and the measured HV/3 values from the experimental result as a function of equivalent strain, $\varepsilon_{eq.\text{-HPT}}$ [424].

In this model, the intrinsic strength, σ_0 is estimated as 15.4 MPa and the solid solution strengthening, $\Delta\sigma_{SS}$ is evaluated as 115.4 MPa, assuming constant for all processing conditions. Thus, the grain size, twinning, and dislocation effects are revealed as the major contributors of strengthening for the HPT-processed AM 316L SS, as shown in Table 5-3. The grain boundary strengthening has an increasing percentage of contribution to the total estimated yield strength with number of HPT revolutions (~ 40% up to ~ 60%), while the contribution from twin strengthening decreases with increasing number of HPT revolutions (~ 10% down to ~ 6%). Dislocation strengthening has a relatively constant contribution to the total estimated yield strength (~ 30%). Nevertheless, the consistently higher strength contribution by grains/grain boundaries compared to dislocations has been confirmed by several studies on HPT-processed CM stainless steels and other CM alloys [479,482,490,495–497].

Table 5-3 Contribution of each strengthening mechanism on the yield strength of as-received and HPT-processed disks based on the linear additive model [424].

Strength (MPa)	As-received	N=1/4	N=1/2	N=1	N=5	N=10
$\boldsymbol{\sigma_0}$	15.4	15.4	15.4	15.4	15.4	15.4
$\boldsymbol{\sigma_{SS}}$	115.4	115.4	115.4	115.4	115.4	115.4
$\boldsymbol{\sigma_\rho}$	146.6	511.2	559.9	590.1	695.4	703.7
$\boldsymbol{\sigma_{GB}}$	442.7	704.5	791.3	985.5	1200.8	1293.8
$\boldsymbol{\sigma_{TW}}$	-	289.8	279.8	206.2	168.3	158.4

5.3.3 Microstructures and strength comparison of UFG/NG CM and AM 316L SS

So far, the microstructures, phase, and hardness evolution of HPT-processed CM 316L SS (wrought and annealed) have been studied extensively by Gubicza et al. [252], which forms the basis for the investigation of HPT-processed AM 316L SS in the present study. The comparison of these aspects for both that study with those obtained from the results in this study is listed in Table 5-4.

Table 5-4 Comparison of microstructures, phase, and hardness evolution of HPT-processed 316L SS in this study and that of Gubicza et al. [252] before HPT processing (initial) and at strain saturation after 10 HPT revolutions (final).

Aspect	**Gubicza et al.** [252]	**This study**
Grain size	Initial: 42 µm Final: 45 nm *Grains at the central region still not refined to UFG regime even after 5 HPT revolutions	Initial: 40 µm Final: 42 nm *Grains at the central region refined to UFG regime after 1/2 HPT revolution (~ 0.98 µm)
Other microstructural features	- After HPT: ε + α' lamellae and severely deformed bands - Dislocation density, ρ (10^{14} m-^{2}); After 1/4 HPT revolution: ~ 66 Final : ~ 133	- Before HPT: Melt pools and cellular (equiaxed and columnar) sub-structures storing dislocations - After HPT: Shear bands and deformation twins (nanotwins) - Dislocation density, ρ (10^{14} m-^{2}); After 1/4 HPT revolution: ~ 8 Final : ~ 17
Phase	Initial: γ + α' (Predominantly γ) Final: γ + ε + α' (Predominantly ε + α')	Single γ phase maintained throughout all processing conditions
Hardness	Strain hardening observed, but hardness saturation not achieved across the disk diameter even after 10 HPT revolutions Initial hardness: ~ 155 HV Final average hardness: ~ 612 HV	Strain hardening observed, hardness saturation achieved throughout the disk diameter after 10 HPT revolutions Initial hardness: ~ 220 HV Final average hardness: ~ 600 HV

The results in these two fundamental studies shown in Table 5-4 provide insight on the differences in several important aspects of HPT-processed CM and AM 316L SS. Firstly, the microstructures of as-received CM 316L SS comprise of coarse equiaxed grains with an average size of ~ 42 µm, largely of γ-FCC austenites and a small amount of α'-BCC martensites, whereas the AM counterpart consist of numerous melt pools, cellular sub-structures, and a mix of fine and coarse grains (average: ~ 40 µm) growing through the melt pools. Such microstructural variation is the result of localised rapid heating/cooling cycles due to the heat source (laser beam) movement during SLM fabrication as opposed to the slow cooling wrought process. Secondly, after HPT processing, ε + α' martensites dominate the microstructure of CM 316L SS, but a single γ austenite phase is maintained throughout all processing conditions for the AM 316L SS. Deformation twins (nanotwins) are introduced in AM 316L SS after HPT processing instead of the martensites, as detailed in Section 5.3.1.

In addition, Table 5-4 also reveals the higher hardness of as-received AM 316L SS compared to CM 316L SS; ~ 220 HV and ~ 155 HV, respectively, which can be attributed to the cellular sub-structures that become locations for the storage of numerous dislocations that are generated due to the rapid heating/cooling cycles during SLM [126,297,298]. XRD analysis estimated the dislocation density, ρ of the as-received AM 316L SS in this study as ~ 0.69 x 10^{13} m-^{2}. Although not mentioned in the study by Gubicza et al., the value of ρ for annealed 316L SS often lies in the range of 10^{9} - x 10^{10} m-^{2} [127]. However, the average hardness value obtained for CM 316L SS by Gubicza et al. upon torsional strain saturation is ~ 612 HV, which is just slightly higher than ~ 600 HV attained for AM 316L SS after 10 HPT revolutions in this study. This can be attributed to the high percentage of strain-induced martensites that are formed with increasing torsional strains, since martensite is known as a harder phase compared to the austenite phase [252,305,306,420,498]. This is reflected by the significantly higher estimated values of ρ, for HPT-processed CM 316L SS obtained by Gubicza et al. compared to those for AM 316L SS in this study, by at least eight times as shown in Table 5-4. It should be noted that the XRD peaks that are analysed to estimate the ρ values are based on the predominant phase in the XRD spectra, i.e. $\varepsilon + \alpha$' martensites for CM 316L SS, and γ austenite for AM 316L SS. Thus, the hardening of HPT-processed CM 316L SS is attributed to the combination of grain boundary, phase transformation, and dislocation strengthening mechanisms.

Interestingly, although strain-induced martensites are not present in AM 316L SS and that the dislocation density values for AM 316L SS in this study are significantly lower than those obtained for CM 316L SS by Gubicza et al. after HPT processing, the HV values for both AM and CM 316L SS do not differ much, only by ~ 12 HV. This could imply the contribution of another additional factor to the hardening of HPT-processed AM 316L SS, for example deformation twins (nanotwins). Indeed, the presence of nanotwins after HPT processing have been shown to provide additional hardening to UFG/NG materials by providing sites to block dislocation motions [303,482,484,485]. Thus, in the absence of strain-induced martensites, the strengthening of the HPT-processed AM 316L SS is contributed by the microstructural features of grain boundaries, dislocations, and nanotwins. Furthermore, hardness saturation is achieved across the diameter of the disk after 10 HPT revolutions in the present study, which is not attained in the study by Gubicza et al. Typically, such microstructural inhomogeneity in HPT-processed materials is often caused by the inability of the local strain to refine larger or harder particles due to inadequate torsional strain applied as the result of the radial dependency of HPT processing [499]. Although not investigated by Gubicza et al. it is possible that the microstructural homogeneity is not achieved for the HPT-processed CM 316L SS even after 10 HPT revolutions due to the inability of the localised strain to refine the hard martensite particles at the central region of the HPT-processed CM 316L SS disks. On the other hand, it is reasonable to infer that the absence of such hard particles throughout all processing conditions for the AM 316L SS in this study could explain the ability to achieve microstructural homogeneity given the applied torsional strain values.

Therefore, the results from both studies suggest similar response of HPT processing for both AM and CM 316L SS in terms of significantly improving hardness and strength, despite the contrasting microstructural features obtained throughout all processing conditions. However, an interesting aspect to consider is that even though martensite is harder than austenite, it has poor corrosion resistant, thereby increasing the susceptibility of 316L SS to catastrophic failure during service, e.g. stress corrosion cracking, corrosion fatigue, and low temperature sensitisation [500–505]. Thus, the results obtained in the present study could potentially yield the advantages of enhanced strength whilst maintaining or improving the corrosion resistance, which will be discussed further in Chapter 7.

5.4 Summary

The microstructural evolution, hardness, and deformation mechanisms of HPT-processed AM 316L SS have been studied through OM, TEM, XRD, and microhardness measurements. A physical-based model for incorporating the contributions of multiple strengthening mechanisms was applied to assess the factors that influence the significant increase in strength of the alloy. The following conclusions can be drawn based on the results in this chapter:

1. Microstructural homogeneity has been achieved after 10 revolutions of HPT processing as indicated by microhardness measurements, which is attributed to the mutual hardening (dislocation accumulation and grain refinement) and softening (dislocation annihilation).
2. HPT processing significantly reduces crystallite size, D_c and increases dislocation density, ρ and has successfully produced sub-micron grains (UFG) and nano-scale grains (NG), with an average size of 42 ± 10 nm after 10 revolutions.
3. Three stages of deformation are observed in the HPT-processed alloy, which are related to the imposed strain and sub-micron and/or nano-scale microstructural features. The estimation of yield strength by the linear additive strengthening model indicates that UFG and/or NG microstructures, dislocations, twins, and solid solution contribute to the super high strength obtained for the HPT-processed AM 316L SS, in which grain boundary strengthening has the highest influence in strengthening, followed by dislocation strengthening, and twinning strengthening.

Chapter 6 Micro-mechanical response of AM 316L SS processed by HPT

6.1 Introduction

In order to assess the practicality of UFG and NG microstructures in AM 316L SS obtained by HPT processing for future applications, the micro-mechanical response, i.e. the mechanism of plastic deformation needs to be evaluated [506]. 316L SS is of particular interest because it is an important engineering material that has been widely used in a broad range of applications, e.g. oil, nuclear and biomedical industries due to its high corrosion and oxidation resistance, and excellent weldability [126,297]. However, so far, no attempt has been made to monitor the evolution of plastic deformation mechanism for AM 316L SS processed by HPT. Strain rate sensitivity (SRS), m and activation volume, V_p^* are important criteria that could relate to the change or transition of microstructure from micro- to nano-scale [507,508]. Both parameters can be estimated via nanoindentation, which is a simple testing procedure, especially for samples with small size [231,509], or for examining local properties of bulk materials [510]. Accordingly, the objective of the present chapter is to investigate the micro-mechanical behaviour of HPT-processed AM 316L SS at RT via nanoindentation experiments. The results were discussed by correlating the evolution of microstructure and hardness detailed in Chapter 5 with the calculated m and V_p^* values obtained in this chapter.

6.2 Results

6.2.1 Micro-mechanical properties of as-received and HPT-processed disks

The micro-mechanical response for as-received and HPT-processed AM 316L SS was evaluated by using nanoindentation technique. The following sections display results from nanoindentation measurements at a constant strain rate, $\dot{\varepsilon}$ of 1.25x10^{-4}, s^{-1}, and at multiple strain rates, $\dot{\varepsilon}$ of 1.25x10^{-4}, 2.5x10^{-4}, 5.0x10^{-4}, and 1.0x10^{-3} s^{-1}, respectively.

6.2.1.1 Nanoindentation results for a constant strain rate

When the indenter penetrates the surface of the material during nanoindentation testing at a constant indentation rate and at a given peak load, force, P and displacement, h data are recorded with a loading and unloading profile, yielding P-h curves that represent the micro-scale response of the tested material [231]. Shorter displacements (curve moves to the left) correspond to increased hardness and reduced ductility, while less broadening/deviation among a set of P-h curves indicate reasonably consistent mechanical response and better plastic stability [506,511]. Therefore, Fig. 6-1 shows a series of representative indentation curves (load, P vs displacement, h) for as-received and

HPT-processed disks both at the centre and edge of the disks through 1/4 – 10 revolutions at a constant strain rate of $\dot{\varepsilon}$ of $1.25\text{x}10^{-1}$, obtained from 15 individual indentations at each location. Two observations could be made based on these curves.

Firstly, it is clear that the displacements of HPT-processed disks become lower with increasing HPT revolutions compared to the as-received disk both at the centre and edge. This suggests higher hardness and reduced ductility that are most likely the result of the dense dislocations generated and grain refinement due to the HPT-imposed torsional strain [506]. Secondly, the displacements of the *P-h* curves for the HPT-processed disks show less broadening with higher number of revolutions compared to the as-received disk, in which such effects are more apparent at the edge (Fig. 6-1(b)) compared to at the centre (Fig. 6-1(a)) of the disks. This indicates improved plastic stability of HPT-processed disks, possibly due to increasingly homogeneous microstructural distribution with increasing number of HPT revolutions [506,511].

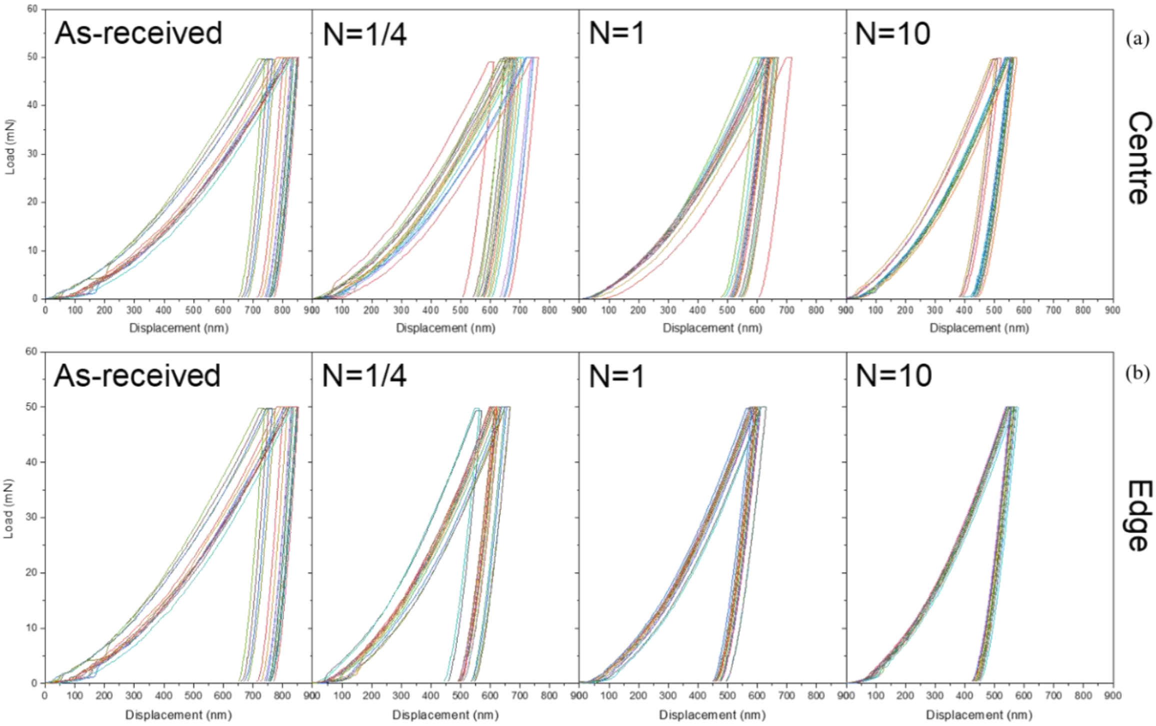

Fig. 6-1 Representative load, *P* vs displacement, *h* curves for as-received and HPT-processed disks at the (a) centre, and (b) edge of the disks [430].

Fig. 6-2 shows the average *P-h* curves for as-received and HPT-processed disks at the centre and edge locations. The shorter displacements of the *P-h* curves for N = 1/4, 1/2, and 1 revolution at the edge (Fig. 6-2(b)) in contrast with that at the centre of the disks (Fig. 6-2(a)) indicate rapid increase in hardness at the peripheral area compared to at the central region of the HPT-processed disks during the earlier deformation stages. On the other hand, the displacements of the *P-h* curves become even shorter at later deformation stages (N = 5 and 10 revolutions) for both the centre and edge of the disks. Nevertheless, this suggests a significant hardness increase and lower ductility are obtained with increasing HPT torsional strains, regardless of the location of indents.

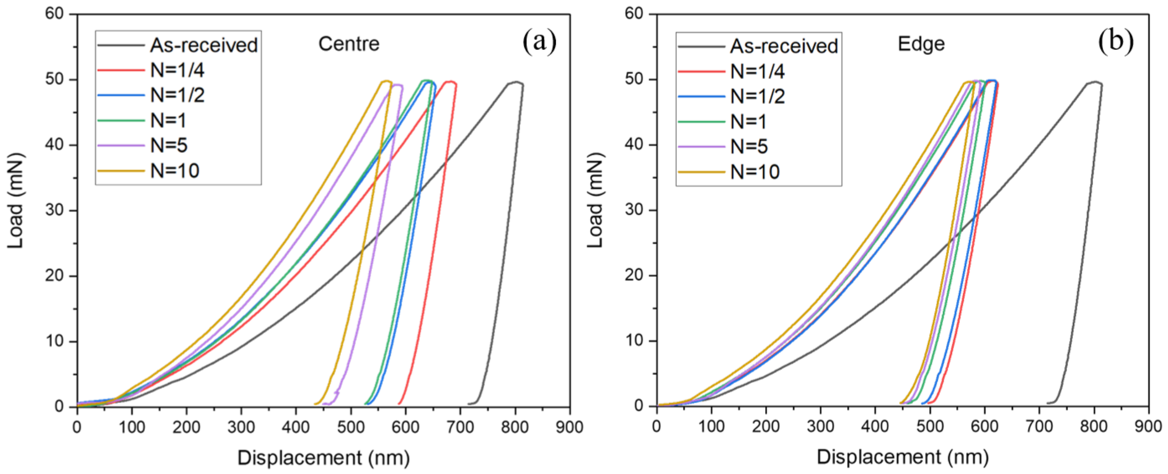

Fig. 6-2 Average load, *P* vs displacement, *h* curves from 15 individual indentations for as-received and HPT-processed disks at the (a) centre, and (b) edge of the disks [430].

Subsequently, the nanoindentation hardness values (nanohardness), *H*, are estimated by using the Oliver-Pharr method [512], and the results of variation in *H* against the number of HPT revolutions, *N* are displayed in Fig. 6-3. Fig. 6-3(a) compares the nanohardness at the centre and edge of the as-received and HPT-processed disks, while Figs. 6-3(b) and (c) show the *H* values in comparison with HV values at the centre and edge of the disks, respectively. The higher *H* values at the edge of the HPT-processed disks compared to that at the centre (Fig. 6-3(a)) are consistent with the HV measurements shown in Figs. 5-1 and 5-2. In addition, the evolution of *H* values exhibit a similar trend with that of HV measurements (Figs. 6-3(b) and (c)), i.e. remarkable hardness increase due to strong work hardening at the initial stages of HPT processing (1/4 to 1 revolution) before only increasing marginally upon reaching saturation after 10 revolutions due to the absence of significant work hardening. In addition, the consistently higher *H* values compared to HV (Fig. 6-3(b) and (c)) could be attributed to: (i) the fact that the area of contact by nanoindentation is measured as projected area, rather than the surface area measured in traditional Vickers microhardness [513], and (ii) the indentation size effect (ISE) that manifests as higher *H* values when the indentation load, *P* and indentation depth, *h* are decreased for sharp indentations such as the pyramid indenter used in this study [514].

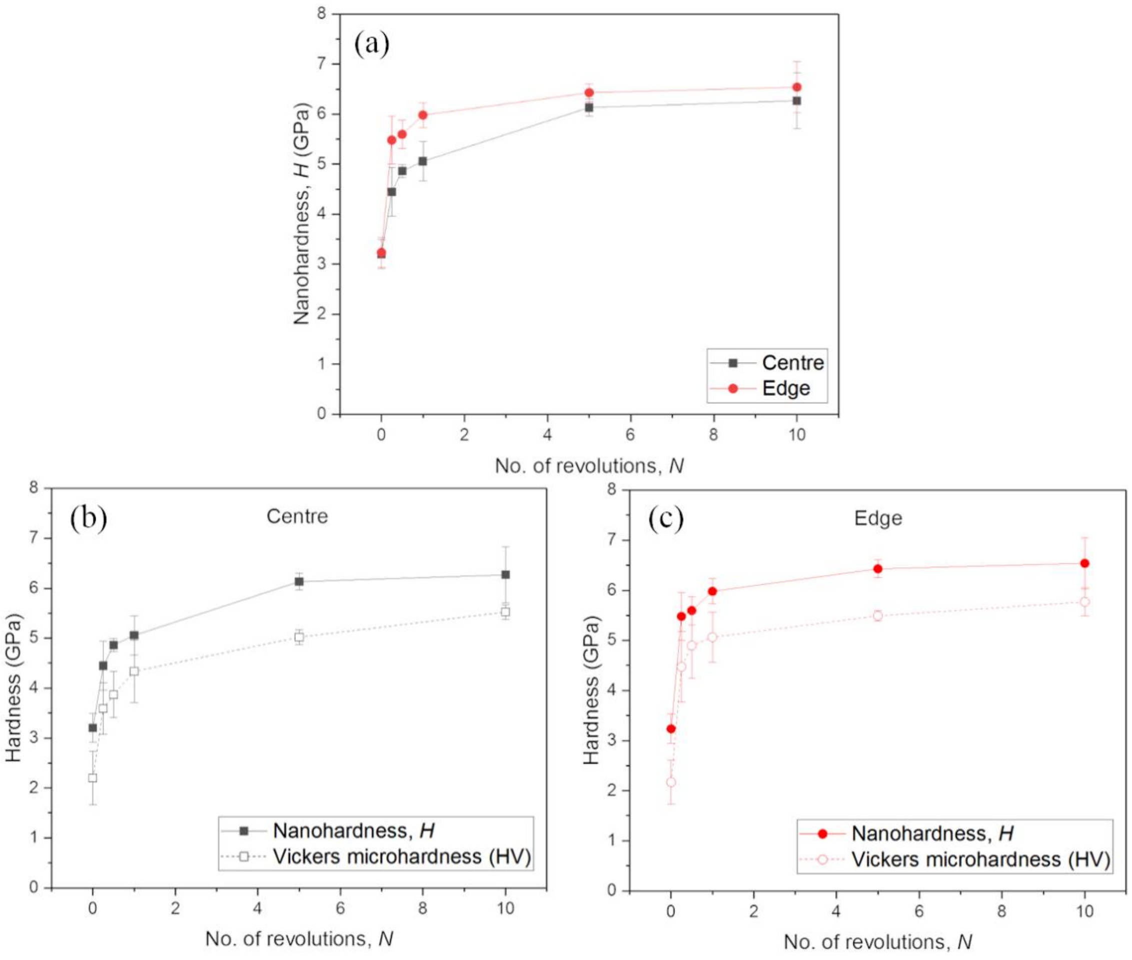

Fig. 6-3 (a) H vs N at centre and edge, H vs HV at the (b) centre and (c) edge of the as-received and HPT-processed disks. HV values taken from microhardness measurements in Fig. 5-1 are included for comparison [430].

6.2.1.2 Nanoindentation results for multiple strain rates

Nanoindentation measurements at various strain rates, $\dot{\varepsilon}$ of 1.25x10^{-4}, 2.5x10^{-4}, 5.0x10^{-4}, and 1.0x10^{-3} s^{-1}, taken both at the centre and edge of the disks reveal continuously lower displacement values with increasing $\dot{\varepsilon}$. This trend is shown in the representative P-h curves in Fig. 6-4 for the as-received disk and HPT-processed disk after 10 revolutions taken at the edge of the disks. This observation demonstrates a strain rate dependency for the displacement shift at peak load, i.e. shift to the left after HPT indicating a decrease of ductility and increase of hardness as the strain rate increases [382,511,515].

On the other hand, the variations in H values as a function of N for various $\dot{\varepsilon}$ values taken at the centre and edge of the disks are displayed in Fig. 6-5, together with HV values obtained in Chapter 5 as comparison. The results shown in Fig. 6-5 show a similar trend as those observed for nanoindentation at a single strain rate shown in Fig. 6-3. In addition, the estimated H values for the as-received and HPT-processed disks are all strain rate-sensitive, as indicated by the consistently higher H values at higher $\dot{\varepsilon}$. Nevertheless, the trend of increasing H with N is not the same for all materials but depends on the response of a particular material to HPT straining. For example, ZK60 Mg alloy and the CoCrFeNiMn high entropy alloy (HEA) exhibit strain hardening behaviour, thus increased *H* with increasing *N* [508,516]. However, Zn-22% Al shows strain softening behaviour, thus decreased *H* at higher *N* [507].

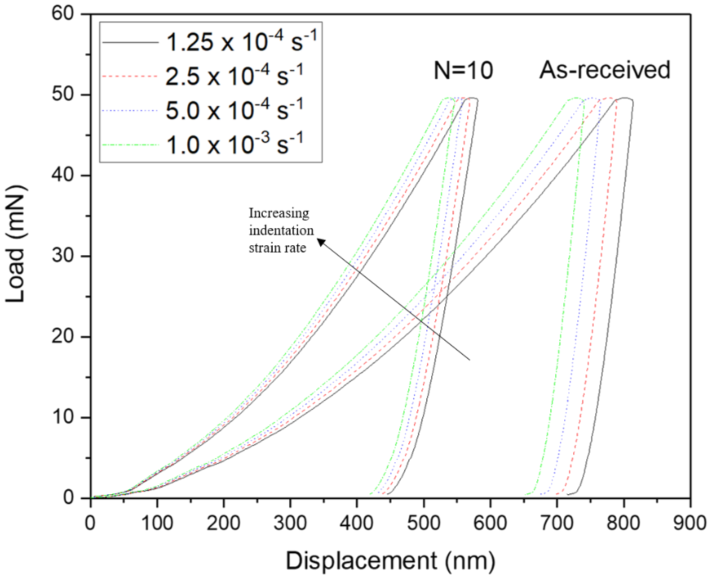

Fig. 6-4 Representative *P-h* curve for as-received and HPT-processed disks through 10 revolutions obtained at different $\dot{\varepsilon}$ values taken at the edge of the disks [430].

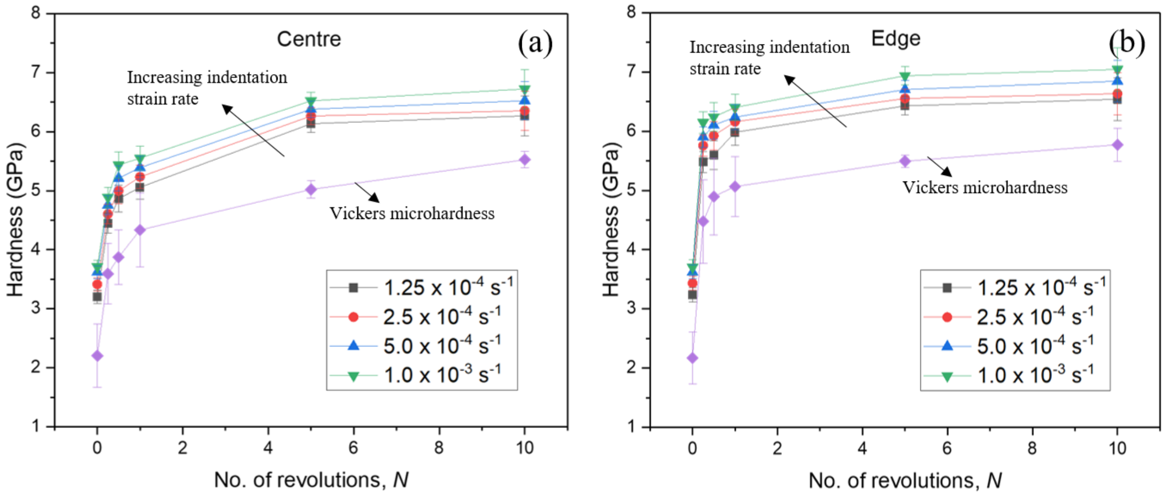

Fig. 6-5 *H* vs *N* for various $\dot{\varepsilon}$ values at the (a) centre and (edge) of the disks. HV values from microhardness measurements are also included for comparison [430].

6.3 Discussion

HPT processing was employed to impose extreme grain refinement on AM 316L SS, and the average final grain size obtained upon saturation after 10 revolutions is ~ 42 nm, as discussed in Chapter 5. The maximum hardness of the HPT-processed disks in the present study (~ 600 HV) is comparable to that attained by Gubicza et al. [252], about 610 HV after 10 HPT revolutions of wrought 316L SS, although hardness saturation throughout the disk was not achieved in that study. This suggests similar response of HPT processing for both AM and wrought 316L SS in terms of significantly improving hardness and strength.

The results from microhardness measurements shown in Figs. 5-1 and 5-2 and nanoindentation tests in this chapter demonstrate strain hardening characteristics for the HPT-processed disks, which is expected from the extreme grain refinement obtained with increasing number of HPT revolutions. The strengthening of HPT-processed materials is commonly observed in various studies and is primarily attributed to the dislocation hardening and grain boundary strengthening [303,469,495], as well as twinning and precipitation hardening in some metals [482,517,518]. In addition, the strain-rate dependency shown in nanoindentation testing provide some clues to the level of plasticity and plastic deformation mechanisms at different strain rates. Therefore, the deformation characteristics for HPT-processed disks at RT can be evaluated by calculating the strain rate sensitivity (SRS), m at a given strain value, ε and absolute temperature, T by the relation between uniaxial flow stress, σ_f and strain rate, $\dot{\varepsilon}$ through the following expression [519,520]:

$$m = \left(\frac{\partial ln\sigma_f}{\partial ln\dot{\varepsilon}}\right)_{\varepsilon,T} = \left(\frac{\partial \ln (H/C_1)}{\partial ln\dot{\varepsilon}}\right)_{\varepsilon,T} \qquad \text{Eqn. 6-1}$$

For nanoindentation, the Tabor empirical relationship of $\sigma_f = H/C$ is used to estimate flow stress, σ_f, in which H is the nanohardness estimated from the P-h curves based on the Oliver-Pharr method [512] and the value of C_1 is taken as 3 for fully plastic deformation at a constant strain rate, $\dot{\varepsilon}$ [519,521]. Thus, the values of m are estimated from the gradient of a double logarithmic plot of $H/3$ vs $\dot{\varepsilon}$ based on Eqn. 6-1 and shown as inset in Fig. 6-6, while the evolution of m values for all processing conditions at the centre and edge with increasing N are summarised in the main figure.

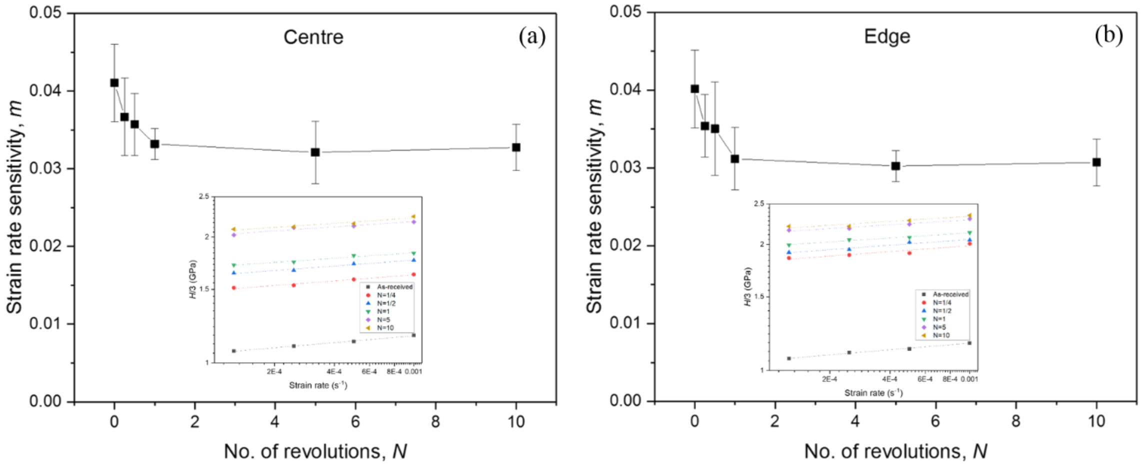

Fig. 6-6 Variation of m with increasing N, and flow stress, $H/3$ vs $\dot{\varepsilon}$ shown inset at the (a) centre and (b) edge of the as-received and HPT-processed disks [430].

The values of m for the as-received AM 316L SS is estimated as ~ 0.041 (centre) and ~ 0.040 (edge), which are of one order higher than 0.0061 obtained for coarse-grained 316L SS [522] and other typical coarse-grained FCC metals, e.g. ~ 0.004 for high-purity Cu [523], ~ 0.0028 for pure Ni [524] and ~ 0.004 for Al 99.5% [525]. However, these values are consistent with the values of m for AM 316L SS obtained by Li et al. [526], ranging from 0.02 – 0.03, when measured by tensile tests at different strain rates and strain rate jump tests. In fact, the high values of m obtained for the as-received AM 316L SS in this study is comparable to those of CM FCC metals with nano-sized grains, e.g. $m \approx 0.015 – 0.034$ for pure Ni with grain sizes < 100 nm [524,527].

The values of m only decrease marginally after the early stages of HPT, i.e. 1/4 up to 1 revolution (~ 0.033 and ~ 0.031 at the centre and edge, respectively) before remaining relatively constant at the later stages of HPT, i.e. 5 and 10 revolutions. Such high m values indicate reasonably high plasticity levels despite the significant hardening achieved through HPT and they are comparable with other FCC metals and alloys with UFG/NG microstructures [231,516]. In this context, plasticity is referred to as the ability of a solid material to be plastically deformed without fracture, which is dependent on its intrinsic crystal structure and available slip systems, and the microstructural features attained after processing [528]. This is unlike the ductility of materials that is influenced by the strain hardening rate, which is significantly decreased in nanostructured metals because the nano-scale grain boundaries could no longer become effective sites for the accumulation of dislocations beyond a critical strain value [529]. Nevertheless, the continuous gradual decrease of m values suggests that the strain rate dependency of HPT-processed AM 316L SS in this study decreases with increasing N.

It is interesting to see that the mix of fine and coarse grains of as-received AM 316L SS in this study already possesses m values comparable to that of HPT-processed CM metals and alloys with UFG/NG microstructures. Thus, there could be a change in the plastic deformation mechanism as the result of microstructural transition from the micro- to nano-scale due to HPT torsional straining. Therefore, the strain rate-dependent plastic deformation mechanism can be assessed by estimating the activation volume, V_p^* based on the following relationship [507,516]:

$$V_p^* = \sqrt{3}kT\left(\frac{\partial n\dot{\varepsilon}}{\partial ln\sigma_f}\right)_{\varepsilon,T} = \sqrt{3}kT\left(\frac{\partial \ln{(0.01\dot{\varepsilon}_i)}}{\partial(H/C)}\right)_{\varepsilon,T} = \frac{C\sqrt{3}kT}{mH} \qquad \text{Eqn. 6-2}$$

where k is Boltzmann’s constant. The results are shown in Fig. 6-7 for the centre and edges of the disk and expressed in terms of the burgers vector, b (taken as 2.5×10^{-10} m for austenitic stainless steels [526]).

Regardless of the location of the disks, a general trend could be observed from Fig. 6-7 that the values of V_p^* for the as-received AM 316L SS are in the region of ~ $11b^3$, which then decreases to the range ~ $6 – 8b^3$ with increasing number of HPT revolutions. It has been reported that the value of V_p^* depends on the orders of magnitude for different strain rate-limiting processes [530], e.g. ~ $100b^3$ –

$1000b^3$ for dislocation glide in FCC metals [531], ~ $10b^3$ for grain boundary sliding (GBS) [530], and ~ $b^3 – 10b^3$ for diffusion through the GB or through the crystalline lattice [531].

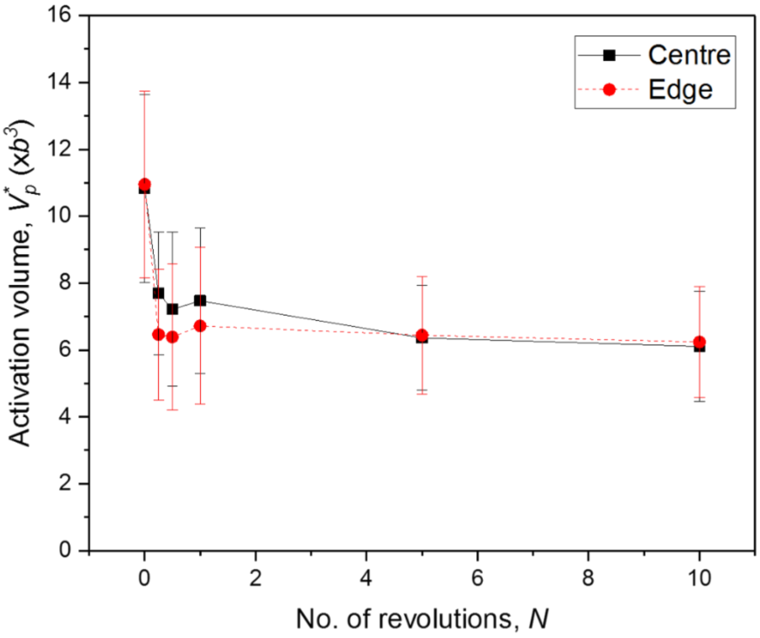

Fig. 6-7 Evolution of V_p^* with increasing N at the centre and edge of the as-received and HPT-processed disks [430].

The estimated V_p^* value for the as-received AM 316L SS in this study is ~ $11b^3$, which is significantly lower than that observed in CM coarse-grained FCC materials that are typically deformed via the forest dislocation cutting mechanism (> $100b^3$) [531,532]. However, it is closer to the range of 22 – $28b^3$ reported by Li et al. for AM 316L SS [526]. This discrepancy can be attributed to the difference in testing method used to determine m; with tensile and strain rate jump tests used in the study by Li et al., and nanoindentation tests in this study. Nevertheless, the rather low V_p^* value in AM 316L SS compared to CM coarse-grained 316L SS and other FCC metals suggest the abundance of barriers to dislocation for deformation via plastic flow, including a mix of high angle and low angle grain boundaries, pre-existing dislocations, nano-precipitates, cellular structure networks, numerous fusion boundaries from solidified melt pools, and localised misorientations [527,533]. In fact, the dislocation density in AM 316L SS obtained in this study is already much higher (> x 10^{13} m^{-2}) compared to their cast or wrought counterparts (x 10^9 – x 10^{10} m^{-2}), in which the cellular structure boundaries become additional storage for dislocations [127,297,298]. Therefore, although the value of V_p^* for the as-received AM 316L SS corresponds to that of GB-driven plasticity, specifically GBS, or diffusion through the GBs or through the crystalline lattice, the plastic deformation of the as-received AM 316L SS in this study cannot be associated with GB phenomena, but rather influenced by numerous sub-micron and nano-scale microstructural features described previously.

During the early and the intermediate stages of HPT deformation, e.g. from 1/4 to 1 revolution, the activation volume decreases to ~ $6 – 8b^3$, which remain reasonably consistent towards the later stages

(5 and 10 revolutions). Kawasaki et al. [231] explained that although significant hardening is observed at early stages of HPT deformation due to the generation and multiplication of dislocations, the overall strain hardening rate of HPT-processed metals decreases with increasing hardness and number of revolutions. This suggests that the mechanism for plastic deformation changes as the microstructures transition from micro- to nano-scale upon continuous torsional straining. This is evident in the present study as the HV values after 1/4 revolution generally doubles that of the as-received disk, but only marginally increase after 1 and 10 revolutions as shown in Fig. 5-1. This is because when the grain sizes continue to decrease to the sub-micron and then nano scales, the amount of grain boundaries also increase, and it becomes increasingly difficult for the dislocations to pile up and stored within the grain interior [534]. At this stage, grain boundaries become the most effective sites in blocking dislocation motions compared to the accumulated dislocations [535–537].

In the current investigation, TEM observations shown in Fig. 5-13 indeed display a significant amount of dislocations and the emergence of sub-micron grainsafter 1/4 revolution without a clear distinction between the dislocations and the grain boundaries. This implies that the predominant deformation mechanism at the early stages of HPT processing is related to the combined dislocations due to both GNDs and SSDs, as well as the UFG microstructures formed as the result of strain gradient at low HPT torsional strains. At the intermediate stage, i.e. after 1 revolution, the microstructures consist of nano-sized grains that begin to emerge with apparent grain boundariess, and dislocations that now appear to be incoherent and no longer continuous as shown in Fig. 5-15. This indicates that the GB-related activities, e.g. GBS, or diffusion through GBs or through the crystalline lattice become the controlling mechanism for plastic deformation at this stage, similar to that observed in nanotwinned nanocrystalline CoCrFeNi alloys studied by Huo et al. [534]. After 10 HPT revolutions, nano-sized grains with clear and distinct grain boundaries dominate the microstructure, with some nanotwins observed within the grain interior at the saturation stage as shown in Figs. 5-16(c) and (d). Here, the majority of the grain interior does not contain dislocations, as they are emitted from inside the grains towards the opposing sides of the grain boundaries, but the nanotwins have been found to act as additional grain boundaries that also impede dislocation motions [538,539]. This suggests that GB-mediated plasticity remains the prevalent deformation mechanism at the HPT saturation stage, either through GB diffusion or crystalline lattice diffusion, similar to the results from other studies on HPT-processed metals [507,508,515,516].

Therefore, the as-received AM 316L SS in this study can be considered to possess reasonably high plasticity characteristics, i.e. superior capability to sustain plastic deformation without fracture, as indicated by the higher m value (~ 0.041) compared to coarse-grain CM 316L SS (e.g. ~ 0.0061) [522]. Even though the values of m slightly decrease at the early stages of HPT, these values remain consistent with increasing number of revolutions, indicating that a good level of plasticity is maintained along with the significant hardening obtained via HPT processing. Furthermore, based on the evolution of V_p^* values and the microstructural observations in the present study, it can be concluded that the predominant deformation mechanism for the as-received AM 316L SS is attributed to the numerous sub-micron and nano-scale microstructural features, rather than GB-related activities, although the low value of V_p^* is often related to GB-regulated plasticity. On the other hand, the dominant deformation mechanism for the HPT-processed disks is ascribed to GB-mediated plasticity based on the consistently lower values of V_p^* for all HPT processing conditions which are lower than that of the as-received counterpart, as well as the increasing amount of sub-micron and nano-scale grain boundaries with higher number of HPT revolutions.

6.4 Summary

The evolution of plastic deformation mechanisms of HPT-processed AM 316L SS was studied through nanoindentation tests at both constant and various strain rates. The values of strain rate sensitivity (SRS), m, and activation volume, V_p^* were calculated based on the parameters obtained from nanoindentation testing. These values were then correlated with the microstructure and microhardness evolution in Chapter 5 to assess the prevalent mechanisms of plastic deformation for the as-received and the HPT-processed disks. The following conclusions can be drawn based on the results of this study:

1. The calculated value of m for the as-received AM 316L SS is higher than that of the CM counterpart, indicating a reasonably high level of plasticity in AM 316L SS. The values of m decrease slightly until 1 HPT revolution, before remaining consistent at higher number if HPT revolutions. This indicates that a good level of plasticity is maintained throughout HPT processing.
2. The estimated values of V_p^* demonstrate that there are changes in the predominant plastic deformation mechanism with the microstructural transition from micro- to nano-scale. By comparing the V_p^* values calculated in this chapter with TEM observations shown in Chapter 5 and the established values of V_p^* from literature, it could be concluded that the prevalent deformation mechanism changes from plasticity driven by numerous sub-micron and nano-scale microstructural features for the as-received AM 316L SS to GB-mediated plasticity after HPT processing.

Chapter 7 Corrosion performance of AM 316L SS processed by HPT

7.1 Introduction

316L SS is well-known as a material that possesses excellent corrosion resistance; hence it is widely used in applications where high level of corrosion resistance is more important than other properties, e.g. hardness and strength. To date, such applications include petrochemical industry, marine engineering, food and beverage preparing and storage, and biomedical implants. This austenitic SS obtains its corrosion resistance characteristic via the presence of Cr (≥ 11 wt. %) which forms a thin layer of passive Cr_2O_3 oxide film on the surface of the material [540]. The addition of a small amount of Mo further enhances the corrosion resistance by preventing corrosion-inhibiting anions that may be present upon exposure to a corrosive environment [441]. Low C content (≤ 0.03 wt. %) in 316L SS is also advantageous as it could inhibit the precipitation of carbides at grain boundaries which contributes to intragranular corrosion, especially in welding process [252,441].

Many studies have revealed numerous factors that could influence the corrosion performance in metals and alloys, including grain sizes, corrosion media (electrolyte solution), and the surface condition of the materials, e.g. defects, surface reactivity or surface modification [229,441]. For example, Di Schino and Kenny [541] attributed the deterioration of corrosion resistance for fine-grained 304 SS (grain sizes < 2 µm) in a sulfuric acid medium to the destabilisation of passive oxide layers at the grain boundaries. Li et al. [542] found that the increase in corrosion rates in nanocrystalline-grained low carbon SS (grain sizes < 50 nm) produced by ultrasonic shot peening was due to the increased amounts of active sites that enhanced corrosion attacks. Another study on ECAP processing of Fe-20%Cr steel observed that the UFG structure improved the pitting resistance when immersed in a 1000 mol m^{-3} NaCl solution. On the other hand, high porosity levels and the presence of cracks in AM-fabricated SS alloys have been found to deteriorate corrosion performance [543].

However, the influence of SPD processing on the corrosion resistance of AM 316L SS is currently unknown because these two techniques (AM and SPD) have never been studied together. In this chapter, 316L SS samples were initially fabricated by SLM and then processed through HPT. The microstructure and corrosion resistance of HPT-processed disks were investigated and compared to that of the as-received specimens. Their corrosion resistance was evaluated by conducting electrochemical tests in a sequence of open-circuit potential (OCP), electrochemical impedance spectroscopy (EIS), and potentiodynamic polarisation in 3.5% NaCl aqueous solution.

7.2 Results

7.2.1 Open circuit potential

The open circuit potential (OCP) is used as an indicator to evaluate the formation, dissolution, and stability of passive oxide layer for the as-received and HPT-processed AM 316L SS in a corrosive environment (3.5% NaCl solution). The change in OCP with immersion time provides an understanding on the corrosion tendency of the metallic disks. A plot of OCP against exposure time for all processing condition is shown in Fig. 7-1.

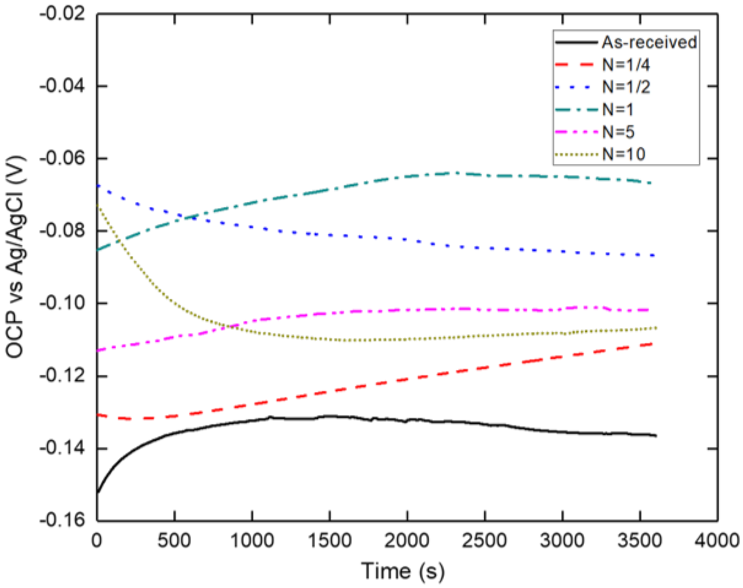

Fig. 7-1 OCP vs. immersion time in 3.5% NaCl solution for as-received and HPT-processed disks [374].

A rise in potential in the positive direction (upwards) indicates the formation of a passive oxide layer on the surface of the disks, implying a reduction in corrosion tendency and hence an improvement in corrosion resistance. On the other hand, a negative shift in potential (downwards) indicates breakage or dissolution of the passive oxide layer, or even the non-existence of such protective layer. This implies increasing tendency to corrosion and hence reduction in corrosion resistance. In contrast, a relatively flat curve infers simultaneous formation and dissolution of the protective oxide layer, indicating that a dynamic equilibrium has been achieved. Similarly, a steady potential throughout immersion time means that the passive layer remains intact and protective.

As shown in Fig. 7-1, the OCP values for HPT-processed disks are in general more positive than that of the as-received disk, indicating that HPT processing generally improves the corrosion performance of AM 316L SS in this study. Similarly, a single steady-state OCP value is achieved for each processing condition after 1 hour of immersion, indicating that a passive, protective oxide layer is formed in each processing condition. However, within the HPT-processed disks, the corrosion tendency showed a different trend. The OCP values shift to more positive values as the number of HPT revolutions increase from 1/4 to 1, exhibiting decreasing corrosion tendency and better corrosion resistance. However, as the number of revolutions further increase to 5 and 10, the OCP values became more negative, indicating increase in corrosion tendencies thus resulting in relatively worse corrosion resistance.

Individually, the OCP value for as-received disk initially rises from 0 s to 500 s before decreasing steadily until the end. This suggests the breakage of the passive oxide layer that was formed earlier after 500 s of immersion time. After 1/4 HPT revolution, a steady increase in OCP value suggests continuous formation of oxide layer throughout the test period. However, a gradual decrease of OCP value along the immersion time after 1/2 HPT revolution may indicate continuous dissolution or even absence of a passive oxide layer on the surface of the disk. After 1 and 5 revolutions, the OCP values exhibit improvement up to 2000 s before stabilising beyond this point, which imply that the passive oxide layer formed remain unbroken and protective. In contrast, the OCP values initially decrease at 10 revolutions until ~ 1000 s before steadily increasing gradually, which imply that the formation of a passive oxide layer after ~ 1000 s could be accompanied by dissolution of the oxide layer as well.

Nevertheless, the as-received and HPT-processed disks do not exhibit any apparent fluctuations, suggesting very little surface defects and metastable pitting are present during the corrosion process. The final OCP values for all processing conditions and their associated errors are displayed in Fig. 7-2 and Table 7-1. A linear increase in OCP values is observed as the number of HPT revolutions increase from 1/4 to 1, i.e. more positive values, indicating that grain refinement plays a major role in improving the corrosion resistance. However, the reduction in OCP values at higher number of HPT revolutions (5 and 10) provide an interesting insight that further grain refinement may degrade the corrosion resistance of the disks. Hence, the homogeneity and distribution of microstructure throughout HPT processing could determine the corrosion behaviour of the HPT-processed disks.

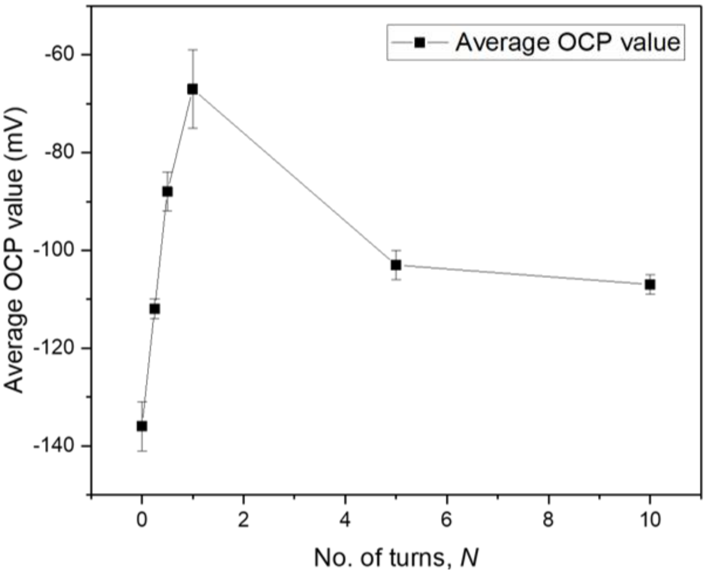

Fig. 7-2 Average final OCP values for as-received and HPT-processed disks [374].

Table 7-1 Average OCP values for as-received and HPT-processed disks [374].

Processing condition	OCP (mV)
As-received	-136 ± 5
N = 1/4	-112 ± 1
N = 1/2	-88 ± 4
N = 1	-67 ± 8
N = 5	-103 ± 3
N = 10	-107 ± 1

7.2.2 Potentiodynamic polarisation

Potentiodynamic polarisation test has been established as a method to quantitatively assess the corrosion performance of a material in a given environment by determining the corrosion rate using a method called the Tafel fitting analysis [544]. Tafel fitting was carried out by determining the corrosion current, i_{corr} from the intersection point by extrapolating the linear cathodic and anodic regions of a potentiodynamic polarisation curve (PPC), as illustrated in Fig. 7-3.

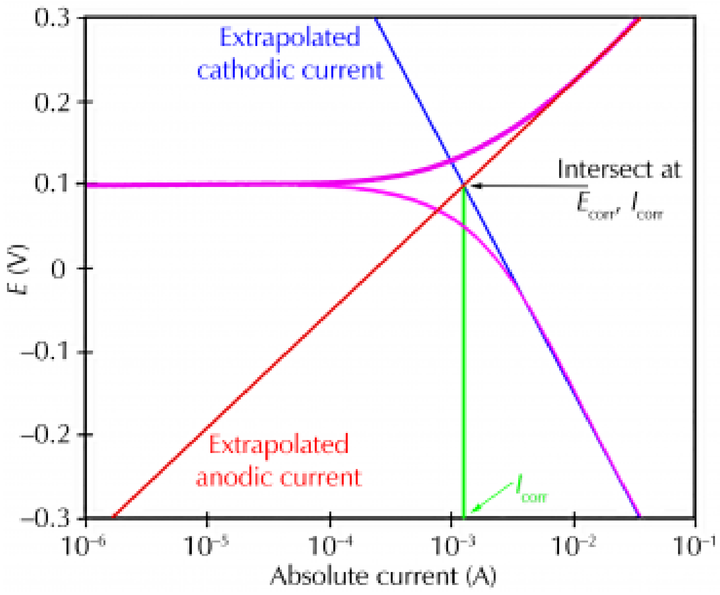

Fig. 7-3 Illustration of Tafel fitting to obtain corrosion parameters from PPC.

Generally, the corrosion rate can be calculated according to ASTMG 102-89 standard using the equation [545]:

$$Corrosion\ rate = \frac{3.27 * 10^{-3} * i_{corr} * EW}{\rho_{mat.}} \qquad \text{Eqn. 7-1}$$

where corrosion rate is in mm per year (mmpy), i_{corr} is the current density obtained from the Tafel fitting (μA cm^{-2}), EW is the equivalent weight, and $\rho_{mat.}$ is the density of the material (g cm^{-3}). The Tafel fitting analysis was carried out using the Gamry Echem Analyst software and the relevant parameters were automatically calculated by the software. A typical polarisation curve for the as-received AM 316L SS is shown in Fig. 7-4. The curve is divided into two regions; cathodic (bottom half – right to left) and anodic (top half – left to right), which is further divided into three distinct points; A, B, and C [546]. The first region (B to A) shows the dissolution of Fe to Fe^{2+} accompanied by a rapid decrease in current density, i_{corr} within a small range of increasing potential. Secondly, from A to C, the dissolution of the as-received AM 316L SS is kinetically limited with a gradual increase of current density, i_{corr} with potential. This region displays a 'passive-like' behaviour indicating the formation of a passive, protective oxide layer that tries to reduce the tendency of corrosion attack by limiting current flow into the disk. However, beyond C, the current density, i_{corr} often increases rapidly due to the breakage of the passive oxide film. This phenomenon is termed pitting corrosion, where small 'pits' begin to form on the surface of the disks at a critical value commonly known as pitting potential, E_{pit} [540].

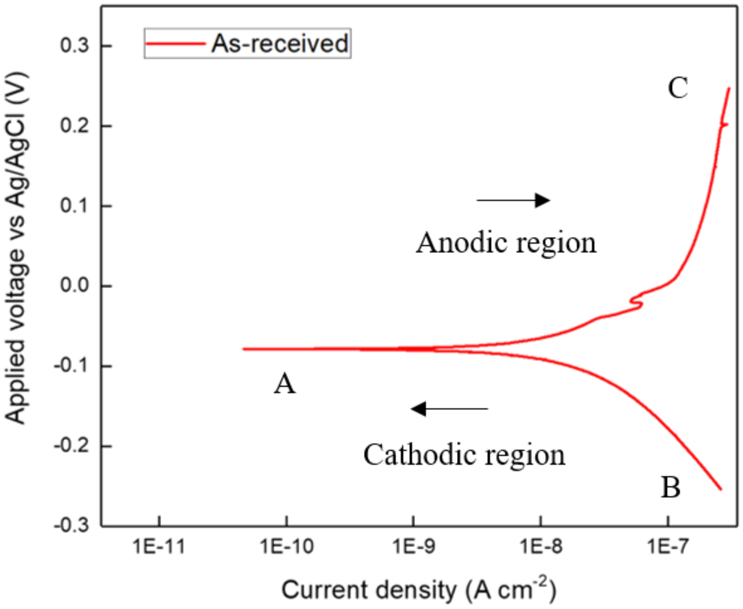

Fig. 7-4 Polarisation curve for as-received AM 316L SS after corrosion test.

Fig. 7-5 compares the potentiodynamic polarisation curves (PPC) of as-received and HPT-processed disks through 1/4, 1/2, 1, 5, and 10 revolutions in the 3.5% NaCl solution at a scan rate of 0.17 mV s^{-1}. The corrosion potential, E_{corr}, corrosion current density, i_{corr} and hence the corrosion rate obtained from Tafel fitting analysis, as well as the pitting potential, E_{pit} are displayed in Table 7-2. Based on Fig. 7-5, the values of i_{corr} for HPT-processed disks are at least one magnitude lower compared to that of the as-received disk. This means that the corrosion resistance of this material could be improved via HPT processing, further confirming the results from the OCP test. Furthermore, the reduction in corrosion rates in this study follows a similar trend of more positive OCP values obtained as the number of HPT revolutions increase from 1/4 to 1, which indicates improvement in corrosion resistance at lower number of revolutions. Both tests indicate that 1 HPT revolution results in the best corrosion performance among all processing conditions.

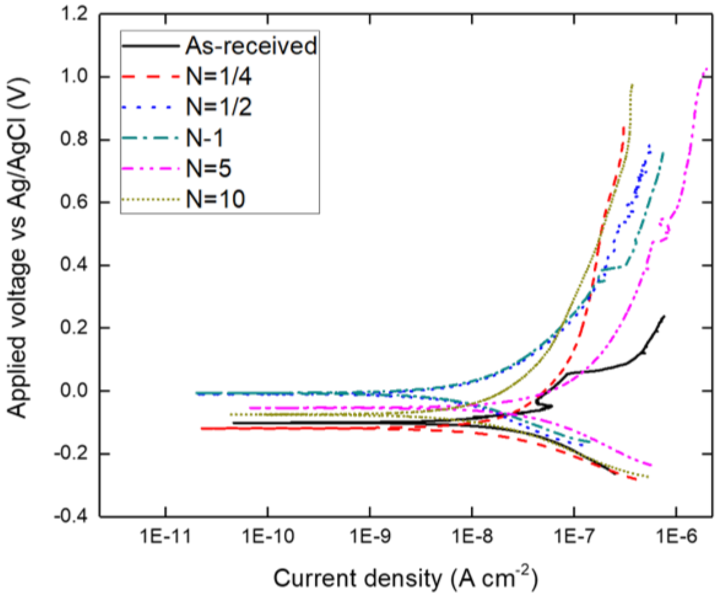

Fig. 7-5 PPC for as-received and HPT-processed disks after corrosion test [374].

Table 7-2 Corrosion performance of as-received and HPT-processed disks in 3.5% NaCl solution [374].

Processing condition	E_{corr} (mV)	i_{corr} (μA cm^{-2})	Corrosion rate (μm year^{-1})	E_{pit} (mV)	$E_{pit} - E_{corr}$ (mV)
As-received	-101 ± 6	0.0616 ± 0.0151	2.53 ± 0.62	256 ± 5	357
N = 1/4	-108 ± 5	0.0348 ± 0.0078	1.43 ± 0.32	875 ± 8	983
N = 1/2	-12 ± 7	0.0136 ± 0.0013	0.56 ± 0.05	840 ± 6	852
N = 1	-7 ± 4	0.0069 ± 0.0051	0.41 ± 0.01	773 ± 9	780
N = 5	-53 ± 2	0.0521 ± 0.0107	2.14 ± 0.44	1028 ± 8	1081
N = 10	-74 ± 7	0.0117 ± 0.0005	0.48 ± 0.21	984 ± 8	1058

However, the corrosion rate after 10 HPT revolutions is surprisingly better than that after 5 HPT revolutions and is actually the second lowest among all processing conditions. This result is contrastingly different compared to the OCP value after 10 HPT revolutions, which is worse than after 5 HPT revolutions. On the other hand, E_{pit} values for all HPT-processed disks are far superior than for the as-received disk, which suggest that pitting becomes more difficult to occur due to further grain refinement at higher number of revolutions. Nevertheless, these values do not follow any particular trend, except that the E_{pit} values at 5 and 10 HPT revolutions are significantly large, at least ~13% higher than the highest E_{pit} value among the lower number of revolutions (1/4 to 1) as shown in Table 7-2.

7.2.3 Electrochemical impedance spectroscopy

Despite OCP and potentiodynamic polarisation tests have been widely used to establish the corrosion tendency and to determine the corrosion rates, respectively, the accuracy of results from both tests could be compromised due to possible interference from preceding cathodic reaction on the surface of the disks [547]. Hence, electrochemical impedance spectroscopy (EIS) was used to characterise the electrochemical interface between electrodes and electrolytes (3.5% NaCl solution in this study) as it is a non-destructive and sensitive technique [548]. The properties of an electrochemical interface that are typically obtained by analysing the EIS spectra, e.g. impedance and capacitance could be used to provide further evidences for the mechanism of the corrosion process [548].

Fig. 7-6 displays the Nyquist plot, while Figs. 7-7 and 7-8 show the bode plots of as-received and HPT-processed disks in a 3.5% NaCl solution obtained at OCP, as well as the best fitting curves with an equivalent circuit (EC) model having χ^2 values $< 2.0 \times 10^{-3}$ at frequencies ranging from $10^{-2} – 10^4$ Hz for all EIS experimental data. The EC model (inset of Fig. 7-6) corresponds to two time constants representing two layers of substance in series. It consists of a solution resistance, R_u corresponding to the resistance of the 3.5% NaCl solution, two constant phase elements, CPE_{out} and CPE_{in}, and two charge transfer resistances, R_{out} and R_{in}. The first time constant corresponds to the parallel combination between R_{in} and CPE_{in} across the inner protective oxide film, while the second time constant is attributed to a parallel combination of R_{out} and CPE_{out} in the porous layer or defects on the outer surface of the disks.

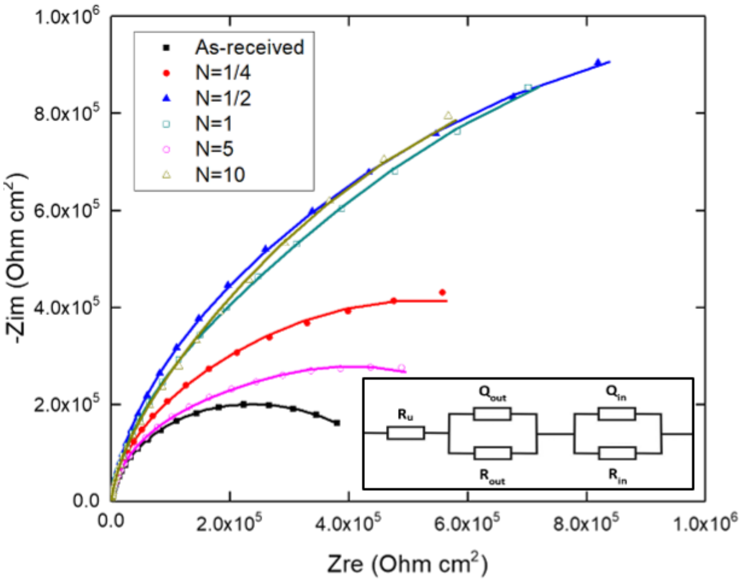

Fig. 7-6 Nyquist plot for as-received and HPT-processed disks after EIS test [374].

In the Nyquist plot (Fig. 7-6), the imaginary impedance, Z_{im} is displayed as a function of real impedance, Z_{re}. Each curve represents a semi-circle, in which a large radius corresponds to a high corrosion resistance. It is clear that the HPT processing generally improves the corrosion resistance of AM 316L SS as indicated by the larger curve radii compared to that of the as-received disks. In addition, disks processed through 1/2, 1 and 10 HPT revolutions have superior curve radii as well as remarkable impedance values, and hence excellent corrosion resistances compared to other processing conditions. This observation is consistent with that of the potentiodynamic polarisation curves shown in Fig. 7-5 and hence confirms the results from both tests. The bode plot in Fig. 7-7(a) shows the impedance modulus, Z_{mod} as a function of frequency, F. Here, the polarisation resistance of the disks in the electrolyte, R_p (sum of R_{out} and R_{in}) is expressed in a low frequency limit ($F < 1$ Hz), R_u is expressed in a high frequency limit ($F > 1$ kHz), while CPE_{out} and CPE_{in} are expressed in the middle frequency (1 Hz < F < 1 kHz) [549]. It is clear that in the high frequency region, the impedance values, i.e. R_u are not influenced by the frequency. Meanwhile, in the low frequency region, disks processed through 1/2, 1 and 10 revolutions have relatively higher impedance values compared to other processing conditions (Fig. 7-7(b)), similar to the results obtained from the Nyquist plot. On the other hand, the middle frequency region shows a linear dependence between log Z_{mod} and log F.

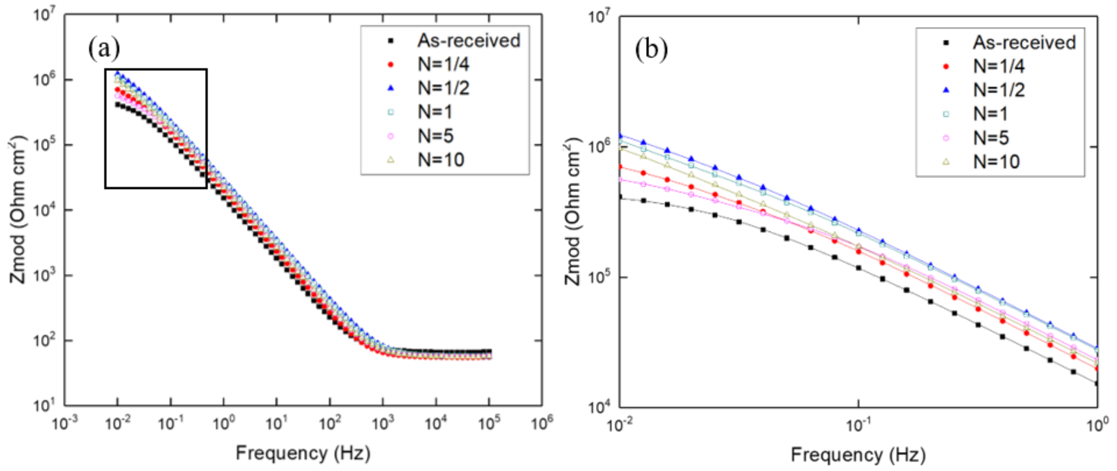

Fig. 7-7 (a) Bode amplitude vs. frequency plot for as-received and HPT-processed disks after EIS test, and (b) magnified view for the low frequency region [374].

Based on the bode plot of phase angle, ϕ vs frequency, F (Fig. 7-8(a)), it could be observed that the phase angles in the middle frequency region for all processing conditions lie very closely to each other, with only a small variation between -82° to -85°. This indicates that the protective oxide layer formed primarily show a capacitive behaviour [550,551].

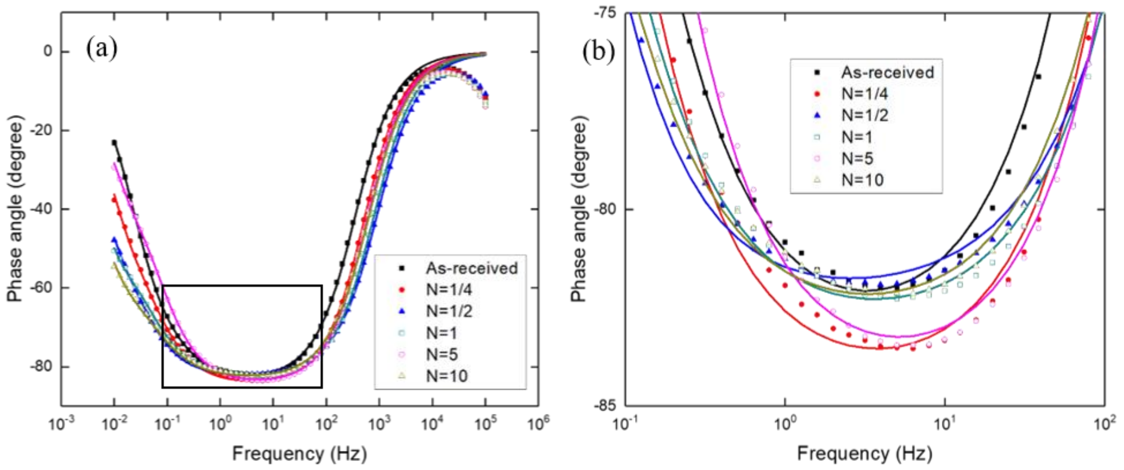

Fig. 7-8 (a) Bode phase angle vs. frequency plot for as-received and HPT-processed disks after EIS test, and (b) magnified view for the middle frequency region of phase angle plot [374].

However, all HPT-processed disks have relatively flatter peaks compared to the as-received counterpart with the ϕ values extending near to 1 Hz (Fig. 7-8(b)). This suggests that in general, the capacitive behaviour of the HPT-processed disks could be observed over a wider range of frequency, and that their protective oxide layers remain intact over a longer period of time compared to the as-received counterpart [552]. However, when compared among the HPT-processed disks, those processed through 1/4 and 5 revolutions have worse capacitive behaviour as they possess lesser flat peaks compared to disks processed through other number of revolutions.

On the other hand, CPE is essentially an element of capacitance, but it is used instead of a pure capacitance to address the non-ideal capacitive response due to surface inhomogeneity as a result of surface roughness, impurities and grain boundaries [553–555]. The CPE impedance, Z_{CPE} is defined by [548]:

$$Z_{CPE} = [Y(j\omega)^{\alpha_{CPE}}]^{-1} \qquad \text{Eqn. 8-2}$$

where Y is the admittance, defined by the ease of alternating current (AC) flow into the circuit having dimensions of Ω^{-1} cm^{-2} s^{α}, j is an imaginary number, ω is the angular frequency, and α_{CPE} is an exponential of the CPE determined empirically with values of $-1 \le \alpha_{\mathrm{CPE}} \le 1$. The term α is related to the non-uniform current distribution due to the surface condition of the disks, e.g. roughness, defects and pores. The CPE could represent a circuit parameter behaving as an ideal capacitor when $\alpha_{\mathrm{CPE}} = 1$, a resistor when $\alpha_{\mathrm{CPE}} = 0$, and an inductor when $\alpha_{\mathrm{CPE}} = -1$ [548]. Furthermore, the total impedance or polarisation resistance, R_{p} representing the overall corrosion resistance of the material in this case is obtained by adding R_{in} and R_{out}. The respective values obtained from this EC model simulation are summarised in Table 7-3.

Table 7-3 Parameters of EC obtained from simulation based on the EIS experiment data [374].

Processing condition	R_{u} **(Ω cm²)**	R_{in} **(kΩ cm²)**	R_{out} **(kΩ cm²)**	R_{p} **(kΩ cm²)**	Y_{in} **(10^{-4} Ω^{-1} cm^{-2} s^{α})**	α_{in}	Y_{out} **(10^{-4} Ω^{-1} cm^{-2} s^{α})**	α_{out}
As-received	66.7±0.1	454±23	7±4	461±5	0.13±0.07	0.92±0.03	1.62±0.22	1.00±0.01
N = 1/4	55±0.1	824±18	155±16	979±1	0.16±0.03	0.93±0.05	0.20±0.04	0.93±0.04
N = 1/2	55.7±0.2	211±15	1860±102	2071±4	0.27±0.04	0.91±0.06	0.09±0.03	0.89±0.06
N = 1	58.4±0.1	160±17	2220±115	2380±7	1.12±0.04	0.91±0.03	0.15±0.02	0.97±0.03
N = 5	57.8±0.3	216±20	513±43	729±4	0.11±0.08	0.93±0.04	0.23±0.05	0.94±0.05
N = 10	56.1±0.1	351±22	1970±125	2330±9	0.17±0.02	0.93±0.02	0.16±0.03	0.98±0.02

It could be observed that the polarisation resistance, R_{p} values of HPT-processed disks are far superior from that of the as-received counterpart, with a remarkable increase from 461 kΩ cm^2 in the as-received condition to 979 kΩ cm^2 after only 1/4 HPT revolution, representing about 100% increase in total impedance. This increasing trend continues until 1 HPT revolution, before a sharp decline observed after 5 revolutions and a dramatic improvement after 10 HPT revolutions. Since high R_{p} values correspond to exceptional corrosion resistance, the trend observed from this EIS spectra analysis is similar to that observed in the OCP and potentiodynamic polarisation tests. Furthermore, after 1/4 HPT revolution, the value of R_{in} is higher than R_{out}, which suggests that the enhancement in corrosion resistance largely contributed by R_{in}. However, as the number of revolutions increase, the corrosion resistance improvement mainly results from the increase in R_{out} values, as indicated by the consistently higher values of R_{out} compared to the values of R_{in}.

7.2.4 SEM and EDX analysis

To gain further insight on the corrosion behaviour of AM 316L SS processed by HPT, SEM observation and EDX analysis were conducted for the as-received and HPT-processed disks. Fig. 7-9 shows the surface morphology of the as-received disk before and after undergoing corrosion process, while the chemical composition at selected areas as obtained from EDX analysis is displayed in Table 7-4.

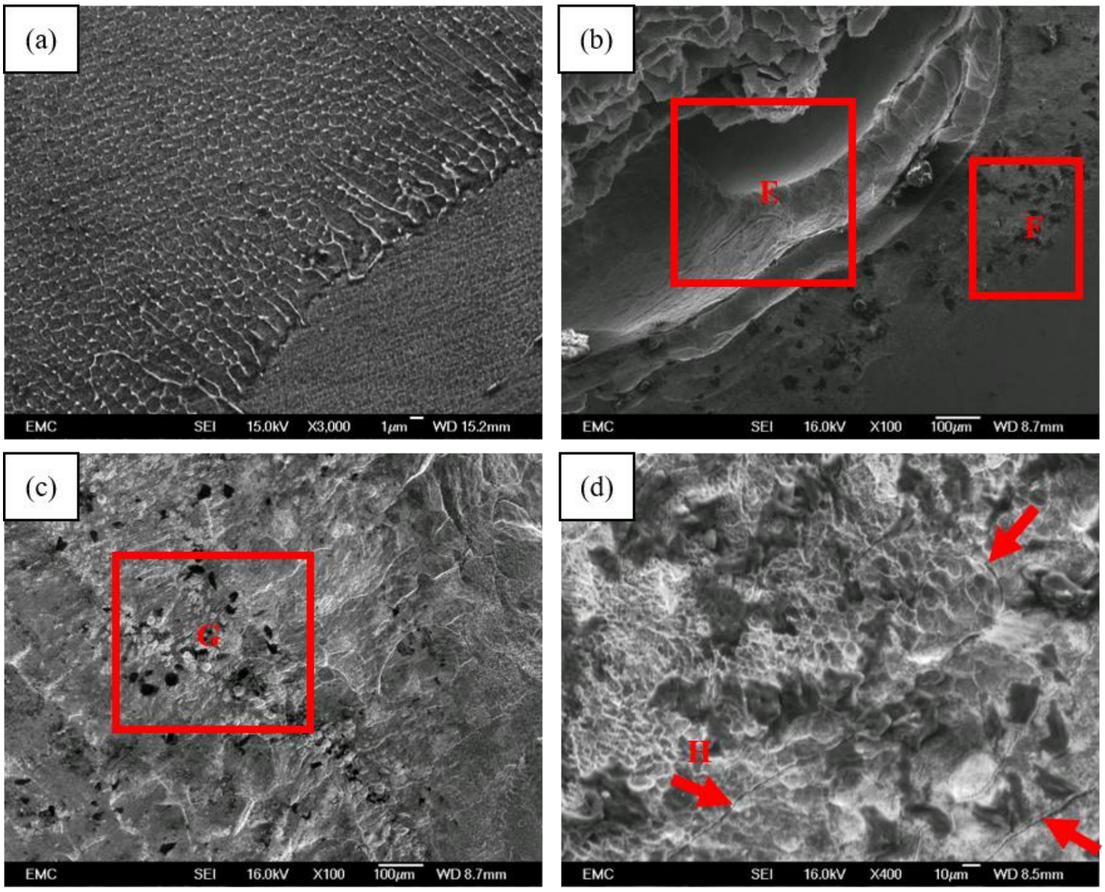

Fig. 7-9 Surface morphology of the as-received disk (a) before, and (b) – (d) after corrosion test [374].

Table 7-4 Chemical composition of marked areas in Fig. 7-9 in wt. % [374].

Area	Cr	Ni	Mo	Mn	Si	S	O	Cl	Fe
E	7.84	10.31	0.67	1.02	-	-	23.72	4.53	51.91
F	12.25	10.67	1.68	3.12	-	1.44	4.05	-	66.79
G	11.23	14.38	1.12	-	10.71	-	26.33	-	50.61
H	16.55	13.07	2.65	2.04	-	-	8.53	1.14	56.02

A large and deep crevice could be seen to form at the periphery of the test region (Fig. 7-9 (b)), with EDX analysis (Table 7-4) revealing the presence of Cl with a big reduction in Cr at the crevice (area E). These suggest that the initially protective Cr_2O_3 passive layer is eventually destroyed due to the increasing attack by the Cl^- ions from the electrolyte and could not re-passivate due to the lack of oxygen [415,552]. As a result, a deep crevice is formed at the periphery of the test area. Severely corroded pits could also be observed near the crevices, suggesting that the growth of pits begin from and scatter around the crevice area (area F). The increasing amount of Mn and the emergence of S near the pits (area F) as shown in Table 7-4 indicate the presence of MnS inclusions which becomes one of the nucleation sites for the pits.

Moreover, surface defects such as pores could also be the locations for corrosion to occur as observed in Fig. 7-9(c), e.g. area G. Such pores, which are typically present in as-received disk suffer from high metal dissolution after being exposed to the electrolyte. This is because the pores provide an easy pathway for anolyte diffusion, hence accelerating the dissolution of metal compared to other areas [556]. The presence of Si and O indicates the presence of Si-rich oxides on the surface of the pores, while Ni segregates to the pore area. Upon higher magnification, corrosion attacks could be observed along the melt pool boundaries (MPBs) as indicated by the arrows in Fig. 7-9(d). This is an interesting observation as corrosion attack normally occurs along the grain boundaries, i.e. intergranular corrosion (IGC), but here the grain boundaries are poorly defined due to the fine and heterogeneous microstructure distribution as a result of metal AM processing. In this case, the melt pool boundary becomes an active site for corrosion attack instead of the actual grain boundary. Hence, this type of corrosion could not be classified as IGC, but more precisely speaking, attack along the MPBs instead. Results from the EDX showed slight segregation of Ni into and the presence of Cl along the attacked melt pool boundary (area H) as indicated in Table 7-4.

The surface morphologies of corroded HPT-processed disks through 1/4, 1/2, and 1 revolutions are shown in Fig. 7-10, while that for 5 and 10 revolutions are shown in Fig. 7-11. In addition, the elemental composition at selected areas are shown in Table 7-5. Crevice and pitting corrosion are common for all HPT-processed disks, but the crevices are smaller and less deep compared to that of the as-received disk (Figs. 7-10(a), (c), and (e), and Figs. 7-11(a) and (c)). Similarly, less pits are observed for the HPT-processed disks as the number of revolutions increase (red arrows). Moreover, the increase in Cr content accompanied by reduction in Fe as the number of revolutions increase (except for 5 HPT revolutions) indicates more uniform oxide layers are formed. In addition, corrosion attack along the MPBs is also a common corrosion mechanism for the disks up until 1 HPT revolution. Interestingly, the attack worsens as the number of HPT revolutions increase from 1/4 to 1/2 and breakage of the MPB is observed after 1 HPT revolution (Fig. 7-10(b), (d), and (f)). In addition, EDX analysis also revealed an increase in the amount (wt. %) of Mn segregation into the melt pool boundary up until 1 HPT revolution, suggesting that Mn plays a key role in the breakage of the MPB. Nevertheless, the overall corrosion resistance improves up to 1 HPT revolution based on the electrochemical tests, thus suggesting that the breakage of melt pool boundary did not significantly influence the corrosion performance compared to the crevices and pits. The significantly higher wt. % of Cr than Mn (Table 7-5) suggests that the formation of passive Cr_2O_3 layer outweighs the negative effect of corrosion attack at the MPB.

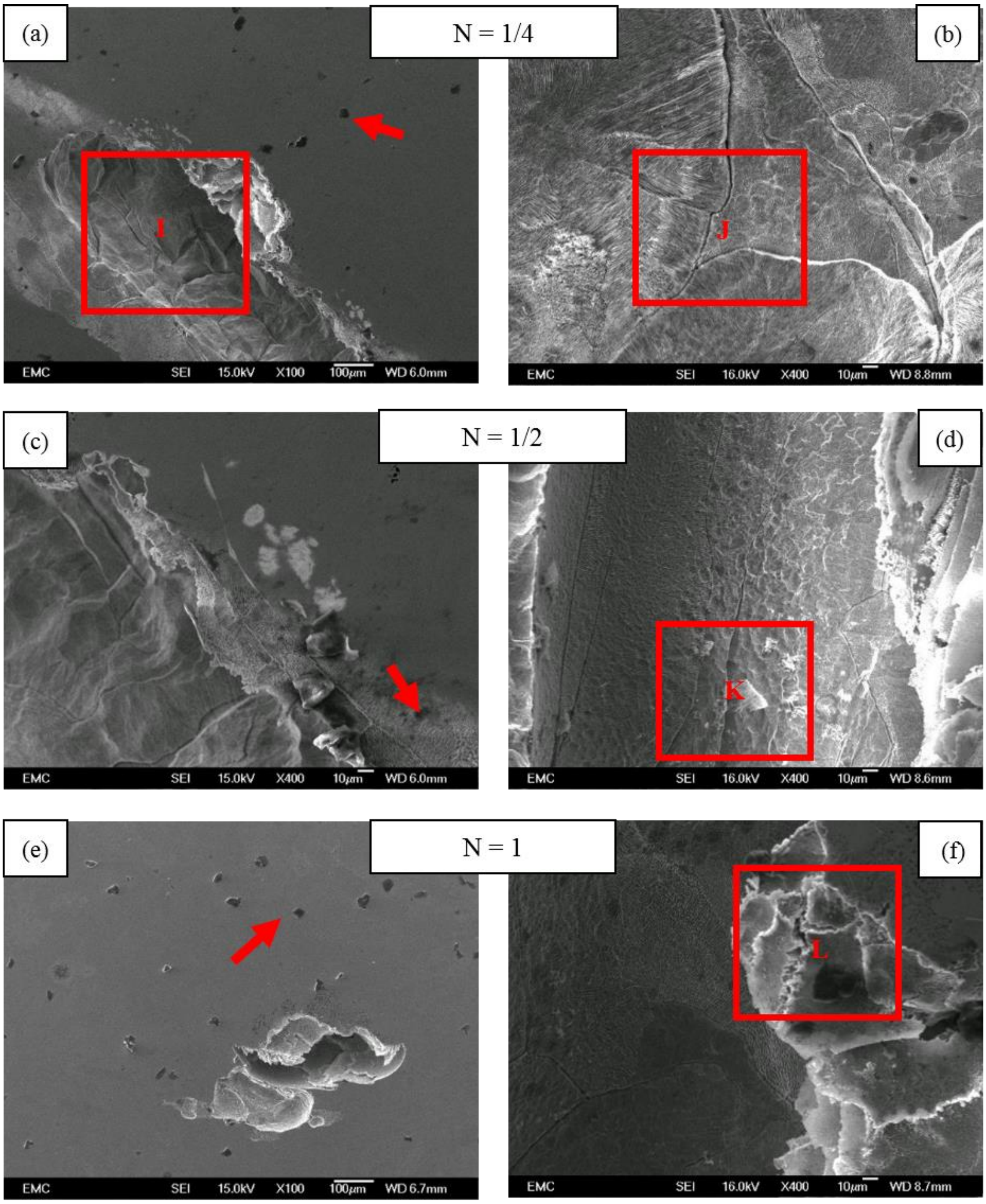

Fig 7-10. Surface morphology of corroded disks after 1/4, 1/2, and 1 HPT revolutions [374].

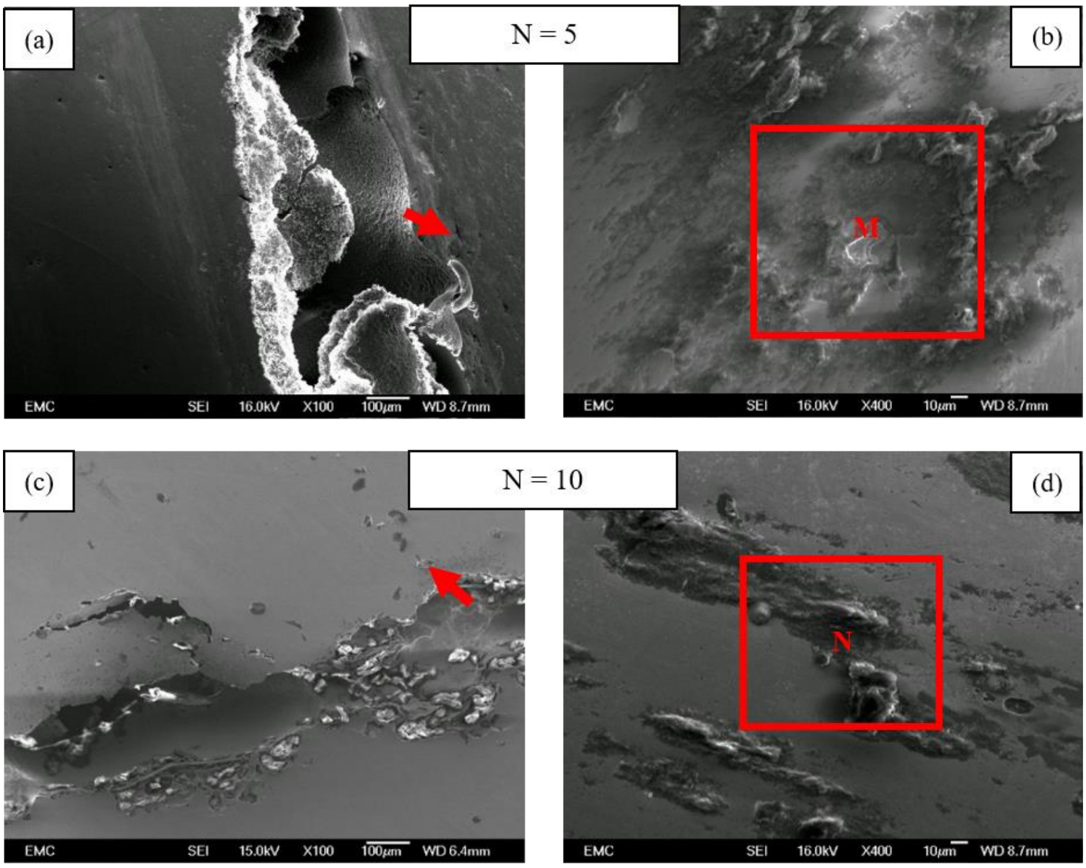

Fig 7-11. Surface morphology of corroded disks after 5 and 10 HPT revolutions [374].

Table 7-5 Chemical composition of marked areas in Figs. 7-10 and 7-11 in wt. % [374].

Area	Cr	Mo	Mn	O	Fe
I	15.05	-	-	29.36	55.59
J	16.25	2.61	1.44	36.42	43.28
K	16.89	2.39	1.57	41.58	36.15
L	18.27	2.23	2.04	50.70	26.76
M	14.92	2.61	1.48	49.96	31.03
N	16.77	2.65	1.45	51.26	27.87

The breakage of, or attack along the melt pool boundary observed at higher magnification no longer occur after 5 and 10 HPT revolutions, most probably due to the extreme grain refinement at this stage. Hence, crevice and pitting corrosion are the main corrosion mechanisms at higher number of revolutions. After 5 HPT revolutions, crevices begin to form again and are even larger and deeper compared to other HPT-processed disks (Fig. 7-11(b)). This might be the reason that disks processed through 5 HPT revolutions show the worst corrosion resistance compared to other number of HPT revolutions, despite still being better than the as-received disk.

EDX analysis also indicates higher formation of Fe-based oxides due to the larger wt. % of Fe after 5 HPT revolutions compared to after 1 and 10 HPT revolutions. However, the size and depth of these crevices decrease after 10 revolutions (Fig. 7-11(d)). Nevertheless, the amount and size of pits in both cases are much smaller compared to the as-received and HPT-processed disks processed at lower number of revolutions (1/4, 1/2, and 1) as indicated by the red arrows. These suggest higher pitting resistance that could possibly explain the superior E_{pit} values for disks processed through 5 and 10 HPT revolutions as determined from the potentiodynamic polarisation test detailed in Table 7-2.

7.3 Discussion

7.3.1 Effects of defects on corrosion resistance

Despite having excellent corrosion resistance, 316L SS could still suffer from localised crevice and pitting corrosion, particularly in the presence of halide ions, e.g. Cl^- ions [552]. Moreover, surface defects such as pores, cracks and surface roughness are found to influence the corrosion behaviour of metallic structures [415]. The as-received disk in this study are free from non-spherical pores due to optimum processing parameters and machined to obtain a good surface finish. Various studies have reported poorer corrosion resistance in AM 316L SS compared to the CM counterpart independent of electrolyte environment due to the presence of pores in the solidified structure [6,415,543]. For example, Sun et al. [6] studied the corrosion and sliding wear behaviour of AM 316L SS in 0.9% NaCl solution. They observed preferential corrosion attack at the pre-existing pores due to the increasing aggressiveness of anolytes in the pores, resulting in breakdown in passivity and accelerated dissolution of metals. Geenen et al. [415] found that corrosion attack on pores continues through the crevices, and in addition with cracks and oxides, further worsen the corrosion resistance of AM 316L SS in H_2SO_4 electrolyte.

In this study, appreciable porosity level is only obvious in the as-received disk. Even though the porosity content seems to be small (0.679 ± 0.051%), their uneven distribution throughout the disk significantly impacts the current density, corrosion rate and hence the corrosion performance of the as-received AM 316L SS. The mechanism in which porosity becomes the onset of corrosion mechanism could be described as follow and illustrated in Fig. 7-12 [557,558]. Initially, there exists a stable passive oxide layer on the surface of the material and on the surface of the pores (Fig. 7-12(a)). However, corrosion attack begins after the disks are immersed into the 3.5% NaCl electrolyte and causes the dissolution of the passive layer, before continuing towards the inside of the pores (Fig. 7-12(b)). Then, this attack reaches the inside of the pores through the crevices formed due to the active-passive cells formed between the insides of the pores and the interface of the material (Fig. 7-12(c)). Finally, the material disintegrates as shown in Fig. 7-12(d)). The disintegration of metal is confirmed by the EDX analysis (Table 7-5), in which a substantial decrease in Fe and Cr is observed at the pore area (Fig. 7-9(c)), accompanied by an increase in O content. However, the attack on grain boundaries as shown in Fig. 7-12(d) is not observed because of the difficulty to distinguish between the actual grain and cellular structure boundaries due to the complicated microstructures formed in the AM 316L SS.

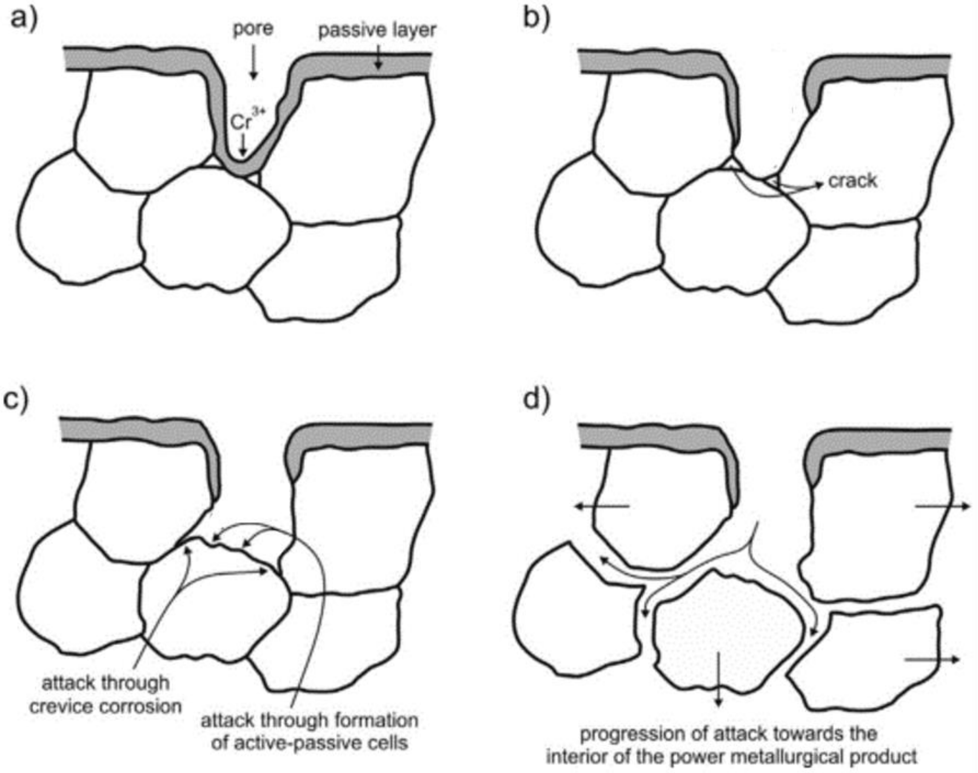

Fig. 7-12 Corrosion mechanism by attack on pores in SS fabricated by powder metallurgy [557,558]. Reproduced with permission of the rights holder.

Apart from pores, the presence of inclusions and oxides are also considered as defects which contribute to pitting corrosion in stainless steel products. Studies have shown MnS inclusions could be nucleating sites for pits inside 316L SS [540,552]. This is because of the increasing Cl^- concentration that preferentially attacks weak points (defects) on the surface of the material until the passive film at the weak points dissolves, forming pit holes [552]. This phenomenon is also found in this study as shown in area F of Fig. 7-9 and Table 7-5, in which a slightly higher amount of Mn and the emergence of Cl are present at the pit area. However, the corroded pits are randomly distributed as the formation of inclusions is a random occurrence [543].

7.3.2 Influence of grain refinement on corrosion performance

The combination of processing temperature, grain size, surface conditions (chemistry and defects), and corrosive media (environment) are found to influence the corrosion performance of 316L SS, hence it is difficult to isolate the effects of individual aspect on the corrosion resistance of the material [229,441]. Various studies have reported mixed results in the influence of grain size and corrosion medium on the corrosion performance of metals and alloys [547,553,559]. For example, Rifai et al. [560] observed an improvement in pitting potential and hence the pitting resistance when UFG Fe-20%Cr steel was produced via ECAP and exposed to 1000 mol m^{-3} NaCl solution. However, Nie et al. [548] observed a worse corrosion resistance in HPT-processed commercially pure Ti exposed to 3.5% NaCl solution after further grain refinements at higher HPT revolutions.

Hence, it is difficult to generalise the relationship between grain size and corrosion performance. However, a review by Ralston and Birbilis attempted to address this issue [228]. They suggested that, in general, the increase or decrease of corrosion resistance in a material due to grain refinement is dependent on the ability of the environment (corrosive media) to passivate. The corrosion resistance of a material is said to decrease with grain refinement in active (non-passivating) media, e.g. HCl and H_2SO_4 solutions. Conversely, grain refinement would improve the corrosion resistance of a material when it is exposed to passive media, e.g. NaOH and NaCl solutions. However, in environments promoting active-passive response, grain refinement would accelerate uniform corrosion but reduces the susceptibility to localised corrosion.

Based on the results of electrochemical tests and TEM observations in this study, the inverse square root of the average grain size is plotted against current density, i_{corr} to determine the influence of extreme grain refinement on the corrosion performance of HPT-processed AM 316L SS (Fig. 7-13). An inverse Hall-Petch type of relationship could be observed, similar to that obtained by Birbilis et al. [561] who investigated the influence of grain refinement attained via ECAP on the corrosion performance of pure Mg in 0.1M NaCl environment. They explained that the improvement of corrosion resistance with grain refinement is attributed to a more compact protective $Mg(OH)_2$ and MgO layer formed on the base metal.

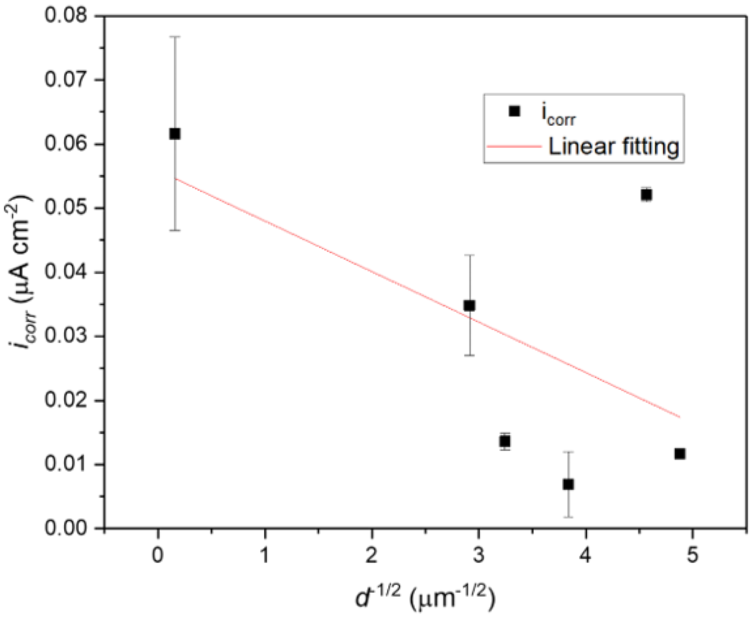

Fig. 7-13 Inverse square root of grain size vs. i_{corr} plot for the as-received and HPT-processed disks in this study.

Another study by Ralston et al. [562] found that this type of Hall-Petch relationship is related to the influence of grain boundary length on its reactivity and conductivity. They hypothesised that higher grain boundary lengths (which depend on $d^{-1/2}$) would cause higher conductivity and reactivity, which translate to larger current densities and hence worse corrosion rates. They further explained that inverse Hall-Petch relationship for grain size and current density, such as obtained in this study, is typical for materials exposed to passivating environments.

The main mechanism of corrosion resistance improvement due to grain refinement in passivating environments is attributed to the enhanced formation and adhesion of passive films on the base metal as a result of increasing grain boundary density [228]. However, peculiarly, the corrosion performance worsen after 5 HPT revolutions before improving after 10 HPT revolutions, as indicated by the highest i_{corr} value among all processing conditions despite the nano-scale grains attained. Overall, HPT processing has improved the corrosion resistance of AM 316L SS. The best corrosion resistance as indicated by the corrosion rate calculations in Table 7-3 is obtained after 1 revolution (-0.41 ± 0.01 μm year^{-1}), followed closely by 10 HPT revolutions (-0.48 ± 0.21 μm year^{-1}). Despite 5 revolutions of HPT producing the worst corrosion rate among HPT-processed disk (-2.14 ± 0.44 μm year^{-1}), it is still better than that of the as-received counterpart (-2.53 ± 0.62 μm year^{-1}).

These results are confusing because the corrosion resistance should continuously improve with further grain refinement as the result of continuous torsional straining as predicted by Ralston and Birbilis [228]. The increasing density of the grain boundaries due to the UFG and NG microstructures obtained with increasing number of revolutions should enhance the formation and adhesion of passive oxide films, but this is not observed after 5 HPT revolutions. It is not possible to attribute this negative performance to pitting corrosion as the value of E_{pit} is substantially higher at 5 revolutions compared to the as-received and HPT-processed diaka through lower number of revolutions (1/4, 1/2, and 1). Such high E_{pit} value indicates superior resistance to pitting. Similarly, the poor corrosion rate at 5 revolutions could not be caused by breakage of MPBs as corrosion attack on MPBs is no longer observed after 5 and 10 HPT revolutions. In addition, porosity defects are also eliminated after HPT processing, hence it could not be the cause of reduced corrosion rate at this point.

Therefore, the most likely explanation for the deteriorating corrosion rate after 5 HPT revolutions could be associated with the extent of crevice corrosion observed on the corroded disk. This observation is supported by EDX analysis shown in Table 7-5, in which the Cr content in the crevice is found to be the lowest among all HPT-processed disks. This indicates limited formation of passive Cr_2O_3 layer which promotes corrosion attack by aggressive Cl^- ions [552]. However, the limitation of passive Cr_2O_3 layer formation HPT 5 HPT revolutions could not be attributed to the extreme grain refinement alone because the higher grain boundary density obtained should in fact further encourage the formation of the passive oxide layer.

Hence, this dichotomy could be explained by considering the grain size distribution throughout the fabricated material instead, and not only in terms of grain refinement, as proposed by Gollapudi et al. [229]. They found an important correlation between the grain size distribution on the corrosion behaviour of materials by using empirical models derived for current density and distribution of grain size. It was explained that in a passivating environment such as 3.5% NaCl solution in this study, a narrower grain size distribution throughout the material yields improved corrosion resistance for grains within a single size regime, e.g. micron grains only or ultrafine grains only, and vice versa. On the other hand, the corrosion performance of materials with bi-modal/gradient microstructures, e.g. a mix of micron and ultrafine grains simultaneously, will be enhanced in a passivating environment if the volume fraction of the ultrafine grains is higher than that of the coarse grains, and vice versa [229].

Indeed, Figs. 5-11 – 5-17 reveal varying grain size distribution with different processing conditions. At lower torsional strain value, $\varepsilon_{eq.\text{-}HPT} = 3.4$ corresponding to 1/4 HPT revolution, coarser elongated micron grains (average: 18 ± 17 µm) and sub-micron grains (UFG microstructures, average: 118 ± 25 nm) are observed at the centre and peripheral regions, respectively. Near-equiaxed UFG microstructures (centre, average: 980 ± 500 nm) and fully equiaxed nano-scale grains (NG microstructures, periphery, average: 68 ± 15 nm) grains are attained at $\varepsilon_{eq.\text{-}HPT} = 13.6$ corresponding to 1 HPT revolution. Up to this point, despite the continuous grain refinement, the HPT-processed disks are still considered to have gradient microstructures with increasing volume fraction of sub-micron and nano-scale grains at higher torsional strain values. These observations confirm the hypothesis of Gollapudi et al. [229] that enhanced corrosion performance in passivating environment could be obtained in bi-modal/gradient grain structures provided that the content of finer grains are more than the coarse grains.

At near-saturation stage, $\varepsilon_{eq.\text{-}HPT} = 68$ corresponding to 5 HPT revolutions, the grain size distribution is in a wide range although they are within the UFG/NG regime at the centre and peripheral disk regions. This is because the UFG microstructures at the centre are in the range of ~ 200 – 600 nm, while the nano-scale grains at the peripheral region are in the range of ~ 30 – 60 nm based on the EBSD and TEM image analysis in Figs. 5-11 – 5-17. Such wide range of grain size distribution throughout the disk could result in the difficulty to form stable and thick passive films required for the corrosion resistance of austenitic SS. This is the most likely explanation for the deteriorating overall corrosion resistance (lowest i_{corr} value) despite the significant increase in pitting resistance (highest E_{pit} value) after 5 HPT revolutions, in accordance with Gollapudi et al. [229]. Nevertheless, the completely equiaxed NG structure with narrow distribution (~ 30 – 50 nm) could justify the improved corrosion performance after 10 HPT revolutions compared to that after 5 HPT revolutions.

7.3.3 Corrosion performance of austenitic SS through various processing routs

Table 7-6 shows the corrosion performance of HPT-processed AM 316L SS in this study and 316L SS and other austenitic SS processed by different techniques obtained from various literature, including conventional processing routes, AM, ball-milling, and SPD techniques as shown in Table 7-6. The current density, i_{corr} parameter is used as the indicator for corrosion resistance, in which lower i_{corr} values correspond to higher corrosion resistance as opposed to lower i_{corr} values. For comparison, grain sizes > 30 µm are classified as coarse-grained (CG), 1 – 30 µm as fine-grained (FG), and < 0.1 µm as UFG or NG.

Two observations could be made from Table 7-6. Firstly, AM fabrication via SLM typically results in FG microstructures, while SPD processing, e.g. ECAP, HPT, and multi-pass cold rolling and high energy ball milling are techniques that could produce UFG and NG microstructures. Secondly, the corrosion resistance of the FG, UFG and NG austenitic stainless steels obtained through SPD and ball-milling is almost always improved, as indicated by the lower i_{corr} values compared to their CG counterparts. Thus, grain refinement could contribute to the improvement of corrosion performance in austenitic SS. However, an exception is observed in the study of cold rolled 301LN SS by Hamada et al. whom found the deterioration in corrosion resistance of 75% CR specimen compared to the initially 25% CR sample [505]. They attributed this phenomenon to the presence of a considerable amount of α'-martensite phase in the heavily CR sample, in which the occurrence of this phase was inferred to decrease the corrosion performance of austenitic SS.

However, mixed results are obtained when evaluating the overall corrosion performance of AM 316L SS. Some studies observed improved corrosion resistance, i.e. lower i_{corr} values [5,563], while other studies attained higher i_{corr} values that indicate worse overall corrosion resistance in AM parts compared to their CM counterparts [6,415,543,564]. Such poor corrosion performance are attributed to the defects obtained in AM materials, e.g. pores, voids, and residual stresses, which results in the difficulty of forming thick and stable passive Cr_2O_3 layers responsible for the corrosion resistance of austenitic SS [415,543]. Nevertheless, despite the varying general corrosion resistance level, the pitting resistance of AM 316L SS is always higher compared to conventionally manufactured (CM) counterparts, as indicated by higher breakdown potential, E_{pit} values [5,415,543,563,564]. Such remarkable resistance to pitting is attributed to the significant reduction in MnS inclusions (known initiators of pitting corrosion) that could inhibit the formation of passive Cr-oxide layers as a result of the high solidification rates in metal AM processing ($10^5 – 10^7$ K s^{-1}) [5,564].

Therefore, if defect-free (pores, cracks, and inclusions) austenitic SS parts could be built via SLM, combined with significant grain refinement down to the UFG and/or NG regime, then structures with far superior corrosion resistance could be attained. These characteristics are precisely achieved by the novel combination of AM and SPD in this study. Firstly, the i_{corr} values for the as-received and HPT-processed disks are always lower than those observed in other studies. This indicates superior corrosion resistance of AM samples that are processed by HPT in a single process sequence. Secondly, no α'-martensite phase could be observed throughout the as-received and HPT-processed disks based on TEM and XRD analysis, indicating a single γ-austenite phase for all conditions. This clearly highlights the advantage of HPT in terms of eliminating pores and achieving extreme grain refinement, thus remarkably improving the corrosion performance of AM 316L SS.

Table 7-6 Corrosion performance of austenitic stainless steels processed through different routes.

Material	Electrolyte	Processing route	Average grain size (μm)	Porosity (%)	i_{corr} (μA cm^{-2})	Reference
316L SS	3.5% NaCl	SLM	40	0.68 ± 0.05	0.0616 ± 0.0151	This study
		SLM + HPT, N=1/4	0.118	0.058 ± 0.01	0.0348 ± 0.0078	
		SLM + HPT, N=1/2	0.095	0	0.0136 ± 0.0013	
		SLM + HPT, N=1	0.068	0	0.0069 ± 0.0051	
		SLM + HPT, N=5	0.048	0	0.0521 ± 0.0107	
		SLM + HPT, N=10	0.042	0	0.0117 ± 0.0005	
	5% H_2SO_4	Casting	39	0	4.9	[415]
		Cast + HIP	266	0	6.5	
		SLM	25	1.1 ± 1.4	6.4	
		SLM (S)	25	2.0 ± 1.0	11.5	
		SLM (S) + HIP	47	4.7 ± 0.5	57.0	
	0.58% Nacl	Wrought		0	0.3 ± 0.15	[543]*
		SLM (1)		0.4	0.45 ± 0.40	
		SLM (2)		< 0.03	0.4 ± 0.15	
	3.5% Nacl	Wrought + quenched	15	0	0.08	[564]
		SLM 800	42		0.09	
		SLM 1083	42		0.12	
		SLM 1200	42		0.15	
		SLM 1400	42		0.73	
	0.6% NaCl	Wrought	~ 12.1		~ 0.1 – 1	[5]
		SLM	~ 8.1		~ 0.01 – 0.1	
		SLM + annealed	> 8.1		< 0.01	
	0.9% NaCl	Wrought		0	0.4	[6]*
		SLM 150		1.8 ± 0.2	0.5	
		SLM 200		6.8 ± 0.7	0.8	
	3.5% NaCl	Wrought			4.16	[563]*
		Wrought + HT			2.69	
		SLM			1.29	
		SLM + HT			1.14	
	3% NaCl	Cold-worked	65		0.34	[565]
		HPT, N=10	0.172		0.19	
	Ringer's solution	Hot-rolled	80		3.12 ± 0.15	[566]
		ECAP 8 passes	0.078		0.42 ± 0.02	
	0.9% NaCl	Wrought	42		6.7	[567]
		Cavitated + annealed	0.091		5.0	
	3.5% NaCl	Multi-pass cold rolled (CR)	0.04		0.075	[568]
301LN	1% NaCl + 0.1% HCl	CR 20%	50		23	[505]
		CR 75%			35	
		CR 75% + annealed	0.6		12	
304L SS	0.5% H_2SO_4	Wrought	50		1.96	[569]
		ECAP 8 passes	0.08-0.12		1.39	
Fe-10%Cr	0.5% H_2SO_4	High-energy ball milled + annealed + compacted + sintered	1.5 ± 0.2 ~ 0.042		0.084 ± 8 0.040 ± 6	[570]

The grain sizes for Refs. marked with * are not stated directly but categorised as FG.

Finally, when compared with AM 316L SS without any post-processing, and with HPT-processed CM stainless steels from various literature, the significant improvement in corrosion performance for AM 316L SS processed by HPT in this study could be ascribed to the elimination of porosity defects, cellular structure refinement, and extreme grain refinement down to the nano-scale region.

7.4 Summary

In this chapter, the corrosion performance of UFG and UG structures in AM 316L SS obtained through HPT processing was evaluated through electrochemical tests in a sequence of open-circuit potential (OCP), electrochemical impedance spectroscopy (EIS), and potentiodynamic polarisation in 3.5% NaCl aqueous solution. The following conclusions can be drawn based on the results of this study:

1. HPT processing enhances the corrosion resistance of AM 316L SS.
2. The corrosion resistance improves with increasing number of revolutions from 1/4 to 1, before deteriorating after 5 revolutions and improving again after 10 revolutions.
3. The superior corrosion performance in HPT-processed AM 316L SS is attributed to the removal of porosity, homogeneous distribution of UFG/NG microstructures, and the absence of martensite phase, all of which result in the formation of thick and stable passive oxide layers.

Chapter 8 Tribological behaviour of AM 316L SS processed by HPT

8.1 Introduction

The importance of tribology in many modern engineering applications cannot be underestimated, particularly for those involving the rubbing or sliding of two materials against each other, e.g. biomedical implants and moving parts in food and beverage (F & B) machineries [571]. Therefore, tribological performance, or more specifically, wear resistance is a crucial criterion in the engineering design stage for applications of 316L SS. So far, research on the tribological properties of 316L SS has involved wear testing at both dry and lubricated conditions. For example, Li et al. [571] studied the influence of build direction, temperature, load, and frequency on the wear properties of AM 316L SS using a ball-on-plate test rig. The following conclusions were made from their study: (i) build-up direction had no impact on wear resistance, (ii) coefficient of friction (COF) decreased at higher test temperatures, with the lowest wear rate obtained at RT, (iii) and higher wear rate was observed at higher loads although the COF was not influenced significantly. In addition, Li et al. [572] also found that there were no significant changes in the COF and wear rate of 316L SS manufactured by SLM when varying the laser power parameter.

Sun et al. [6] studied the influence of laser scan speed on the tribological behaviour of AM 316L SS. They tested samples with porosities ranging from 1.7 to 6.7% and found that all of them had poor sliding wear resistance and suggested that improved wear performance could be achieved for samples with high densification levels. Zhu et al. [573] investigated the tribological properties of AM 316L SS under lubricated condition using a ring-on-disk configuration, and reported improved COF compared to CM 316L SS. Bartolomeu et al. [574] compared the mechanical and wear behaviour of AM 316L SS with cast and hot-pressed 316L SS, and they found that AM 316L SS had the highest yield and tensile strengths and the best wear performance. They concluded that the improved wear resistance in AM 316L SS compared to CM counterparts could be attributed to the higher hardness in the AM material [575].

On the other hand, only a few studies have been conducted on the tribological properties of bulk UFG/NG CM 316L SS produced by SPD processing. For example, Muley et al. [576] assessed the corrosion and wear behaviours of UFG 316L SS obtained by multiaxial forging (MAF) for implant applications. They found that the improved sliding wear resistance was due to the change of abrasive wear mechanism from micro-cutting to wedge-formation as a result of high hardness and much finer grain sizes with increasing MAF strain levels. Nevertheless, there are indeed some studies on the wear performance of surface-nanostructured 316L SS obtained by other techniques. Sami and Mahdi [577] used surface mechanical attrition treatment (SMAT) to produce a nanocrystalline layer on the surface of 316L SS and studied the wear performance using a ball-on-disk tribometer. Improvements in COF and wear resistance were observed in the nanocrystalline layer compared to that of the coarse-grained due to the higher hardness, reduced grain sizes, and martensitic transformation at the SMAT-modified layer. Amanov et al. [578] found remarkable enhancements in COF and wear resistance, together with high yield strength of a nanocrystalline layer on 316L SS obtained by ultrasonic nanocrystalline surface modification (UNSM) treatment, which were attributed to the increased hardness after the treatment. Rezaei-Najad et al. [579] studied the microstructural alteration on the surface of a 316L SS plate using friction stir processing (FSP). Remarkable reductions in COF and wear rate were attained, which were ascribed to the low plastic deformation level at the hardened FSP surface, leading to lower frictions and decreased adhesive and abrasive wear mechanisms.

However, the influence of UFG and NG microstructures obtained by HPT processing on the wear performance of 316L SS fabricated by SLM has not been studied yet. In this study, 316L SS samples were initially additively manufactured by SLM technique and then processed through HPT. The wear performance of the HPT-processed disks were studied and compared with the as-received counterpart. The wear performance was tested via a dry sliding wear approach using a pin-on-disk test configuration. The coefficient of friction (COF) and wear rate parameters were also evaluated quantitatively to assess the wear resistance of the as-received and HPT-processed disks.

8.2 Results

8.2.1 Microhardness of as-received and HPT-processed disks

Fig. 8-1 shows the HV values for the as-received (N = 0) and HPT-processed (N = 1/4, 1, and 10) disks at eight peripheral locations (3 mm from disk centre) corresponding to the wear test area as described in Fig. 3-17, with the associated error bars. The hardness value for the as-received disk is ~ 220 HV and increases significantly to ~ 550 HV at the early stages of HPT torsional strain (N = 1/4). The remarkable hardening at this stage is attributed to both grain refinement and strong strain hardening effect as the result of generation and multiplication of dislocations [429,580–582]. After 1 HPT revolution, the hardness only slightly increases to ~ 590 HV and saturates at ~ 600 HV after 10 HPT revolutions. At these stages, the generation and multiplication of dislocations are not as much as during the initial HPT straining, thus the hardening is now mainly associated with grain refinement at the sub-micron and nano-scales [583,584]. These results are consistent with the HV measurements in Chapter 5. The trend of hardness variation in this study is in agreement with many studies on HPT-processed CM metals and alloys, which reported continuous increment in hardness with increasing equivalent strain at the early stages of HPT, and then saturates to a relatively constant value above certain strain values [580,582,585].

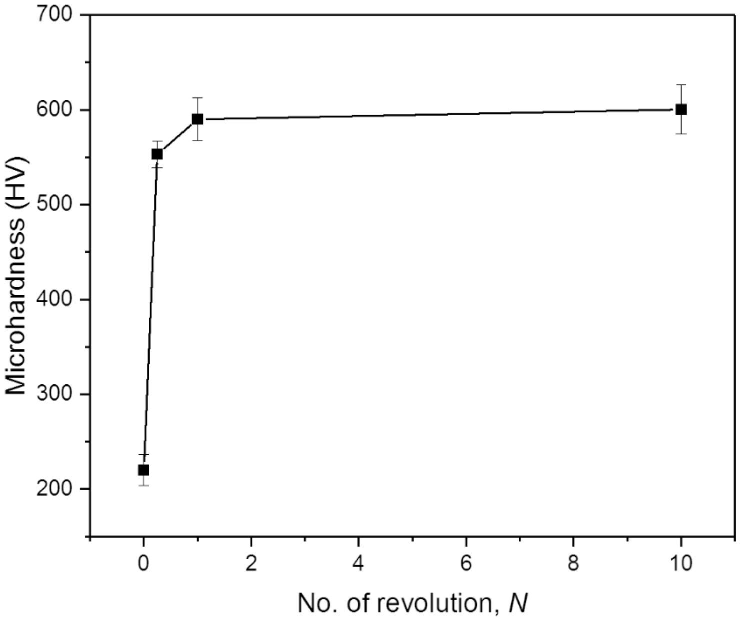

Fig. 8-1 Microhardness of as-received and HPT-processed disks taken averaged at 8 different locations 3 mm from the centre of the disks following the description in Chapter 3.

8.2.2 Wear properties

Fig. 8-2 displays the average COF and mass loss, m_{loss} as a function of the number of HPT revolutions, N after wear testing at a constant load, L_W = 5 N for a total sliding distance, S_W = 20 m. The wear test in this study was conducted with a reciprocating frequency of 1 Hz and continued for ~ 2000 s, thus the COF was recorded for a total of 2000 test points at 1 point per second. It is clear that HPT processing influences the measured COF values under the loading condition, with a continuous decrease from ~ 0.58 for the as-received disk to ~ 0.43 after 10 revolutions, representing a ~ 26% reduction. Similarly, a 57% reduction in the mass loss is also observed with increasing HPT revolutions, from 26 ± 1 mg for the as-received condition to 11 ± 2 mg after 10 revolutions. It is reasonable to anticipate a reduced mass loss as the result of higher hardness in HPT-processed disks compared to the as-received counterpart. This is in line with Archard's equation, in which the volume removed from the disks after wear testing, V (mass x density) is inversely proportional to the hardness, H_{mat} of that material, i.e. $V \propto 1/ H_{\text{mat}}$ [586].

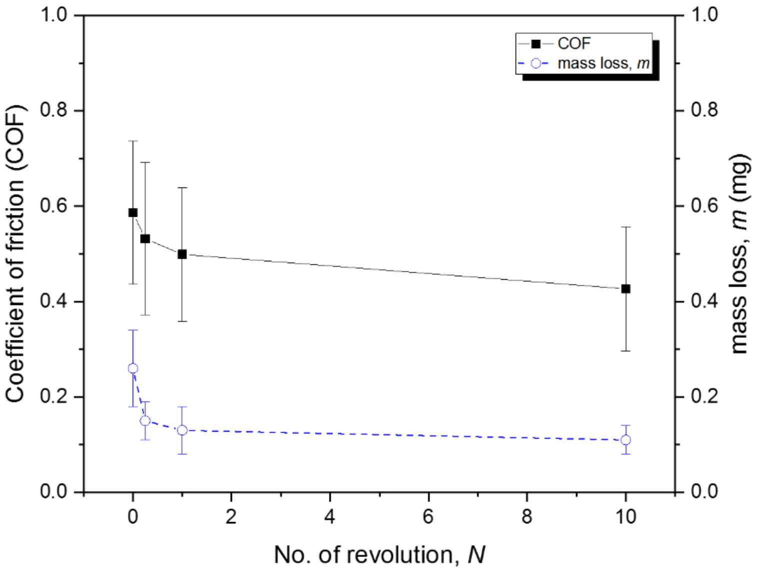

Fig. 8-2 Coefficient of friction (COF) and mass loss, m_{loss} for as-received and HPT-processed disks after wear test.

Fig. 8-3 shows the evolution of wear scar topography for the as-received and HPT-processed disks. These colour-coded two-dimensional (2D) visualisations were generated using the TAICAAN XYRIS 2000 TL/CL metrology system to illustrate and compare the depth along the wear scar for all processing conditions. After repeated sliding of the alumina ball on the wear track, the wear scar profiles evaluated using the surface profilometers indicate that the wear scar in the as-received disk is much deeper than that of the HPT-processed disks and it steadily decreases with increasing number of HPT revolutions (Fig. 8-3). It is also evident that the depth of the wear scar for the HPT-processed disks decreases from the edge to the middle of the scar with increasing number of HPT revolutions (Figs. 8-3(b) – (d)), represented by the colour change from purple (deepest) to red (shallowest). It should be noted that the scale of the colour bars representing the wear track depth is different for the as-received (-12 – 12 μm) and HPT-processed disks (-6 – 2 μm). Such difference in wear depth between as-received and HPT-processed disks could be attributed to the hardness variation. Since the as-received disk is relatively softer, i.e. more ductile, its surface can be easily deformed by the sliding action of the counter surface (alumina ball), thus allowing it to be penetrated deeper into the material. On the other hand, the HPT-processed disks are harder, thus they are more difficult to be penetrated by the alumina ball. Therefore, only a small area of the surface could be deformed and some of the pressed surface are pushed towards the sides of the wear scar. As the hardness increases with higher number of HPT revolutions, more pressed surfaces are pushed sideways, resulting in the higher surfaces at the edges and much shallower wear scar depth (Figs. 8-3(b) – (d)). These observations are consistent with the shallower wear track depth on nano-grained surface layers of 316L SS obtained by various surface modification techniques [577–579], and in bulk commercially-pure Ti having sub-micron grains after undergoing ECAP processing [587].

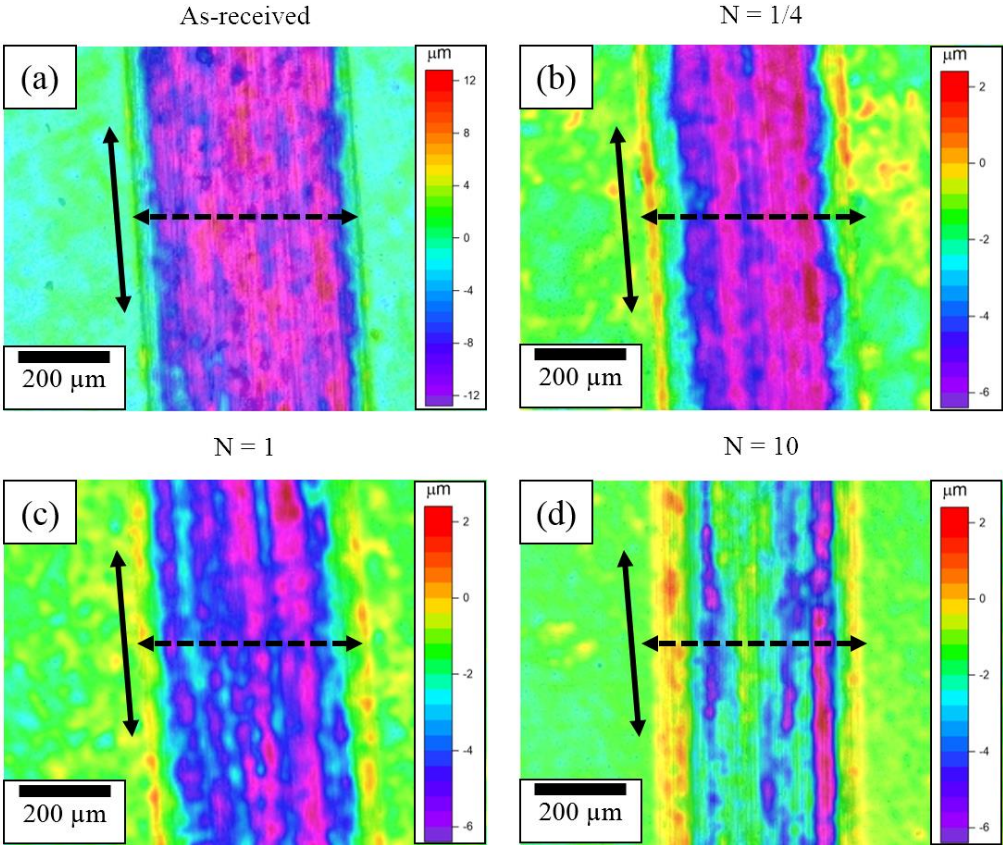

Fig. 8-3 2D analysis of the overall wear track depth of as-received and HPT-processed disk after wear test. Solid line shows sliding direction, dashed line show wear track width.

Fig. 8-4 demonstrates the averaged depth profile of the cross-sectional wear scar, taken from five randomly chosen lines along the wear scar for each processing condition and then evaluated using the Alicona IFM system. The dashed line across the 0 μm represents the boundary between wear grooves (inward curves towards more negative values) and wear ridges (outward curves towards more positive values). In general, a similar trend as Fig. 8-3 is observed; the wear scar depths (grooves) become progressively shallower with increasing number of HPT revolutions compared to the as-received disk. Within the HPT-processed disks, the groove after 1 HPT revolution is much shallower compared to that after 1/4 revolution, but only decreases slightly after 10 HPT revolutions. In addition, some ridges are also formed at the edges of the wear scar, with the as-received disk having the largest amount compared to the HPT-processed disks as indicated by the highest peak and coverage area of the curve above the dashed line. The formation of ridges indicates the pile-up of material at the edges of the wear scar due to plastic deformation as the alumina ball slides along the wear track, commonly known as ploughing [588]. However, the ploughing effect is less pronounced for the HPT-processed disks compared to the as-received disk, as indicated by the lower ridge peaks. These observations could be correlated to the fact that the hardness of the disk after saturation (10 HPT revolutions) is close to that after 1 HPT revolution, thus it becomes increasingly difficult to deform the disks [585,589].

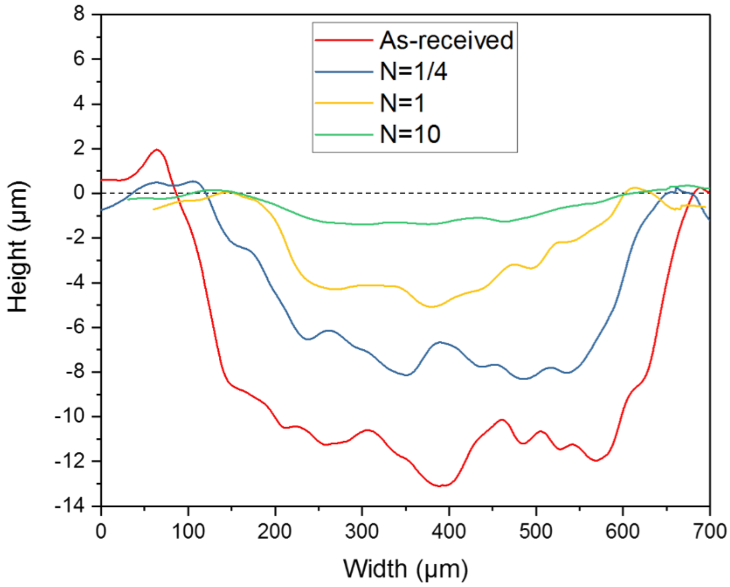

Fig. 8-4 Average wear depth taken from five different locations along the wear track measured using the surface profilometers. Dashed line indicates the original disk surface.

8.2.3 Worn surface morphologies

SEM observations and EDX analysis were conducted to further understand the wear behaviour and characteristics for the as-received and HPT-processed disks after wear test. SEM images in Fig. 8-5 show the evolution of surface morphology of the worn track before and after HPT processing through 1/4, 1, and 10 revolutions, in which the double-arrow line indicates the sliding direction. The images consist of individual wear tracks taken at the centre and edge that are stitched together carefully to form a single continuous image for each processing condition. All disks exhibit sliding grooves parallel to the sliding direction, which are indicative of abrasive wear for the as-received and HPT-processed disks [590,591]. The abrasive grooves appear deep, rough, and are closely spaced for the as-received disk (Fig. 8-5(a)). However, as the hardness increase with increasing HPT straining, the sliding grooves becomes progressively shallower, smoother, and more widely spaced (Figs. 8-5(b) – (d)) and the average COF values also gradually decrease (Fig. 8-2).

Furthermore, it is apparent that the characteristics of abrasive wear differ between the as-received and HPT-processed disks based on the surface morphology of the worn disks shown in Fig. 8-5. As can be observed for the as-received disk (Fig. 8-5(a)), some material on the surface of the softer 316L SS are pushed sideway and form ridges along the sides of the groove. This confirms the occurrence of ploughing as shown in Fig. 8-3. However, ploughing does not occur in the HPT-processed disks. Instead, the harder counter surface (alumina ball) now removes and pushes some material on the relatively harder 316L SS surface from the centre towards the end of the wear tracks, which increase with the number of HPT revolutions (Figs. 8-5(b) – (d)). This phenomenon is called wedge formation or shear-tongue formation, another mode of abrasive wear [592].

(a) As-received

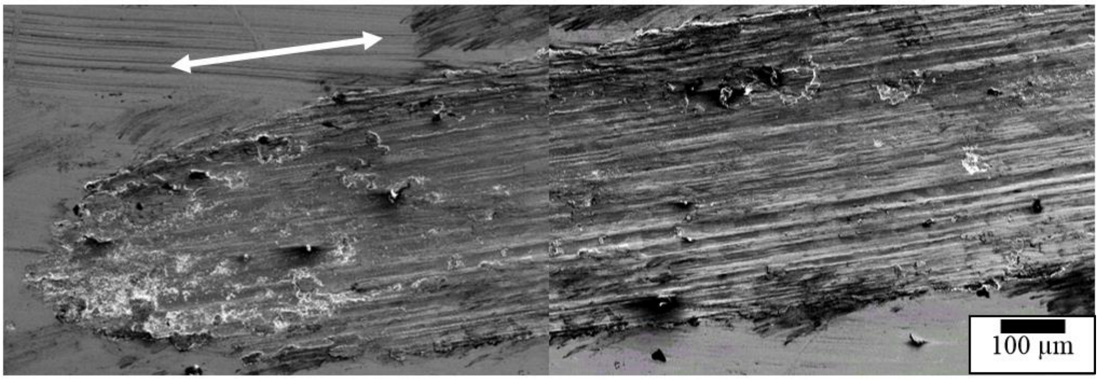

(b) N = 1/4

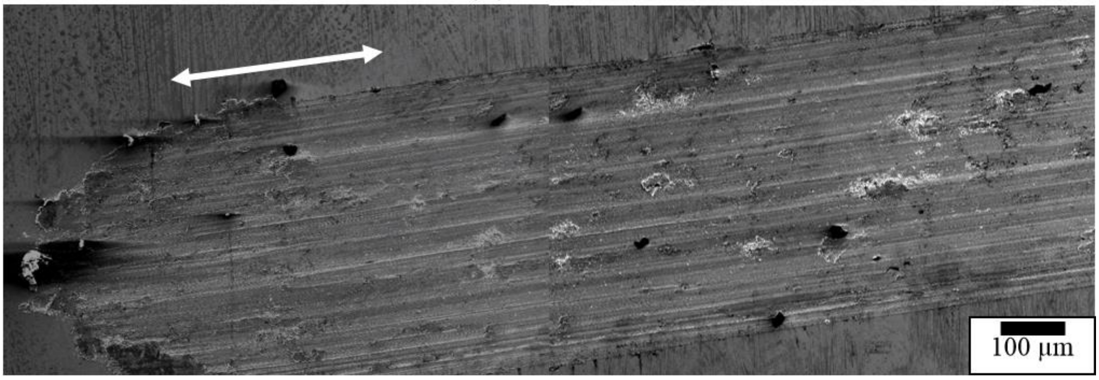

(c) N = 1

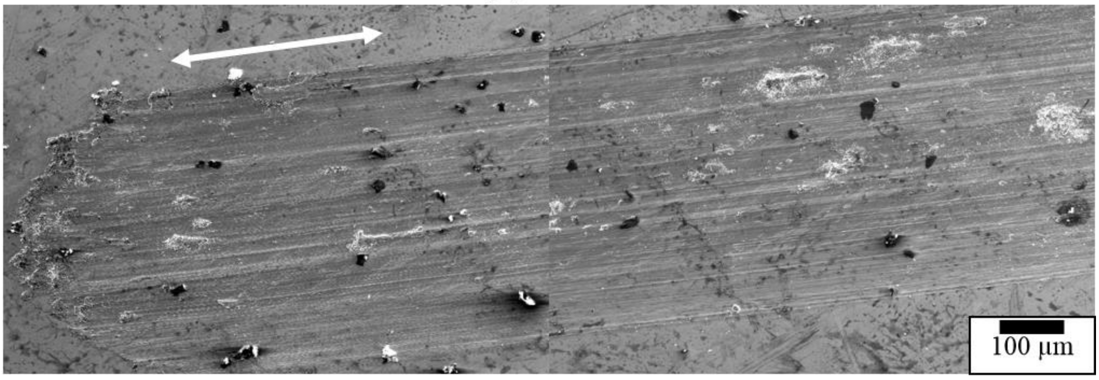

(d) N = 10

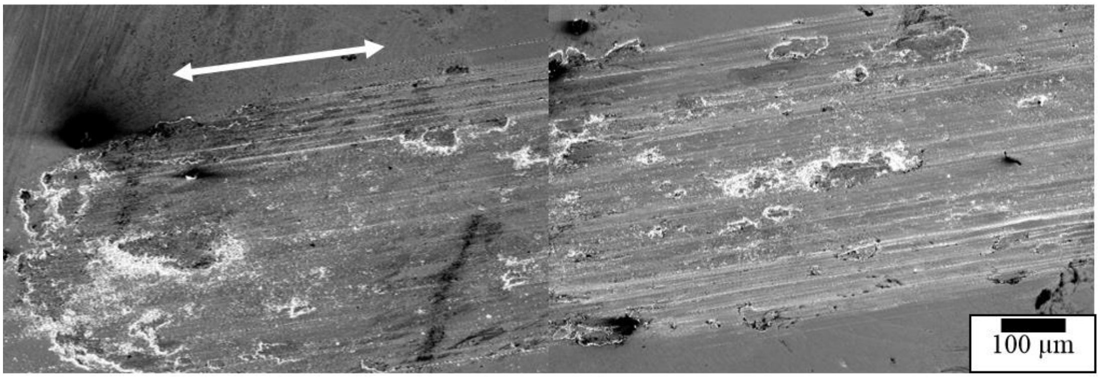

Fig. 8-5 SEM images of worn track surface for as-received and HPT-processed disks after wear test. Double-arrowed lines indicate sliding direction.

In addition, Figs. 8-5(b) – (d) also show that some of the areas within the wear tracks of HPT-processed disks are partly covered by irregularly shaped adhered wear particles as indicated by the bumpy surfaces, and their surface areas increase with higher torsional strains from 1 to 10 HPT revolutions. These adhered particles could be produced by the adhesion of wear debris or the back transfer of 316L SS (which is initially removed from the disk and attached to the alumina ball) from the surface of the alumina ball to the wear track surface, or even the material transfer of some alumina particles that are removed from the counter surface due to friction and then attached to the disk surface [574,589]. However, adhesive wear is less pronounced for the as-received disk because it is relatively soft and the alumina ball can penetrate deep beyond its surface, resulting in minimal material removal. In addition, spherical (or close to spherical) black particles that seem to be wear debris could also be seen to be more apparent on the HPT-processed disks compared to the as-received disk.

Fig. 8-6 displays SEM images of the wear features in the as-received and HPT-processed disks under higher magnification. The solid arrows in Fig. 8-6(a) show tear-like cuts perpendicular to the sliding grooves at the end of the wear track from the as-received disk. These tears indicate micro-cutting, another mode of abrasive wear, which involves the removal of small chips from the surface of the softer material (316L SS) due to sliding of the counter surface (alumina ball) [576,588]. On the other hand, the dashed arrows in Figs. 8(b) and (c) indicate the adhered wear particles representing adhesive wear for disks processed through 1/4 and 1 HPT revolutions, respectively.

To evaluate the characteristics of the wear features in more detail, EDX analysis was carried out on three areas marked A, B, and C as shown in Fig. 8-6, and the results of the elemental composition of each area is shown in Table 8-1.

Table 8-1 Elemental composition of wear features marked A, B, and C in Fig. 8-6 (wt. %).

Area	Fe	Cr	Ni	Al	O
A	77.25	4.16	2.04	-	16.55
B	-	-	-	83.34	16.66
C	72.11	2.59	-	-	25.33

It is revealed that the adhered wear particles (areas A and C) contain relatively large amounts of iron and oxygen and much less chromium and nickel, implying the occurrence of a mild tribo-oxidative wear [593–595]. This is a common phenomenon in tribology tests on 316L SS, in which the protective Cr-based oxide layer is constantly removed by the repetitive rubbing of the counter surface on the base material. Hence, the bare 316L SS surface is exposed to air and can be easily oxidised to form an Fe-based passive layer that is susceptible to rust and corrosion instead of the protective Cr-based oxide layer [571]. Oxidation typically occurs in steel alloys and has been found to reduce the frictional force between the disk and the sliding ball via compaction of fine oxidised wear particles that often results in smooth wear tracks and lower wear rates [596–598]. The COF values and EDX analysis clearly demonstrate that this is the case in the present study, suggesting improved wear performance for AM 316L SS by HPT processing compared to the as-received counterpart. In particular, the white and bright areas or spots surrounding the adhered wear particles are indicative of a mixed adhesive and mild tribo-oxidative wear mechanisms for the HPT-processed disks, in addition to abrasive wear.

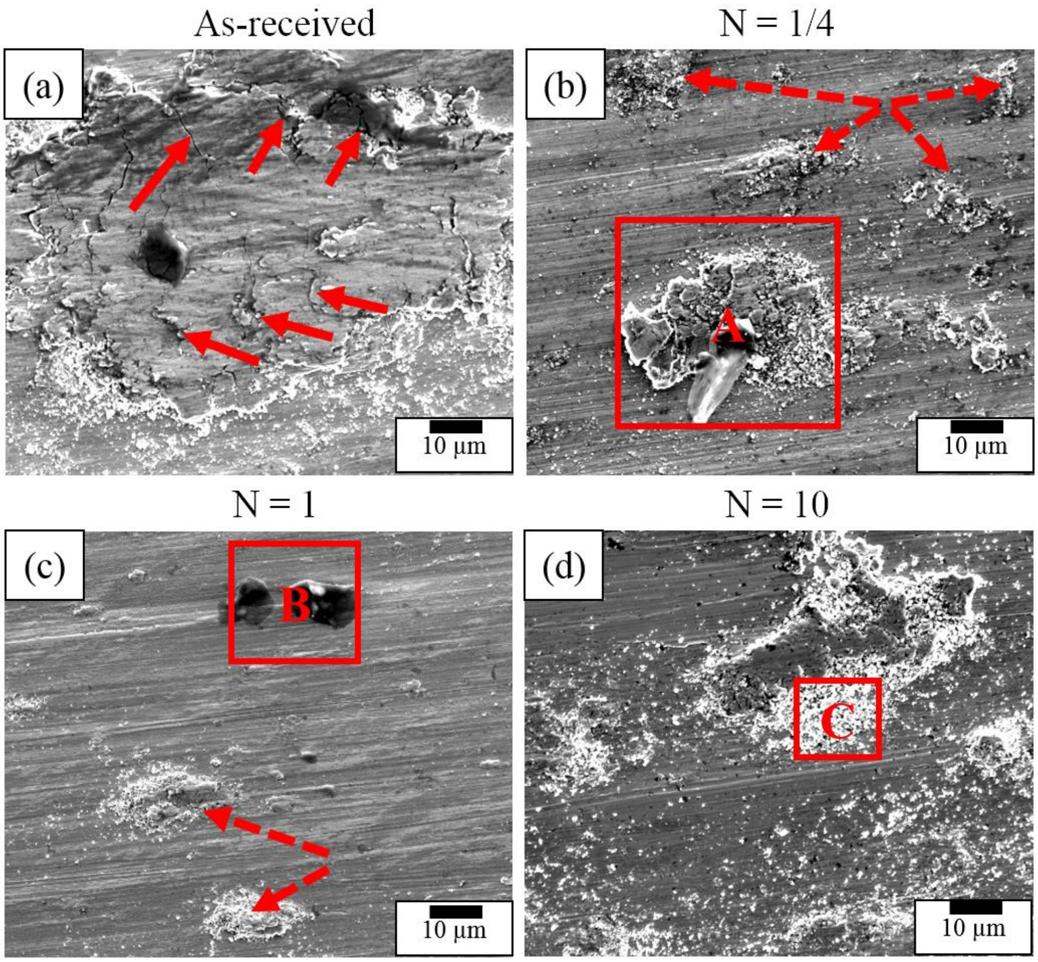

Fig. 8-6 Some wear features on the as-received and HPT-processed disks after wear test. Solid arrow shows micro-cutting, dashed arrows show material adhesion, and areas A, B, and C were subjected to EDX analysis.

Interestingly, the black particles that are initially thought to be just wear debris actually consists of aluminium and oxygen as shown by the EDX analysis for area B in Table 8-1, which is similar to the results of sliding wear test study on ECAP-processed commercially pure Al reported by Wang et al. [381]. Therefore, it is suggested that the black particles that are present on the surface of HPT-processed disks are Al-based oxides. They most likely detach from the alumina ball due to slightly higher friction upon sliding with the 316L SS surface as a result of higher hardness with increasing number of HPT revolutions. Therefore, it can be inferred that the wear mechanism in the current study transitions from severe abrasive wear for the as-received disk to a combination of mild abrasive, adhesive, and tribo-oxidative wear for the HPT-processed disks.

In addition, Fig. 8-7 shows a representative SEM image of the alumina ball surface (counter surface) after the dry sliding wear tests. Some wear particles are observed to be attached to the surface of the alumina ball, which could be 316L SS material removed from the disk surface due to the repeated sliding between both materials. EDX analysis reveal the following chemical compositions (in wt. %); Fe: 35.9, Cr: 12.33, Ni: 8.46, Al: 19.07, and O: 24.24. Thus, the adhered wear particles on the alumina ball surface are indeed 316L SS material removed from the disk and then transferred to the alumina ball due to the higher hardness of alumina compared to 316L SS [12,13].

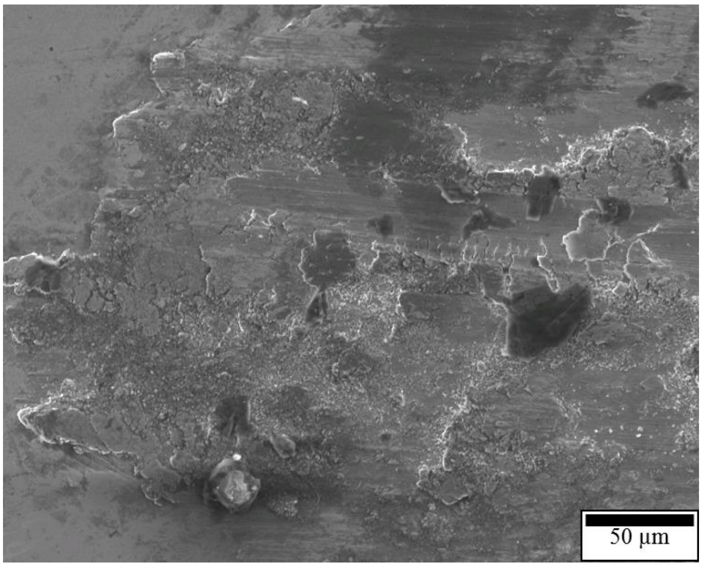

Fig. 8-7 Some wear features on the as-received and HPT-processed disks after wear test. Solid arrow shows micro-cutting, dashed arrows show material adhesion, and areas A, B, and C were subjected to EDX analysis.

8.3 Discussion

HPT processing was employed to impose extreme grain refinement on AM 316L SS, and a final average grain size of ~ 42 nm is obtained upon saturation after 10 revolutions compared to ~ 40 µm for the as-received disk (Chapter 5). In addition, the HV value also significantly increases from ~ 220 HV for the as-received disk to ~ 600 HV after 10 HPT revolutions, which is consistent with the results in Chapter 5. This maximum hardness value obtained at the saturation stage is comparable to that attained by Gubicza et al. [252], ~ 610 HV after 10 HPT revolutions of wrought 316L SS, although hardness saturation across the disk diameter was not achieved in that study. This suggests similar response of HPT processing for both AM and wrought 316L SS in terms of significantly improving hardness and strength due to the extreme grain refinement down to the UFG/NG regime.

The results of the dry sliding wear tests in the current investigation provide valuable insight to the wear characteristics of UFG and NG AM 316L SS obtained through HPT processing. In addition to remarkable improvement in hardness, HPT processing also results in steady decrease in both COF and m_{loss} values with higher torsional strain levels as the number of HPT revolutions increase compared to the as-received disk (Fig. 8-2). The lower COF values in HPT-processed AM 316L SS can be explained in terms of the larger yield stress required to produce plastic deformation as the hardness increases due to the extreme grain refinement down to the nano-scale, thus increasing the resistance to sliding and reduces the friction between the base material (316L SS) and the counter surface (alumina ball) [578].

Such reduction in COF due to refined grain sizes has also been observed in various studies on both surface and bulk nanostructuring of 316L SS and other SS alloys. For example, Roland et al. [599] and Sami and Mahdi [577] attributed the lower friction coefficient in SMAT-treated 316L SS layer compared to the untreated counterpart due to the nanostructured grains obtained on the surface layer via SMAT. Rezaie-Najed et al. [579] studied the nanostructure layer formation on a 316L SS plate after FSP treatment. A reduction of grain size from 30 µm to 50 – 200 nm was observed, accompanied by significant hardness increase and enhancement in wear resistance. It was explained that the reduction in friction coefficient on the FSP-treated layer could be attributed to the higher hardness that limits plastic deformation compared to the untreated regions for the same loading conditions of the wear test. Qin et al. [600] compared the tribological behaviour in a dry air condition of a wrought 316L SS and a heterogeneous lamella-structured (HLS) 316L SS obtained by cold rolling and annealing. The HLS 316L SS possessed a mix of numerous lamella grains, nano-scale grains, and nanotwins that resulted in the increase of grain boundaries throughout the bulk of the material. It was found that the reduced friction and therefore, the COF value of HLS 316L SS compared to wrought 316L SS can be ascribed to the hard oxidative particles formed upon sliding at the interface during wear test as the result of these microstructural features [601].

Similarly, the reduced mass loss, m_{loss} in HPT-processed disks compared to the as-received material in this study is consistent with the conventional Archard's relationship that correlates mass loss with hardness given by [586]:

$$V = k_W \frac{S_W L_W}{3H_{mat.}} \qquad \text{Eqn. 8-1}$$

where V is the wear volume loss after wear test, k_{W} is the material-specific dimensionless wear coefficient, S_{W} is the sliding distance, L_{W} is the load force applied by the counter surface to the base material, and H_{mat}. is the hardness of the material. This equation uses volume loss as an indicator of wear performance and suggests improved wear resistance i.e. reduced volume loss with increase in the hardness of the HPT-processed disks. Kato et al. [589] studied the HPT processing of pure iron and also found out that the increase in hardness with HPT revolutions correspond to reduced volume loss and improved wear rates, thus confirming Archard's relationship between wear volume and hardness to assess the wear performance of HPT-processed materials.

The wear scar profiles evaluated using the surface profilometers (Figs. 8-3 and 8-4) indicate that the wear scar in the as-received disk is much deeper than that of the HPT-processed disks and it steadily decreases with increasing number of HPT revolutions. In addition, the wear scar morphologies observed through SEM (Fig. 8-5) show that all the as-received and HPT-processed disks experience abrasive wear. This occurs upon sliding due to either: (i) asperities or particles of harder materials (alumina ball in this study) on softer materials (316L SS in this study) [590], or (ii) two similar materials that may cause the formation of hard particles [591]. The occurrence of abrasive wear essentially removes some material from the surface of the softer 316L SS due to the repetitive sliding of the alumina ball on the disk surface.

It could be observed that the sliding grooves obtained for the as-received disk shown in Fig. 8-5(a) is very deep, rough and closely spaced between each other due to severe abrasive wear, which is related to the higher level of penetration into the as-received disk due to hard asperities [602]. In addition, the deeper grooves correspond to larger contact and impact between the base material and the counter surface, resulting in higher COF values [603]. Therefore, the increasingly shallower, smoother and more widely spaced grooves observed on the disks with higher HPT torsional straining shown in Figs. 8-5(b) – (d) imply lesser contact and impact between both 316L SS and alumina ball surfaces since it becomes harder to deform the HPT-processed disks compared to the as-received counterpart. This could explain the reduction in COF values displayed in Fig. 8-2 and indicate that the initially severe abrasive wear mechanism for the as-received disk become gradually weaker after HPT processing at higher number of revolutions.

Furthermore, Figs. 8-5(b) – (d) also show evidence of mild adhesive wear mechanism that could be produced by the adhesion of wear debris or the back transfer of 316L SS from the surface of the alumina ball to the wear track surface [589]. In 316L SS subjected to sliding wear tests, adhesive wear occurs due to the rubbing of the counter surface on the base material that eventually breaks down the protective oxide layer due to contact stress and results in a direct interfacial contact between both surfaces [604]. In the present study, it is possible that the formation of adhered wear particles is related to back transfer of 316L SS and material transfer of alumina particles from the counter surface. This is because, as the material progressively becomes harder with increasing HPT torsional strain, it is more difficult to penetrate deep into the material, thus only the oxide layer and a few additional layers could be removed by the repetitive sliding. Thus, most of the surface of the material remain intact, and the removed 316L SS material could be attached to the alumina ball, before being transferred back and essentially welded onto the surface of the disk. Similarly, the friction between the harder HPT-processed disks and the alumina ball could remove some alumina particles, which are then attached to the surface of the HPT-processed disks.

Therefore, the evolution of wear surface profiles, together with the results of COF and mass loss from the wear test (Fig. 8-2) provide strong indications of progressive improvement of wear performance with increasing HPT torsional strain levels compared to the as-received disk. To confirm this inference and quantitatively evaluate the wear performance of the as-received and HPT-processed disk in this study, the specific wear rate, k_W, i.e. the dimensionless wear coefficient derived from Eqn. 8-1 is used to estimate and directly compare the wear properties across all processing conditions given by [382]:

$$k_W = \frac{V}{S_W L} \quad \text{Eqn. 8-2}$$

where V, S_W, and L_W are defined as in Eqn. 8-1. The volume loss, V is estimated by multiplying the area loss, A with stroke length, l. The area loss is estimated by analysing the wear scar profiles using the TAICAAN XYRIS 2000 TL/CL surface profilometer to include both ridges and grooves of the wear tracks. The results of the calculated V and the corresponding k_W values by applying Eqn. 8-2 for a constant load of 5 N and stroke length of 2 mm, and total sliding distance of 20 m are displayed in Table 8-2.

Table 8-2 Calculated area loss, A, volume loss, V, and specific wear rate, k_W for all processing conditions after wear test.

Processing condition	**Area loss, A (mm^2)**	**Volume loss, V (mm^3)**	**Specific wear rate, k_W (x 10^{-3} mm^3/Nm)**
As received	0.01625	0.0325	0.33
N = 1/4	0.00924	0.0185	0.19
N = 1	0.00798	0.0159	0.16
N = 10	0.00624	0.0125	0.13

The calculated k_W values confirm that HPT-processing indeed improve the wear resistance of AM 316L SS, with reduction of k_W from 0.33 x 10^{-3} mm^3/Nm for the as-received disk to 0.19 x 10^{-3} mm^3/Nm after 1/4 revolutions (~ 42% reduction) and further decreases to 0.13 x 10^{-3} mm^3/Nm after 10 revolutions. This result is consistent with the Archard's relationship that suggests improvement in wear resistance with higher hardness of a material in general.

In addition, the influence of grain refinement down to the UFG and/or NG regime on the strength and wear performance of the studied material is further illustrated in Fig. 8-8, showing the evolution of microhardness, HV and specific wear rate, k_W as functions of inverse square root of grain size, $d^{-1/2}$. For the HV vs $d^{-1/2}$ plot (circle and solid line), a conventional linear Hall-Petch relationship is observed, and an inverse linear relationship that agrees with the Archard's equation is also attained for the k_W vs $d^{-1/2}$ plot (square and dashed line).

Interestingly, although the hardness appears to be saturated after 1 HPT revolutions, the COF and wear rate, k_W values continue to decrease until 10 HPT revolutions. This implies that the continuous improvement in wear performance is not only a straightforward interrelationship with decreased grain size and increased hardness, but could also be contributed by other factors. Indeed, upon observation and EDX analysis of the wear features in Figs. 8-5 and 8-6, have revealed the increasing amount of adhered wear particles comprising of largely iron-based oxides with increasing number of HPT revolutions. Such wear features have been found to act as solid lubricants that reduce the frictional force between the test subject (316L SS disks) and the counter surface (alumina ball) that produce smoother wear tracks and lower wear rates [596–598]. Thus, it is reasonable to infer that the higher amounts of these adhered wear particles present on the surface of the HPT-processed disks after 1 and 10 HPT revolutions are also the main contributors to the improved wear performance, in addition to the decreased grain size and increased hardness.

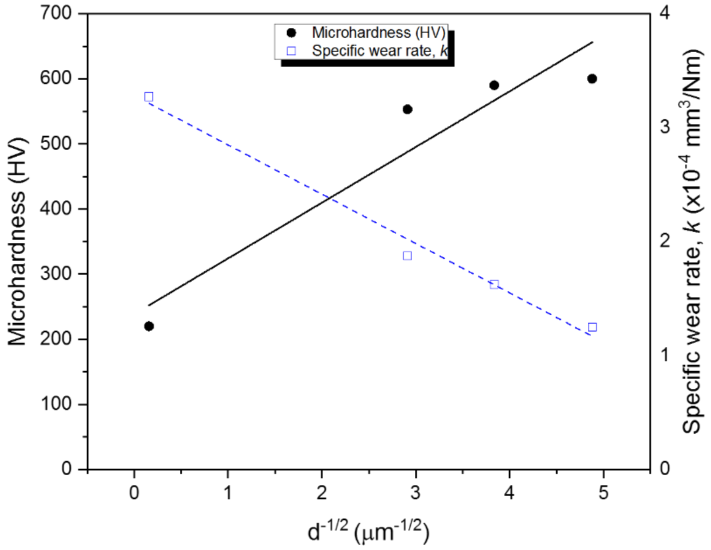

Fig. 8-8 Microhardness, HV (circle and solid line) and specific wear rate, k_W (square and dashed line) vs inverse square root of grain size.

It is well-known that the wear behaviour of a material is strongly influenced by various factors, including applied load, sliding speed, test period, counter surface material, and the atmosphere during testing. However, some conflicting results have been reported for the tribological behaviour of various SPD-processed metals and alloys [230].

The study of HPT processing of ultra-low carbon steel by Kato et al. [585] produced mixed results for both COF and wear resistance of the HPT-processed material when using two different materials for the counter surface, WC-Co and high C-Cr bearing steel (SUJ2) balls. When using WC-Co balls, the COF values were relatively constant, but the wear resistance increased with increasing number of HPT revolutions, which agrees well with Archard's wear equation. However, when using SUJ2 balls, the COF values and wear resistance decreased because of the similarity between both base and counter surface materials that resulted in intensive adhesion and oxidation. In the investigation of the tribological behaviour of wrought and HLS 316L SS by Qin et al. [600], it was found that although the friction coefficient of HLS 316L SS decreased, the wear resistance was poorer than its wrought counterpart. They explained that even though the numerous grain boundaries produced by the accumulation of lamella grains, nano-scale grains, and nanotwins were able to increase the hardness of the HLS 316L SS, the dry air testing condition made it more susceptible to oxidation. A lot of oxidation species were produced and subsequently crushed continuously. They were then absorbed into the HLS structure, particularly at higher applied loads, resulting in severe tribo-oxidative wear. Therefore, the smaller COF values in pure iron and steels do not necessarily always result in enhanced wear performance, but also depend on the applied load and counter surface material.

Bartolomeu et al. [574] systematically compared the tribological behaviour of conventionally cast, hot-pressed (HP), and AM 316L SS using a ball-on-plate configuration under lubrication (Phosphate Buffered Solution, PBS). It was found that the AM 316L SS possesses the best wear performance (lowest COF and k_W values) compared to the cast and HP counterparts. This is because of the highest hardness and finer microstructures in the AM 316L SS as the result of short laser-material interaction and rapid solidification cycles during processing. Similar studies by other authors confirm that as long as high densification levels and low porosity content are attained, 316L SS structures manufactured by SLM will have higher hardness and better wear resistance than their CM counterparts [571–573], in line with the conventional Archard's relationship. The current investigation clearly demonstrates increased hardness and enhanced wear performance for 316L SS manufactured by SLM and then processed through HPT within the testing conditions and parameters.

Finally, Table 8-3 summarises some of the recent results of wear testing results from different researchers by using different wear rig setup on pure iron, carbon steel, and 316L SS that have undergone both bulk and surface SPD procedures. It could be observed from Table 8-3 that bulk and surface SPD processing most likely result in decreased COF and better wear resistance regardless of the wear rig setup, although all of them experience similar wear mechanisms (adhesive, abrasive, tribo-oxidative, or some combination among them).

Table 8-3 Wear properties and mechanisms of materials processed by bulk and surface grain refinements.

Material (Fabrication)	**Grain refinement method (bulk/surface)**	**Wear rig (lubrication)**	**Effect on COF**	**Effect on wear resistance**	**Wear mechanism**	**Reference**
316L SS (SLM)	HPT (bulk)	Pin-on-disk (unlubricated)	Decreases	Increases	Transition from severe abrasive to combination of mild abrasive, adhesive and tribo-oxidative wear	This study
Ultra-low carbon steel (wrought)	HPT (bulk)	Ball-on-disk (unlubricated)	Mixed	Mixed	Mild to severe adhesive and oxidative wear	[585]
Pure iron (wrought)	HPT (bulk)	Ball-on-disk (unlubricated)	Decreases	Increases	Transition from adhesive to asperity plastic deformation (sliding) wear	[589]
Pure iron (wrought)	HPT (bulk)	Ball-on-disk (unlubricated)		Increases	Adhesive and abrasive wear	[605]
316L SS (wrought)	Multi-axial Forging, MAF (bulk)	Pin-on-disk (unlubricated)	Decreases	Increases	Abrasive wear	[576]
316L SS (wrought)	Cold-rolled and annealed (bulk)	Ball-on-disk (unlubricated)	Decreases	Decreases	Mild to severe adhesive and oxidative wear	[600]
316L SS (wrought)	Surface mechanical attrition treatment, SMAT (surface)	Ball-on-plate (unlubricated)	Decreases	Increases		[577]
316L SS (wrought)	Ultrasonic nanocrystalline surface modification, UNSM (surface)	Cylinder-on-cylinder (unlubricated)	Decreases	Increases	Oxidative-adhesive to oxidative-abrasive wear	[578]
316L SS (wrought)	Friction stir processing, FSP (surface)	Pin-on-disk (unlubricated)	Decreases	Increases	Adhesive and abrasive wear	[579]
316L SS (SLM) * No grain refinement	Comparison of AM, cast, and hot pressing (HP)	Ball-on-plate (lubricated)	No change	Increases	Adhesive and abrasive wear	[574]

8.4 Summary

In this chapter, tribology test was carried out to determine the wear performance of as-received and HPT-processed AM 316L SS. The following conclusions can be drawn based on the results obtained after wear test:

1. Dry sliding wear tests demonstrate improved overall wear performance of AM 316L SS after HPT processing. This is indicated by the reduced coefficient of friction and specific wear rate values with increasing torsional straining from 1/4 up to 10 HPT revolutions.
2. The observed worn disk surfaces show shallower, smoother, and widely spaced grooves of the wear tracks in the HPT-processed disks compared to the deeper, rougher, and narrow spaced grooves in the as-received counterpart.
3. The wear mechanism transitions from severe abrasive wear in the as-received disk to a combination of mild abrasive, adhesive, and tribo-oxidative wear after HPT processing.
4. The enhancement in wear performance could be attributed to the higher hardness and UFG and NG microstructures, together with increased amounts of iron oxide-based adhered wear particles that act as solid lubricant to lower the friction between the contact surfaces, both as the result of increasing number of HPT revolutions and the corresponding torsional strains.

Chapter 9 Interfacial microstructure and strengthening of AM 316L SS/IN 718 processed by HPT

9.1 Introduction

Traditionally, fusion welding techniques have been used to join two dissimilar materials, which is often required to obtain the best properties of both materials within a single component, e.g. for aerospace, automotive, and nuclear reactor components [606,607]. However, the welded joints, i.e. the diffused interfacial region are often prone to cracks and porosity due to the presence of precipitates, intermetallics, and distortion of the weld interface as has been reported in various literature [608–610]. These defects weaken the strength of the welded joints, thus rendering their applications less useful. High energy fusion welding techniques such as laser beam welding (LBW) and electron beam welding (EBW), and non-fusion welding technologies such as solid-state welding are more widely used to join two dissimilar materials compared to low energy arc fusion welding processes. This is because of the higher quality welded joints and diffusion bonded regions, and lesser problems that are often associated with the use of filler metals in arc fusion welding [209,611].

These welding processes require the combination of two different metallic materials together and then machined or formed into the desired part geometry. Recently, the development of metal AM technology has enabled the direct integration of multiple metallic parts within a single machine operation, either by DED or PBF techniques, both using laser or electron beam as the heat source [84,192,198,199,205,208,612]. Thus, AM offers the advantage of simultaneously manufacturing two different materials with the capability to form complex shapes and intricate features. In addition, AM can shorten processing time, reduce material waste and lower the associated manufacturing costs when compared to conventional welding techniques.

Metal AM processes can be regarded as mini fusion welding due to the creation of localised melt pools upon heat source-material reaction. Therefore, the AM-bonded joint between two materials (interfacial region) also feature typical microstructural features such as fusion zone (FZ), heat affected zone (HAZ), and unmixed zone (UZ), but they are often characterised by fine microstructures and grain sizes, which usually lead to high hardness and strength [12–14,209]. However, defects that are commonly observed within traditionally welded joints, such as cracks and porosity still could not be eliminated completely, thereby requiring post-processing heat treatments [84,209].

On the other hand, it is known that UFG and/or NG microstructures can significantly increase the hardness, improve yield and tensile strengths, enhance corrosion and wear performances, and extend fatigue life of metallic materials compared to the coarse-grained counterparts [22–24]. HPT is one of the most widely used SPD processing techniques that produces ultrafine- and nano-scale grain sizes via combined hydrostatic pressure and extreme torsional strains on bulk metallic materials [18,221,233,372]. To date, numerous studies have been conducted on the HPT processing of CM multi-material (MM) metals and alloys, all of which have focused on developing exceptionally strong novel metal-matrix nanocomposites (MMNC), particularly through the combination of separate Al and Mg disks deformed together at the same time [382,506,511,613–617].

However, the influence of SPD processing on additively manufactured MM metallic components has never been investigated before. Therefore, in this study, HPT processing was conducted on MMAM structures comprising of 316L SS and IN 718. This material combination is chosen because of their wide range of commercial engineering applications, including chemical processing equipment, aerospace engine parts, nuclear power plant components, and components in the oil and gas industries [606,610,618]. In addition, both materials have γ-austenite FCC crystal structure with similar lattice parameters, similar coefficient of thermal expansion (CTE) values, and high mutual solubility [209]. This enables baseline results to be established as reference for further processing, testing, and characterisations in the future.

A MM 316L SS/IN 718 bar structure was fabricated by an in-house SLM system developed at the University of Southampton that is equipped with multiple nozzles for powder delivery and a powder cleaning/removal system. The details of the manufacturing process have been described in Section 3.2.2. A series of thin disks (10 mm diameter, 1 mm thickness) were cut from the bar with the interfacial region that separates 316L SS and IN 718 at the centre of the disks. HPT processing was then conducted under 6 GPa of pressure at RT for 1/4, 1, and 10 revolutions corresponding to various amounts of equivalent torsional strain values, $\varepsilon_{\text{eq.-HPT}}$. The evolution of porosity, microstructure, and hardness at the interfacial region were evaluated using EBSD, TEM, XRD, and microhardness and nanoindentation measurements. A physical-based model based on the linear additive theory was constructed to assess the contribution of individual strengthening mechanisms at the interfacial region of the as-received and HPT-processed disks.

9.2 Results

9.2.1 Evolution of interfacial microstructures

9.2.1.1 As-received interfacial microstructures

Fig. 9-1 shows the interfacial microstructures of the as-received MMAM 316L SS/IN 718 observed at the surface-parallel (x-z plane) obtained from EBSD analysis.

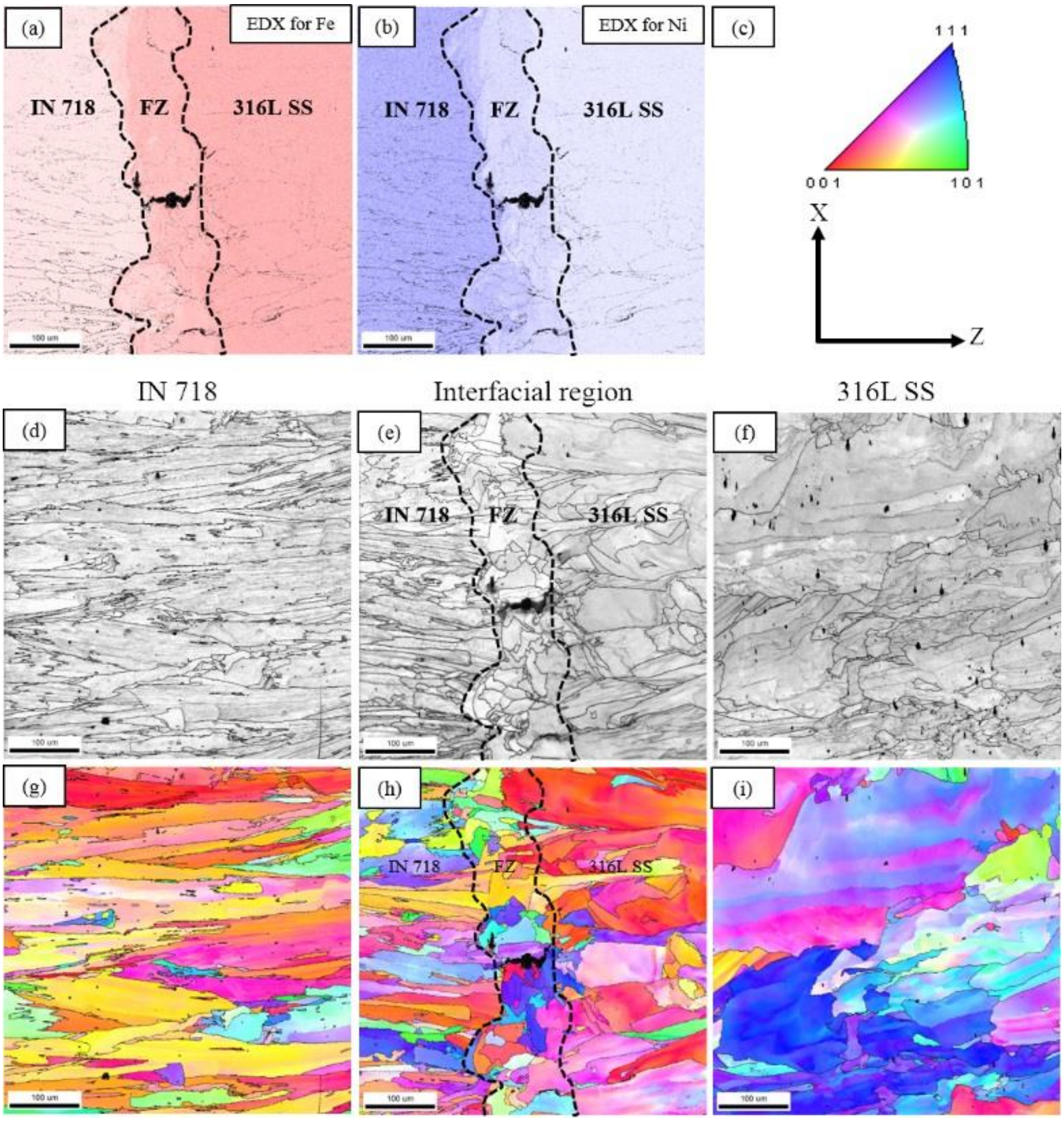

Fig. 9-1 (a) and (b) EDX maps at the interfacial region, (c) IPF colour legend with x-z axis indicating surface-parallel direction, (d) – (f) BSE images showing porosity at respective areas within the interfacial region, and (g) – (h) EBSD maps showing crystallographic orientation for the respective interfacial region areas. All images are from the as-received MM disk.

The interfacial microstructures consist of the fusion zone (FZ) as well as the IN 718 and 316L SS regions within its vicinity, ~ 0.5 mm from either side of the FZ, which can be collectively referred to as the interfacial region. EDX maps in Figs. 9-1(a) and (b) demonstrate distinct Fe- and Ni-rich regions as illustrated by dark pink and dark purple, respectively. The FZ consists of a continuous and coherent intermixed region of fused Fe and Ni as marked by lighter pink and lighter purple, respectively. The intermixed FZ region is estimated to be ~ 100 µm wide, indicating significant dilution and interfacial diffusion of Fe and Ni across 3 – 4 layers of powder bed depositions, since the thickness of each powder bed layer used for SLM in this study is ~ 30 µm. These suggest that a good metallurgical bonding has been achieved at the FZ of the MMAM alloy in this study. In addition, no obvious HAZ is formed due to the very high cooling rates in AM compared to traditional fusion welding, suggesting that common welding problems associated with HAZ such as increased brittleness, low joint strength, and high corrosion susceptibility could be avoided.

The BSE-SEM images in Figs. 9-1(d) – (f) illustrate that there are some irregular-shaped, process-induced porosity in the interfacial region of the as-received MM alloy. In particular, a relatively large elongated pore is observed at the centre across the FZ as shown in Fig. 9-1(e). No cracks are visible at the interfacial region and throughout the as-built structure. However, the prevalence of process-induced pores in the present study compared to gas-induced pores obtained from the study of single-material AM 316L SS in Chapter 5 can be ascribed to the difficulty in selecting a single set of optimum processing parameters for both materials due to the difference in some intrinsic properties, such as thermal conductivity and coefficient of thermal expansion (CTE). Nevertheless, the overall porosity content throughout the as-received MM alloy is found to be quite low, ~ 0.81%, indicating high densifications level of > 99% is achieved upon solidification.

EBSD maps in Figs. 9-1(g) – (i) reveal the grain size, distribution, and crystallographic orientation at the interfacial region of the as-received MM disk. The colour-coded inverse pole figure (IPF) in Fig. 9-1(c) denotes different grain misorientations as depicted in the unit triangle. A mixture of grain size distribution without any preferred crystallographic orientation is observed. Fine elongated columnar grains with average grain size of 55 ± 5 µm is attained at the IN 718 region (Fig. 9-1(g)), while the 316L SS region exhibit coarse elongated columnar grains with average grain size of 85 ± 3 µm as shown in Fig. 9-1(i). Although the IPF images indicate random grain growth without any preferred crystallographic orientation, the columnar morphology observed at the individual 316L SS and IN 718 regions suggests an epitaxial mode of grain growth. Interestingly, fine, equiaxed grains with a mean size of 45 ± 3 µm are obtained at the FZ. This is most likely to be associated with the abrupt material change, i.e. from 316L SS to IN 718 powders and vice versa, and multiple thermal excursions occurring within the fused 3 – 4 powder layers.

On the other hand, SEM images in Fig. 9-2 taken at the surface-parallel show the cellular sub-structures that make up the grains at the interfacial region of the as-received MM disk. Fig. 9-2(a) exhibits a clear distinction between 316L SS and IN 718 at the centre of the FZ as indicated by the different etching contrast between both materials. The FZ is distinguished from the other two unmixed regions by the solid, vertical red lines, and a sharp FZ boundary is indicated by the dashed red line in Fig. 9-2(b).

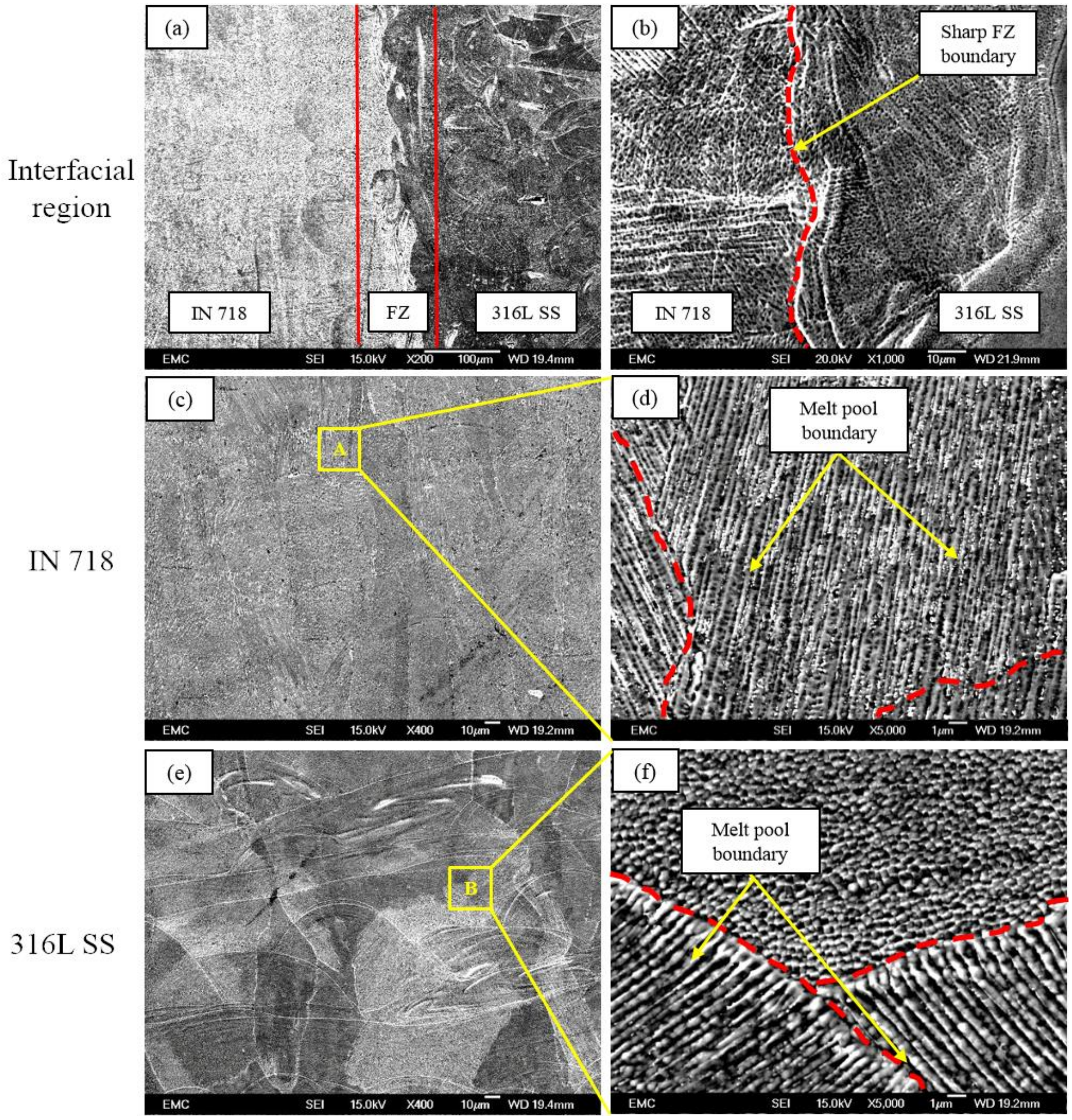

Fig. 9-2 SEM images taken at surface-parallel of the as-received MM disk showing (a) the interfacial region, (b) sharp FZ boundary, (c) the IN 718 region, (d) columnar cells growing through different melt pools at the IN 718 region (area A in (c)), (e) the 316L region, and (f) various cell morphologies at different melt pools in the 316L SS region (area B in (e)).

Careful observation of the sharp FZ demonstrates that the IN 718 region comprises of mostly fine sub-micron columnar dendritic cells, while the 316L SS region consists of a mixture of fine sub-micron equiaxed and columnar cells. In addition, these various cellular morphologies seem to cohesively fuse together across the boundary of both materials (dashed red line), further indicating a good metallurgical bonding has been successfully achieved at the FZ. In Figs. 9-2(c) and (e), respectively, multiple grain growth across a single melt pool and a single grain growing through several melt pools can be observed at the 316L SS and IN 718 regions. The high-magnification SEM images of area A in Fig. 9-2(c) (also shown in Fig. 9-2(d)) and that of area B in Fig. 9-2(e) (also illustrated in Fig. 9-2(f)) clearly demonstrate that the growth of the cellular sub-structures within a melt pool ends at the melt pool boundary (MPB) as indicated by the dashed red lines, before growing again in new melt pools at different orientations.

In addition, EDX area scan along the FZ (Fig. 9-2(a)) reveals the following elemental compositions (in wt. %); Cr: 20.34, Nb: 9.55, Mo: 3.6, Ti: 1.14, and ~ 32.7 of Fe and Ni each. This indicates that the Fe and Ni matrix from both 316L SS and IN 718 are homogeneously distributed within the FZ, while the contents of Nb and Ti are much higher than their initial compositions in the starting IN 718 powder (~ 5.1 and ~ 0.89 wt. %, respectively).

TEM and STEM images in Fig. 9-3 reveal sub-micron and nano-scale microstructural features at the interfacial region of the as-received MM disk, including dislocation tangling networks and secondary phase precipitates. The bright field (BF) TEM images in Figs. 9-3(a) and (b), respectively show equiaxed and columnar cellular sub-structures with thick boundaries, which can be attributed to the dense entangled dislocations and/or segregation of heavier elements. These cellular sub-structures can be considered as dislocation cells that are formed due to the high internal stress induced during SLM processing [277,312]. The BF TEM image in Fig. 9-3(c) exhibits dense dislocation networks within the solidified MM structure, which evidently is denser than dislocations in annealed CM alloys [278]. The BF TEM image in Fig. 9-3(d) displays a higher density of dislocation tangles and dislocation pile-up at the boundaries of two adjacent equiaxed cells compared to the cell interior, indicating the preferred location for dislocation concentration.

Two distinct Laves phase and carbide phase precipitates are formed inside the solidified as-received structure as displayed by the BF TEM images in Figs. 9-3(e) and (f), respectively. Laves phase is characterised as near-spherical globules with the chemical formula $(Ni,Fe)_2(Nb,Ti,Mo)$, while carbides are typically spherical and have the chemical formula (Nb,Ti)C. The average fraction of these two precipitates is ~ 1.87 vol. % with an average diameter of ~ 30.58 nm, as determined from microscopy analysis through ImageJ software. Figs. 9-3(h) – (m) show the EDX maps for the equiaxed cells shown by the high angle angular dark field STEM (HAADF-STEM) image in Fig. 9-3(g), and Figs. 9-3(o) – (t) for columnar cells shown by the HAADF-STEM image in Fig. 9-3(n). In both cases, homogeneous dispersions of Fe, Ni and Cr elements within the matrix at the interfacial region with some segregations of heavier Nb element into the cell boundaries. Furthermore, the black spherical particles are indeed confirmed as Nb- and Ti-rich carbides.

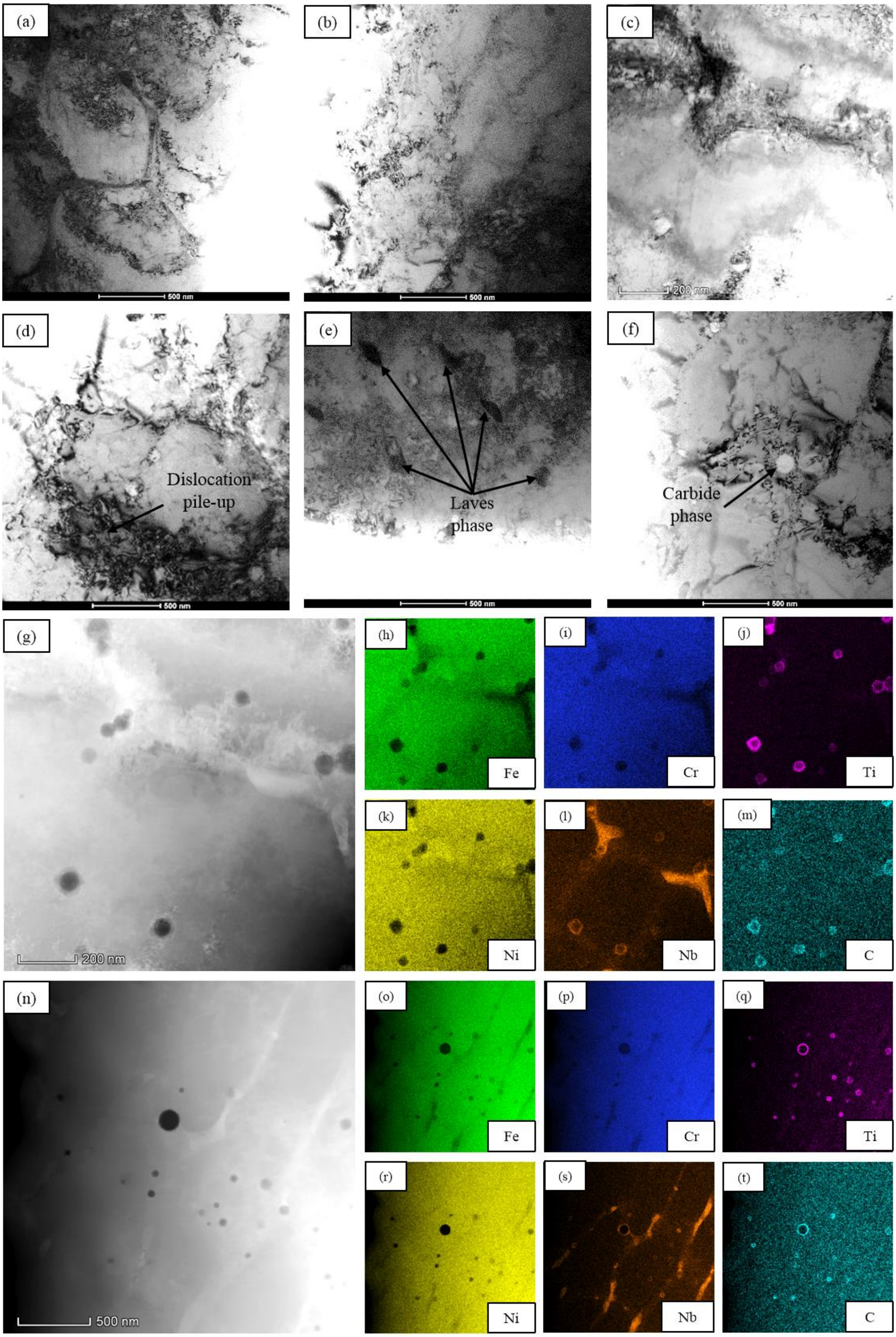

Fig. 9-3 TEM; (a) – (f) HAADF-STEM; (g) and (n) images, and corresponding EDX maps; (h) – (m) and (o) – (t) for specific areas at the interfacial region of the as-received MM disk.

9.2.3.2 Interfacial microstructures after HPT processing

Fig. 9-4 shows a series of SEM, TEM and STEM images of the MMAM disk taken at the periphery along the interfacial region (~ 3 mm from its centre) after 1/4 HPT revolution ($\varepsilon_{eq.}$ = 3.4). The relatively large irregular-shaped pore observed at the centre of the FZ in Fig. 9-1 has become elongated and almost closed, as illustrated by the SEM image in Fig. 9-4(a). A nearly pore-free structure is obtained, with the overall porosity content significantly decreases to ~ 0.066% representing ~ 91% reduction. This is consistent with the results obtained in the HPT processing of AM 316L SS detailed in Chapter 4 and further highlights the effectiveness of HPT in eliminating porosity in AM metallic parts via combined compressive force and torsional strain. The width of the FZ is ~ 100 µm, similar to the as-received condition although it appears wavy and slightly rotated in the straining direction. In addition, the SEM image in Fig. 9-4(b) exhibits the expected cellular elongation and distortion due to the HPT-induced torsional strain.

The newly generated dislocations due to torsional strain after 1/4 HPT revolution accumulate and further pile-up at the cell boundaries, resulting in denser and thicker dislocation cells as shown by the BF TEM image in Fig. 9-4(c). In addition, the high internal stress induced by HPT processing, combined with the pre-existing internal stress from SLM fabrication, result in the formation of some sub-micron grains, as displayed by the BF TEM image in Fig. 9-4(d). This is supported by the selected area diffraction (SAD) pattern (inset of Fig. 9-4(d)) displaying elongated diffraction spots with short arcs. The average grain size is 268 ± 15 nm.

Furthermore, EDX maps of the HAADF-STEM image in Fig. 9-4(e) indicate that Fe (matrix element of 316L SS), Ni (matrix element of IN 718), and Cr (common in both materials) are mixed homogeneously within the matrix of the interfacial region (Figs. 9-4(f) – (j)). Higher concentration of Nb is observed along the boundaries of the columnar cells, suggesting that the accumulation of dislocations at the cell boundaries also coincide with the segregation of Nb. This further affirms that the thick cellular sub-structure boundaries (dislocation cells) are attributed to the combined influence of dislocation accumulation and/or segregation of heavier elements. The HAADF-STEM image in Fig. 9-4(k) exhibits a region of accumulated dislocations within the matrix of the interfacial region. The resulting EDX maps (Figs. 9-4(l) – (p)) demonstrate that they comprise of well-distributed Fe, Ni, and Cr with high Nb concentration at the edges. The average volume fraction of precipitates (Laves phase, NbC, and TiC) is evaluated as ~ 1.91 vol. % with an average diameter of ~ 31.72 nm. In addition, EDX area scan along the FZ (Fig. 9-4(a)) reveals the following elemental compositions (in wt. %); Cr: 19.85, Nb: 9.67, Mo: 3.1, Ti: 1.12, and ~ 33.13 of Fe and Ni each, which do not differ much from the as-received disk.

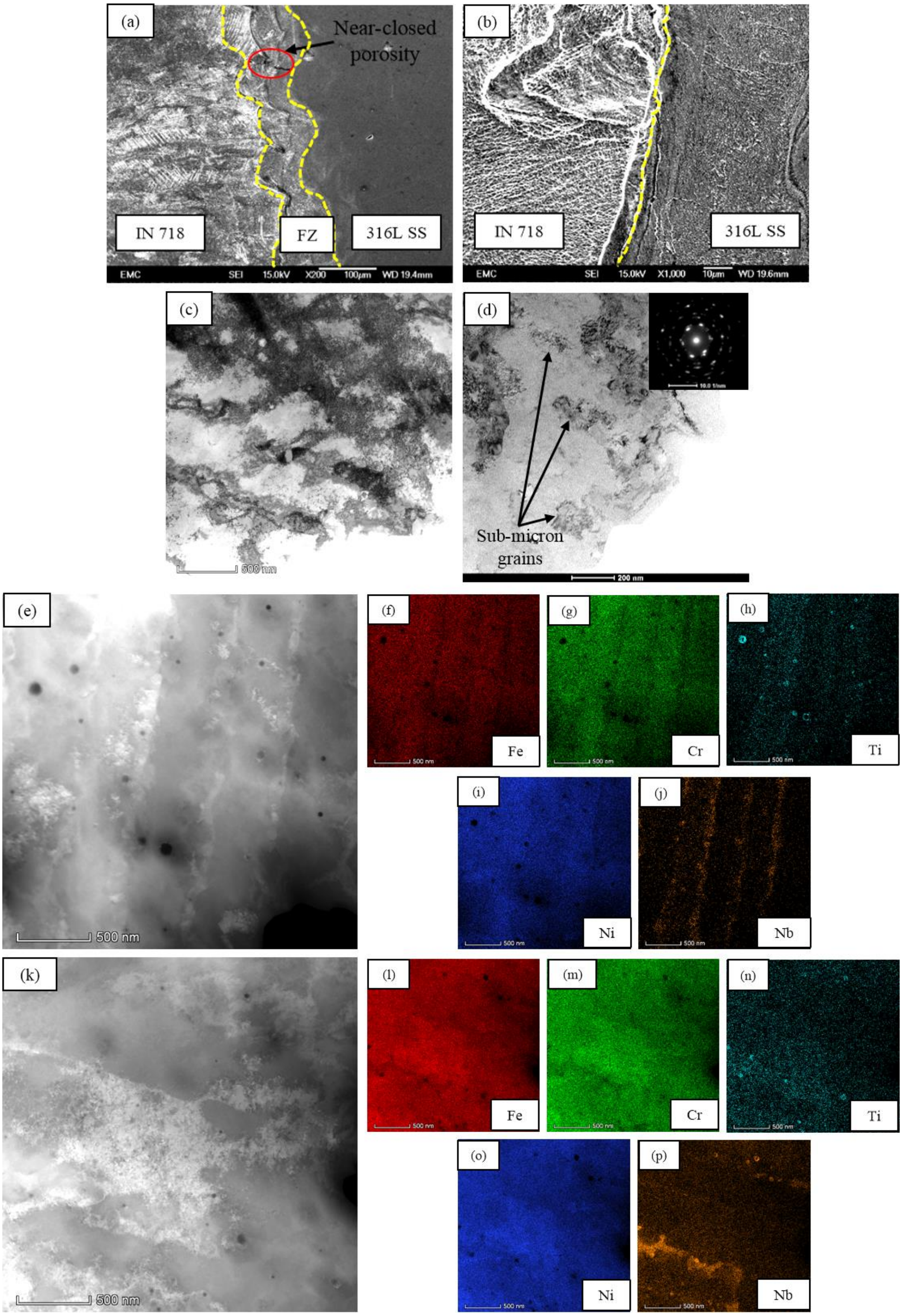

Fig. 9-4 SEM; (a) and (b), TEM; (c) and (d), and HAADF-STEM; (e) and (k) images, and corresponding EDX maps; (f) – (j) and (l) – (p) for specific areas at the interfacial region after 1/4 HPT revolution.

Fig. 9-5 displays a series of SEM, TEM, and STEM images of the MMAM disk taken at the periphery along the interfacial region (~ 3 mm from its centre) after 1 HPT revolution ($\varepsilon_{eq.} = 13.6$).

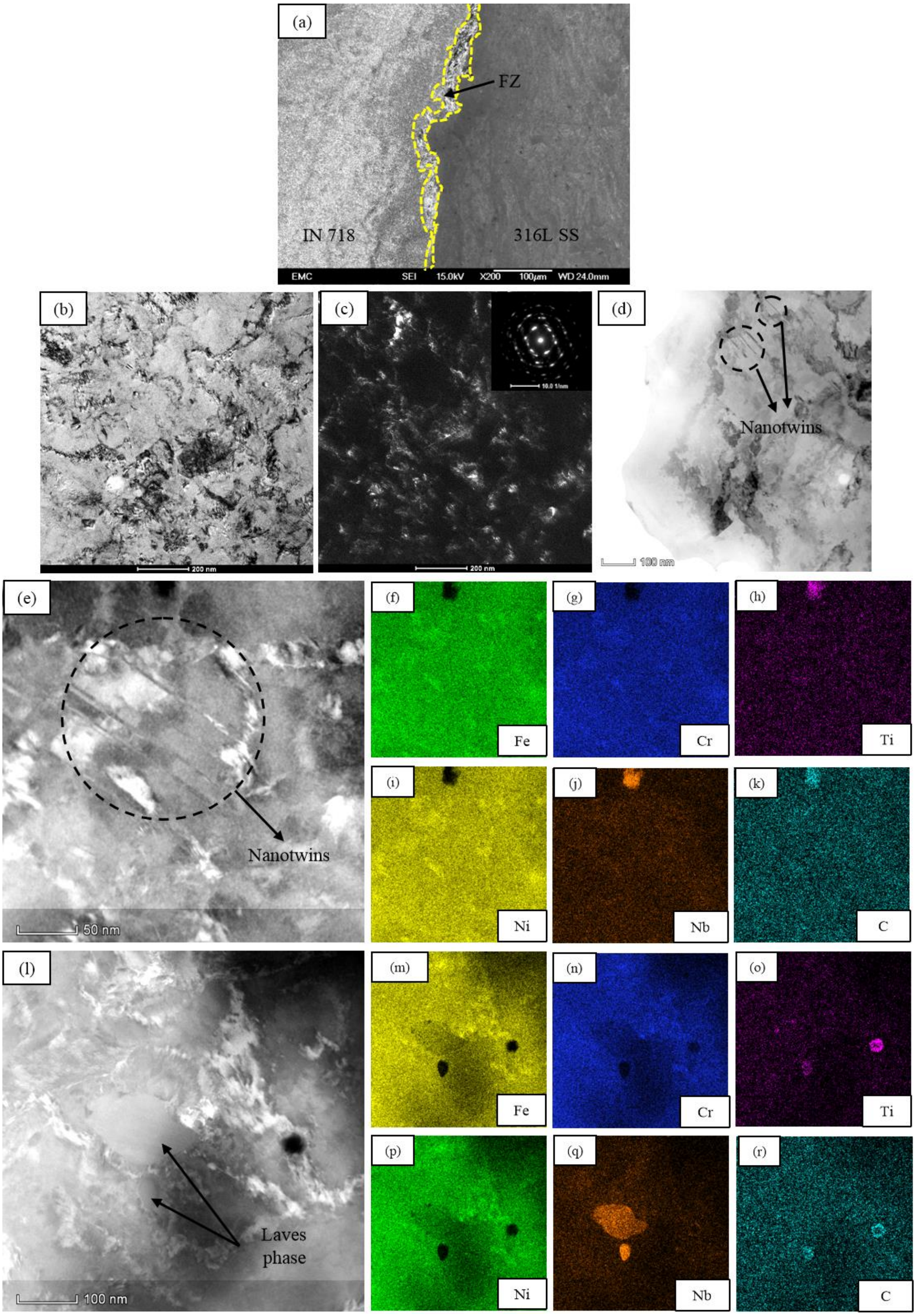

Fig. 9-5 SEM; (a), TEM; (b) – (d), and HAADF-STEM; (e) and (l) images, and corresponding EDX maps; (f) – (k) and (m) – (r) for specific areas at the interfacial region after 1 HPT revolution.

A pore-free structure is observed in Fig. 9-5(a) as the result of further HPT torsional straining. However, the width of the FZ significantly decreases to ~ 40 µm, which could either result in further diffusion and higher concentration of diffused elements into the FZ, or vice versa. BF and dark field (DF) TEM images in Figs.9-5(b) and (c), respectively show that while the dislocation density continues to increase, most of the dislocation cells and sub-micron grains have evolved into nano-scale grains with an average size of 96 ± 8 nm due to the continuous grain refinement. This is confirmed by the SAD pattern that shows elongated diffraction spots with diffused rings (inset of Fig. 9-5(c)). Nanotwins also start to appear as shown by the BF TEM images in Figs. 9-5(d).

The results of EDX mapping (Figs. 9-5(f) – (k)) of a region containing nanotwins shown by the HAADF-STEM image in Fig. 9-5(e) indicate that it consists of a homogeneously dispersed Fe, Ni, and Cr. The black sphere on top of Fig. 9-5(e) is determined to be a Nb- and Ti-rich carbide particle. On the other hand, the near-spherical globules shown in Fig. 9-5(l) is ascertained as the Laves phase from the results of EDX mapping in Figs. 9-5(m) – (r) based on the high concentrations of Fe, Ni, Nb, and Ti. At this stage, the average volume fraction of precipitates (Laves phase, NbC, and TiC) is evaluated as ~ 1.85 vol. % with an average diameter of ~ 31.2 nm. In addition, EDX area scan along the FZ (Fig. 9-5(a)) reveals the following elemental compositions (in wt. %); Cr: 19.22, Nb: 7.86, Mo: 2.7, Ti: 1.04, and ~ 34.59 of Fe and Ni each. Indeed, the content of alloying elements are now decreased compared to the as-received condition and after processed through 1/4 HPT revolution.

On the other hand, a series of SEM and TEM images of the MMAM disk taken at the periphery along the interfacial region (~ 3 mm from its centre) after 10 HPT revolution ($\varepsilon_{eq.}$ = 136) are shown in Fig. 9-6. The SEM image in Fig. 9-6(a) shows that the width of the FZ has been considerably reduced to < 5 µm and a relatively sharp interface boundary that distinctively separates the individual 316L SS and IN 718 regions are formed due to the extremely large torsional strain imposed by HPT at this stage. BF and DF TEM images in Figs. 9-6(b) and (c), respectively show further grain refinement with increasing HPT revolutions, and an average grain size of 50 ± 5 nm is obtained. The corresponding SAD pattern now exhibits brighter and increasing number of diffused rings, which indicate higher amounts of nano-scale grains with random orientation (inset of Fig. 9-6(c)). Furthermore, the BF TEM image in Figs. 9-6(d) reveal the prevalence of nanotwins, and that the formation of dislocation networks have reached a saturation level. Nevertheless, the nano-scale grains obtained after 10 HPT revolutions not only exhibit grains that contain nanotwins and dislocations within the grain interior, but also grains that are free from any microstructural features or internal sub-structures (Figs. 9-6(b) – (e)).

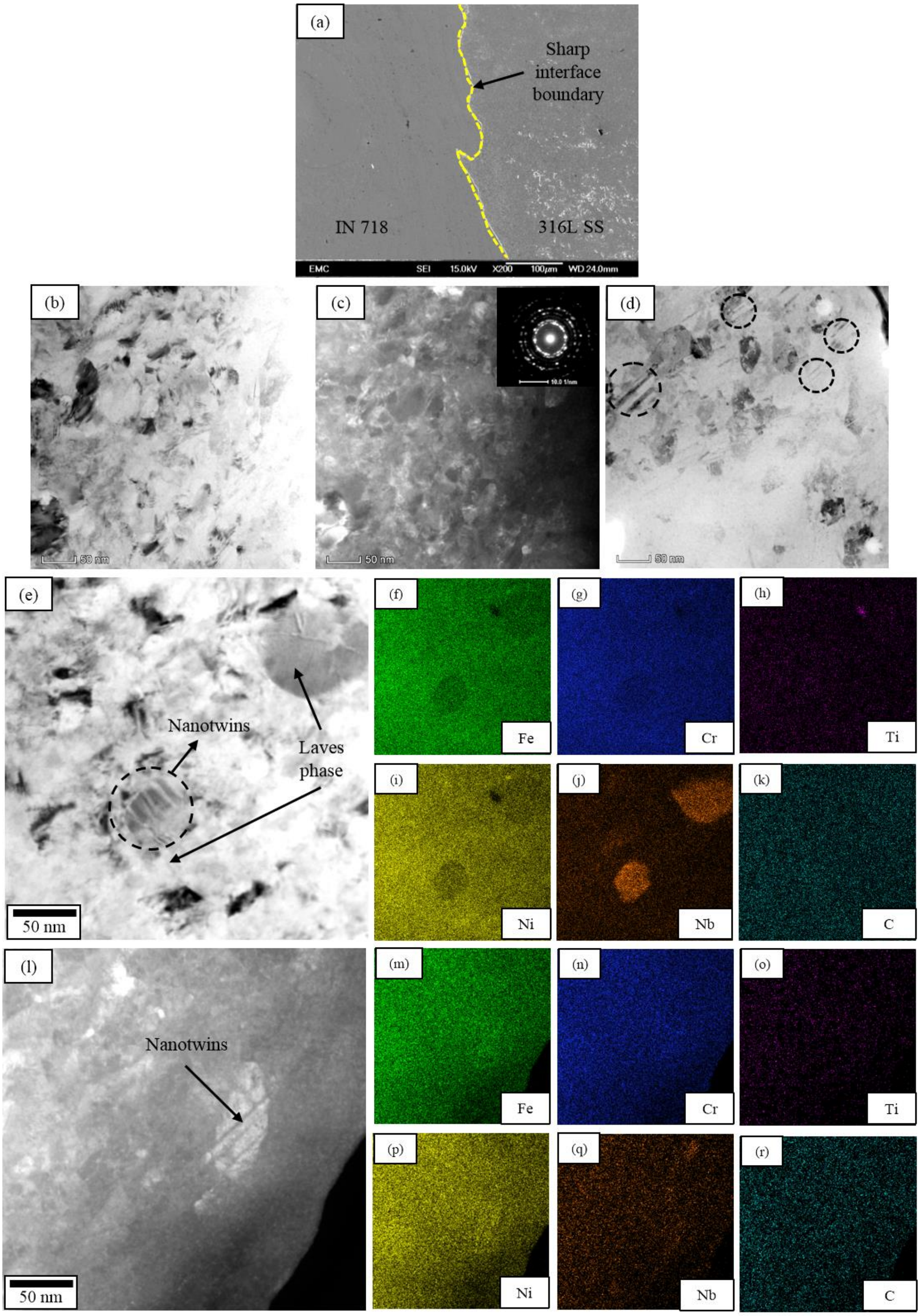

Fig. 9-6 SEM; (a), TEM; (b) – (d), and HAADF-STEM; (e) and (l) images and corresponding EDX maps; (f) – (k) and (m) – (r) for specific areas at the interfacial region after 10 HPT revolutions.

The EDX mapping results for the BF TEM image in Fig. 9-6(e) clearly indicate that the two grey globules are in fact the Laves phase based on the high concentrations of Fe, Ni, Nb, and Ti (Figs. 9-

6(f) – (k)). Furthermore, the nanotwins that exist within the interior of a nano-scale grain shown in Fig. 9-6(l) contain homogeneous dispersions of higher concentrations of Fe and Ni matrices, as well as relatively lower concentrations of other alloying elements (Cr, Nb, Ti, and C) as indicated by the EDX maps in Figs. 9-6(m) – (r). At this stage, the average volume fraction of precipitates (Laves phase, NbC, and TiC) is evaluated as ~ 1.79 vol. % with an average diameter of ~ 32 nm. In addition, EDX area scan along the FZ (Fig. 9-6(a)) reveals the following elemental compositions (in wt. %); Cr: 19.21, Nb: 7.2, Mo: 1.22, Ti: 0.8, and ~ 35.79 of Fe and Ni each. The content of alloying elements further decreases when compared to the as-received and other HPT-processed conditions with lower number of revolutions.

9.2.2 X-ray diffraction analysis

Fig. 9-7(a) display the XRD spectra for the as-received and HPT-processed disks obtained at the interfacial region, measured ~ 1 mm from either side of the FZ, while the XRD spectra collected at the IN 718 region, determined ~ 1 mm away from the FZ into the IN 718 region are shown in Fig. 9-7(b). Both sets of XRD data demonstrate that all disk conditions at these two regions mainly comprise of the γ-FCC peaks that coincide with γ''-BCT phase. The γ-FCC structure is the matrix phase of both 316L SS and IN 718, while the γ''-BCT structure is the primary strengthening phase of IN 718. It is known that γ''-BCT peaks overlap that of γ-FCC in typical XRD spectra of IN 718, thus unambiguous identification of their morphologies and structures must be distinguished via TEM observations [180,311,417]. However, TEM observations in Figs 9-3 – 9.6 indicate the absence of any formation of γ''-BCT precipitates that are often characterised as coherent disks with diameter of ~ 60 nm and thickness ~ 5 – 9 nm. Therefore, it could be confirmed that the XRD peaks in Figs. 9-7(a) and (b) correspond to γ-FCC only.

Furthermore, two weak peaks corresponding to (Nb,Ti)C phase are observed at the interfacial region (Figs. 9-7(c) and (d)), compared to only one peak obtained at the IN 718 region (Fig. 9-7(e)) for the as-received disk. This is confirmed by the presence of both Nb- and Ti-rich carbides determined from the results of EDX mapping in the previous section. These diffraction peaks remain consistent and no new peaks arise after HPT processing. Furthermore, the peaks of the HPT-processed samples appear to be broadened and slightly shift to lower angles compared to the initial positions in the as-received disk. These phenomena are attributed to lattice defects induced by HPT processing, e.g. small crystallite sizes, internal microstrains, and generated dislocations [431]. The XRD spectra taken at the 316L SS region is not present here because they are similar to that shown in Fig. 5-3 for the as-received and HPT-processed AM 316L SS in Chapter 5 (a single γ-FCC phase with broadened peaks after HPT processing). Thus, the results from the XRD spectra show that the overall AM 316L SS/IN 718 in this study solidifies with γ-FCC crystal structure without any phase transformation occurring after HPT processing.

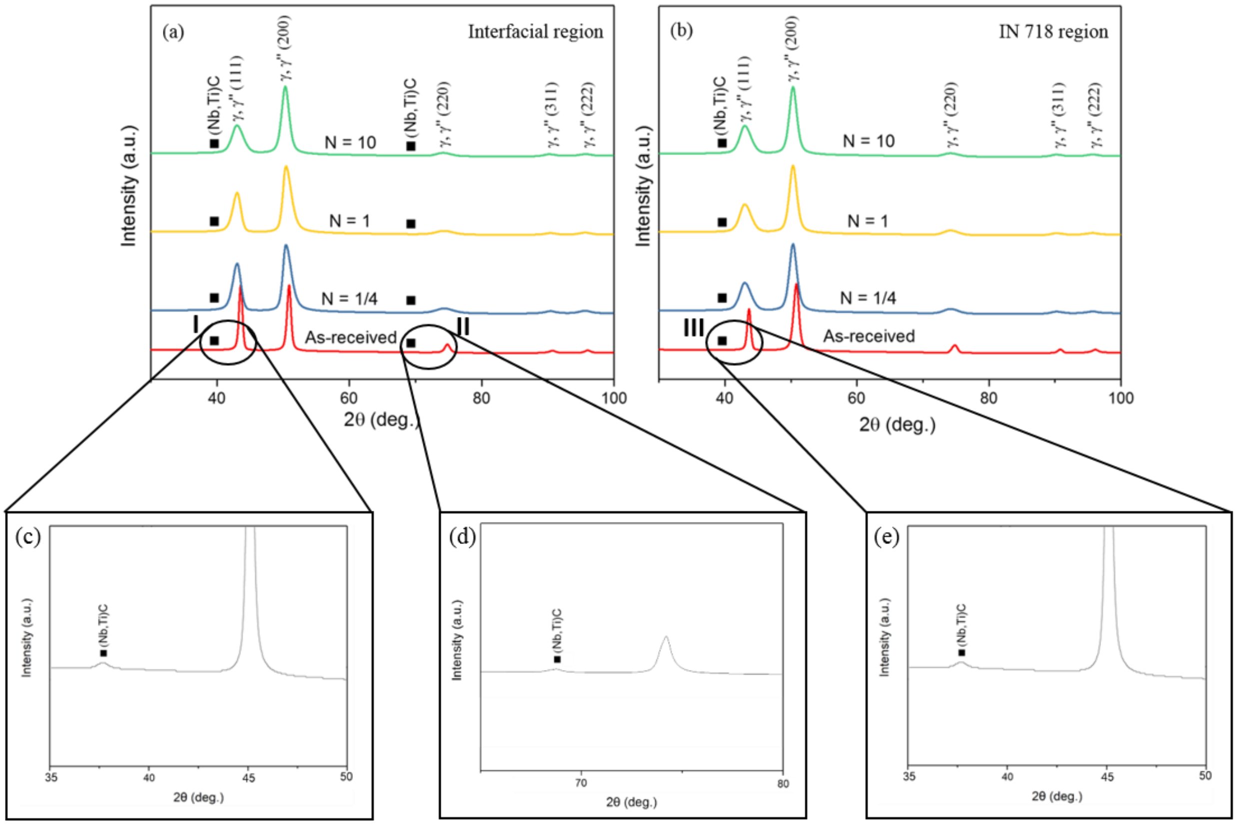

Fig. 9-7 XRD spectra taken at (a) the interfacial and (b) IN 718 regions for the as-received and HPT-processed MM disks; (c), (d), and (e) show zoomed-in examples of XRD peaks of the weak (Nb,Ti)C signals from regions I, II, and III of the main XRD spectra.

The average lattice microstrain, $\langle \varepsilon^2 \rangle^{1/2}$ and average crystallite size, D_c determined from the XRD line broadening peak analysis using the Rietveld refinement method applied in the MAUD software are used to estimate the dislocation density values, ρ at the interfacial region via Eqn. 5-1 described in Chapter 5. The corresponding values of ρ at the interfacial region calculated based on Eqn. 5-1 are shown in Fig. 9-8. It is revealed that the dislocation density, ρ significantly increases from ~ 0.94 x 10^{13} m^{-2} for the as-received MM disk to ~ 8.91 x 10^{14} m^{-2} after 1/4 HPT revolutions ($\varepsilon_{eq.\text{-}HPT} = 3.4$), before further increasing to ~ 1.06 x 10^{15} m^{-2} after 1 HPT revolution ($\varepsilon_{eq.\text{-}HPT} = 13.6$) and saturate at ~ 1.10 x 10^{15} m^{-2} after 10 HPT revolutions ($\varepsilon_{eq.\text{-}HPT} = 136$). The average crystallite size, D_c considerably decreases from 280 ± 20 nm for the as-received disk to 35 ± 4 nm after 1/4 HPT revolution before only reducing slightly to 30 ± 2 nm and 28 ± 2 nm after 1 and 10 HPT revolutions, respectively.

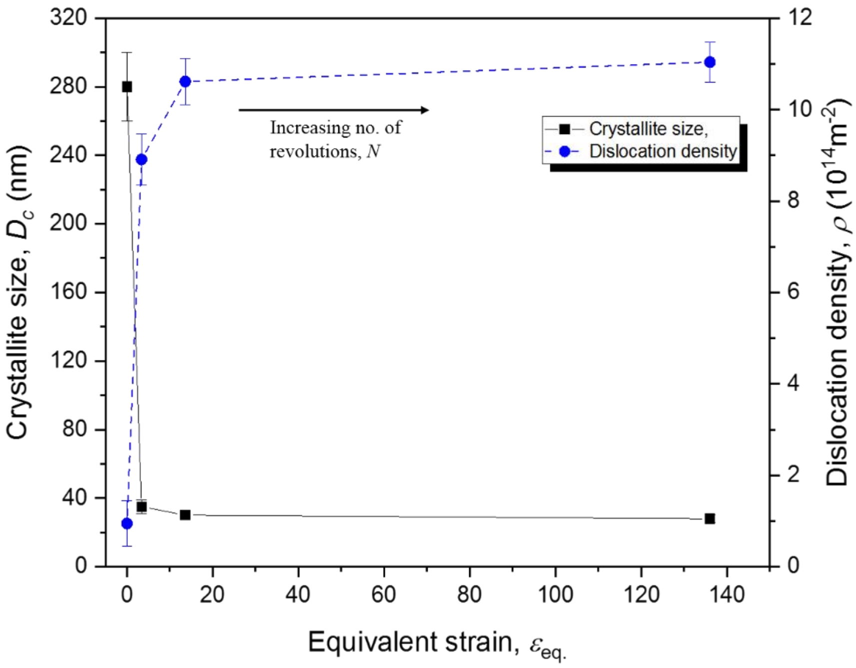

Fig. 9-8 Evolution of crystallite size and dislocation density at the interfacial region of the as-received and HPT-processed disks.

9.2.3 Hardness evolution

9.2.3.1 Microhardness across different materials

Fig. 9-9 displays the Vickers microhardness (HV) as a function of distance from the disk centre across the centre of the interfacial region, as well as the 316L SS and IN 718 regions. For the as-received condition, the HV values at the 316L SS region average at 220 ± 10 HV up to ~ 2 mm towards the interfacial region. The HV values then continuously increase until ~ 2 mm away from the centre of the FZ, before becoming relatively constant at the IN 718 region (average: 306 ± 6 HV). These values are consistent with that obtained in similar studies of MMAM 316L SS/IN 718 in literature [9,209]. The higher hardness of IN 718 compared to 316L SS is usually attributed to the formation of γ''-BCT precipitates (precipitation strengthening). However, the absence of any γ''-BCT precipitates based on the TEM observations in Figs. 9-3 – 9-6 suggest other contributors to the higher hardness of the interfacial region away from the 316L SS region and within the IN 718 region.

Firstly, the high stress condition induced during AM fabrication yield numerous cellular (equiaxed and columnar) sub-structures that store dislocations, forming dense dislocation networks that is known to impede dislocation motions and increase the strength of AM materials [127,277,312]. XRD line broadening analysis in Chapters 5 and 9 reveal higher dislocation density in IN 718 (~ 0.94 x 10^{13} m^{-2}) compared to 316L SS (~ 0.69 x 10^{13} m^{-2}). Secondly, carbide precipitates have also been shown to become effective sites to block dislocation motions to contribute to the strength of various metals and alloys via precipitation strengthening [180,203,417,619]. Thus, it is reasonable to infer that the presence of (Nb,Ti)C precipitates at the interfacial region provide precipitation strengthening in the absence of γ''-BCT precipitates in this study. Therefore, the higher hardness of the interfacial region compared to that of the 316L SS region can be attributed to the combined dense dislocation networks (dislocation strengthening), precipitation strengthening via (Nb,Ti)C precipitates, and solid solution strengthening, compared to only dislocation strengthening and solid solution strengthening for 316L SS.

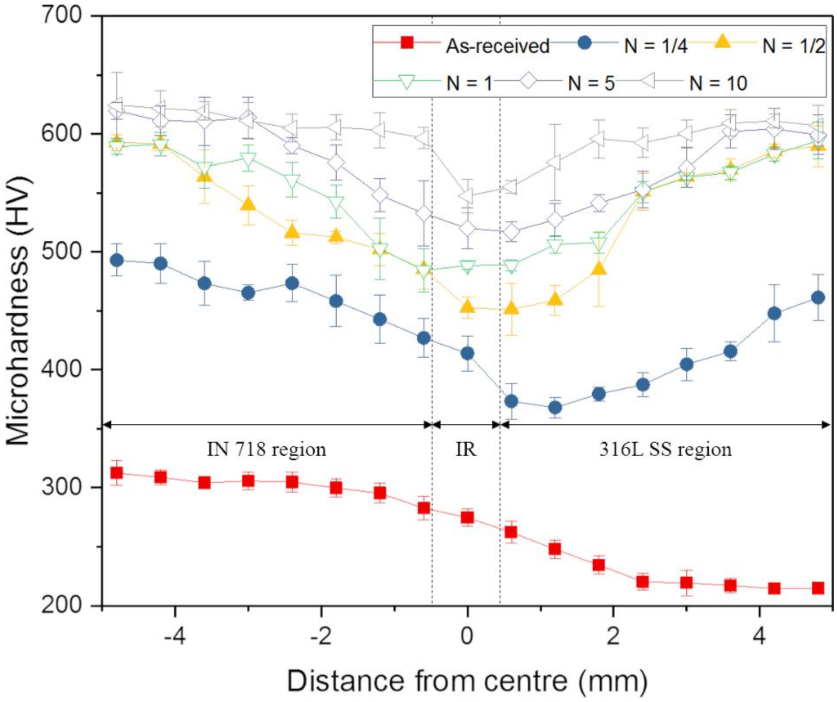

Fig. 9-9 HV distribution across the diameter of the as-received and HPT-processed MM disks across the centre of the interfacial region, as well as the 316L SS and IN 718 regions.

In addition, Fig. 9-9 also demonstrates that despite the significant increase in overall HV values with higher number HPT revolutions, hardness saturation is not achieved across the diameter of the disks through different material regions even after 10 HPT revolutions. The central region (including the interfacial region) exhibits lower HV values compared to the peripheral region (~ 3 mm away from the centre of the disk). This is the result of relatively lower plastic deformation at the central region due to the radial dependency of the HPT-induced torsional straining [620]. Nevertheless, an uneven hardening is attained after 1/4 HPT revolution ($\varepsilon_{\text{eq.-HPT}} = 3.4$), as indicated by the lower HV values at the 316L SS region compared to those at the IN 718 region. It is more likely that the strain level imposed at this stage is not sufficient to overcome the effects of precipitation strengthening (through (Nb,Ti)C precipitates rather than γ''-BCT precipitates) that initially provide additional strengthening to IN 718, despite the increased generation and multiplication of dislocation tangling networks due to HPT straining at this stage.

This discrepancy diminishes after 1/2 HPT revolution, ($\varepsilon_{\text{eq.-HPT}} > 6.8$), and a relatively even hardening is observed across the diameter of the disks through the different materials. This could be explained by the more significant influence of even larger dislocation densities and much smaller UFG/NG microstructures introduced with increased torsional straining that offset the effects of initial precipitation strengthening in providing more effective sites to impede dislocation motions. Furthermore, as has been detailed in Chapter 5, the formation of nanotwins after 1/2 HPT revolution in the AM 316L SS also contributes towards its hardening. Thus, although not evaluated in this chapter, it is highly possible that nanotwins are also present to provide additional strengthening for the 316L SS region to reach hardness values close to that at the IN 718 region with increasing HPT torsional strain. Moreover, the HV values at the periphery of both individual material regions become increasingly closer beyond 1 HPT revolution, indicating the slowing down of the hardening effect. This is commonly ascribed to the reduced strain hardening effect as the grain size undergoes refinement from the micron scale to the sub-micron and nano-scale regimes [231].

On the other hand, other studies have also attributed the inhomogeneous hardness distribution to the difficulty to produce UFG/NG microstructures due to the presence of considerable vol. % of intermetallics or secondary phases that could not be fully dissolved or homogeneously dispersed within the microstructure at the central region or close to the centre of the disks [450,621,622]. In this study, the content of precipitates (Laves and carbides) are relatively low (< 2 vol. %). However, it is reasonable to infer that the local torsional strains applied at the central region of the disks are still insufficient to produce sufficient grain refinement that can fully dissolve or homogeneously disperse both precipitates, even after 10 HPT revolutions [263]. Furthermore, even though hardness saturation across the diameter of the disks through the interfacial, 316L SS, and IN 718 regions is not observed, the HV distribution at the peripheral region on both sides of the disks (> 3 mm from the centre) appear uniform and reaches an average hardness of 618 ± 14 HV after 10 HPT revolutions ($\varepsilon_{\text{eq.-HPT}} = 136$).

9.2.3.2 Microhardness mapping at the peripheral areas of the interfacial region

In this study, it is found that the width of the interfacial region (including the FZ) becomes narrower with increasing torsional strain imposed at higher number of HPT revolutions (Figs. 9-1(a), 9-4(a), 9-5(a), and 9-6(a)), and the interfacial region becomes increasingly rotated in the direction of the applied torsional strain, as illustrated by the dashed red line in the schematic shown in Fig. 9-10.

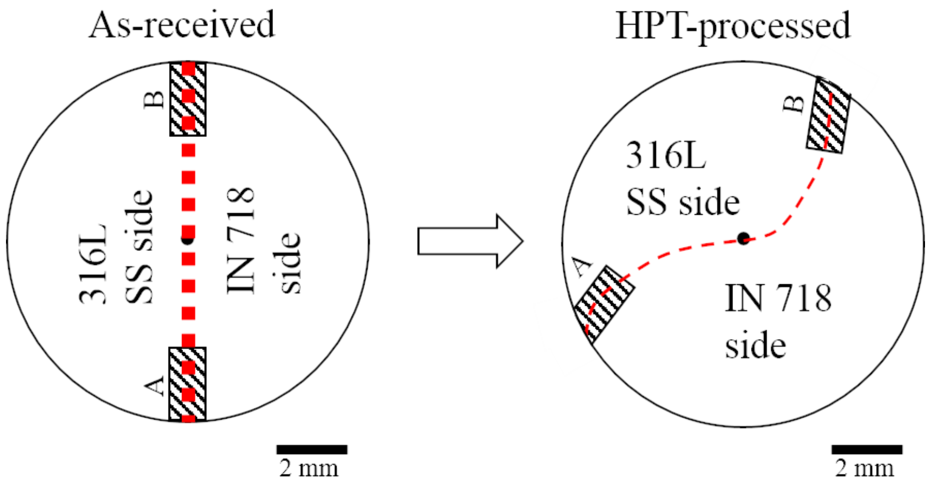

Fig. 9-10 Schematic of the evolution of shape and direction of the interfacial region, including the FZ before and after HPT processing (dashed red line). Shaded areas A and B demonstrate locations of microhardness mapping.

Therefore, it is difficult to determine the hardness evolution along the length of the interfacial region. Thus, microhardness mapping was carried out at the periphery along the interfacial region (which includes the FZ), ~ 3 mm from its centre at both opposing sides of the disks (labelled side A and side B in Fig. 9-10). The indent spacing is set as 0.1 mm, both horizontally and vertically between each indent to include the FZ, and the results are shown in Fig. 9-11. The colour legend is displayed on the right-hand side of Fig. 9-11, in which the colour key ranges from dark blue (lower hardness) to red (high hardness). In the figures, the datum point ‘0.0’ at the y-axis represent the centre of the FZ, while the values 0.1 and -0.1 represent the edges on either side of the FZ.

The trend of increasing hardness with higher number of HPT revolutions along the periphery of the interfacial region at both sides A and B (shown in Fig. 9-11) follows a similar trend as demonstrated in Fig. 9-9. Until 1 HPT revolution ($\varepsilon_{\text{eq.-HPT}}$ = 13.6), the hardness closer to the IN 718 region is relatively higher than that nearer to the 316L SS region (Fig. 9-11(a) – (f)). The average HV values measured from both sides A and B are 262 ± 14 HV (as-received), 456 ± 24 HV (N = 1/4), and 580 ± 10 HV (N = 1) However, the hardness seems to saturate at 622 ± 10 HV throughout the overall interfacial region for both sides A and B after 10 HPT revolutions (Figs. 9-11(g) and (h)). This value is consistent with the average HV value obtained at the peripheral regions shown in Fig. 9-9 (618 ± 14 HV). Therefore, it can be concluded that hardness saturation is indeed achieved at the peripheral areas for all three distinctive material regions; 316L SS, IN 718, and interfacial region after 10 HPT revolutions ($\varepsilon_{\text{eq.-HPT}}$ = 136).

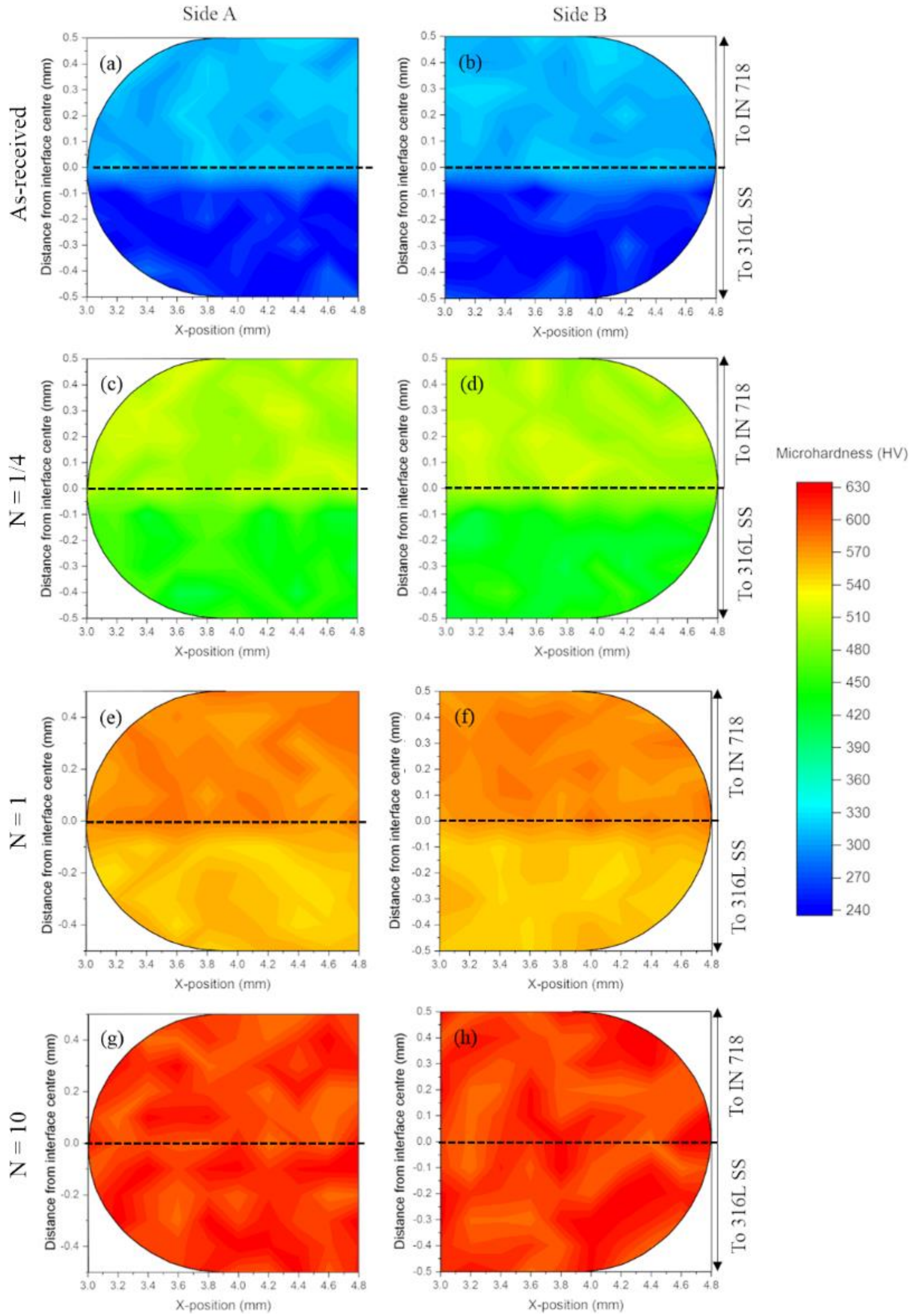

Fig. 9-11 Vickers microhardness mapping at the periphery along the interfacial region, taken ~ 3 mm from its centre on either side of the as-received and HPT-processed disks (sides A and B).

9.2.3.3 Nanoindentation measurements within the fusion zone

Although the microhardness measurements in the previous two sections shed light on the hardness evolution at the 316L SS, IN 718, and interfacial regions, they still do not show the hardness variation within the FZ itself. This is because the width of the FZ is too small (~ 100 µm) and the minimum distance of 0.1 mm between each indent that can be obtained from the HV indenter could not capture the hardness evolution inside the FZ. Therefore, nanoindentation measurements were conducted within the FZ at the periphery along the interfacial region, ~ 3 mm from its centre. The total coverage distance was 200 µm; 100 µm inside the FZ, and 50 µm each from the boundary of the FZ to the unmixed individual 316L SS and IN 718 sides. The distance between each indent inside the FZ is 10 µm, and 20 µm for locations outside of the FZ. The nanohardness, *H* value at each location is averaged from five different indents (the main indent and four other indents around it), as illustrated in Fig. 9-12. The results are displayed in Fig. 9-13.

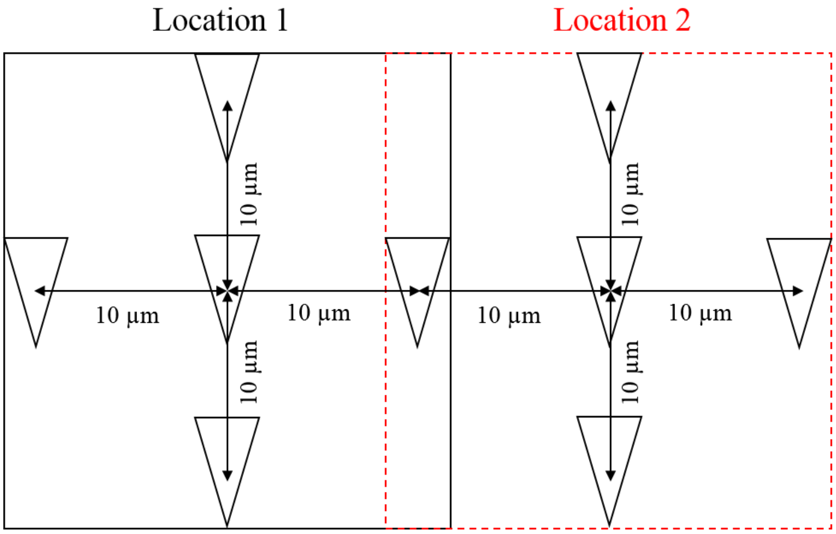

Fig. 9-12 Distance between each indent for the nanoindentation measurements, and the five individual indents used to determine the average nanohardness at each location.

A generally increasing trend of hardness is observed with higher number of HPT revolutions and the associated torsional strains as shown in Fig. 9-13(a). The nanohardness values at the IN 718 side are consistently higher than at the 316L SS side, with the *H* values within the FZ are somewhere between the individual material regions. However, this discrepancy decreases and an essentially homogenenous nanohardness distribution throughout the tested region is obtained with an average of 10.5 ± 0.5 GPa after 10 HPT revolutions. On the other hand, Fig. 9-13(b) shows the average distribution of Fe and Ni matrix elements and other alloying elements (Cr, Nb, Ti, and Mo) within the FZ and its vicinity for the as-received and HPT-processed disks. These results are obtained from EDX line scan analysis and averaged from several locations at the periphery across the interfacial region (~ 3 mm from its centre). It can be seen that the concentration of Fe and Ni vary fairly linearly among the individual 316L SS and IN 718 regions and inside the FZ. The concentration of Cr and

Mo do not vary much across all regions. Interestingly, some Ti and Nb contents could be observed towards the 316L SS region although both elements are originally absent in the precursor 316L SS powder. Thus, it can be inferred that the presence of Ti and Nb in the small 316L SS region could be due to the following reasons: (i) contamination of IN 718 powder when 316L SS powder layer is spread onto a previously solidified IN 718 layer due to incomplete powder removal/cleaning, or (ii) preferential segregation of the heavier Nb element along the cell boundaries and the affinity of Nb and Ti towards C to form NbC and TiC upon solidification when fresh IN 718 powder layer is spread onto a previously solidified 316L SS layer.

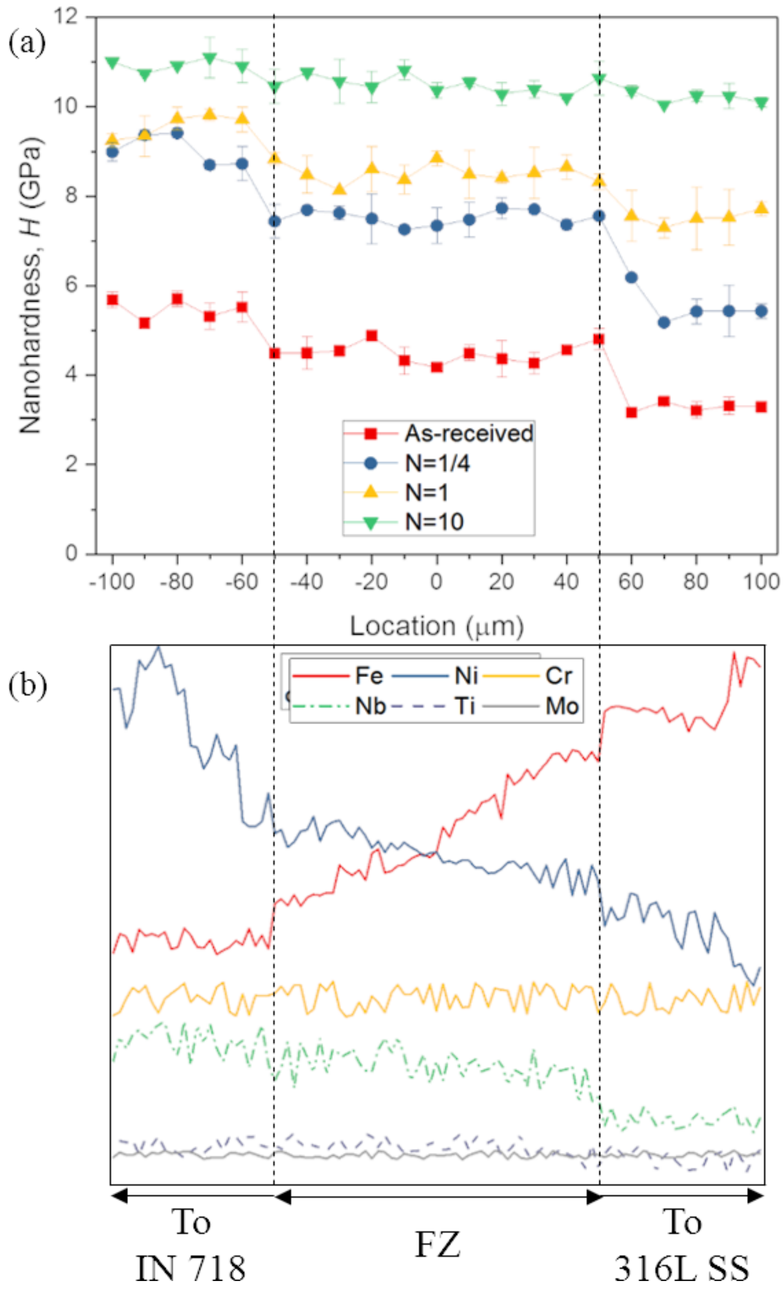

Fig. 9-13 (a) Nanohardness variation within the FZ and small regions outside it towards individual 316L SS and IN 718 regions outside the FZ, and (b) average distribution of Fe and Ni matrix elements and other alloying elements (Cr, Nb, Ti, and Mo) within the FZ and its vicinity obtained from EDX line scan analysis.

9.3 Discussion

9.3.1 Interfacial microstructures of the as-received MMAM 316L SS/IN 718 alloy

In this chapter, a MM 316L SS/IN 718 alloy structure was successfully additively manufactured via an in-house-developed SLM system. The EDX maps, BSE-SEM images, and EBSD maps of the as-received structure taken from the surface-parallel (x-z plane) clearly indicate that a dense interfacial region is obtained upon solidification. It comprises of distinct 316L SS and IN 718 regions, and an intermixed region of Fe and Ni termed as fusion zone (FZ) (Fig. 9-1). The width of the FZ is small (~ 100 µm), and it is obviously determined by the interfacial diffusion between Fe and Ni, in which the diffusion distance is influenced by the layer thickness and scan speed used during SLM [12–14]. Liu et al. [12] studied the SLM fabrication of MM 316L SS/C18400 Cu and used a layer thickness of 50 µm and varied the scan speed from 150 – 400 mm s^{-1} to obtain a FZ with a width of ~ 750 µm. Sing et al. [13] obtained ~ 200 µm wide FZ when using a layer thickness of 50 µm and varying the scan speed between 400 and 1140 mm s^{-1} to manufacture MM AlSi10Mg/C18400 Cu via SLM. Chen et al. [14] determined the FZ width of a SLM-built 316L SS/CuSn10 alloy as ~ 550 µm when the layer thickness was set as 30 µm and the scan speed ranged from 700 – 1200 mm s^{-1}.

Nevertheless, the results from the previous studies and in the present study demonstrate significant dilution and diffusion between the two dissimilar materials, signifying a good metallurgical bonding has been achieved at the FZ and at the overall interfacial region. The cohesive dilution and diffusion of individual matrix elements (e.g. Fe in 316L SS and Ni in IN 718) can be attributed to the continuous partial re-melting and melting of previously solidified and successively deposited powder layers, respectively, creating a sound metallurgical bonding commonly observed in cladding processes [12,623]. When the first layer of IN 718 powder is deposited and melted on the previously solidified 316L SS layer, the top portion of the solidified 316L SS layer also melts and mixes with the freshly melted IN 718 layer, resulting in a high percentage of Fe in the first IN 718 layer. As subsequently deposited IN 718 powder layers are melted and fused, the percentage of Fe continuously decreases while the percentage of Ni steadily increases. This process is repeated until the percentage of Fe reduces to a minimum value and that of Ni rises close to its initial composition in the precursor IN 718 powder, in this case at the edge of the FZ after ~ 100 µm. Beyond that, only IN 718 powder undergoes melting and fusion as it moves further away from the FZ (Fig. 9-13 (b)). These observations imply that a gradual variation of elemental Fe and Ni matrices are obtained within the FZ rather than an abrupt change, which could result in improved bonding strength of the joint, i.e. the interfacial region [14].

On the other hand, the EBSD maps in Figs. 9-1(g) – (i) and the SEM images in Fig. 9-2 taken at the surface-parallel (x-z plane) of the interfacial region of the as-received MM disk reveal an epitaxial growth trend approximately parallel to the build direction (x-z plane), which is manifested by the formation of columnar grains and elongated columnar cellular sub-structures. These phenomena are common in AM materials at the surface-parallel direction, resulting from the partial re-melting of previously solidified powder bed layers, enabling the already-formed grains to become nucleation sites for subsequent grain growth in successively deposited powder bed layers [84,208,624]. The directional growth of the grains and cellular sub-structures through several melt pools across multiple powder bed layers can be ascribed to the scan strategy, temperature gradient, cooling rates, and the nature of heat flow during SLM processing [205,278,337,342,386].

Pham et al. [278], Popovich et al. [205], and Ni et al. [337] found that the heat conduction through the build substrate and successively solidified powder layers are superior than the thermal conductivity through metal powders, and better than the heat convection between newly formed melt pool and the surrounding environment. This results in very high cooling rates that favour rapid directional solidification, which promotes elongated columnar grains to grow parallel to the build direction (x-z plane). This is the most likely explanation to describe the growth of columnar grains and elongated columnar cells observed in Figs 9-1 and 9-2. However, Deng et al. [342] and Kuo et el. [625] explained that the temperature gradient and heat flux direction may not necessarily be directly parallel to the build direction, but can be rotated to slightly different orientations, In fact, they can be influenced by the scan strategy used during SLM processing and the overlapping melt pools. Thus, the lack of preferred growth orientation observed in the present study might be explained by the uni-directional scan strategy that rotates by 90° for each powder layer deposited.

Similarly, the nucleation and growth of the elongated columnar cells are strongly controlled by the localised temperature gradient and heat flux direction [278,342]. Within a single melt pool, the existing columnar sub-structures might have already solidified in a preferred orientation due to the epitaxial growth. If the localised thermal condition and temperature gradient of a new melt pool favour the preferred growth direction of the existing columnar sub-structures, then new columnar sub-structures can nucleate and grow in the same direction as the existing ones, thereby creating a continuous growth of columnar sub-structures across multiple melt pools. However, if these conditions are not met, then the growth of new columnar sub-structures will be suppressed at the adjacent MPB and follow the more thermally favoured direction in the new melt pool. Based on the SEM images in Figs. 9-2, most of the columnar sub-structures grow in a stop-start manner, i.e. stop at the MPBs and nucleate at different directions in different melt pools across the interfacial region (the individual 316L and IN 718 regions, and the FZ). Thus, it is highly possible that the growth of the columnar sub-structures in this stop-start manner can be attributed to the varying laser beam movements that follow the pre-set scan strategy, which constantly change the heat flux direction and create highly localised temperature gradients.

Moreover, EBSD maps in Figs. 9-1(g) – (i) reveal that the 316L SS region have relatively coarser grains (average: 85 ± 3 μm) than that at the IN 718 region (average: 55 ± 5 μm). This can be ascribed to the slightly higher CTE value of 316L SS (~ 16 μm m^{-1} $°C^{-1}$) compared to IN 718 (~ 13 μm m^{-}

^{1} °C^{-1}), which allows for larger area and volume expansion for the solidified grains at a given temperature gradient [626,627]. Furthermore, it is interesting to see that the FZ consists of fine, equiaxed grains (average: 45 ± 3 μm) rather than columnar grains observed in the respective individual material regions. This could most possibly be the result of abrupt discrete material change, i.e. from 316L SS to IN 718 powders and vice versa and multiple thermal excursions that occur within the 3 – 4 fused powder layers. Combined with the rapid heating/cooling cycles of SLM processing, these two factors result in much steeper thermal gradients that suppress grain growth to yield the fine, equiaxed grains comprising of mixed Fe and Ni matrices [12,84].

In addition to the structure, morphology, and orientation of grain and cellular sub-structures, the distribution of phase and precipitation also play significant roles in determining the mechanical properties of AM metals and alloys. Hence, it is interesting to see the types of phases and precipitates that are formed at the interfacial region, particularly at the intermixed region (FZ) of the as-received MMAM 316L SS/IN 718 alloy, which are characterised by XRD analysis and TEM observations in this chapter. The XRD analysis at the interfacial region shown in Fig. 9-7(a) reveals strong γ-FCC peaks that typically coincide with those of γ''-BCT, which usually correspond to the austenite matrix and primary strengthening phases, respectively. IN 718 contains Nb that promotes the formation of γ''-Ni_3Nb phase. Although this phase has a BCT structure, it is coherent with the γ matrix, which results in XRD peaks that coincide with those associated with the γ-FCC structure [625]. In addition, two weak signals corresponding to (Nb,Ti)C carbide phase are also obtained, and no signal of Laves phase is observed, which is probably due to their significantly smaller vol. % in the microstructure. Although it is known that γ''-BCT is the primary strengthening phase of IN 718, the absence of any such precipitates based on TEM observations in Figs. 9-3 – 9-6 suggest that the higher hardness of the interfacial region compared to that of the 316L SS region is contributed by other factors, which has been revealed to be the high dislocation density and the (Nb,Ti)C carbide phase precipitates instead.

The TEM images and EDX maps of the as-received MM disk shown in Fig. 9-3 clearly exhibit the presence of nearly spherical globules of Laves phase, spherical Nb-rich carbides (NbC) mostly along the cellular boundaries, and also spherical Ti-rich carbides (TiC) largely within the matrix of the solidified structure. It is known that Laves phase is a brittle intermetallic compound that is typically formed in IN 718 as the result of heavy Nb segregation, which is detrimental to the mechanical properties and therefore undesirable [180]. Although the SLM fabrication technique has shown the ability to prevent heavy macrosegregation due to the rapid melt pool solidification, which could theoretically suppress or minimise the formation of Laves phase, it is very difficult to completely prevent microsegregations [312,341]. Such microsegregation is attributed to the rapid growth of columnar cells and columnar grains resulting from the fast solidification and high cooling rates of SLM process [339]. Therefore, the enrichment of Nb along the boundaries of the columnar sub-structures shown in Figs. 9-3(g) – (t) is inferred to be driven by the microsegregation effect.

Furthermore, the formation of NbC along the cell boundaries and TiC within the matrix upon solidification can be ascribed to the affinity of both Nb and Ti towards C to form the respective carbides. In fact, the formation of NbC and Laves phase along the cell boundaries can also be obtained from the eutectic reactions; L → γ + NbC and/or L → γ + Laves [336,339]. However, the significantly low vol. % of the laves phase and carbides compared to the γ and γ'' phases within the interfacial region of the as-received MM alloy (~ 1.87 vol. %) might explain the weak (Nb,Ti)C signals and the absence of Laves phase in the XRD spectra (Fig. 9-7).

Interestingly, the segregation of Mo into the cellular boundaries and the formation of Cr-based spherical nano-silicates commonly observed in AM 316L SS are not observed at the interfacial region of the as-received MM disk based on TEM and EDX analysis. The lack of Mo segregation into the cellular boundaries may be explained by the much lower Mo content (~ 2.5 wt. %) compared to Nb (~ 5.01 wt. %) in the raw precursor powders, and the higher propensity of Nb for microsegregation due to its relatively lower partition coefficient than Mo [126,341,443]. Similarly, it is found that the Cr-based nano-silicates are formed due to the high affinity of Si and Cr to oxygen at high temperatures [126,277]. However, the considerably low Si content in the initial powders (~ 0.09 wt. %) and the scarcity of oxygen due to Ar gas being purged inside the build chamber are very unlikely to result in the formation of this type of nano-inclusions, at least at the FZ and the overall interfacial region of the MM alloy. Therefore, it is reasonable to infer that the microstructural features within the FZ are dominated by those commonly observed in AM IN 718, particularly the Laves phase $(Ni,Fe)_2(Nb,Ti)$ and carbides (NbC and TiC). This is most likely due to the preferential microsegregation of Nb within the matrix and into the cell boundaries in IN 718 as a result of its higher vol. % compared to Mo in both IN 718 and 316L SS powders.

Moreover, the FZ and the overall interfacial region of the as-received MM alloy are also characterised by dense dislocation tangling networks both at the cellular boundaries and within the matrix (Figs. 9-3(a) – (d)). When measured by using XRD line broadening data through the MAUD software, the dislocation density, ρ is estimated as ~ 0.94×10^{13} m^{-2}, which is much higher than ~ 10^{9} – 10^{10} m^{-2} typically attained in CM metals and alloys [127,278]. However, this value is consistent with that obtained in the AM 316L SS detailed in Chapter 5, and in the study of DMLS-fabricated AlSi10Mg by Hadadzadeh et al. [130,628,629]. In fact, the presence of dense entangled dislocations is commonly observed in AM metals and alloys [296–298]. It is known that the formation of dislocation networks is primarily caused by the accumulation of high internal stresses within a material. The repeated rapid heating/cooling cycles and high cooling rates in AM processes act as a mean of continuous addition and removal of energy from a material, which induces a certain level of plastic deformation that results in piling up of internal stress inside the material [277,312].

9.3.2 Evolution of porosity and interfacial microstructures after HPT processing

HPT processing through 1/4 revolution ($\varepsilon_{\text{eq.-HPT}} = 3.4$) has considerably reduced the porosity in the as-received MM alloy from ~ 0.81% to only ~ 0.066% (Figs. 9-1 and 9-4(a)). The high percentage of porosity reduction (~ 91%) is consistent with that obtained in the HPT processing of AM 316L SS described in Chapter 4 (Fig. 4-3). Although the pores observed in the MM alloy are largely process-induced, as characterised by their irregular morphologies, the mechanisms for pore closure via the combined compressive force and torsional strain are the same as that observed in the HPT-processed AM 316L SS (Chapter 4) and in other CM materials [372]. In fact, the relatively large elongated pore observed within the FZ of the as-received disk (Fig. 9-1) is nearly closed after 1/4 HPT revolution (Fig. 9-4(a)). Further torsional straining to $\varepsilon_{\text{eq.-HPT}} = 13.6$ (1 HPT revolution) results in an essentially pore-free structure as shown in Fig. 9-5(a). However, although various studies on joining 316L SS and IN 718 alloys either by conventional welding or brazing processes, or by AM techniques indeed show pores, cracks, and voids at the bonding interface, they are rarely quantified [8,9,209,609,610,630–632]. Thus, it is difficult to directly compare with the results of porosity evolution in the present chapter. Only one study conducted by Bansal et al. [606] on the joining of these two materials by microwave hybrid heating (MHH) attempted to quantify the porosity at the interface, which was determined as ~ 0.94%. Nevertheless, the significant porosity reduction obtained for the MM alloy in this study further confirms the effectiveness of HPT processing in eliminating both gas-induced (spherical) and process-induced (irregular shaped) pores.

Moreover, increasing the HPT torsional strains with higher number of HPT revolutions significantly reduce the width of the FZ along the interfacial region periphery, from ~ 100 μm before HPT processing to ~ 5 μm after 10 HPT revolutions ($\varepsilon_{\text{eq.-HPT}} = 136$). This observation is consistent with the study by Kawasaki et al. [615] who developed a Al 1050/ZK 60 Mg MMNC structure by HPT processing the individual Al and Mg alloys simultaneously. A diffusion width of 2.5 μm was observed at the interface between both materials after 5 HPT revolutions. Similarly, Chen et al. [633] attained a diffusion length of ~ 2 μm at the interfacial region after simultaneously processing pure Al 100 with AZ 31 Mg alloys through three ARB cycles. No cracks or voids were observed at the diffused interface due to repeated plastic deformation straining and diffusion bonding. Thus, a sharp boundary was created at the interface between the two materials and an abrupt change in the composition of the matrix elements, Al and Mg was observed.

Although the width of the FZ is significantly reduced, and a similarly sharp boundary is obtained after 10 HPT revolutions in the present study of MMAM 316L SS/IN718, the compositional variation of the matrix elements (Fe and Ni) still exhibits a gradual shift across the interfacial region, rather than an abrupt change. This is most likely the result of the homogeneous distribution of Fe and Ni that is observed in the as-received disk due to complete diffusion, which carries on through all HPT processing conditions as shown by the EDX maps and line scan analysis results in Figs. 9-3 – 9.6, and Fig. 9-13(b), respectively.

9.3.3 Evolution of hardness at the interfacial region before and after HPT processing

The microhardness mapping at the periphery along the interfacial region (~ 3 mm from its centre) shown in Fig. 9-11 exhibit homogeneous HV distribution after 10 HPT revolutions, which saturate at 622 ± 10 HV. This value is consistent with the average HV value calculated from the peripheral areas of the individual 316L SS and IN 718 regions after 10 HPT revolutions (618 ± 14 HV) displayed in Fig. 9-9. These results suggest that a reasonable hardness saturation and microstructural homogeneity can be achieved if sufficiently high torsional strain is able to produce adequate grain refinement to completely dissolve or homogenously disperse the intermetallics and secondary phases within the matrix of the HPT-processed material. This is in line with the results of the study by Kawasaki et al. [506,615] who studied the HPT processing of separate Al 1050 and ZK 60 Mg disks to produce a hybrid Al/Mg MMNC structure. They obtained high HV values at the disk periphery (~ 3 mm from the centre) after 5 revolutions, which was attributed to the homogeneous distribution of Mg within the Al matrix.

In fact, the EDX mapping results from the present study shown in Figs. 9-3 – 9-6 clearly indicate the dissolution of Laves phase that are normally found along the cellular boundaries due to microsegregation of Nb with increasing number of HPT revolutions. Some Laves phase that are still present after HPT processing are no longer concentrated at the cellular boundaries, but exist as individual globules, e.g. (Figs. 9-5(l) and 9-6(e)). However, most of them are dissolved and distributed homogeneously as Nb within the matrix at the interfacial region. Furthermore, it is known that the highest torsional strain value and the smallest grain size formed as the result of HPT straining are often produced at the peripheral disk regions (~ 3 mm from the centre) [495,496,517,634]. Therefore, it is plausible to associate the reasonable hardness saturation achieved throughout the peripheral areas of the HPT-processed disks after 10 HPT revolutions for different material regions (individual 316L SS and IN 718 regions, and the interfacial region) with the highest torsional strain imposed at this stage ($\varepsilon_{\text{eq.-HPT}} = 136$).

Nevertheless, upon further inspection of the microhardness mapping results (Fig. 9-11), the hardness increase with higher HPT torsional strain values does follow the trend of typical HPT-processed materials, in which strong hardening is obtained after 1/4 HPT revolution with progressively smaller hardness increase attained after further HPT straining. The average HV values measured from both opposing sides of the interfacial region peripheries (sides A and B in Fig. 9-10) are 262 ± 14 HV for the as-received disk, 456 ± 24 HV (N = 1/4), 580 ± 10 HV (N = 1), and 622 ± 10 HV (N = 10). In this study, the hardness evolution at the interfacial region peripheries can be associated with the microstructural features analysed through TEM and STEM observations, EDX maps and area scans, and XRD analysis.

For the as-received MM disk, the hardness of the interfacial region is ascribed to the contribution of friction stress and the alloying elements from both 316L SS and IN 718 (solid solution strengthening), precipitation hardening due to the reinforcement Nb- and Ti-rich carbides (the Laves phase neither add nor reduce the strength of the material due to their very low content), and dislocation tangling networks (measured as ~ 0.94 x 10^{13} m^{-2} from XRD line broadening analysis). TEM and STEM images and EDX maps in Fig. 9-3 indicate that TiC particles are prevalent within the matrix, while NbC particles are concentrated along the cellular boundaries, together with the Laves phase. This is because of the preferential microsegregation of Nb at the cellular boundaries, although both Nb and Ti have high affinity to C [205,312,341]. In addition, Fig. 9-3(a) – (d) exhibit dense dislocations concentrated along the cellular boundaries and within the matrix, and also dislocation pile-up at the cellular boundaries, which correlate well with the relatively high dislocation density estimated from XRD analysis. The average HV value obtained at the interfacial region for the as-received condition is 262 ± 14 HV, which is higher than that obtained at the diffusion region of fusion-welded 316L SS/IN 718 joints (~ 155 – 250 HV) [606,610,630], but comparable to those obtained via SLM (~ 260 – 280 HV) [9,209]. The higher HV values of the AM joints is attributed to the higher dislocation densities and fine grain sizes obtained due to the repeated rapid heating/cooling cycle, which induces very high cooling rates and suppresses grain growth compared to conventional fusion welding processes [635].

After 1/4 HPT revolution ($\varepsilon_{eq.} = 3.4$), TEM images in Fig. 9-4 and XRD analysis in Fig. 9-8 suggest increased contribution by dislocation strengthening and grain boundary strengthening to the overall hardening of the interfacial region peripheries. Significant generation and multiplication of dislocations (ρ = ~ 8.91 x 10^{14} m^{-2}) compared to the as-received disk are observed due to the strong strain hardening effect, which is typically observed during the early stage of HPT processing [261–263]. Furthermore, grain refinement to the UFG regime (average: 268 ± 15 nm) is also obtained at this stage.

Interestingly, deformation twins (nanotwins) begin to appear both within a grain interior and through multiple grains after 1 HPT revolution ($\varepsilon_{eq.} = 13.6$) as shown in Figs. 9-5(d) and (e). They compete with the accumulated dislocations to provide additional strengthening at the interfacial region, together with the continuous grain refinement (average grain size: 96 ± 8 nm) at this stage. The deformation of metals and alloys via combined dislocation and twinning strengthening is typically observed in materials with high stacking fault energy (SFE) [300,307,426,463]. In addition, the deformation rate has also been shown to influence the formation of deformation twins, where high strain rates and relatively lower temperatures are able to produce numerous nanotwins in Cu that possess medium SFE [636]. When the conditions that favour the development of nanotwins are met, the critically resolved shear stress (CRSS) for twinning will be reduced compared to that of dislocation slip and/or glide, thus activating the nanotwin formation [636].

In the present study, HPT processing was conducted at room temperature (RT), while the SFE for 316L SS was estimated as ~ 64 mJ m^{-2} in Chapter 5. Although not measured directly, the SFE for IN 718 is assumed to be relatively high based on the works on Ni evaluated in Refs. [448,637].

Therefore, it is reasonable to infer that the torsional strain applied after 1 HPT revolution ($\varepsilon_{\text{eq.-HPT}}$ = 13.6), together with the RT HPT processing and high SFE are optimum conditions to trigger the formation of nanotwins. Since the nanotwins are in the nanometer regime, it is believed that they are generated when nano-scale grains (grains sizes < 100 nm) are first formed from the rotation of the cellular sub-structure boundaries, rather than via nucleation of primary micron-sized twins through shear bands that are typically observed in other HPT-deformed FCC alloys [638]. The nanotwin boundaries can become additional sites that impede dislocation motions and contribute to additional strengthening in HPT-processed materials [482].

The grain size further reduces to an average of 50 ± 5nm upon continuous grain refinement after 10 HPT revolutions ($\varepsilon_{\text{eq.-HPT}}$ = 136). The dislocation density, ρ estimated via XRD analysis only slightly increases to = ~ 1.10 x 10^{15} m^{-2}) from ~ 1.06 x 10^{15} m^{-2} after 1 HPT revolution. The nano-scale grains observed at this stage (Figs. 9-6) are observed to be mostly free from any sub-structures within their interior, but some of the grain interior still contain dislocations and nanotwins. This is because below a critical nanometer grain size, larger amounts of internal stresses are required to emit dislocation partials and cause difficulty for twinning to occur [639]. Therefore, it is believed that the formation of dislocations and twins have reached a saturation level, and are unlikely to produce further strengthening beyond 10 HPT revolutions.

Finally, an important aspect to note is that, although Laves phase is known to be detrimental to the mechanical properties due to its brittle nature, but its presence in small quantities of either granular or block morphologies with < 2 vol. % has been shown to have little to no impact on the overall strength of metals and alloys [640]. In the present chapter, the content of precipitates (both Laves phase and carbides) at the interfacial region is very small (average: ~ 1.9 vol. %), throughout all processing conditions, in which only ~ 25% is attributed to the Laves phase as determined from the analysis of TEM micrographs through ImageJ software. In addition, they indeed appear as small granules or globules as shown in Fig. 9-5(l) and 9-6(e). Therefore, this is the most likely reason to explain how the high hardness values at the interfacial region are maintained, despite the presence of Laves phase. Overall, the EDX maps (Figs. 9-3 – 9.6) and EDX line scan analysis results (Fig. 9-13(b)) show homogeneous dispersions of Fe and Ni into the matrix at the interfacial region. These indicate complete diffusion of these matrix phases with gradient compositional change across the FZ and the individual 316L SS and IN 718 regions.

9.3.4 A model for multiple strengthening mechanisms of the interfacial region

As mentioned previously, the significant hardening of the interfacial region for the as-received and HPT-processed MMAM 316L SS/IN 718 is contributed by the combination of intrinsic strength of the material, σ_0, solid solution strengthening, $\Delta\sigma_{SS}$, precipitation strengthening, $\Delta\sigma_{ORO}$, dislocation strengthening, $\Delta\sigma_{\rho}$, grain boundary strengthening, $\Delta\sigma_{GB}$, and twinning strengthening $\Delta\sigma_{TW}$. The contribution of each strengthening component to the overall strengthening can be estimated by modifying the additive theory that has already been described as Eqn. 5-4 in Chapter 5, with an additional component, $\Delta\sigma_{ORO}$, expressed by [477]:

$$\sigma_y = \sigma_0 + \Delta\sigma_{SS} + \Delta\sigma_{ORO} + \Delta\sigma_\rho + \Delta\sigma_{GB} \qquad \text{Eqn. 9-1}$$

The value of σ_0 for γ-Fe is ~ 15.4 MPa as determined in Chapter 5, and ~ 22 MPa for γ-Ni [641,642]. Assuming equal contribution of both lattice structures within the interfacial region, which is reasonable due to the similar wt. % of Fe and Ni for as-received and HPT-processed disks as determined by EDX area scan analysis, the average value of both (18.7 MPa) is taken and used as the value of σ_0 in this model.

Eqn. 5-6 from Chapter 5 is used to evaluate the contribution of solid solution strengthening, $\Delta\sigma_{SS}$. However, it is slightly modified to include a constant, *n* with the value of 2/3 for better experimental data fitting that includes Ni superalloys following the assessment by Goodfellow [643]. The modified equation is shown as follows [483,643]:

$$\Delta\sigma_{SS} = \sum k_i c_i^n \qquad \text{Eqn. 9-2}$$

The values of c_i for different alloying elements are determined from the EDX area scan analysis taken at the interfacial region peripheries as presented in previous sections.

The presence of Nb- and Ti-rich carbide particles (NbC and TiC) along the cellular boundaries and within the matrix at the interfacial region, respectively act as obstacles against dislocation motions, in which they are bypassed by the dislocations via Orowan looping, cross-slip or particle shearing [644]. The presence of secondary particles and precipitates have been found to provide additional strengthening to metals and alloys via precipitation strengthening [130,628,629]. In the present study, the dislocations are observed to bypass the carbides via the Orowan looping mode rather than shearing through them (Figs. 9-3(c), (d), and (f)). The contribution of precipitation strengthening can be assessed by the Orowan mechanism, $\Delta\sigma_{ORO}$ as follows:

$$\Delta\sigma_{ORO} = M\Delta\tau_{ORO} = M\frac{Gb}{\lambda_{ppt.}} \qquad \text{Eqn. 9-3}$$

where *M* is the Taylor orientation factor, taken as 3.05 for FCC materials [479], *b* is the burgers vector (0.26 nm for both 316L SS and IN 718 [304,641,645], *G* is the shear modulus (77000 MPa for both 316L SS and IN 718 [479,646], and $\lambda_{ppt.}$ is the average spacing of the carbides, determined by the following equation [299]:

$$\lambda_{ppt.} = \frac{4(1-f_{ppt.})r_{ppt.}}{f_{ppt.}} \qquad \text{Eqn. 9-4}$$

where $f_{ppt.}$ and $r_{ppt.}$ are the average volume fraction of the carbides and average radius between each other, respectively.

The contribution of dislocation strengthening, $\Delta\sigma_\rho$ in HPT-processed materials, considering both statistically stored dislocations (SSDs) and geometrically necessary dislocations (GNDs) is estimated by using Eqn. 5-5 previously described in Chapter 5. On the other hand, the contribution of grain boundary strengthening, $\Delta\sigma_{\mathrm{GB}}$ and twinning strengthening, $\Delta\sigma_{\mathrm{TW}}$ are determined from Eqn. 5-7 detailed in Chapter 5.

The yield strength, σ_{y} of the as-received and HPT-processed disks are predicted by using the linear additive model that considers the contribution of various strengthening mechanisms as described previously. The data obtained from microhardness mapping, XRD analysis, and TEM observations with EDX analysis, all taken at the periphery along the interfacial region (~ 3 mm from its centre), and values for constants and other parameters extracted from available literature are used for the present model. They are presented in Table 9-1. Dislocation density, ρ values are estimated from XRD line broadening analysis using the MAUD software shown in Fig. 9-8.

Table 9-1 Parameter values used in calculations for the strengthening mechanism model.

Mechanism	**Symbol**	**Value**	**References**
Solid solution strengthening	$\boldsymbol{C_\mathrm{i}}$	3	[488]
	$\boldsymbol{M}$	3.05	[479]
	$\boldsymbol{b}$	0.26 nm	[304,641,645]
	$\boldsymbol{G}$	77000 GPa	[479,646]
	$\boldsymbol{\alpha_1}$	0.3	[482]
	$\boldsymbol{k_{\mathrm{Cr}}}$	6.96 MPa/at. $\%^{2/3}$ Cr	[643]
	$\boldsymbol{k_{\mathrm{Nb}}}$	10.58 MPa/at. $\%^{2/3}$ Nb	[643]
	$\boldsymbol{k_{\mathrm{Mo}}}$	10.05 MPa/at. $\%^{2/3}$ Mo	[643]
	$\boldsymbol{k_{\mathrm{Ti}}}$	9.18 MPa/at. $\%^{2/3}$ Ti	[643]
Orowan strengthening	$\boldsymbol{f_{\mathrm{ppt.}}}$	1.43 vol. %– 1.50 vol. %	This work (TEM)
	$\boldsymbol{r_{\mathrm{ppt.}}}$	15.0 nm – 16.0 nm	This work (TEM)
Dislocation strengthening	$\boldsymbol{\rho_{\mathrm{total}}}$	0.942×10^{13} m^{-2}–1.10×10^{15} m^{-2}	This work (XRD)
	$\boldsymbol{D_\mathrm{C}}$	280 nm – 28 nm	This work (XRD)
Grain boundary/twin strengthening	$\boldsymbol{K_{\mathrm{HP}}}$	As-received: 2.8 MPa m$^{-1/2}$ HPT-processed: 0.3 MPa m$^{-1/2}$	[252,479]
	$\boldsymbol{K_{\mathrm{TW}}}$	0.3 MPa m$^{-1/2}$	[252,479]
	$\boldsymbol{d}$	45 µm – 50 nm	This work (TEM)
	$\boldsymbol{e}$	4 nm (N=1), 3.8 nm (N=10)	This work (TEM)
	$\boldsymbol{f}$	0.166 (N=1), 0.164 (N=10)	This work (TEM)
	$\boldsymbol{\lambda}$	41 nm (N=1, N=10)	This work (TEM)

The modelling results for the contribution of individual strengthening mechanisms are summed up to predict the overall yield strength. These values are then compared with the results of microhardness mapping at the periphery along the interfacial region (~ 3 mm from its centre) in the present chapter. The relationship between Vickers microhardness (HV) and yield strength, σ_{y} is often approximated by the empirical relationship $\Delta\ \sigma_{\mathrm{y}}$ = HV/3 [488]. This relation can be used as a good approximation for the yield strength of SPD-processed metals and alloys due to the decreasing strain hardening effect with increasing strain values, resulting in σ_y values close to the ultimate tensile strength σ_{UTS} [489,490]. Therefore, the values of σ_y can be estimated from HV values measured from microhardness mapping as σ_y = HV/3 with the unit of MPa. Fig. 9-14(a) displays the comparison between the overall predicted strength and measured HV/3, while Fig. 9-14 (b) compares the contribution of individual strengthening mechanisms from the modelling results.

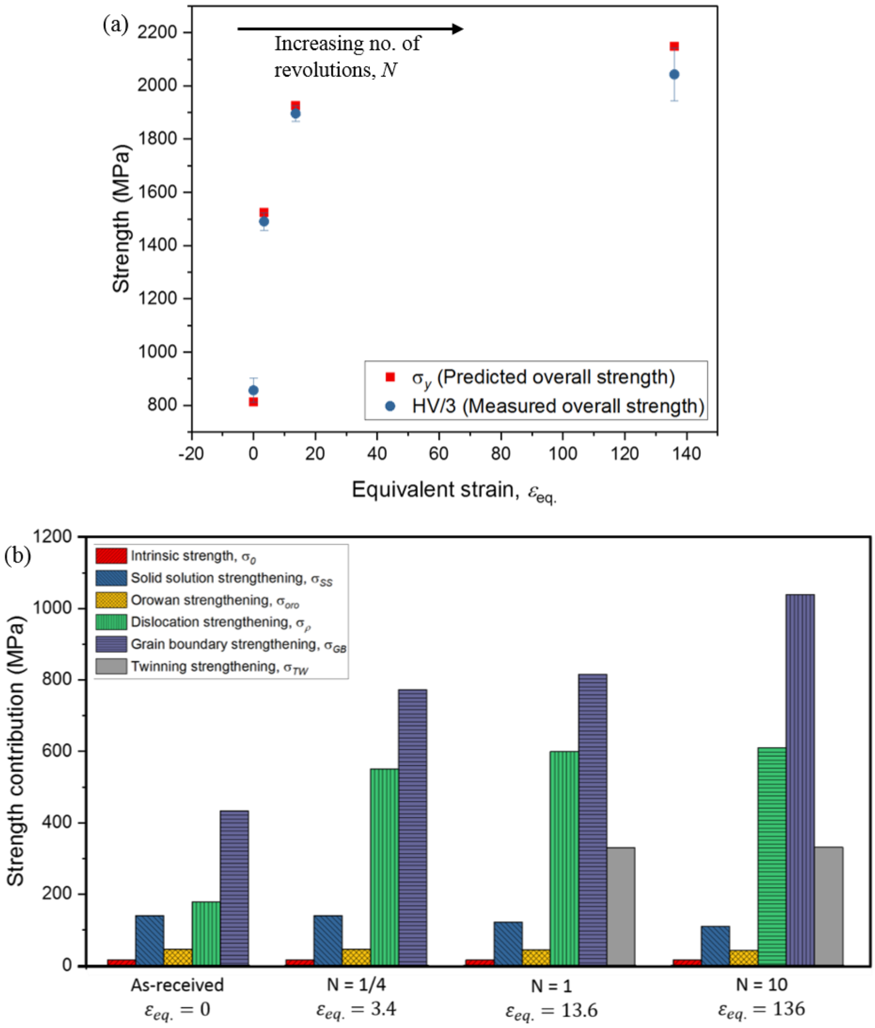

Fig. 9-14 (a) Comparison between overall predicted strength and measured HV/3 and (b) contribution of individual strengthening mechanisms on the overall strengthening of the as-received and HPT-processed disks obtained from the modelling results.

A good correspondence between the predicted and measured strengths, with a small deviation (average: ~ 3.5%) is observed based on the results shown in Fig. 9-14(a). Therefore, the present modelling approach is able to coherently describe the evolution of strength at the interfacial region for the MMAM 316L SS/IN 718 before and after HPT processing. Similar physical-based modelling approach has been widely used to correctly predict the evolution of hardness and strength of various HPT-processed metals and alloys in literature [496,497,517,518,634,647].

In the current modelling results presented in Fig. 9-14(b), the contribution of intrinsic strength and precipitation strengthening are consistently the lowest for the as-received and HPT-processed disks, respectively accounting for only ~ 0.87 – 2.23% and ~ 1.95 – 5.52%, with grain boundary strengthening always the highest (~ 42 – 53%). While the grain boundary strengthening is the primary mechanism of hardening for the as-received disk (433 MPa, ~ 53.1%), solid solution and dislocation strengthening mechanisms exhibit a competing role to provide additional hardening, 140 MPa (~ 17.3%) and 179 MPa (~ 21.9%), respectively from the overall strength, 816 MPa. This could be the result of high segregation of heavy alloying elements such as Nb, Mo, and Ti along the cellular boundaries and within the matrix of the interfacial region, as well as the high density of dislocation tangling network and dislocation pile-up compared to CM metals and alloys as mentioned previously.

After 1/4 HPT revolution ($\varepsilon_{\text{eq.-HPT}} = 3.4$), the contribution from dislocation strengthening jumps to 550 MPa (~ 36%) of the overall strength (1527 MPa), which is expected due to the strong strain hardening effect during the early stage of HPT processing [231,647]. Meanwhile, although the actual value of the solid solution strengthening is the same as that in the as-received alloy (140 MPa), its percentage of contribution actually decreases significantly to ~ 9.17%. This is reflected by the content of alloying elements that do not differ much as determined via EDX area scan analysis, which implies that the considerable increase in dislocations outweighs the contribution of alloying elements. The contribution of grain boundary strengthening remains the highest, 773 MPa corresponding to > 50%, which is consistent with that for the as-received alloy and can be ascribed to the significant grain refinement down to the UFG regime.

The emergence of nanotwins that contribute ~ 17.1% (330 MPa) to the overall strength value of 1929 MPa after 1 HPT revolution ($\varepsilon_{\text{eq.-HPT}} = 13.6$) is observed to reduce the percentage of contribution by dislocation strengthening (~ 31.1%) and grain boundary strengthening (~ 42.3%). This is demonstrated by the marginal increase in their numerical values to 600 MPa and 815 MPa, respectively when compared to those after 1/4 HPT revolution. In particular, the nanotwins have been found to act as supplementary grain boundaries, thereby competing with the initial grain boundaries to increase the strength at the interfacial region [303,482,484,485]. Furthermore, it is evident that the work hardening effect is decreased with increasing number of HPT revolution, indicating that a near-saturation condition is reached as has been observed in most HPT-processed metals and alloys [261–263]. In addition, the percentage contribution of solid solution strengthening has also decreased to ~ 6.27% (121 MPa). This could be related to the alteration and/or redistribution of the alloying elements due to extreme torsional strain, which has been shown to reduce the solid solution strengthening effect in SPD-processed alloys [220,494]. Indeed, the EDX area scan analysis at the interfacial region periphery reveals the reduced content of Nb from 9.67 wt. % after 1/4 HPT revolution to 7.86 wt. % after 1 HPT revolution, confirming the previous explanation.

After further straining to $\varepsilon_{\text{eq.-HPT}} = 136$ via 10 HPT revolutions, the overall strength increases to 2150 MPa. The percentage of contribution from both dislocation and twinning strengthening mechanisms slightly decrease to ~ 28.4% (610 MPa) and ~ 15.4%, (332 MPa), respectively. The reduced contribution of dislocation strengthening can be attributed to the saturation in the strain hardening at a critical strain value, beyond which only minimal change in the dislocation generation is attained [475]. In fact, only a small increase in the value of dislocation density, ρ is observed in this study after 10 HPT revolutions, ~ 1.10 x 10^{15} m^{-2} compared to ~ 1.06 x 10^{15} m^{-2} after 1 HPT revolution, which affirms that the saturation in the strain hardening effect has been achieved. On the other hand, the essentially unchanged value of the twinning strengthening at this stage relative to after 1 HPT revolution might be explained by the continuous grain refinement within the NG regime, from 96 ± 8 nm (N = 1) to 50 ± 5 nm. At this point, it is reasonable to infer that the increasing amount of nano-scale grain boundaries can no longer accommodate further twinning due to the larger internal stress levels that are necessary to emit dislocation partials and activate nanotwin formation [639]. This is evidenced by the nano-scale grains that are mostly free from sub-structures such as dislocations and nanotwins within the interior, as shown in Figs. 9-6(b) and (d). Thus, the percentage of contribution from grain boundary strengthening increases to ~ 48.3% (1039 MPa). Nevertheless, the consistently higher contribution of grain boundary strengthening to the overall strength of HPT-processed CM metals and alloys compared to other strengthening mechanisms has been confirmed in various literature [479,482,490,495–497].

9.4 Summary

In this chapter, the porosity, microstructural evolution and strengthening at the interfacial region of HPT-processed MMAM 316L SS/IN 718 have been investigated through EBSD, SEM, TEM, XRD, and hardness measurements. A linear additive model was established to evaluate the contribution of various strengthening mechanisms on the overall strength of the alloy. The following conclusions can be drawn based on the results in this chapter:

1. The largely irregular-shaped (process-induced) porosity is significantly reduced from the as-received condition to only after 1/4 HPT revolution, which represents ~ 91% reduction.
2. Hardness saturation and microstructural homogeneity are only achieved at the peripheral areas of the disk after 10 HPT revolutions.
3. At the interfacial region periphery, significant reduction in crystallite size, D_c and increased dislocation density, ρ are attained with increasing HPT revolutions, and a final average grain size of 50 ± 5 nm is obtained after 10 HPT revolutions.
4. TEM and EDX analysis reveal the presence of Nb- and Ti-rich carbides and Laves phase at the interfacial region of the as-received and HPT-processed disks.
5. The modelling results show that the significant hardness increase of the interfacial region due to HPT processing is primarily contributed by grain boundary strengthening, followed by dislocation strengthening, twinning strengthening, and solid solution strengthening. Precipitation strengthening and intrinsic strength provide the least contributions to the overall strength.

Chapter 10 General discussion

It is clear that AM possesses many advantages over CM for manufacturing a wide range of metals and alloys. In particular, the tremendous design flexibility and the capability of microstructure tailoring according to the desired applications make AM the superior manufacturing technology compared to CM. PBF and DED metal AM techniques, such as SLM, EBM, LENS and DMD have been used to manufacture complex parts with cellular lattice structures and graded porosity that have low mass, good energy absorption, and good thermal properties [62,648–650]. The characteristics of parts with a complete lattice structure, or solid outer profile with inner lattice structure allow for lightweighting of advanced engineering components, such as biomedical implants, aircraft wing spars, aero-engine components, and energy storage devices for electric vehicles [73,651,652]. In addition, solid structures with tailored microstructures and mechanical properties have also been produced by these metal AM processes by controlling process parameters and scan strategy for applications in the nuclear, power, aerospace, and other high-temperature applications [653–656].

Several studies have shown that AM-fabricated metallic components possess better or comparable mechanical properties than the CM counterparts. For example, the yield strength of AM 316L SS has been reported to be as high as ~ 600 MPa compared to ~ 200 – 300 MPa for the wrought or cast 316L SS [35,68]. The improvement in mechanical properties of AM metallic parts is often attributed to the fine grain sizes (< 30 µm) and high dislocation densities (> x 10^{13} m^{-2}) [127]. This is in contrast with CM parts that typically have relatively coarser grain sizes (40 – 60 µm) and much lower dislocation densities (x 10^{9} – x 10^{10} m^{-2}) [127]. Thus, it is apparent that the Hall-Petch relationship still applies for AM materials, in which grain refinement leads to higher yield strength. Therefore, if continuous grain refinement down to the sub-micron and/or nano-scale regime (UFG/NG microstructures) can be obtained in AM metallic parts, then it is highly likely that their yield and tensile strengths can exceed those of the as-built components.

So far, SPD processes, such as ECAP and HPT are the two of the most effective techniques to produce UFG and/or NG microstructures [19,20]. Various studies have shown not only significantly enhanced yield and tensile strength in UFG/NG CM metals and alloys, but considerably improved corrosion, wear, creep, and fatigue properties [22–24]. However, SPD processing has never been studied in AM materials before, which motivates the current study. In this study, HPT processing was used to produce UFG and/or NG microstructures in AM alloys, and their influence on the porosity, hardness, deformation and strengthening mechanisms, and corrosion and wear performances were investigated. Indeed, the results and discussion in Chapters 4 – 9 show promising results, including significant reduction in porosity, considerably high hardness, and enhanced corrosion and wear performances in AM-fabricated alloys, as the result of the sub-micron and nano-scale grain refinement obtained by SPD processing.

10.1 Establishing process-microstructure-property relationships for SPD-processed AM alloys

In this study, HPT processing is applied to AM 316L SS (single-material) and AM 316L SS/IN 718 (multi-material) to produce UFG/NG microstructures, and the process-microstructure-property relationships are subsequently investigated.

In particular, the results in Chapter 5 reveal that SPD processing through HPT is able to significantly enhance the hardness of AM 316L SS as the result of extreme grain refinement down to the UFG and UG regime (grain size factor) and sub-micron/nano-scale dislocations and twins (nanostructural elements). Furthermore, the phase transformation from a single γ-austenite FCC phase into strain-induced α'-BCC or ε-HCP martensite can sometimes occur in 316L SS due to the significantly high straining imposed by various SPD processing techniques. Table 10-1 compares the grain size, phase evolution, and hardness of HPT-processed AM 316L SS in this study with those of SPD-processed CM 316L SS and other CM austenitic SS available in literature.

It is clear that HPT yields the highest strength enhancement for the various austenitic SS due to its capability of imposing larger strains to produce smaller nano-scale grains compared to other SPD techniques. Furthermore, the formation of martensite phase due to martensitic transformation upon severe deformation also provides additional hardening to the austenitic SS. In fact, the hardness values obtained upon saturation of HPT straining, i.e. after 10 revolutions are relatively higher (> 600 HV) with the presence of martensites within the austenite matrix compared to those for austenitic SS with only a single γ-austenite phase (~ 300 – 600 HV). However, although the martensite phase is harder than austenite and contributes to phase transformation hardening [252,305,306,420,498], it is less ductile and less corrosion resistant, thereby increasing the susceptibility of austenitic SS to catastrophic failure during service, e.g. stress corrosion cracking, corrosion fatigue, and low temperature sensitisation [500–505]. Thus, the formation of strain-induced martensites need to be prevented so that the corrosion resistance of austenitic SS, particularly 316L SS can be maintained while gaining the advantage of enhanced strength after being processed by SPD.

Interestingly, based on Table 10-1, two studies on HPT-processed CM 316L SS, which maintain a single γ-austenite phase with grain sizes between 40 – 100 nm also show higher HV values (570 – 597 HV) [303,469]. It was revealed that deformation twins (nanotwins) were present after HPT processing, in which they have been found to provide additional strengthening to nanostructured materials [303,482,484,485]. Similarly, nanotwins are also observed in the HPT-processed AM 316L SS in this study, while maintaining its single γ-austenite FCC phase without martensitic formation to attain 600 HV upon saturation stage after 10 HPT revolutions. The factors that contribute to the strengthening of the material and the suppression of martensites throughout the HPT-processed disks have been discussed in detail in Chapter 5. Therefore, it can be reasonably inferred that in the absence of martensitic transformation, the presence of nanotwins can provide additional strengthening to achieve total strength close to that in SPD-processed CM or AM austenitic SS that undergo martensitic phase transformation.

Table 10-1 Comparison of grain size, phase, and microhardness of various SPD methods for CM 316L SS and other CM austenitic SS in literature, and AM 316L SS in this study.

Material	**Processing conditions**	**Average grain size (nm)**	**Phase**	**Hardness (HV)**	**Reference**
316L SS	SLM (as-received)	40000	γ	220	This study
	SLM + HPT RT (N=10, $\varepsilon_{eq.}$=136)	42	γ	600	
	Wrought	42000	$\gamma + \alpha'$	143	[252]
	Wrought + HPT RT (N=10, $\varepsilon_{eq.}$=136)	45	$\gamma + \varepsilon + \alpha'$	612	
	Wrought	20000	γ	143	[301]
	Wrought + HPT RT (N=10, $\varepsilon_{eq.}$=136)	62	γ	500	
	Wrought + HPT RT (N=10, $\varepsilon_{eq.}$=136) + HT (500°C, 1 hr)	53	γ	571	
	Wrought	42000	$\gamma + \alpha'$	153	[426]
	Wrought + HPT RT (N=10, $\varepsilon_{eq.}$=136)	45	$\gamma + \varepsilon + \alpha'$	624	
	Wrought + HPT RT (N=20, $\varepsilon_{eq.}$=272)	48	$\gamma + \varepsilon + \alpha'$	626	
	Wrought	42000	$\gamma + \alpha'$	144	[307]
	Wrought + CR 20%, $\varepsilon_{eq.}$=0.27	26000	$\gamma + \alpha'$	265	
	Wrought + HPT RT (N=10, $\varepsilon_{eq.}$=136)	45	$\gamma + \varepsilon + \alpha'$	625	
	Wrought	32000	γ	172	[576]
	Wrought + MAF ($\varepsilon_{eq.}$=4.2)	860	γ	334	
	Wrought	22000	$\gamma + \alpha'$	159	[466]
	Wrought + 2D LPSM 0° ($\varepsilon_{eq.}$=2.0)	200	$\gamma + \alpha'$	489	
	Wrought + 2D LPSM 20° ($\varepsilon_{eq.}$=1.7)	42	$\gamma + \alpha'$	442	
	Wrought	20000	γ	204	[270]
	SMAT ($\varepsilon_{eq.}$=3.4)	40	γ	459	
A220	Wrought	500000	γ	160	[420]
	Wrought + HPT -196°C (N=4, $\varepsilon_{eq.}$=45)	60	$\gamma + \varepsilon$	475	
316 SS	Wrought	22000	γ	170	[303]
	Wrought + HPT RT (N=10, $\varepsilon_{eq.}$=136)	40	γ	597	
	Wrought + HPT 400°C (N=10, $\varepsilon_{eq.}$=136)	90	γ	586	
	Wrought	22000	γ	170	[469]
	Wrought + HPT RT (N=10, $\varepsilon_{eq.}$=136)	60	γ	585	
	Wrought + HPT 430°C (N=10, $\varepsilon_{eq.}$=136)	110	γ	575	
304H SS	Wrought	7000	γ		
	Wrought + HPT RT (N=10, $\varepsilon_{eq.}$=136)	23	γ	584	[304]
	Wrought + HPT 400°C (N=10, $\varepsilon_{eq.}$=136)	26	γ	552	
304 SS	Wrought	N/A	γ	177	[300]
	Wrought + HPT 300°C	70	γ	540	
16/9 SS	Wrought	40000	γ	185	[479]
	Wrought + ECAP	350	γ	400	
	Wrought + CR 77%	560	γ	387	
	Wrought + ECAP (B_c) 400°C + CR 77%	110	γ	513	

However, it is expected that the nanostructured AM 316L SS obtained through HPT processing will have reduced ductility as has been the case for typical CM materials with UFG/NG microstructures, but it was not investigated in this study due to the difficulty in manufacturing miniature tensile test samples from the HPT-processed disks and the non-compliance of the test results with current ASTM standards. However, the micro-mechanical response investigated through nanoindentation tests at various strain rates reported in Chapter 6 suggests that the as-received AM 316L SS exhibits a higher level of plasticity compared to CM 316L SS, which is maintained throughout all HPT processing conditions. This is important to ensure that the nanostructured 316L SS can maintain its formability to produce structural components with the desired shape and geometry [528,532].

In addition, the UFG/NG microstructures and porosity elimination attained after HPT processing are shown to significantly enhance the corrosion performance of AM 316L SS in 3.5% NaCl solution, as shown by the results in Chapter 7. Interestingly, it is found that the best corrosion performance can be attained either through the narrow distribution of gradient microstructures (sub-micron and nano-scale grains) throughout the disk, or when a homogeneous distribution of nano-scale grains is attained, i.e. after 1 and 10 HPT revolutions in this study, respectively. Furthermore, the results in Chapter 8 show that HPT processing also enhances the wear performance of AM 316L SS via the combination of significantly high hardness and iron oxides that act as solid lubricant, both as the result of the continuous extreme grain refinement down to the nano-scale.

Therefore, the UFG/NG microstructures produced by HPT processing without any formation of strain-induced martensites not only result in high strength and plasticity, but also superior corrosion and wear resistances for the AM 316L SS in the current study when compared to those for SPD-processed CM 316L SS and other austenitic SS, and for AM 316L SS post-processed by conventional HIP and heat treatment procedures. However, a reduction in ductility is a trade-off that is expected with such extreme grain refinement as the dislocation motions are pinned by the numerous sub-micron/nano-scale grain boundaries and nanotwins. Nevertheless, a compromise can be achieved in terms of strength/ductility and corrosion and wear performances, depending on the requirements of the applications for 316L SS.

For example, corrosion and wear resistances are more critical than strength/ductility for orthopaedic implants, thus needing the smallest grain sizes, which can be obtained at the highest number of HPT revolutions. On the other hand, structural components for the marine and oil and gas industries such as underwater pipe network not only need superior corrosion and wear resistances, but also high strength and adequate ductility. Although UFG/NG microstructures are often associated with relatively lower ductility, various studies have shown that high strength with reasonably high ductility can be achieved in nanostructured materials having bi-modal/gradient grain sizes [241,657,658]. This can theoretically be achieved through the gradient grain microstructures obtained for the HPT-processed AM 316L SS in this study due to the inhomogeneous nature of the applied torsional strain, particularly at the early stages of HPT processing. Nevertheless, this hypothesis requires further investigations in the future.

Similarly, the results in Chapter 9 reveal that the UFG/NG microstructures obtained through HPT processing are able to enhance the strength at the interfacial region of MMAM 316L SS/IN 718. Combined with the unique microstructural feature of dense sub-micron dislocation networks obtained through AM fabrication, the combination of AM and SPD for joining dissimilar materials could potentially meet the increasing demand from manufacturers to produce lightweight, high strength dissimilar multi-material joints [659]. However, achieving UFG/NG microstructures for MMAM materials through HPT alone is difficult because recent studies on two phase materials such as duplex stainless steel demonstrated mass transfer in addition to in-plane shear strain due to the development of turbulent eddy flows within the HPT disks [660–669]. As has been observed in the joining of immiscible alloys via HPT processing, such turbulent eddy flows contribute to the redistribution of different metallic elements within the immiscible alloy system [670,671]. In fact, a study on the HPT processing of four specimens of two Cu and two Al 6061 disks each (radius: 20 mm, thickness: 1 mm) revealed that the interfacial region between the Cu and Al 6061 constituents consists of larger spiral architectures compared to their initial geometry after 1/2 revolution [672]. Thus, joining dissimilar AM materials through SPD processing is difficult to be realised because it will induce elemental mixing to form new composites or intermetallics that might have larger grain sizes or even brittle, thus contradict the aim of producing UFG/NG microstructures with enhanced properties for AM materials in the present study.

Furthermore, although HPT processing is able to eliminate porosity in both single-material AM 316L SS and multi-material AM 316L SS/IN 718 as evidenced in Chapters 4 and 9, respectively, it is currently not feasible to be carried out in practice. This is because HPT, or SPD processing in general is only limited to processing simple geometries. In addition, the extreme strain imposed by SPD processing will destroy the AM structures, thus negating the benefits of design flexibility of AM techniques that allow for complex shapes with intricate features to be built. Nevertheless, the results obtained from SPD processing of AM alloys as detailed in Chapters 4 – 9 are important in establishing process-microstructure-property relationships, particularly in determining the response of UFG/NG microstructures in AM metallic materials to the evolution in porosity, strength, and corrosion and wear performances, as described in Section 1.2.

10.2 Potential applicability for commercialisation in the metal AM industry

Metal AM is described as a ‘bottom-up’ manufacturing approach to build metallic structures in a layer-wise freeform manner that does not require additional tooling. Hence, parts with complex geometries, intricate features, and tailored microstructures and properties, i.e. tremendous design flexibility can be achieved in a single process step, thus reducing material waste, time, and overall manufacturing costs. Although post-processing is sometimes required to improve surface finish and eliminate porosity and other defects, AM has proven to have many advantages, particularly for applications that require low to medium volume production and design customisation, e.g. high-performance automotive parts, medical implants, aerospace components, and functionally graded materials (FGM).

Although superior mechanical properties in metals and alloys can be achieved by SPD processing as the result of the sub-micron and/or nano-scale grain refinement, SPD processing still has some limitations. So far, only thin disk samples have processed by HPT in most studies. However, recently the application of HPT have been up-scaled to larger cylinders [250], U-shaped sheets [673], and ring-shaped samples [674,675]. Meanwhile, ECAP processing has been successfully up-scaled to process larger billets and fabricate micro-gears, net-shaped micro-electromechanical system (MEMS) devices, dental implants, and monolithic sputtering targets [676–678]. Nevertheless, both HPT and ECAP techniques apply the same processing principle, i.e. imposing extremely high strains on bulk metallic materials to produce UFG/NG microstructures.

The integration of AM and SPD to obtain UFG and/or NG microstructures with unique properties seems a novel idea. However, it still has a long way to go before it can be implemented for practical applications. This is because the benefits of design flexibility in AM will be lost by the extreme strains imposed in SPD processing. In addition, the geometrical limitation in materials that can be processed by SPD prohibits its widespread application within the industry. However, the recent up-scaling of HPT and ECAP processes will provide the opportunity to further exploit the advantages of AM and SPD to fabricate components with specific requirements, such as hip replacement bio-implants. Furthermore, a hybrid AM/SPD approach can be introduced in the near future, in which both techniques can be utilised simultaneously such that AM parts can be built on nanostructured CM components obtained via SPD processing. In particular, two applications are envisaged to benefit from the integration of AM and SPD within this context; hip replacement bio-implants and small turbine blades used for power generation

A hip replacement bio-implant mimics the ball-socket configuration of the natural hip joint. The bio-implant consist of an acetabular cap that is inserted into the socket structure at the pelvis, a main body, or the femoral stem that is cemented into the thigh bone, a ball-shaped femoral head, and a plastic liner to reduce friction between the femoral head and the acetabular cap. Several requirements need to be met when choosing the material to fabricate this bio-implant. Firstly, they need to be biocompatible with the human body physiology to avoid rejection response by the body. Secondly, the materials need to be highly resistant to corrosion and wear to avoid degradation with time. Thirdly, the materials should have good mechanical properties, such as high strength and high fatigue life to withstand the body weight of the recipients and the cyclic loading experienced by the implants.

Here, it is proposed that the acetabular component and femoral head could be manufactured by nanostructured CM 316L SS obtained by HPT or ECAP to achieve the high strength, enhanced corrosion performance, and superior wear resistance compared to coarse-grained CM 316L SS. On the other hand, the flexibility of SLM, or other metal AM processes could enable the fabrication of femoral stem design that is tailored to specific patients. In fact, the femoral stem can be built with a lattice structure configuration to allow for lightweighting that can reduce the overall weight of the bio-implant, which could be beneficial for the patients [679]. Other materials that possess similar properties as 316L SS, such as CoCrMo and Ti6Al4V can also be used with similar configurations proposed for fabricating the individual components (nanostructured acetabular cap and nanostructured femoral head as a build substrate to fabricate femoral stem via SLM). In fact, multi-material combinations can also be used to fabricate the bio-implant, as long as they meet the requirements described previously. Therefore, the hybrid AM/SPD approach introduced in the particular context; i.e. using SPD to produce nanostructured acetabular component and femoral head from CM alloys and utilising AM to fabricate the femoral stem is deemed worthwhile to be explored and considered to be a feasible approach to fabricate the hip replacement bio-implant.

On the other hand, if the HPT or ECAP processes can be further up-scaled in the future, it is highly possible that even small turbine blades used in the power generation industry can be manufactured via the hybrid AM/SPD approach. A turbine blade consists of the root and aerofoil sections, in which the root is then inserted to the gas turbine disk. During power plant operations, the turbine blades typically experience extreme loading condition (e.g. rotating at ~ 13000 rotations per minute) and the temperature can reach 1250°C [680]. Therefore, materials with high strength and fatigue life are required. It is envisaged that the turbine blade can be built using multi-material combinations. For example, since the root section often encounters high cyclic loading upon contact with the turbine disk, it needs to have high strength and high fatigue life, which can be made from nanostructured SS alloys. The nanostructured root section can then be used as a build substrate to fabricate the aerofoil section that has a relatively complex geometry with intricate internal cooling channels by SLM. IN 718 can be used as the aerofoil material due to its high creep strength at elevated temperatures. Furthermore, the epitaxial grain growth of SLM processing favours directional solidification, which typically results in columnar microstructures that have been shown to be beneficial for increased creep resistance at high temperatures.

Chapter 11 Conclusions and future works

11.1 Conclusions

316L SS and 316L SS/IN 718 alloys were initially fabricated by SLM and then processed by HPT through 1/4, 1/2, 1, 5, and 10 revolutions corresponding to different equivalent strain, $\varepsilon_{\text{eq.-HPT}}$ values at RT under 6 GPa of pressure at 1 rpm.

For the AM 316L SS, high densification level is attained (> 99%) with low porosity level (< 1%), which is dominated by spherical gas-induced pores. A significant porosity reduction (~ 89 – 91%) is achieved after only 1/4 HPT revolution. A pore-free structure is attained after 1/2 revolution, suggesting the effectiveness of HPT to eliminate porosity in AM parts.

Significant hardness increase (by ~ 2 to 3 times from the initial value) is obtained with increasing HPT straining at higher number of revolutions. For single-material 316L SS, a hardness saturation is attained throughout the disk after 10 HPT revolutions, with an average value of 600 HV. EBSD and TEM observations indicate that gradient microstructures, i.e. fine micron-grains/UFG microstructures at the centre, and UFG/NG microstructures at the periphery are attained after HPT processing from 1/4 to 5 revolutions. The amount of UFG and NG microstructures increase with higher HPT revolutions and a homogeneous distribution of nano-scale grains are obtained at the saturation stage after 10 revolutions. The mean grain size obtained after 10 HPT processing is 42 ± 10 nm which is significantly refined from ~ 40 µm for the as-received alloy.

TEM observations also suggest that there are three stages of plastic deformation during HPT processing of AM 316L SS, which can be related to the number of HPT revolutions and the corresponding $\varepsilon_{\text{eq.-HPT}}$ values. The deformation in stage 1 ($\varepsilon_{\text{eq.-HPT}} = \sim 0 – 10$) can be attributed to the UFG microstructure, followed by the accumulation of generated dislocations, and primary twins. In stage 2 ($\varepsilon_{\text{eq.-HPT}} = \sim 10 – 40$), the deformation can be associated with the nano-scale grains, followed by further multiplication of dislocations, and nanotwins. In the final stage 3 ($\varepsilon_{\text{eq.-HPT}} > 40$), the deformation is largely contributed by much finer nano-scale grains, whereas no further dislocations and nanotwins are generated at this saturation level.

XRD line broadening analysis reveals significant reduction of crystallite size, D_c (from 295 nm to 20 nm) and remarkably high dislocation density, ρ value (1.69×10^{15} m^{-2}) obtained at the saturation stage after 10 HPT revolutions. This is the result of the strain hardening effect attained through the extreme torsional straining. No martensitic phase transformation is observed and the AM 316L SS retains its γ-austenite FCC structure throughout all HPT processing conditions.

The estimated values of strain rate sensitivity (SRS), m (~ 0.04) and activation volume, V_p^* (~ $11b^3$) for the as-received AM 316L SS from nanoindentation tests are respectively one order higher and lower compared to those of coarse-grained CM 316L SS. When correlated with microscopy observations, the deformation mechanism for the as-received alloy is attributed to the numerous sub-micron and nano-scale microstructural features rather than grain boundary sliding (GBS) although the estimated m and V_p^* values in this study typically correspond to the GBS mechanism. However, the increasing amount of grain boundaries due to the UFG/NG microstructures attained with higher HPT torsional strains suggest that the predominant deformation mechanism in HPT-processed disks is related to GB-mediated activities.

The results of electrochemical tests in 3.5% NaCl solution for AM 316L SS demonstrate superior corrosion resistance after HPT processing compared to the as-received alloy as the result of significant porosity elimination and the sub-micron/nano-scale grain refinement, which promote the formation of thick, homogeneous protective passive oxide layer.

HPT processing enhances the wear performance of AM 316L SS as indicated by the decreasing coefficient of friction (COF) and specific wear rate, k_W values with increasing number of revolutions. This is corroborated with the qualitative SEM observations and surface profilometry analysis of the wear scar topologies and morphologies, which is in line with Archard's relationship. The wear mechanism evolves from severe adhesive wear for the as-received alloy to a combination of much milder adhesive, abrasive, and mild tribo-oxidative wear after HPT processing.

For the MMAM 316L SS/IN 718, a similarly high densification level is attained (> 99%) with low porosity content (< 1%). However, the solidified structure is dominated by irregular-shaped process-induced pores. HPT processing through 1/4 revolution yields ~ 91% porosity reduction similar to the single-material AM 316L SS, which implies the consistency of HPT straining in effectively closing both gas-induced and process-induced pores.

Although significant hardness increase is observed after HPT processing, hardness saturation and microstructural homogeneity are only achieved at the disk periphery, including the interfacial region and the individual 316L SS and IN 718 regions) after 10 HPT revolutions. The mean grain size at the interfacial region after 10 HPT revolutions is 50 ± 5 nm compared to 45 ± 3 µm before HPT processing. The XRD spectra and TEM observations at the interfacial region reveal that it solidifies as a γ-FCC structure and (Nb,Ti)C phases, which are maintained throughout all processing conditions. Significant decrease in crystallite sizes D_c and increase in dislocation density values, ρ are obtained. The hardness increases with increasing number of dislocations and continuous grain refinement down to the UFG/NG regime.

The physical-based model established for the AM 316L SS reveals that the strength of the as-received alloy is primarily contributed by grain boundary strengthening followed by dislocation strengthening, while HPT processing introduces twins that contribute to the additional strengthening of the alloy. However, when a similar model applied to the interfacial region of the MMAM 316L SS/IN 718, it is revealed that the strength of the as-received disk is contributed primarily by grain boundary strengthening, followed by dislocation strengthening and solid solution strengthening. The contribution of solid solution strengthening declines considerably after 1/4 HPT revolution, whereas the emergence of nanotwins provide additional contribution to the overall strengthening after 1 and 10 HPT revolutions. Precipitation strengthening via Orowan looping through the Nb-and Ti-rich provides minimal contribution to the total strengthening for all processing conditions.

Overall, the results from this hybrid AM/SPD approach in exploring advanced high-performance engineering materials provide useful information that could be applied to actual applications of metal AM. In particular, process-microstructure-property relationships have been established for SPD-processed AM alloys (316L SS and IN 718) based on the results in Chapters 4 – 9, which could guide the development of future manufacturing processes and post-processing treatments for AM materials based on the required applications. Specifically, the development of pore-free AM structures that undergo continuous grain refinement down to the UFG/NG regime without martensitic transformation could yield a combined superior strength and enhanced corrosion and wear performances, or even tailored properties depending on the target applications. Finally, the up-scaling of SPD processes to fabricate larger engineering components as reported in recent literature will provide a new horizon in utilising the hybrid AM/SPD technique to develop functional materials in the future.

11.2 Future works

The processing parameters used for SLM fabrication in the present thesis were fixed. Therefore, future works can focus on changing various parameters, such as laser power, scan speed, scan line spacing, and layer thickness to produce parts with different densification levels and porosity contents. The effectiveness of HPT to eliminate pores and other defects can then be studied on these structures.

The results in the present thesis show that gradient UFG/NG microstructures obtained through HPT processing can result in a combination of high hardness and enhanced corrosion performance. Studies have shown that a combined high strength and high ductility can be obtained via bi-modal/gradient microstructures. However, only hardness measurements were conducted in the present thesis instead of tensile testing. Therefore, tensile tests can be conducted on miniature tensile specimens extracted from the HPT-processed disks to evaluate the uniform elongation or elongation to failure, i.e. ductility and compared with HPT-processed disks that possess different grain size distributions.

The contribution of various strengthening mechanisms described in the present thesis broadly captures the trend of increasing hardness for HPT-processed disks. However, the rapid heating/cooling cycle during SLM and the extreme torsional strain imposed during HPT might cause some solute segregation at the grain and/or cell boundaries and introduce the formation of co-clusters. Although these phenomena could provide additional strengthening, they could not be readily detected by TEM observations. Therefore, 3D atom probe tomography (APT) technique can be applied to determine the occurrence of these phenomena. If they do occur, then the contribution of solute segregation and co-cluster strengthening mechanisms can be included to improve the accuracy of the current strengthening model.

The improvements in corrosion performance for the HPT-processed AM 316L SS are attained for specific testing conditions as described in the present thesis. Future works could include conducting electrochemical tests in different electrolytes than 3.5% NaCl solution, or on MMAM 316L SS/IN 718 and other AM austenitic SS. The results can then be used to compare the corrosion performance with that obtained from the testing parameters used in this study.

The enhanced wear performance for the HPT-processed AM 316L SS are attained for sliding wear tests under dry condition and at specific testing conditions as described in the present thesis. In the future, similar tests can be done under lubricated condition and/or with different testing conditions, e.g. varied load, speed, and temperature. Tests can also be conducted on MMAM 316L SS/IN 718 or other AM austenitic SS. The wear performance can then be compared with that based on the results obtained from the present testing parameters in this study.

Although 316L SS is not traditionally an alloy that can be heat-treated to increase its strength. several studies have shown the presence of Cr-based nano-oxide silicates in AM 316L SS that contributes to the high yield strength via Orowan looping mechanism (precipitation strengthening). Thus, it is interesting to see whether heat-treating AM 316L SS could yield any changes in the trend of contribution to hardness increase after HPT processing.

It is known that IN 718 is a precipitation-hardened superalloy. Therefore, it is worthwhile to consider carrying out various heat treatment procedures on the MMAM 316L SS/IN 718 or on AM IN 718, and then conduct HPT processing on the heat-treated samples. The resulting microstructure and hardness evolutions throughout the disk for AM IN 718, and at different material regions (the interfacial region and the individual 316L SS and IN 718 regions) for the MMAM 316L SS/IN 718 could be explored in the future.

The envisaged near-future applications for the integration of AM and SPD techniques are dependent upon the up-scaling of SPD processing. Current up-scaling efforts have been extended to small cylinders in the millimetre region, which is suitable for the acetabular cap and femoral head of the bio-implant and can be applied in the near future. If facilities that can cater for SPD processing of larger cylinders in the centimetre range can be developed in the foreseeable future, then the anticipated fabrication of the root section of the small gas turbine blade for the power generation industry can be realised.

References

[1] A. Riemer, S. Leuders, M. Thöne, H.A. Richard, T. Tröster, T. Niendorf, On the fatigue crack growth behavior in 316L stainless steel manufactured by selective laser melting, Eng. Fract. Mech. 120 (2014) 15–25.

[2] B.E. Carroll, T. a. Palmer, A.M. Beese, Anisotropic tensile behavior of Ti-6Al-4V components fabricated with directed energy deposition additive manufacturing, Acta Mater. 87 (2015) 309–320.

[3] M.W. Wu, J.K. Chen, B.H. Lin, P.H. Chiang, Improved fatigue endurance ratio of additive manufactured Ti-6Al-4V lattice by hot isostatic pressing, Mater. Des. 134 (2017) 163–170.

[4] S. Karnati, I. Axelse, F.F. Liou, J.W. Newkirk, Investigation of Tensile Properties of Bulk and SLM Fabricated 304L Stainless Steel Using Various Gage Length Specimens, Solid Free. Fabr. (2016) 13.

[5] Q. Chao, V. Cruz, S. Thomas, N. Birbilis, P. Collins, A. Taylor, P.D. Hodgson, D. Fabijanic, On the enhanced corrosion resistance of a selective laser melted austenitic stainless steel, Scr. Mater. 141 (2017) 94–98.

[6] Y. Sun, A. Moroz, K. Alrbaey, Sliding wear characteristics and corrosion behaviour of selective laser melted 316L stainless steel, J. Mater. Eng. Perform. 23 (2014) 518–526.

[7] M. Vaezi, S. Chianrabutra, B. Mellor, S. Yang, Multiple material additive manufacturing – Part 1: a review, Virtual Phys. Prototyp. 8 (2013) 19–50.

[8] C. Wei, Multiple Material Selective Laser Melting: A New Approach, Laser User. (2018) 18–19.

[9] C. Wei, L. Li, X. Zhang, Y.H. Chueh, 3D printing of multiple metallic materials via modified selective laser melting, CIRP Ann. 67 (2018) 245–248.

[10] I. Gibson, D.W. Rosen, B. Strucker, Additive Manufacturing Technologies: Rapid Prototyping to Direct Digital Manufacturing, Springer, 2009.

[11] K. Salonitis, J. Pandremenos, J. Paralikas, G. Chryssolouris, Multifunctional materials: Engineering applications and processing challenges, Int. J. Adv. Manuf. Technol. 49 (2010) 803–826.

[12] Z.H. Liu, D.Q. Zhang, S.L. Sing, C.K. Chua, L.E. Loh, Interfacial characterization of SLM parts in multi-material processing: Metallurgical diffusion between 316L stainless steel and C18400 copper alloy, Mater. Charact. 94 (2014) 116–125.

[13] S.L. Sing, L.P. Lam, D.Q. Zhang, Z.H. Liu, C.K. Chua, Interfacial characterization of SLM parts in multi-material processing: Intermetallic phase formation between AlSi10Mg and C18400 copper alloy, Mater. Charact. 107 (2015) 220–227.

[14] J. Chen, Y. Yang, C. Song, M. Zhang, S. Wu, D. Wang, Interfacial microstructure and mechanical properties of 316L /CuSn10 multi-material bimetallic structure fabricated by selective laser melting, Mater. Sci. Eng. A. 752 (2019) 75–85.

[15] W.J. Sames, F.A. List, S. Pannala, R.R. Dehoff, S.S. Babu, The metallurgy and processing science of metal additive manufacturing, Int. Mater. Rev. 61 (2016) 1–46.

[16] B. AlMangour, J.M. Yang, Improving the surface quality and mechanical properties by shot-peening of 17-4 stainless steel fabricated by additive manufacturing, Mater. Des. 110 (2016) 914–924.

[17] L.N. Carter, M.M. Attallah, R.C. Reed, Laser Powder Bed Fabrication of Nickel-Base Superalloys: Influence of Parameters; Characterisation, Quantification and Mitigation of Cracking, Superalloys 2012. (2012) 577–586.

[18] A. Azushima, R. Kopp, A. Korhonen, D.Y. Yang, F. Micari, G.D. Lahoti, P. Groche, J. Yanagimoto, N. Tsuji, A. Rosochowski, A. Yanagida, Severe plastic deformation (SPD) processes for metals, CIRP Ann. - Manuf. Technol. 57 (2008) 716–735.

[19] R. Valiev, Nanostructuring of metals by severe plastic deformation for advanced properties, Nat. Mater. 3 (2004) 511–516.

[20] R.Z. Valiev, I. Sabirov, A.P. Zhilyaev, T.G. Langdon, Bulk nanostructured metals for innovative applications, Jom. 64 (2012) 1134–1142.

[21] R.Z. Valiev, Y. Estrin, Z. Horita, T.G. Langdon, M.J. Zehetbauer, Y. Zhu, Producing Bulk Ultrafine-Grained Materials by Severe Plastic Deformation, Jom. 68 (2006) 1216–1226.

[22] R.Z. Valiev, R.K. Islamgaliev, I. V. Alexandrov, Bulk nanostructured materials from severe plastic deformation, 2000.

[23] Y.T. Zhu, T.G. Langdon, The fundamentals of nanostructured materials processed by severe plastic deformation, J. Mater. 56 (2004) 58–63.

[24] R.Z. Valiev, Y. Estrin, Z. Horita, T.G. Langdon, M.J. Zehetbauer, Y. Zhu, Producing Bulk Ultrafine-Grained Materials by Severe Plastic Deformation: Ten Years Later, J. Mater. 68 (2006) 1216–1226.

[25] A.P. Zhilyaev, G. V. Nurislamova, B.K. Kim, M.D. Baró, J.A. Szpunar, T.G. Langdon, Experimental parameters influencing grain refinement and microstructural evolution during high-pressure torsion, Acta Mater. 51 (2003) 753–765.

[26] A.P. Zhilyaev, B.K. Kim, G. V. Nurislamova, M.D. Baró, J.A. Szpunar, T.G. Langdon, Orientation imaging microscopy of ultrafine-grained nickel, Scr. Mater. 46 (2002) 575–580.

[27] A.P. Zhilyaev, B.K. Kim, J.A. Szpunar, M.D. Baró, T.G. Langdon, The microstructural characteristics of ultrafine-grained nickel, Mater. Sci. Eng. A. 391 (2005) 377–389.

[28] J. Wongsa-Ngam, H. Wen, T.G. Langdon, Microstructural evolution in a Cu-Zr alloy processed by a combination of ECAP and HPT, Mater. Sci. Eng. A. 579 (2013) 126–135.

[29] J. Wongsa-Ngam, M. Kawasaki, T.G. Langdon, A comparison of microstructures and mechanical properties in a Cu-Zr alloy processed using different SPD techniques, J. Mater. Sci. 48 (2013) 4653–4660.

[30] F.P.W. Melchels, J. Feijen, D.W. Grijpma, A review on stereolithography and its applications in biomedical engineering., Biomaterials. 31 (2010) 6121–30.

[31] K. V. Wong, A. Hernandez, A Review of Additive Manufacturing, ISRN Mech. Eng. 2012 (2012) 1–10.

[32] C. Cozmei, F. Caloian, Additive Manufacturing Flickering at the Beginning of Existence, Procedia Econ. Financ. 3 (2012) 457–462.

[33] V. Petrovic, J. Vicente, H. Gonzalez, Additive layered manufacturing: sectors of industrial application shown through case studies, Int. J. Prod. Res. 49 (2011) 1061–1079.

[34] ASTM-International, Additive manufacturing - General principles - Terminology, 52900:2015(E), 2015.

[35] D. Herzog, V. Seyda, E. Wycisk, C. Emmelmann, Additive manufacturing of metals, Acta Mater. 117 (2016) 371–392.

[36] Y. Zhang, L. Wu, X. Guo, S. Kane, Y. Deng, Y.G. Jung, J.H. Lee, J. Zhang, Additive Manufacturing of Metallic Materials: A Review, J. Mater. Eng. Perform. 27 (2018) 1–13.

[37] V. Bhavar, P. Kattire, V. Patil, S. Khot, K. Gujar, R. Singh, A review on powder bed fusion technology of metal additive manufacturing, Addit. Manuf. Handb. Prod. Dev. Def. Ind. (2017) 251–261.

[38] R. Bogue, 3D printing: the dawn of a new era in manufacturing?, Assem. Autom. 33 (2013) 307–311.

[39] N. Guo, M.C. Leu, Additive manufacturing: technology, applications and research needs, Front. Mech. Eng. 8 (2013) 215–243.

[40] W.E. Frazier, Metal Additive Manufacturing: A Review, J. Mater. Eng. Perform. 23 (2014) 1917–1928.

[41] T. Scharowsky, F. Osmanlic, R.F. Singer, C. Körner, Melt pool dynamics during selective electron beam melting, Appl. Phys. A. 114 (2013) 1303–1307

[42] M. a. Lodes, R. Guschlbauer, C. Körner, Process development for the manufacturing of 99.94% pure copper via selective electron beam melting, Mater. Lett. 143 (2014) 298–301.

[43] C. Guo, W. Ge, F. Lin, Effects of scanning parameters on material deposition during Electron Beam Selective Melting of Ti-6Al-4V powder, J. Mater. Process. Technol. 217 (2014) 148–157.

[44] R.J. Hebert, Viewpoint: metallurgical aspects of powder bed metal additive manufacturing, J. Mater. Sci. 51 (2016) 1165–1175.

[45] W.J.J. Sames, F. Medina, W.H.H. Peter, S.S.S. Babu, R.R.R. Dehoff, Effect of process control and powder quality on IN 718 produced using Electron Beam Melting, in: 8th Int. Symp. Superalloy 718 Deriv., Wiley-Blackwell, Pittsburgh, 2014: pp. 409–423.

[46] B. Song, X. Zhao, S. Li, C. Han, Q. Wei, S. Wen, J. Liu, Y. Shi, Differences in microstructure and properties between selective laser melting and traditional manufacturing for fabrication of metal parts: A review, Front. Mech. Eng. 10 (2015) 111–125.

[47] F. Mangano, L. Chambrone, R. van Noort, C. Miller, P. Hatton, C. Mangano, Direct metal laser sintering titanium dental implants: a review of the current literature., Int. J. Biomater. (2014) 1–11.

[48] P. Fischer, V. Romano, H.P. Weber, N.P. Karapatis, E. Boillat, R. Glardon, Sintering of commercially pure titanium powder with a Nd:YAG laser source, Acta Mater. 51 (2003) 1651–1662.

[49] E.O. Olakanmi, Selective laser sintering/melting (SLS/SLM) of pure Al, Al–Mg, and Al–Si powders: Effect of processing conditions and powder properties, J. Mater. Process. Technol. 213 (2013) 1387–1405.

[50] D. Gu, Y. Shen, Effects of processing parameters on consolidation and microstructure of W–Cu components by DMLS, J. Alloys Compd. 473 (2009) 107–115.

[51] D. Gu, Y. Shen, S. Fang, J. Xiao, Metallurgical mechanisms in direct laser sintering of Cu–CuSn–

CuP mixed powder, J. Alloys Compd. 438 (2007) 184–189.

[52] B. Almangour, D. Grzesiak, J. Yang, Selective laser melting of TiB 2 / 316L stainless steel composites : The roles of powder preparation and hot isostatic pressing post-treatment, Powder Technol. 309 (2017) 37–48.

[53] B. AlMangour, D. Grzesiak, Jenn-MingYang, Selective laser melting of TiC reinforced 316L stainless steel matrix nanocomposites: Influence of starting TiC particle size and volume content, Mater. Des. 104 (2016) 141–151.

[54] B. Almangour, D. Grzesiak, J.M. Yang, Rapid fabrication of bulk-form TiB2/316L stainless steel nanocomposites with novel reinforcement architecture and improved performance by selective laser melting, J. Alloys Compd. 680 (2016) 480–493.

[55] X.P. Li, G. Ji, Z. Chen, A. Addad, Y. Wu, H.W. Wang, J. Vleugels, J. Van Humbeeck, J.P. Kruth, Selective laser melting of nano-TiB2 decorated AlSi10Mg alloy with high fracture strength and ductility, Acta Mater. (2017).

[56] H. Attar, L. Löber, A. Funk, M. Calin, L.C. Zhang, K.G. Prashanth, S. Scudino, Y.S. Zhang, J. Eckert, Mechanical behavior of porous commercially pure Ti and Ti-TiB composite materials manufactured by selective laser melting, Mater. Sci. Eng. A. 625 (2015) 350–356.

[57] T. Vilaro, C. Colin, J.D. Bartout, As-Fabricated and Heat-Treated Microstructures of the Ti-6Al-4V Alloy Processed by Selective Laser Melting, Metall. Mater. Trans. A. 42 (2011) 3190–3199.

[58] B. Vrancken, L. Thijs, J.-P. Kruth, J. Van Humbeeck, Heat treatment of Ti6Al4V produced by Selective Laser Melting: Microstructure and mechanical properties, J. Alloys Compd. 541 (2012) 177–185.

[59] L.E. Murr, S.M. Gaytan, D. a. Ramirez, E. Martinez, J. Hernandez, K.N. Amato, P.W. Shindo, F.R. Medina, R.B. Wicker, Metal Fabrication by Additive Manufacturing Using Laser and Electron Beam Melting Technologies, J. Mater. Sci. Technol. 28 (2012) 1–14.

[60] H. Attar, M. Calin, L.C. Zhang, S. Scudino, J. Eckert, Manufacture by selective laser melting and mechanical behavior of commercially pure titanium, Mater. Sci. Eng. A. 593 (2014) 170–177.

[61] Y.J. Liu, H.L. Wang, S.J. Li, S.G. Wang, W.J. Wang, W.T. Hou, Y.L. Hao, R. Yang, L.C. Zhang, Compressive and fatigue behavior of beta-type titanium porous structures fabricated by electron beam melting, Acta Mater. 126 (2017) 58–66.

[62] W. van Grunsven, E. Hernandez-Nava, G. Reilly, R. Goodall, Fabrication and Mechanical Characterisation of Titanium Lattices with Graded Porosity, Metals (Basel). 4 (2014) 401–409.

[63] D. Manfredi, F. Calignano, M. Krishnan, R. Canali, E.P. Ambrosio, S. Biamino, D. Ugues, M. Pavese, P. Fino, Additive Manufacturing of Al Alloys and Aluminium Matrix Composites (AMCs), in: W.A. Monteiro (Ed.), Light Met. Alloy. Appl., 2014: pp. 3–34.

[64] A. Simchi, F. Petzoldt, H. Pohl, On the development of direct metal laser sintering for rapid tooling, J. Mater. Process. Technol. 141 (2003) 319–328.

[65] D. Novichenko, L. Thivillon, P. Bertrand, I. Smurov, Carbide-reinforced metal matrix composite by direct metal deposition, Phys. Procedia. 5 (2010) 369–377.

[66] A. Gasser, G. Backes, I. Kelbassa, A. Weisheit, K. Wissenbach, Laser Additive Manufacturing Laser Metal Deposition (LMD) and Selective Laser Melting (SLM) in Turbo-Engine applications, Laser Tech. J. 7 (2010) 58–63.

[67] I. Shishkovsky, F. Missemer, I. Smurov, Direct Metal Deposition of Functional Graded Structures in Ti- Al System, Phys. Procedia. 39 (2012) 382–391.

[68] J.J. Lewandowski, M. Seifi, Metal Additive Manufacturing: A Review of Mechanical Properties, Annu. Rev. Mater. Res. 46 (2016) 151–186.

[69] P. Kazanas, P. Deherkar, P. Almeida, H. Lockett, S. Williams, Fabrication of geometrical features using wire and arc additive manufacture, Proc. Inst. Mech. Eng. Part B J. Eng. Manuf. 226 (2012) 1042–1051.

[70] F. Wang, S. Williams, P. Colegrove, A. a. Antonysamy, Microstructure and Mechanical Properties of Wire and Arc Additive Manufactured Ti-6Al-4V, Metall. Mater. Trans. A. 44 (2013) 968–977.

[71] R. Martukanitz, J. Hollingsworth, Taking the next step in Additive Manufacturing, Weld. J. 93 (2014) 40.

[72] A. Uriondo, M. Esperon-Miguez, S. Perinpanayagam, The present and future of additive manufacturing in the aerospace sector: A review of important aspects, Proc. Inst. Mech. Eng. Part G J. Aerosp. Eng. 229 (2015) 2132–2147.

[73] P.L. Blackwell, The mechanical and microstructural characteristics of laser-deposited IN718, J. Mater. Process. Technol. 170 (2005) 240–246.

[74] G. Marinelli, F. Martina, H. Lewtas, D. Hancock, S. Ganguly, S. Williams, Functionally graded structures of refractory metals by wire arc additive manufacturing, Sci. Technol. Weld. Join. 24

(2019) 495–503.

[75] A. Strondl, O. Lyckfeldt, H. Brodin, U. Ackelid, Characterization and Control of Powder Properties for Additive Manufacturing, Jom. 67 (2015) 549–554.

[76] J. Dawes, R. Bowerman, R. Trepleton, Introduction to the Additive Manufacturing Powder Metallurgy Supply Chain, Johnson Matthey Technol. Rev. 59 (2015) 243–256.

[77] X. Zhao, J. Chen, X. Lin, W. Huang, Study on microstructure and mechanical properties of laser rapid forming Inconel 718, Mater. Sci. Eng. A. 478 (2008) 119–124.

[78] H. Qi, M. Azer, A. Ritter, Studies of standard heat treatment effects on microstructure and mechanical properties of laser net shape manufactured INCONEL 718, Metall. Mater. Trans. A Phys. Metall. Mater. Sci. 40 (2009) 2410–2422.

[79] B. Liu, R. Wildman, C. Tuck, I. Ashcroft, R. Hague, Investigation the Effect of Particle Size Distribution on Processing Parameters Optimisation in Selective Laser Melting Process, in: Solid Free. Fabr. Symp., Austin, Texas, 2011: pp. 227–238.

[80] J.P. Kruth, L. Froyen, J. Van Vaerenbergh, P. Mercelis, M. Rombouts, B. Lauwers, Selective laser melting of iron-based powder, J. Mater. Process. Technol. 149 (2004) 616–622.

[81] M.. Griffith, M.. Schlienger, L.. Harwell, M.. Oliver, M.. Baldwin, M.. Ensz, M. Essien, J. Brooks, C.. Robino, J.. Smugeresky, W.. Hofmeister, M.. Wert, D.. Nelson, Understanding thermal behavior in the LENS process, Mater. Des. 20 (1999) 107–113.

[82] X. Wu, A review of laser fabrication of metallic engineering components and of materials, Mater. Sci. Technol. 23 (2007) 631–640. [83] S.M. Yusuf, N. Gao, Influence of energy density on metallurgy and properties in metal additive manufacturing, Mater. Sci. Technol. 33 (2017) 1269–1289.

[84] A. Reichardt, R.P. Dillon, J.P. Borgonia, A.A. Shapiro, B.W. McEnerney, T. Momose, P. Hosemann, Development and characterization of Ti-6Al-4V to 304L stainless steel gradient components fabricated with laser deposition additive manufacturing, Mater. Des. 104 (2016) 404–413.

[85] M. Svensson, U. Ackelid, Titanium Alloys Manufactured with Electron Beam Melting Mechanical and Chemical Properties, in: Proc. Mater. Process. Med. Devices Conf., 2009.

[86] U. Ackelid, M. Svensson, Additive Manufacturing of Dense Metal Parts by Electron Beam Melting, in: Proc. Mater. Sci. Technol. Conf., 2009: pp. 2711–2719.

[87] A.R. Vinod, C.K. Srinivasa, R. Keshavamurthy, P.V. Shashikumar, A novel technique for reducing lead-time and energy consumption in fabrication of Inconel-625 parts by laser-based metal deposition process, Rapid Prototyp. J. 22 (2016) 269–280.

[88] M. Seifi, D. Christiansen, J. Beuth, O. Harrysson, J.J. Lewandowski, Process Mapping, Fracture and Fatigue Behaviour of Ti-6Al-4V Produced by EBM Additive Manufacturing, in: A. Pilchak (Ed.), Ti-2015-The 13th World Conf. Titan., The Minerals, Metals & Materials Society, 2016: pp. 1373–1378.

[89] J.K. Algardh, T. Horn, H. West, R. Aman, A. Snis, H. Engqvist, J. Lausmaa, O. Harrysson, Thickness dependency of mechanical properties for thin-walled titanium parts manufactured by Electron Beam Melting (EBM)®, Addit. Manuf. 12 (2016) 45–50.

[90] H. Gong, K. Rafi, H. Gu, T. Starr, B. Stucker, Analysis of defect generation in Ti–6Al–4V parts made using powder bed fusion additive manufacturing processes, Addit. Manuf. 1–4 (2014) 87–98.

[91] Z. Nie, G. Wang, J.D. McGuffin-Cawley, B. Narayanan, S. Zhang, D. Schwam, M. Kottman, Y. (Kevin) Rong, Experimental study and modeling of H13 steel deposition using laser hot-wire additive manufacturing, J. Mater. Process. Technol. 235 (2016) 171–186.

[92] A.F.H. Kaplan, J. Powell, Spatter in laser welding, J. Laser Appl. 23 (2011) 032005-1-032005–7.

[93] Y. Liu, Y. Yang, S. Mai, D. Wang, C. Song, Investigation into spatter behavior during selective laser melting of AISI 316L stainless steel powder, Mater. Des. 87 (2015) 797–806.

[94] D. Bäuerle, Laser Processing and Chemistry, Springer Berlin Heidelberg, Berlin, 2000.

[95] M. Simonelli, C. Tuck, N.T. Aboulkhair, I. Maskery, I. Ashcroft, R.D. Wildman, R. Hague, A Study on the Laser Spatter and the Oxidation Reactions During Selective Laser Melting of 316L Stainless Steel, Al-Si10-Mg, and Ti-6Al-4V, Metall. Mater. Trans. A Phys. Metall. Mater. Sci. 46 (2015) 3842–3851.

[96] B.H. Rabin, G.R. Smolik, G.E. Korth, Characterization of entrapped gases in rapidly solidified powders, Mater. Sci. Eng. A. 124 (1990) 1–7.

[97] S.A. Khairallah, A.T. Anderson, A. Rubenchik, W.E. King, Laser powder-bed fusion additive manufacturing: Physics of complex melt flow and formation mechanisms of pores, spatter, and denudation zones, Acta Mater. 108 (2016) 36–45.

[98] N. Hopkinson, R.J.M. Hague, P.M. Dickens, Rapid Manufacturing: An Industrial Revolution for the Digital Age, John Wiley & Sons, Ltd, Chichester, 2006.

[99] K.A. Mumtaz, N. Hopkinson, Selective Laser Melting of thin wall parts using pulse shaping, J.

Mater. Process. Technol. 210 (2010) 279–287.

[100] M.J. Matthews, G. Guss, S.A. Khairallah, A.M. Rubenchik, P.J. Depond, W.E. King, Denudation of metal powder layers in laser powder bed fusion processes, Acta Mater. 114 (2016) 33–42.

[101] J.A. Kanko, A.P. Sibley, J.M. Fraser, In situ morphology-based defect detection of selective laser melting through inline coherent imaging, J. Mater. Process. Technol. 231 (2016) 488–500.

[102] I. Yadroitsev, P. Bertrand, G. Antonenkova, S. Griogoriev, S. I., Use of track/layer morphology to develop functional parts by selective laser melting, J. Laser Appl. 25 (2013) 1–7.

[103] D.E. Cooper, The High Deposition Rate Additive Manufacture of Nickel Superalloys and Metal Matrix Composites, University of Warwick, 2016.

[104] D.D. Gu, W. Meiners, K. Wissenbach, R. Poprawe, Laser additive manufacturing of metallic components: materials, processes and mechanisms, Int. Mater. Rev. 57 (2012) 133–164.

[105] E. Olatunde Olakanmi, K.W. Dalgarno, R.F. Cochrane, Laser sintering of blended Al-Si powders, Rapid Prototyp. J. 18 (2012) 109–119.

[106] W. Yan, W. Ge, J. Smith, S. Lin, O.L. Kafka, F. Lin, W. Kam, Multi-scale modeling of electron beam melting of functionally graded materials, Acta Mater. 115 (2016) 403–412.

[107] I. Shishkovsky, I. Yadroitsev, I. Smurov, Direct Selective Laser Melting of Nitinol Powder, Phys. Procedia. 39 (2012) 447–454.

[108] D. Gu, Y. Shen, Balling phenomena in direct laser sintering of stainless steel powder: Metallurgical mechanisms and control methods, Mater. Des. 30 (2009) 2903–2910.

[109] E. Louvis, P. Fox, C.J. Sutcliffe, Selective laser melting of aluminium components, J. Mater. Process. Technol. 211 (2011) 275–284.

[110] U. Scipioni Bertoli, A.J. Wolfer, M.J. Matthews, J.P.R. Delplanque, J.M. Schoenung, On the limitations of Volumetric Energy Density as a design parameter for Selective Laser Melting, Mater. Des. 113 (2017) 331–340.

[111] J. Jhabvala, E. Boillat, T. Antignac, R. Glardon, On the effect of scanning strategies in the selective laser melting process, Virtual Phys. Prototyp. 5 (2010) 99–109.

[112] L. Parry, I.A. Ashcroft, R.D. Wildman, Understanding the effect of laser scan strategy on residual stress in selective laser melting through thermo-mechanical simulation, Addit. Manuf. 12 (2016) 1–15.

[113] S. Bland, N.T. Aboulkhair, Reducing porosity in additive manufacturing, Met. Powder Rep. 70 (2015) 79–81.

[114] I. Yadroitsava, I. Yadroitsev, Residual stress in metal specimens produced by direct metal laser sintering, J. Chem. Inf. Model. 53 (2013) 1689–1699.

[115] L. Thijs, F. Verhaeghe, T. Craeghs, J. Van Humbeeck, J.-P. Kruth, A study of the microstructural evolution during selective laser melting of Ti–6Al–4V, Acta Mater. 58 (2010) 3303–3312.

[116] Y. Lu, S. Wu, Y. Gan, T. Huang, C. Yang, L. Junjie, J. Lin, Study on the microstructure, mechanical property and residual stress of SLM Inconel-718 alloy manufactured by differing island scanning strategy, Opt. Laser Technol. 75 (2015) 197–206.

[117] J. Suryawanshi, K.G. Prashanth, U. Ramamurty, Mechanical behavior of selective laser melted 316L stainless steel, Mater. Sci. Eng. A. 696 (2017) 113–121.

[118] L. N. Carter, M. M. Attallah, R. C. Reed, Laser powder bed fabrication of nickel-base superalloys: influence of parameters; characterisation, quantification and mitigation of cracking, in: E.S. Haron, R.C. Reed, M.C. Hardy, M.J. Mills, R.E. Montero, P.D. Portella, J. Telesman (Eds.), Superalloys 2012, John Wiley & Sons, Inc., Philadelphia, 2012: pp. 577–586.

[119] A.S. Wu, D.W. Brown, M. Kumar, G.F. Gallegos, W.E. King, An Experimental Investigation into Additive Manufacturing-Induced Residual Stresses in 316L Stainless Steel, Metall. Mater. Trans. A Phys. Metall. Mater. Sci. 45 (2014) 6260–6270.

[120] D. Buchbinder, W. Meiners, N. Pirch, K. Wissenbach, J. Schrage, Investigation on reducing distortion by preheating during manufacture of aluminum components using selective laser melting, J. Laser Appl. 26 (2014) 012004.

[121] C. Hauser, Selective Laser Sintering of a Stainless Steel Powder, Uiversity of Leeds, 2003.

[122] L. Katgerman, Principles of Solidification: An Introduction to Modern Casting and Crystal Growth Concepts, Wiley, New York, 2005.

[123] S.A. David, J.M. Vitek, Correlation between solidification parameters and weld microstructures, Int. Mater. Rev. 34 (1989) 213–245. .

[124] C. Hagenlocher, F. Fetzer, D. Weller, R. Weber, T. Graf, Explicit analytical expressions for the influence of welding parameters on the grain structure of laser beam welds in aluminium alloys, Mater. Des. 174 (2019) 107791.

[125] D. Samantaray, V. Kumar, a K. Bhaduri, P. Dutta, Microstructural Evolution and Mechanical Properties of Type 304 L Stainless Steel Processed in Semi-Solid State, Int. J. Metall. Eng. 2 (2013) 149–153.

[126] K. Saeidi, X. Gao, Y. Zhong, Z.J. Shen, Hardened austenite steel with columnar sub-grain structure formed by laser melting, Mater. Sci. Eng. A. 625 (2015) 221–229.

[127] S. Gorsse, C. Hutchinson, M. Gouné, R. Banerjee, Additive manufacturing of metals: a brief review of the characteristic microstructures and properties of steels, Ti-6Al-4V and high-entropy alloys, Sci. Technol. Adv. Mater. 18 (2017) 584–610.

[128] D. Zhang, Z. Feng, C. Wang, W. Wang, Z. Liu, W. Niu, Comparison of microstructures and mechanical properties of Inconel 718 alloy processed by selective laser melting and casting, Mater. Sci. Eng. A. 724 (2018) 357–367.

[129] F. Yan, W. Xiong, E. Faierson, G.B. Olson, Characterization of nano-scale oxides in austenitic stainless steel processed by powder bed fusion, Scr. Mater. 155 (2018) 104–108.

[130] A. Hadadzadeh, B.S. Amirkhiz, M. Mohammadi, Contribution of Mg2Si precipitates to the strength of direct metal laser sintered AlSi10Mg, Mater. Sci. Eng. A. 739 (2019) 295–300.

[131] L.N. Carter, C. Martin, P.J. Withers, M.M. Attallah, The influence of the laser scan strategy on grain structure and cracking behaviour in SLM powder-bed fabricated nickel superalloy, J. Alloys Compd. 615 (2014) 338–347.

[132] C.A. Brice, N. Dennis, Cooling Rate Determination in Additively Manufactured Aluminum Alloy 2219, Metall. Mater. Trans. A Phys. Metall. Mater. Sci. 46 (2015) 2304–2308.

[133] Y. Li, D. Gu, Parametric analysis of thermal behavior during selective laser melting additive manufacturing of aluminum alloy powder, Mater. Des. 63 (2014) 856–867.

[134] M. Das, V.K. Balla, D. Basu, S. Bose, A. Bandyopadhyay, Laser processing of SiC-particle-reinforced coating on titanium, Scr. Mater. 63 (2010) 438–441.

[135] J.P. Choi, G.H. Shin, S. Yang, D.Y. Yang, J.S. Lee, M. Brochu, J.H. Yu, Densification and microstructural investigation of Inconel 718 parts fabricated by selective laser melting, Powder Technol. 310 (2017) 60–66.

[136] C. Li, Y.B. Guo, J.B. Zhao, Interfacial phenomena and characteristics between the deposited material and substrate in selective laser melting Inconel 625, J. Mater. Process. Technol. 243 (2017) 269–281.

[137] W. Xu, E.W. Lui, A. Pateras, M. Qian, M. Brandt, In situ tailoring microstructure in additively manufactured Ti-6Al-4V for superior mechanical performance, Acta Mater. 125 (2017) 390–400.

[138] A.A. Raus, M.S. Wahab, M. Ibrahim, K. Kamarudin, A. Ahmed, S. Shamsudin, Mechanical and Physical Properties of AlSi10Mg Processed through Selective Laser Melting, Int. J. Eng. Technol. 8 (2016) 2612–2618.

[139] Z. Mao, D.Z. Zhang, P. Wei, K. Zhang, Manufacturing feasibility and forming properties of Cu-4Sn in selective laser melting, Materials (Basel). 10 (2017).

[140] J. Han, Microstructure and mechanical property of selective laser melted Ti6Al4V dependence on laser energy density, Rapid Pro. 23 (2017).

[141] J. Jue, D. Gu, K. Chang, D. Dai, Microstructure evolution and mechanical properties of Al-Al2O3 composites fabricated by selective laser melting, Powder Technol. 310 (2017) 80–91.

[142] L. Löber, F.P. Schimansky, U. Kühn, F. Pyczak, J. Eckert, Selective laser melting of a beta-solidifying TNM-B1 titanium aluminide alloy, J. Mater. Process. Technol. 214 (2014) 1852–1860.

[143] B. Zhang, H. Liao, C. Coddet, Effects of processing parameters on properties of selective laser melting Mg–9%Al powder mixture, Mater. Des. 34 (2012) 753–758.

[144] J. Yang, H. Yu, Z. Wang, X. Zeng, Effect of crystallographic orientation on mechanical anisotropy of selective laser melted Ti-6Al-4V alloy, Mater. Charact. 127 (2017) 137–145.

[145] H. Yu, J. Yang, J. Yin, Z. Wang, X. Zeng, Comparison on mechanical anisotropies of selective laser melted Ti-6Al-4V alloy and 304 stainless steel, Mater. Sci. Eng. A. 695 (2017) 92–100.

[146] M. Tang, P.C. Pistorius, Anisotropic Mechanical Behavior of AlSi10Mg Parts Produced by Selective Laser Melting, Jom. 69 (2017) 516–522.

[147] B.E. Carroll, T.A. Palmer, A.M. Beese, Anisotropic tensile behavior of Ti-6Al-4V components fabricated with directed energy deposition additive manufacturing, Acta Mater. 87 (2015) 309–320.

[148] M. Simonelli, Y.Y. Tse, C. Tuck, Effect of the build orientation on the mechanical properties and fracture modes of SLM Ti-6Al-4V, Mater. Sci. Eng. A. 616 (2014) 1–11.

[149] P. Kanagarajah, F. Brenne, T. Niendorf, H.J. Maier, Inconel 939 processed by selective laser melting: Effect of microstructure and temperature on the mechanical properties under static and cyclic loading, Mater. Sci. Eng. A. 588 (2013) 188–195.

[150] A. Basak, S. Das, Epitaxy and Microstructure Evolution in Metal Additive Manufacturing, Annu.

Rev. Mater. Res. 46 (2016) 125–149.

[151] L. Thijs, M.L. Montero Sistiaga, R. Wauthle, Q. Xie, J.P. Kruth, J. Van Humbeeck, Strong morphological and crystallographic texture and resulting yield strength anisotropy in selective laser melted tantalum, Acta Mater. 61 (2013) 4657–4668.

[152] E. Chlebus, B. Kuźnicka, T. Kurzynowski, B. Dybała, Microstructure and mechanical behaviour of Ti—6Al—7Nb alloy produced by selective laser melting, Mater. Charact. 62 (2011) 488–495.

[153] T. Bormann, R. Schumacher, B. Müller, M. Mertmann, M. Wild, Tailoring Selective Laser Melting Process Parameters for NiTi Implants, J. Mater. Eng. Perform. 21 (2012) 2519–2524.

[154] S. M. Yusuf, Y. Chen, R. Boardman, S. Yang, N. Gao, Investigation on Porosity and Microhardness of 316L Stainless Steel Fabricated by Selective Laser Melting, Metals (Basel). 7 (2017) 1–12.

[155] B. Baufeld, O. Van Der Biest, R. Gault, Additive manufacturing of Ti–6Al–4V components by shaped metal deposition: Microstructure and mechanical properties, Mater. Des. 31 (2010) S106–S111.

[156] D. Wang, Y. Yang, X. Su, Y. Chen, Study on energy input and its influences on single-track,multi-track, and multi-layer in SLM, Int. J. Adv. Manuf. Technol. 58 (2012) 1189–1199.

[157] F. Calignano, D. Manfredi, E.P. Ambrosio, S. Biamino, M. Pavese, P. Fino, Direct Fabrication of Joints based on Direct Metal Laser Sintering in Aluminum and Titanium Alloys, Procedia CIRP. 21 (2014) 129–132.

[158] D. Manfredi, F. Calignano, M. Krishnan, R. Canali, E. Ambrosio, E. Atzeni, From Powders to Dense Metal Parts: Characterization of a Commercial AlSiMg Alloy Processed through Direct Metal Laser Sintering, Materials (Basel). 6 (2013) 856–869.

[159] Z. Wang, K. Guan, M. Gao, X. Li, X. Chen, X. Zeng, The microstructure and mechanical properties of deposited-IN718 by selective laser melting, J. Alloys Compd. 513 (2012) 518–523.

[160] T. Bormann, B. Müller, M. Schinhammer, A. Kessler, P. Thalmann, M. de Wild, Microstructure of selective laser melted nickel–titanium, Mater. Charact. 94 (2014) 189–202.

[161] B. Song, S. Dong, P. Coddet, H. Liao, C. Coddet, Fabrication of NiCr alloy parts by selective laser melting: Columnar microstructure and anisotropic mechanical behavior, Mater. Des. 53 (2014) 1–7.

[162] T. Amine, J.W. Newkirk, F. Liou, An investigation of the effect of direct metal deposition parameters on the characteristics of the deposited layers, Case Stud. Therm. Eng. 3 (2014) 21–34.

[163] L.E. Murr, S. a. Quinones, S.M. Gaytan, M.I. Lopez, A. Rodela, E.Y. Martinez, D.H. Hernandez, E. Martinez, F. Medina, R.B. Wicker, Microstructure and mechanical behavior of Ti-6Al-4V produced by rapid-layer manufacturing, for biomedical applications., J. Mech. Behav. Biomed. Mater. 2 (2009) 20–32.

[164] G. Kasperovich, J. Hausmann, Improvement of fatigue resistance and ductility of TiAl6V4 processed by selective laser melting, J. Mater. Process. Technol. 220 (2015) 202–214.

[165] E. Wycisk, S. Siddique, D. Herzog, F. Walther, C. Emmelmann, Fatigue Performance of Laser Additive Manufactured Ti–6Al–4V in Very High Cycle Fatigue Regime up to 109 Cycles, Front. Mater. 2 (2015) 2–9.

[166] H. Gong, K. Rafi, T. Starr, B. Stucker, Effect of defects on fatigue tests of as-built Ti6Al4V parts fabricated by SLM, in: 2012: pp. 499–506.

[167] M. Seifi, A. Salem, D. Satko, J. Shaffer, J.J. Lewandowski, Defect distribution and microstructure heterogeneity effects on fracture resistance and fatigue behavior of EBM Ti–6Al–4V, Int. J. Fatigue. 94 (2017) 263–287.

[168] A.B.B. Spierings, T.L.L. Starr, K. Wegener, Fatigue performance of additive manufactured metallic parts, Rapid Prototyp. J. 19 (2013) 88–94.

[169] E. Brandl, U. Heckenberger, V. Holzinger, D. Buchbinder, Additive manufactured AlSi10Mg samples using Selective Laser Melting (SLM): Microstructure, high cycle fatigue, and fracture behavior, Mater. Des. 34 (2012) 159–169.

[170] M. Ma, Z. Wang, X. Zeng, A comparison on metallurgical behaviors of 316L stainless steel by selective laser melting and laser cladding deposition, Mater. Sci. Eng. A. 685 (2017) 265–273.

[171] X. Zhao, S. Li, M. Zhang, Y. Liu, T.B. Sercombe, S. Wang, Y. Hao, R. Yang, L.E. Murr, Comparison of the microstructures and mechanical properties of Ti–6Al–4V fabricated by selective laser melting and electron beam melting, Mater. Des. 95 (2016) 21–31.

[172] G. Marchese, X. Garmendia Colera, F. Calignano, M. Lorusso, S. Biamino, P. Minetola, D. Manfredi, Characterization and Comparison of Inconel 625 Processed by Selective Laser Melting and Laser Metal Deposition, Adv. Eng. Mater. 19 (2017) 1–9.

[173] R. Li, J. Liu, Y. Shi, L. Wang, W. Jiang, Balling behavior of stainless steel and nickel powder during selective laser melting process, Int. J. Adv. Manuf. Technol. 59 (2012) 1025–1035.

[174] N.K. Tolochko, S.E. Mozzharov, I. a. Yadroitsev, T. Laoui, L. Froyen, V.I. Titov, M.B. Ignatiev,

Balling processes during selective laser treatment of powders, Rapid Prototyp. J. 10 (2004) 78–87.

[175] D. Gu, Y. Shen, Balling phenomena during direct laser sintering of multi-component Cu-based metal powder, J. Alloys Compd. 432 (2007) 163–166.

[176] X. Zhou, X. Liu, D. Zhang, Z. Shen, W. Liu, Balling phenomena in selective laser melted tungsten, J. Mater. Process. Technol. 222 (2015) 33–42.

[177] M.F. Zäh, S. Lutzmann, Modelling and simulation of electron beam melting, Prod. Eng. 4 (2010) 15–23.

[178] H. Zhang, H. Zhu, T. Qi, Z. Hu, X. Zeng, Selective laser melting of high strength Al-Cu-Mg alloys: Processing, microstructure and mechanical properties, Mater. Sci. Eng. A. 656 (2016) 47–54.

[179] P.A. Kobryn, S.L. Semiatin, Mechanical Properties of Laser-Deposited Ti-6Al-4V, in: Solid Free. Fabr. Proc., Texas, 2001: pp. 179–186.

[180] K.N. Amato, S.M. Gaytan, L.E. Murr, E. Martinez, P.W. Shindo, J. Hernandez, S. Collins, F. Medina, Microstructures and mechanical behavior of Inconel 718 fabricated by selective laser melting, Acta Mater. 60 (2012) 2229–2239.

[181] B. Song, S. Dong, Q. Liu, H. Liao, C. Coddet, Vacuum heat treatment of iron parts produced by selective laser melting: Microstructure, residual stress and tensile behavior, Mater. Des. 54 (2014) 727–733.

[182] P.A. Kobryn, S.L. Semiatin, The Laser Additive Manufacture of Ti-6Al-4V, J. Manuf. (2001) 40–42.

[183] K.A. Unocic, L. Kolbus, O. Ridge, R.R. Dehoff, High-Temperature Performance of UNS N07718 Processed by Additive Manufacturing, in: NACE Corros. 2014, Texas, 2014: pp. 1–12.

[184] V. Flint, G.M. Davidson, R.L. Boring, cheryl L. Powers, A.P. Pauna, Nickel-based superalloys, in: H. Chandler (Ed.), Heat Treater's Guid. Pract. Proced. Nonferrous Alloy., ASTM International, 1996: pp. 41–58.

[185] H.C. Man, S. Zhang, F.T. Cheng, X. Guo, Laser fabrication of porous surface layer on NiTi shape memory alloy, Mater. Sci. Eng. A. 404 (2005) 173–178.

[186] D.C. Hofmann, J. Kolodziejska, S. Roberts, R. Otis, R.P. Dillon, J.-O. Suh, Z.-K. Liu, J.-P. Borgonia, Compositionally graded metals: A new frontier of additive manufacturing, J. Mater. Res. 29 (2014) 1899–1910.

[187] S.Y. Choy, C.N. Sun, K.F. Leong, K.E. Tan, J. Wei, Functionally graded material by additive manufacturing, in: C. Kai Chua, W. Yee Yeong, M. Jen tan, E. Liu, S. Beng Tor (Eds.), Proc. 2nd Int. Conf. Prog. Addit. Manuf., Research Publishing, Singapore, 2016: pp. 206–211.

[188] T. Niendorf, S. Leuders, A. Riemer, F. Brenne, T. Tröster, H.A. Richard, D. Schwarze, Functionally graded alloys obtained by additive manufacturing, Adv. Eng. Mater. 16 (2014) 857–861.

[189] M. Ott, M.F. Zaeh, Multi-material processing in additive manufacturing, 21st Solid Free. Fabr. Symp. (2010) 195–203.

[190] H. Sahasrabudhe, R. Harrison, C. Carpenter, A. Bandyopadhyay, Stainless steel to titanium bimetallic structure using LENS, Addit. Manuf. 5 (2015) 1–8.

[191] A. Bandyopadhyay, B. V Krishna, W. Xue, S. Bose, Application of laser engineered net shaping (LENS) to manufacture porous and functionally graded structures for load bearing implants., J. Mater. Sci. Mater. Med. 20 (2009) S29–S34.

[192] B. Vamsi Krishna, W. Xue, S. Bose, A. Bandyopadhyay, Functionally graded Co-Cr-Mo coating on Ti-6Al-4V alloy structures., Acta Biomater. 4 (2008) 697–706.

[193] S. Suresh, A. Mortesnsen, Fundamentals of Functionally Graded Materials, IOM Communications Ltd., London, 1998.

[194] C. Anstaett, C. Seidel, Multi-Material Processing Next step in laser-based powder bed fusion, Laser Tech. J. 4 (2016) 28–31.

[195] T.E. Abioye, P.K. Farayibi, P. Kinnel, a. T. Clare, Functionally graded Ni-Ti microstructures synthesised in process by direct laser metal deposition, Int. J. Adv. Manuf. Technol. 79 (2015) 843–850.

[196] L.D. Bobbio, R.A. Otis, J.P. Borgonia, R.P. Dillon, A.A. Shapiro, Z.K. Liu, A.M. Beese, Additive manufacturing of a functionally graded material from Ti-6Al-4V to Invar: Experimental characterization and thermodynamic calculations, Acta Mater. 127 (2017) 133–142.

[197] T. Abe, H. Sasahara, Dissimilar metal deposition with a stainless steel and nickel-based alloy using wire and arc-based additive manufacturing, Precis. Eng. 45 (2016) 387–395.

[198] B.E. Carroll, R.A. Otis, J.P. Borgonia, J.O. Suh, R.P. Dillon, A.A. Shapiro, D.C. Hofmann, Z.K. Liu, A.M. Beese, Functionally graded material of 304L stainless steel and inconel 625 fabricated by directed energy deposition: Characterization and thermodynamic modeling, Acta Mater. 108 (2016) 46–54.

[199] K. Shah, I.U. Haq, A. Khan, S.A. Shah, M. Khan, A.J. Pinkerton, Parametric study of development of Inconel-steel functionally graded materials by laser direct metal deposition, Mater. Des. 54 (2014) 531–538.

[200] F. Liu, X. Lin, G. Yang, M. Song, J. Chen, W. Huang, Microstructure and residual stress of laser rapid formed Inconel 718 nickel-base superalloy, Opt. Laser Technol. 43 (2011) 208–213.

[201] A. Levy, A. Miriyev, A. Elliott, S.S. Babu, N. Frage, Additive manufacturing of complex-shaped graded TiC/steel composites, Mater. Des. 118 (2017) 198–203. h

[202] Y. Liu, C. Liu, W. Liu, Y. Ma, C. Zhang, Q. Cai, B. Liu, Microstructure and properties of Ti/Al lightweight graded material by direct laser deposition, Mater. Sci. Technol. (United Kingdom). 34 (2018) 945–951.

[203] C.H. Zhang, H. Zhang, C.L. Wu, S. Zhang, Z.L. Sun, S.Y. Dong, Multi-layer functional graded stainless steel fabricated by laser melting deposition, Vacuum. 141 (2017) 181–187.

[204] Q. Wang, S. Zhang, C.H. Zhang, C. Wu, J. Wang, J. Chen, Z. Sun, Microstructure evolution and EBSD analysis of a graded steel fabricated by laser additive manufacturing, Vacuum. 141 (2017) 68–81.

[205] V.A. Popovich, E. V. Borisov, A.A. Popovich, V.S. Sufiiarov, D. V. Masaylo, L. Alzina, Functionally graded Inconel 718 processed by additive manufacturing: Crystallographic texture, anisotropy of microstructure and mechanical properties, Mater. Des. 114 (2017) 441–449.

[206] S. Li, S. Zhao, W. Hou, C. Teng, Y. Hao, Y. Li, R. Yang, R.D.K. Misra, Functionally Graded Ti-6Al-4V Meshes with High Strength and Energy Absorption, Adv. Eng. Mater. 18 (2016) 34–38.

[207] X. Tan, Y. Kok, Y.J. Tan, M. Descoins, D. Mangelinck, S.B. Tor, K.F. Leong, C.K. Chua, Graded microstructure and mechanical properties of additive manufactured Ti-6Al-4V via electron beam melting, Acta Mater. 97 (2015) 1–16.

[208] C. a. Terrazas, S.M. Gaytan, E. Rodriguez, D. Espalin, L.E. Murr, F. Medina, R.B. Wicker, Multi-material metallic structure fabrication using electron beam melting, Int. J. Adv. Manuf. Technol. (2013) 33–45.

[209] A. Hinojos, J. Mireles, A. Reichardt, P. Frigola, P. Hosemann, L.E. Murr, R.B. Wicker, Joining of Inconel 718 and 316 Stainless Steel using electron beam melting additive manufacturing technology, Mater. Des. 94 (2016) 17–27.

[210] O.M. Al-Jamal, S. Hinduja, L. Li, Characteristics of the bond in Cu–H13 tool steel parts fabricated using SLM, CIRP Ann. - Manuf. Technol. 57 (2008) 239–242.

[211] S. Chianrabutra, B.G. Mellor, S. Yang, A Dry Powder Material Delivery Device for Multiple Material Additive Manufacturing, Proc. Solid Free. Fabr. Symp. (2014) 36–48.

[212] Y. Chivel, New approach to multi-material processing in selective laser melting, Phys. Procedia. 83 (2016) 891–898.

[213] S.K. Everton, M. Hirsch, P. Stravroulakis, R.K. Leach, A.T. Clare, Review of in-situ process monitoring and in-situ metrology for metal additive manufacturing, Mater. Des. 95 (2016) 431–445.

[214] S. Everton, P. Dickens, C. Tuck, B. Dutton, D. Wimpenny, H.G. Salem, H.G. Salem, M.M. Attallah, TMS 2017 146th Annual Meeting & Exhibition Supplemental Proceedings, (2017) 105–116.

[215] A. Thompson, I. Maskery, R.K. Leach, X-ray computed tomography for additive manufacturing: a review, Meas. Sci. Technol. 27 (2016) 072001.

[216] X. Cai, A.A. Malcolm, B.S. Wong, Z. Fan, Measurement and characterization of porosity in aluminium selective laser melting parts using X-ray CT, Virtual Phys. Prototyp. 10 (2015) 195–206.

[217] R. Cunningham, S.P. Narra, T. Ozturk, J. Beuth, A.D. Rollett, Evaluating the Effect of Processing Parameters on Porosity in Electron Beam Melted Ti-6Al-4V via Synchrotron X-ray Microtomography, Jom. 68 (2016) 765–771.

[218] M. Seifi, A. Salem, J. Beuth, O. Harrysson, J.J. Lewandowski, Overview of Materials Qualification Needs for Metal Additive Manufacturing, Jom. 68 (2016) 747–764.

[219] M. Seifi, M. Gorelik, J. Waller, N. Hrabe, N. Shamsaei, S. Daniewicz, J.J. Lewandowski, Progress Towards Metal Additive Manufacturing Standardization to Support Qualification and Certification, Jom. 69 (2017) 439–455.

[220] I. Sabirov, M.Y. Murashkin, R.Z. Valiev, Nanostructured aluminium alloys produced by severe plastic deformation: New horizons in development, Mater. Sci. Eng. A. 560 (2013) 1–24.

[221] A.P. Zhilyaev, T.G. Langdon, Using high-pressure torsion for metal processing: Fundamentals and applications, Prog. Mater. Sci. 53 (2008) 893–979.

[222] H. Gleiter, Nanostructured materials: basic concepts and microstructure, Acta Mater. 48 (2000) 1–29.

[223] Y.T. Zhu, T.C. Lowe, T.G. Langdon, Performance and applications of nanostructured materials produced by severe plastic deformation, Scr. Mater. 51 (2004) 825–830.

[224] Y.H. Zhao, Y.T. Zhu, X.Z. Liao, Z. Horita, T.G. Langdon, Tailoring stacking fault energy for high ductility and high strength in ultrafine grained Cu and its alloy, Appl. Phys. Lett. 89 (2006) 2004–2007.

[225] R.Z. Valiev, T.G. Langdon, Principles of equal-channel angular pressing as a processing tool for grain refinement, Prog. Mater. Sci. 51 (2006) 881–981.

[226] R.Z. Valiev, I.P. Semenova, V. V. Latysh, A. V. Shcherbakov, E.B. Yakushina, Nanostructured titanium for biomedical applications: New developments and challenges for commercialization, Nanotechnologies Russ. 3 (2008) 593–601.

[227] Y. Ivanisenko, R.K. Wunderlich, R.Z. Valiev, H.J. Fecht, Annealing behaviour of nanostructured carbon steel produced by severe plastic deformation, Scr. Mater. 49 (2003) 947–952. [228] K.D. Ralston, N. Birbilis, Effect of grain size on corrosion, Corrosion. 66 (2010) 1–4.

[229] S. Gollapudi, Grain size distribution effects on the corrosion behaviour of materials, Corros. Sci. 62 (2012) 90–94.

[230] N. Gao, C.T. Wang, R.J.K. Wood, T.G. Langdon, Tribological properties of ultrafine-grained materials processed by severe plastic deformation, J. Mater. Sci. 47 (2012) 4779–4797.

[231] M. Kawasaki, B. Ahn, P. Kumar, J. Il Jang, T.G. Langdon, Nano- and Micro-Mechanical Properties of Ultrafine-Grained Materials Processed by Severe Plastic Deformation Techniques, Adv. Eng. Mater. 19 (2017) 1–17.

[232] Y. Qi, A. Kosinova, A.R. Kilmametov, B.B. Straumal, E. Rabkin, Generation and healing of porosity in high purity copper by high-pressure torsion, Mater. Charact. 145 (2018) 1–9.

[233] C.R.M. Afonso, A. Amigó, V. Stolyarov, D. Gunderov, V. Amigó, From Porous to Dense Nanostructured β-Ti alloys through High-Pressure Torsion, Sci. Rep. 7 (2017) 1–6.

[234] D. Setman, G. Wilde, M. Wegner, J. Leuthold, M. Zehetbauer, S. V. Divinski, R. Pippan, M. Peterlechner, Percolating porosity in ultrafine grained copper processed by High Pressure Torsion, J. Appl. Phys. 114 (2013) 183509.

[235] G. Wilde, M. Zehetbauer, M. Wegner, J. Leuthold, S. V. Divinski, D. Setman, Deformation Induced Percolating Porosity In High Pressure Torsioned (HPT) Copper, Mater. Sci. Forum. 702–703 (2011) 105–108.

[236] E. Schafler, G. Steiner, E. Korznikova, M. Kerber, M.J. Zehetbauer, Lattice defect investigation of ECAP-Cu by means of X-ray line profile analysis, calorimetry and electrical resistometry, Mater. Sci. Eng. A. 410–411 (2005) 169–173.

[237] J.Y. Huang, Y.T. Zhu, H. Jiang, T.C. Lowe, Microstructures and dislocation configurations in nanostructured Cu processed by repetitive corrugation and straightening, Acta Mater. 49 (2001) 1497–1505.

[238] R.Y. Lapovok, The role of back-pressure in equal channel angular extrusion, J. Mater. Sci. 40 (2005) 341–346.

[239] Y.T. Zhu, X. Liao, Nanostructured metals: Retaining ductility, Nat. Mater. 3 (2004) 351–352.

[240] Y. Zhao, T. Topping, J.F. Bingert, J.J. Thornton, A.M. Dangelewicz, Y. Li, W. Liu, Y. Zhu, Y. Zhou, E.J. Lavernia, High tensile ductility and strength in bulk nanostructured nickel, Adv. Mater. 20 (2008) 3028–3033.

[241] N. Tsuji, N. Kamikawa, R. Ueji, N. Takata, H. Koyama, D. Terada, Managing both strength and ductility in ultrafine grained steels, ISIJ Int. 48 (2008) 1114–1121.

[242] M. Furukawa, Z. Horita, M. Nemoto, T.G. Langdon, Review: Processing of metals by equal-channel angular pressing, J. Mater. Sci. 36 (2001) 2835–2843.

[243] T.G. Langdon, Processing of ultrafine-grained materials using severe plastic deformation: Potential for achieving exceptional properties, Rev. Metal. 44 (2008) 556–564.

[244] Y. Estrin, A. Vinogradov, Extreme grain refinement by severe plastic deformation: A wealth of challenging science, Acta Mater. 61 (2013) 782–817.

[245] T.G. Langdon, The principles of grain refinement in equal-channel angular pressing, Mater. Sci. Eng. A. 462 (2007) 3–11.

[246] C. Xu, Z. Horita, T.G. Langdon, The evolution of homogeneity in an aluminum alloy processed using high-pressure torsion, Acta Mater. 56 (2008) 5168–5176.

[247] T.G. Langdon, Twenty-five years of ultrafine-grained materials: Achieving exceptional properties through grain refinement, Acta Mater. 61 (2013) 7035–7059.

[248] J.J. Jonas, C. Aranas, Problems associated with use of the logarithmic equivalent strain in high pressure torsion, IOP Conf. Ser. Mater. Sci. Eng. 63 (2014).

[249] J.J. Jonas, C. Ghosh, L.S. Toth, The equivalent strain in high pressure torsion, Mater. Sci. Eng. A. 607 (2014) 530–535.

[250] G. Sakai, K. Nakamura, Z. Horita, T.G. Langdon, Developing high-pressure torsion for use with bulk samples, Mater. Sci. Eng. A. 406 (2005) 268–273.

[251] G.B. Rathmayr, R. Pippan, Influence of impurities and deformation temperature on the saturation microstructure and ductility of HPT-deformed nickel, Acta Mater. 59 (2011) 7228–7240.

[252] J. Gubicza, M. El-Tahawy, Y. Huang, H. Choi, H. Choe, J.L. Lábár, T.G. Langdon, Microstructure, phase composition and hardness evolution in 316L stainless steel processed by high-pressure torsion, Mater. Sci. Eng. A. 657 (2016) 215–223.

[253] G. Sakai, Z. Horita, T.G. Langdon, Grain refinement and superplasticity in an aluminum alloy processed by high-pressure torsion, Mater. Sci. Eng. A. 393 (2005) 344–351.

[254] C. Xu, Z. Horita, T.G. Langdon, The evolution of homogeneity in processing by high-pressure torsion, Acta Mater. 55 (2007) 203–212.

[255] A. Loucif, R.B. Figueiredo, T. Baudin, F. Brisset, T.G. Langdon, Microstructural evolution in an Al-6061 alloy processed by high-pressure torsion, Mater. Sci. Eng. A. 527 (2010) 4864–4869.

[256] A.P. Zhilyaev, G. V. Nurislamova, B.K. Kim, M.D. Bar??, J.A. Szpunar, T.G. Langdon, M.D. Baró, J.A. Szpunar, T.G. Langdon, Experimental parameters influencing grain refinement and microstructural evolution during high-pressure torsion, Acta Mater. 51 (2003) 753–765.

[257] S. V Dobatkin, J. Zrnik, I. Mamuzic, Nanostructures by severe plastic deformation of steels: Advantages and problems, Metalurgija. 45 (2006) 313–321.

[258] L. Kurmanaeva, Y. Ivanisenko, J. Markmann, C. Kübel, A. Chuvilin, S. Doyle, R.Z. Valiev, H.J. Fecht, Grain refinement and mechanical properties in ultrafine grained Pd and Pd-Ag alloys produced by HPT, Mater. Sci. Eng. A. 527 (2010) 1776–1783.

[259] N. Hu, N. Gao, Y. Chen, M.J. Starink, Achieving homogeneous anodic TiO2 nanotube layers through grain refinement of the titanium substrate, Mater. Des. 110 (2016) 346–353.

[260] M. Kawasaki, H.J. Lee, B. Ahn, A.P. Zhilyaev, T.G. Langdon, Evolution of hardness in ultrafine-grained metals processed by high-pressure torsion, J. Mater. Res. Technol. 3 (2014) 311–318.

[261] J. Wongsa-Ngam, M. Kawasaki, T.G. Langdon, Achieving homogeneity in a Cu-Zr alloy processed by high-pressure torsion, J. Mater. Sci. 47 (2012) 7782–7788.

[262] Y.C. Wang, T.G. Langdon, Effect of heat treatment on microstructure and microhardness evolution in a Ti-6Al-4V alloy processed by high-pressure torsion, J. Mater. Sci. 48 (2013) 4646–4652.

[263] H.J. Lee, B. Ahn, M. Kawasaki, T.G. Langdon, Evolution in hardness and microstructure of ZK60A magnesium alloy processed by high-pressure torsion, J. Mater. Res. Technol. 4 (2015) 18–25.

[264] Y. Ito, Z. Horita, Microstructural evolution in pure aluminum processed by high-pressure torsion, Mater. Sci. Eng. A. 503 (2009) 32–36.

[265] K. Edalati, A. Yamamoto, Z. Horita, T. Ishihara, High-pressure torsion of pure magnesium: Evolution of mechanical properties, microstructures and hydrogen storage capacity with equivalent strain, Scr. Mater. 64 (2011) 880–883.

[266] K. Edalati, Z. Horita, Significance of homologous temperature in softening behavior and grain size of pure metals processed by high-pressure torsion, Mater. Sci. Eng. A. 528 (2011) 7514–7523.

[267] M. Kawasaki, B. Ahn, T.G. Langdon, Microstructural evolution in a two-phase alloy processed by high-pressure torsion, Acta Mater. 58 (2010) 919–930.

[268] C. Xu, Z. Horita, T.G. Langdon, Microstructural Evolution in Pure Aluminum in the Early Stages of Processing by High-Pressure Torsion, Mater. Trans. 51 (2010) 2–7.

[269] B. Al-Mangour, R. Mongrain, E. Irissou, S. Yue, Improving the strength and corrosion resistance of 316L stainless steel for biomedical applications using cold spray, Surf. Coatings Technol. 216 (2013) 297–307.

[270] X.H. Chen, J. Lu, L. Lu, K. Lu, Tensile properties of a nanocrystalline 316L austenitic stainless steel, Scr. Mater. 52 (2005) 1039–1044.

[271] A. Ahmadi, R. Mirzaeifar, N.S. Moghaddam, A.S. Turabi, H.E. Karaca, M. Elahinia, Effect of manufacturing parameters on mechanical properties of 316L stainless steel parts fabricated by selective laser melting: a computational framework, Mater. Des. 112 (2016) 328–338.

[272] A. Mertens, S. Reginster, Q. Contrepois, T. Dormal, O. Lemaire, J. Lecomte-Beckers, Microstructures and Mechanical Properties of Stainless Steel AISI 316L Processed by Selective Laser Melting, Mater. Sci. Forum. 783–786 (2014) 898–903.

[273] Outokumpu, Handbook of Stainless Steel, Outokumpu Oyj, Espoo, 2013.

[274] I. Gotman, Characteristics of Metals Used in Implants, J. Endourol. 11 (1997) 383–389.

[275] Y. Kim, Y. Kim, D. Kim, S. Kim, W. Nam, H. Choe, Effects of Hydrogen Diffusion on the Mechanical Properties of Austenite 316L Steel at Ambient Temperature, Mater. Trans. 52 (2011) 507–513.

[276] D.N. Wasnik, G.K. Dey, V. Kain, I. Samajdar, Precipitation stages in a 316L austenitic stainless steel, Scr. Mater. 49 (2003) 135–141.

[277] W.M. Tucho, V.H. Lysne, H. Austbø, A. Sjolyst-Kverneland, V. Hansen, Investigation of effects of process parameters on microstructure and hardness of SLM manufactured SS316L, J. Alloys Compd. 740 (2018) 910–925.

[278] M.S. Pham, B. Dovgyy, P.A. Hooper, Twinning induced plasticity in austenitic stainless steel 316L made by additive manufacturing, Mater. Sci. Eng. A. 704 (2017) 102–111.

[279] A. Bayode, E.T.A. Member, S. Pityana, Characterization of Laser Metal deposited 316L Stainless Steel, in: Proc. World Congr. Eng. 2016 Vol II ,WCE 2016, WCE, London, 2016: pp. 1–3.

[280] M. DURAND-CHARRE, The basic phase diagrams, in: Microstruct. Steels Cast Irons, Springer, 2004: pp. 51–73.

[281] K.H. Lo, C.H. Shek, J.K.L. Lai, Recent developments in stainless steels, Mater. Sci. Eng. R Reports. 65 (2009) 39–104.

[282] J.C. Lippold, W.F. Savage, Solidification of Austenitic Stainless Steel Weldments : Part I — A Proposed Mechanism, Weld. J. 58 (1979) 362s-374s.

[283] J.C. Lippold, D.J. Kotecki, Welding Metallurgy of Stainless Steels, John Wiley & Sons, Inc., New Jersey, 2005.

[284] A.L. Schaeffler, Constitution diagram for stainless steel weld metal, Met. Prog. 56 (1949) 680-680B.

[285] S.A. David, J.M. Vitek, T.L. Hebble, Effect of Rapid Solidification on Stainless Steel Weld Metal Microstructures and Its Implications on the Schaeffler Diagram, Weld. Res. Suppl. (1987) 289–300.

[286] Y. Nakao, K. Nishimoto, W.-P. Zhang, Effects of Rapid Solidification by Laser Surface Melting on Solidification Modes, Trans. Japan Weld. Soc. 19 (1988) 100–106.

[287] J.C. Lippold, Solidification Behavior and Cracking Susceptibility of Pulsed-Laser Welds in Austenitic Stainless Steels A shift in solidification behavior under rapid solidification conditions promotes an increase in cracking susceptibility, Weld. J. Incl. Weld. Res. Suppl. 73 (1994) 129.

[288] X.P. Li, X.J. Wang, M. Saunders, A. Suvorova, L.C. Zhang, Y.J. Liu, M.H. Fang, Z.H. Huang, T.B. Sercombe, A selective laser melting and solution heat treatment refined Al-12Si alloy with a controllable ultrafine eutectic microstructure and 25% tensile ductility, Acta Mater. 95 (2015) 74–82.

[289] E. Abele, H.A. Stoffregen, M. Kniepkamp, S. Lang, M. Hampe, Selective laser melting for manufacturing of thin-walled porous elements, J. Mater. Process. Technol. 215 (2015) 114–122.

[290] F. Geiger, K. Kunze, T. Etter, Tailoring the texture of IN738LC processed by selective laser melting (SLM) by specific scanning strategies, Mater. Sci. Eng. A. 661 (2016) 240–246.

[291] J. Olsen, X. Zhou, Y. Zhong, L. Liu, D. Wang, C. Yu, Y. Wang, K. Li, L. Xing, J. Ma, D. Cui, W. Liu, Z. Shen, Tailoring hierarchical structures in selective laser melted materials, IOP Conf. Ser. Mater. Sci. Eng. 219 (2017) 1–8.

[292] X. Lou, M. Song, P.W. Emigh, M.A. Othon, P.L. Andresen, On the stress corrosion crack growth behaviour in high temperature water of 316L stainless steel made by laser powder bed fusion additive manufacturing, Corros. Sci. (2017) 0–1.

[293] L. Zhang, X.-Q. Ni, D.-C. Kong, Y. Wen, W.-H. Wu, B.-B. He, L. Lu, D.-X. Zhu, Anisotropy in mechanical properties and corrosion resistance of 316L stainless steel fabricated by selective laser melting, Int. J. Miner. Metall. Mater. 26 (2019) 319–328.

[294] K. Solberg, S. Guan, S.M.J. Razavi, T. Welo, K.C. Chan, F. Berto, Fatigue of additively manufactured 316L stainless steel: The influence of porosity and surface roughness, Fatigue Fract. Eng. Mater. Struct. 42 (2019) 2043–2052.

[295] O. Fergani, A. Bratli Wold, F. Berto, V. Brotan, M. Bambach, Study of the effect of heat treatment on fatigue crack growth behaviour of 316L stainless steel produced by selective laser melting, Fatigue Fract. Eng. Mater. Struct. 41 (2018) 1102–1119.

[296] K. Saeidi, X. Gao, F. Lofaj, L. Kvetková, Z.J. Shen, Transformation of austenite to duplex austenite-ferrite assembly in annealed stainless steel 316L consolidated by laser melting, J. Alloys Compd. 633 (2015) 463–469.

[297] Y. Zhong, L. Liu, S. Wikman, D. Cui, Z. Shen, Intragranular cellular segregation network structure strengthening 316L stainless steel prepared by selective laser melting, J. Nucl. Mater. 470 (2016) 170–178.

[298] Z. Sun, X. Tan, S.B. Tor, W.Y. Yeong, Selective laser melting of stainless steel 316L with low porosity and high build rates, Mater. Des. 104 (2016) 197–204.

[299] N. Chen, G. Ma, W. Zhu, A. Godfrey, Z. Shen, G. Wu, X. Huang, Enhancement of an additive-manufactured austenitic stainless steel by post-manufacture heat-treatment, Mater. Sci. Eng. A. 759 (2019) 65–69.

[300] Y. Mine, D. Haraguchi, Z. Horita, K. Takashima, High-pressure torsion of metastable austenitic

stainless steel at moderate temperatures, Philos. Mag. Lett. 95 (2015) 269–276.

[301] H. Wang, I. Shuro, M. Umemoto, K. Ho-Hung, Y. Todaka, Annealing behavior of nano-crystalline austenitic SUS316L produced by HPT, Mater. Sci. Eng. A. 556 (2012) 906–910.

[302] O. Renk, A. Hohenwarter, R. Pippan, Cyclic deformation behavior of a 316L austenitic stainless steel processed by high pressure torsion, Adv. Eng. Mater. 14 (2012) 948–954.

[303] M.M. Abramova, N.A. Enikeev, R.Z. Valiev, A. Etienne, B. Radiguet, Y. Ivanisenko, X. Sauvage, Grain boundary segregation induced strengthening of an ultrafine-grained austenitic stainless steel, Mater. Lett. 136 (2014) 349–352.

[304] M. Tikhonova, N. Enikeev, R.Z. Valiev, A. Belyakov, R. Kaibyshev, Submicrocrystalline austenitic stainless steel processed by cold or warm high pressure torsion, Mater. Sci. Forum. 838–839 (2016) 398–403.

[305] M. El-Tahawy, Y. Huang, T. Um, H. Choe, J.L. Lábár, T.G. Langdon, J. Gubicza, Stored energy in ultrafine-grained 316L stainless steel processed by high-pressure torsion, J. Mater. Res. Technol. (2017) 1–9.

[306] M. El-Tahawy, Y. Huang, H. Choi, H. Choe, J.L. Lábár, T.G. Langdon, J. Gubicza, High temperature thermal stability of nanocrystalline 316L stainless steel processed by high-pressure torsion, Mater. Sci. Eng. A. 682 (2017) 323–331.

[307] M. El-Tahawy, J. Gubicza, Y. Huang, H.L. Choi, H.M. Choe, J.L. Lábár, T.G. Langdon, The Influence of Plastic Deformation on Lattice Defect Structure and Mechanical Properties of 316L Austenitic Stainless Steel, Mater. Sci. Forum. 885 (2017) 13–18.

[308] D.F. Paulonis, J.J. Schirra, Alloy 718 at Pratt & Whitney - Historical perspective and future challenges, in: Proc. Int. Symp. Superalloys Var. Deriv., 2001: pp. 13–23.

[309] J.W. Brooks, P.J. Bridges, Metallurgical Stability of Inconel Alloy 718, in: Superalloys 1988, 1988: pp. 33–42.

[310] E.A. Loria, The Status and Prospects of Alloy 718, Jom. 40 (1988) 36–41.

[311] G.H. Cao, T.Y. Sun, C.H. Wang, X. Li, M. Liu, Z.X. Zhang, P.F. Hu, A.M. Russell, R. Schneider, D. Gerthsen, Z.J. Zhou, C.P. Li, G.F. Chen, Investigations of γ′ γ″ and δ precipitates in heat-treated Inconel 718 alloy fabricated by selective laser melting, Mater. Charact. 136 (2018) 398–406.

[312] W.M. Tucho, P. Cuvillier, A. Sjolyst-Kverneland, V. Hansen, Microstructure and hardness studies of Inconel 718 manufactured by selective laser melting before and after solution heat treatment, Mater. Sci. Eng. A. 689 (2017) 220–232.

[313] H. Xiao, S. Li, X. Han, J. Mazumder, L. Song, Laves phase control of Inconel 718 alloy using quasi-continuous-wave laser additive manufacturing, Mater. Des. 122 (2017) 330–339.

[314] R.C. Reed, The Superalloys: Fundamentals and Applications, Cambridge University Press, Cambridge, 2006.

[315] C.T. Sims, A History of Superalloy Metallurgy for Superalloy Metallurgists, Superalloys. (1984) 399–419.

[316] B. Geddes, H. Leon, X. Huang, Superalloys: Alloying and Performance, ASM International, 2010.

[317] A.J. Ardell, Order hardening: Comparison between revised theory and experiment, Met. Sci. 14 (1980) 221–224.

[318] M.C. Chaturvedi, Y. Han, Strengthening mechanisms in Inconel 718, Met. Sci. 17 (1983) 145–149.

[319] M.J. Donachie, S.J. Donachie, Superalloys: a technical guide, Second Edi, ASM International, 2002.

[320] Y.C. Lin, J. Deng, Y.Q. Jiang, D.X. Wen, G. Liu, Hot tensile deformation behaviors and fracture characteristics of a typical Ni-based superalloy, Mater. Des. 55 (2014) 949–957.

[321] S. Azadian, L.Y. Wei, R. Warren, Delta phase precipitation in inconel 718, Mater. Charact. 53 (2004) 7–16.

[322] J.N. DuPont, J.C. Lippold, S.D. Kiser, Welding Metallurgy and Weldability of Nickel-Base Alloys, Wiley, New Jersey, 2009.

[323] Y. Huang, T.G. Langdon, The evolution of delta-phase in a superplastic Inconel 718 alloy, J. Mater. Sci. 42 (2007) 421–427.

[324] S. Li, J. Yang, J. Zhuang, Q. Deng, J. Du, X. Xie, B. Li, Z. Xu, Z. Cao, Z. Su, C. Jiang, The Effect of Delta-Phase on Crack Propagation Under Creep and Fatigue Conditions in Alloy 718, in: E.A. Loria (Ed.), Superalloys 718, 625, 706 Var. Deriv., THe Minerals, Metals and Materials Society, 1994: pp. 545–555.

[325] B. Pieraggi, J.F. Uginet, Fatigue and creep properties in relation with Alloy 718 microstructure, in: E.A. Loria (Ed.), Superalloys 718, 625, 706 Var. Deriv., THe Minerals, Metals and Materials Society, 1994: pp. 535–544.

[326] D. Gopikrishna, S.N. Jha, L.N. Dash, Influence of microstructure on fatigue properties of Alloy 718,

in: E.A. Loria (Ed.), Superalloys 718, 625, 706 Var. Deriv., THe Minerals, Metals and Materials Society, 1997: pp. 567–573.

[327] J.F. Muller, M.J. Donachie, The effects of solution and intermediate heat treatments on the notch-rupture behavior of Inconel 718, Metall. Mater. Trans. A. 6 (1975) 2221–2227.

[328] R.B. Bhavsar, A. Collins, S. Silverman, Use of alloy 718 and 725 in oil and gas industry, Proc. Int. Symp. Superalloys Var. Deriv. 1 (2001) 47–55.

[329] G.D. Janaki Ram, A. Venugopal Reddy, K. Prasad Rao, G. Madhusudhan Reddy, Microstructure and mechanical properties of Inconel 718 electron beam welds, Mater. Sci. Technol. 21 (2005) 1132–1138.

[330] M. Sundararaman, P. Mukhopadhyay, S. Banerjee, Carbide Precipitation in Nickel Base Superalloys 718 and 625 and Their Effect on Mechanical Properties, in: E.A. Loria (Ed.), Superalloys 718,625,706 Var. Deriv., THe Minerals, Metals and Materials Society, 1997: pp. 367–378.

[331] J.F. Radavich, The physicall metallurgy of cast and worught alloy 718, in: E.A. Loria (Ed.), Superalloy 718-Metallurgy Appl., THe Minerals, Metals and Materials Society, 1989: pp. 229–240.

[332] M.J. Cieslak, G.A. Knorovsky, T.J. Headley, A.D. Romig, The Solidification Metallurgy of Alloy 718 and Other Nb-Containing Superalloys, in: E.A. Loria (Ed.), Superalloy 718--Metallurgy Appl., The Minerals, Metals & Materials Society, 1989, 1989: pp. 59–68.

[333] K.M. Chang, H.J. Lai, J.Y. Hwang, Existence of Laves Phase in Nb-Hardened Superalloys, in: E.A. Loria (Ed.), Superalloys 718, 625, 706 Var. Deriv., THe Minerals, Metals and Materials Society, 1994: pp. 683–694.

[334] J.J. Schirra, R.H. Caless, R.W. Hatala, The effect of Laves phase on the mechanical properties of wrought and cast + HIP inconel 718, in: E.A. Loria (Ed.), Superalloys 718, 625 Var. Deriv., THe Minerals, Metals and Materials Society, 1991: pp. 375–388.

[335] G.A. Rao, M. Kumar, M. Srinivas, D.S. Sarma, Effect of standard heat treatment on the microstructure and mechanical properties of hot isostatically pressed superalloy inconel 718, Mater. Sci. Eng. A. 355 (2003) 114–125.

[336] G.A. Knorovsky, M.J. Cieslak, T.J. Headley, A.D. Romig, W.F. Hammetter, INCONEL 718: A solidification diagram, Metall. Trans. A. 20 (1989) 2149–2158.

[337] M. Ni, C. Chen, X. Wang, P. Wang, R. Li, X. Zhang, K. Zhou, Anisotropic tensile behavior of in situ precipitation strengthened Inconel 718 fabricated by additive manufacturing, Mater. Sci. Eng. A. 701 (2017) 344–351.

[338] A. Strondl, R. Fischer, G. Frommeyer, A. Schneider, Investigations of MX and Gamma prime/Gamma double prime precipitates in the nickel-based superalloy 718 produced by electron beam melting, Mater. Sci. Eng. A. 480 (2008) 138–147.

[339] T. Antonsson, H. Fredriksson, Effect of cooling rate on the solidification of INCONEL 718, Metall. Mater. Trans. B. 36B (2005) 85–96.

[340] S. Il Kwon, S.H. Bae, J.H. Do, C.Y. Jo, H.U. Hong, Characterization of the Microstructures and the Cryogenic Mechanical Properties of Electron Beam Welded Inconel 718, Metall. Mater. Trans. A Phys. Metall. Mater. Sci. 47 (2016) 777–787.

[341] E. Chlebus, K. Gruber, B. Kuźnicka, J. Kurzac, T. Kurzynowski, Effect of heat treatment on the microstructure and mechanical properties of Inconel 718 processed by selective laser melting, Mater. Sci. Eng. A. 639 (2015) 647–655.

[342] D. Deng, R.L. Peng, H. Brodin, J. Moverare, Microstructure and mechanical properties of Inconel 718 produced by selective laser melting: Sample orientation dependence and effects of post heat treatments, Mater. Sci. Eng. A. 713 (2018) 294–306.

[343] T. Trosch, J. Strößner, R. Völkl, U. Glatzel, Microstructure and mechanical properties of selective laser melted Inconel 718 compared to forging and casting, Mater. Lett. 164 (2016) 428–431.

[344] A. Mostafa, I. Picazo Rubio, V. Brailovski, M. Jahazi, M. Medraj, Structure, Texture and Phases in 3D Printed IN718 Alloy Subjected to Homogenization and HIP Treatments., Metals (Basel). 7 (2017) 315.

[345] R.G. Thompson, J.R. Dobbs, D.E. Mayo, The Effect of Heat Treatment on Microfissuring in Alloy 718, Weld. Journal, Res. Suppl. 65 (1986) 299–304.

[346] F. Zupanič, T. Bončina, A. Križman, F.D. Tichelaar, Structure of continuously cast Ni-based superalloy Inconel 713C, J. Alloys Compd. 329 (2001) 290–297.

[347] R.J. Patterson, A.R. Cox, E.C. van Reuth, Rapid Solidification Rate Processing and Application To Turbine Engine Materials., J. Met. 32 (1980) 34–39.

[348] R. Mehrabian, B.H. Kear, M. Cohen, Rapid solidification processing: principles and technologies, in: Proc. Int. Conf. Rapid Solidif. Process., Claitor’s Pub. Division, Virginia, 1977.

[349] Y. Mei, Y. Liu, C. Liu, C. Li, L. Yu, Q. Guo, H. Li, Effect of base metal and welding speed on fusion

zone microstructure and HAZ hot-cracking of electron-beam welded Inconel 718, Mater. Des. 89 (2016) 964–977.

[350] N.L. Richards, X. Huang, M.C. Chaturvedi, Heat affected zone cracking in cast inconel 718, Mater. Charact. 28 (1992) 179–187.

[351] Q. Jia, D. Gu, Selective laser melting additive manufacturing of Inconel 718 superalloy parts: Densification, microstructure and properties, J. Alloys Compd. 585 (2014) 713–721.

[352] A. Strondl, S. Milenkovic, A. Schneider, U. Klement, G. Frommeyer, Effect of processing on microstructure and physical properties of three nickel-based superalloys with different hardening mechanisms, Adv. Eng. Mater. 14 (2012) 427–438.

[353] N. Raghavan, S. Simunovic, R. Dehoff, A. Plotkowski, J. Turner, M. Kirka, S. Babu, Localized melt-scan strategy for site specific control of grain size and primary dendrite arm spacing in electron beam additive manufacturing, Acta Mater. 140 (2017) 375–387. [354] H. Xiao, S.M. Li, W.J. Xiao, Y.Q. Li, L.M. Cha, J. Mazumder, L.J. Song, Effects of laser modes on Nb segregation and Laves phase formation during laser additive manufacturing of nickel-based superalloy, Mater. Lett. 188 (2017) 260–262.

[355] M.M. Kirka, K.A. Unocic, N. Raghavan, F. Medina, R.R. Dehoff, S.S. Babu, Microstructure Development in Electron Beam-Melted Inconel 718 and Associated Tensile Properties, J. Mater. Sci. 68 (2016) 1012–1020.

[356] Y.R. Kolobov, G.P. Grabovetskaya, M.B. Ivanov, A.P. Zhilyaev, R.Z. Valiev, Grain boundary diffusion characteristics of nanostructured nickel, Scr. Mater. 44 (2001) 873–878.

[357] A. Zhilyaev, G. Nurislamova, S. Surinach, M. Baro, T. Langdon, Calorimetric measurements of grain growth in ultrafine-grained nickel, Mater. Phys. Mech. 5 (2002) 23–30.

[358] A.P. Zhilyaev, G. V. Nurislamova, M.D. Baró, R.Z. Valiev, T.G. Langdon, Thermal stability and microstructural evolution in ultrafine-grained nickel after equal-channel angular pressing (ECAP), Metall. Mater. Trans. A Phys. Metall. Mater. Sci. 33 (2002) 1865–1868.

[359] A.P. Zhilyaev, J. Gubicza, G. Nurislamova, Á. Révész, S. Suriñach, M. D. Baró, T. Ungár, Microstructural characterization of ultrafine-grained nickel, Phys. Status Solidi Appl. Res. 198 (2003) 263–271.

[360] A.P. Zhilyaev, M.D. Baró, T.G. Langdon, T.R. McNelley, An examination of microtexture and microstructure in ultrafine-grained nickel, Rev. Adv. Mater. Sci. 7 (2004) 41–49.

[361] A.P. Zhilyaev, A.A. Gimazov, E.P. Soshnikova, Á. Révész, T.G. Langdon, Microstructural characteristics of nickel processed to ultrahigh strains by high-pressure torsion, Mater. Sci. Eng. A. 489 (2008) 207–212.

[362] G. Reglitz, B. Oberdorfer, N. Fleischmann, J.A. Kotzurek, S. V. Divinski, W. Sprengel, G. Wilde, R. Würschum, Combined volumetric, energetic and microstructural defect analysis of ECAP-processed nickel, Acta Mater. 103 (2016) 396–406.

[363] Q.H. Bui, G. Dirras, S. Ramtani, J. Gubicza, On the strengthening behavior of ultrafine-grained nickel processed from nanopowders, Mater. Sci. Eng. A. 527 (2010) 3227–3235.

[364] A. Hohenwarter, R. Pippan, Fracture toughness evaluation of ultrafine-grained nickel, Scr. Mater. 64 (2011) 982–985.

[365] S.S. Satheesh Kumar, T. Raghu, Tensile behaviour and strain hardening characteristics of constrained groove pressed nickel sheets, Mater. Des. 32 (2011) 4650–4657.

[366] A.P. Zhilyaev, A.A. Gimazov, T.G. Langdon, Recent developments in modelling of microhardness saturation during SPD processing of metals and alloys, J. Mater. Sci. 48 (2013) 4461–4466.

[367] S. V. Divinski, G. Reglitz, I.S. Golovin, M. Peterlechner, R. Lapovok, Y. Estrin, G. Wilde, Effect of heat treatment on diffusion, internal friction, microstructure and mechanical properties of ultra-fine-grained nickel severely deformed by equal-channel angular pressing, Acta Mater. 82 (2015) 11–21.

[368] A. Nazarova, R. Mulyukov, Y. Tsarenko, V. Rubanik, A. Nazarov, Effect of ultrasonic treatment on the microstructure and properties of nanostructured nickel processed by high pressure torsion, Mater. Sci. Forum. 667–669 (2011) 605–609.

[369] A.P. Zhilyaev, A.A. Samigullina, A.E. Medvedeva, S.N. Sergeev, J.M. Cabrera, A.A. Nazarov, Softening and hardening of ECAP nickel under ultrasonic treatment, Mater. Sci. Eng. A. 698 (2017) 136–142.

[370] A.A. Samigullina, A.A. Mukhametgalina, S.N. Sergeyev, A.P. Zhilyaev, A.A. Nazarov, Y.R. Zagidullina, N.Y. Parkhimovich, V. V. Rubanik, Y. V. Tsarenko, Microstructure changes in ultrafine-grained nickel processed by high pressure torsion under ultrasonic treatment, Ultrasonics. 82 (2018)

[371] Q. Jia, D. Gu, Selective laser melting additive manufactured Inconel 718 superalloy parts: High-temperature oxidation property and its mechanisms, Opt. Laser Technol. 62 (2014) 161–171.

[372] Y. Qi, A. Kosinova, A.R. Kilmametov, B.B. Straumal, E. Rabkin, Generation and healing of porosity in high purity copper by high-pressure torsion, Mater. Charact. 145 (2018) 1–9.

[373] K. Edalati, Z. Horita, A review on high-pressure torsion (HPT) from 1935 to 1988, Mater. Sci. Eng. A. 652 (2016) 325–352.

[374] S. Mohd Yusuf, M. Nie, Y. Chen, S. Yang, N. Gao, Microstructure and corrosion performance of 316L stainless steel fabricated by Selective Laser Melting and processed through high-pressure torsion, J. Alloys Compd. 763 (2018) 360–375.

[375] A. Thorvaldsen, The intercept method—1. Evaluation of grain shape, Acta Mater. 45 (1997) 587–594.

[376] L. Lutterotti, S. Gialanella, X-Ray Diffraction Characterization of Heavily Deformed Metallic Specimens, Acta Mater. 46 (1998) 101–110.

[377] L.B. Mccusker, R.B. Von Dreele, D.E. Cox, D. Louër, P. Scardi, Rietveld refinement guidelines, J. Appl. Crystallogr. 32 (1999) 36–50.

[378] R.A. Young, D.B. Wiles, Profile Shape Functions in Rietveld Refinements, J. Appl. Crystallogr. 15 (1982) 430–438.

[379] M. Kawasaki, T.G. Langdon, The significance of strain reversals during processing by high-pressure torsion, Mater. Sci. Eng. A. 498 (2008) 341–348.

[380] N.G. Thompson, J.H. Payer, Corrosion Testing Made Easy: DC Electrochemical Test Methods, NACE International, 1998.

[381] C.T. Wang, N. Gao, R.J.K. Wood, T.G. Langdon, Wear behavior of an aluminum alloy processed by equal-channel angular pressing, J. Mater. Sci. 46 (2011) 123–130.

[382] J.K. Han, H.J. Lee, J. il Jang, M. Kawasaki, T.G. Langdon, Micro-mechanical and tribological properties of aluminum-magnesium nanocomposites processed by high-pressure torsion, Mater. Sci. Eng. A. 684 (2017) 318–327.

[383] N.P. Lavery, J. Cherry, S. Mehmood, H. Davies, B. Girling, E. Sackett, S.G.R. Brown, J. Sienz, Effects of hot isostatic pressing on the elastic modulus and tensile properties of 316L parts made by powder bed laser fusion, Mater. Sci. Eng. A. 693 (2017) 186–213.

[384] H.P. Tang, J. Wang, C.N. Song, N. Liu, L. Jia, J. Elambasseril, M. Qian, Microstructure, Mechanical Properties, and Flatness of SEBM Ti-6Al-4V Sheet in As-Built and Hot Isostatically Pressed Conditions, Jom. 69 (2017) 466–471.

[385] B. Zhou, J. Zhou, H. Li, F. Lin, A study of the microstructures and mechanical properties of Ti6Al4V fabricated by SLM under vacuum, Mater. Sci. Eng. A. 724 (2018) 1–10.

[386] W. Tillmann, C. Schaak, J. Nellesen, M. Schaper, M.E. Aydinöz, K.P. Hoyer, Hot isostatic pressing of IN718 components manufactured by selective laser melting, Addit. Manuf. 13 (2017) 93–102.

[387] J. Damon, S. Dietrich, F. Vollert, J. Gibmeier, V. Schulze, Process dependent porosity and the influence of shot peening on porosity morphology regarding selective laser melted AlSi10Mg parts, Addit. Manuf. 20 (2018) 77–89.

[388] X.T. Luo, Y.K. Wei, Y. Wang, C.J. Li, Microstructure and mechanical property of Ti and Ti6Al4V prepared by an in-situ shot peening assisted cold spraying, Mater. Des. 85 (2015) 527–533.

[389] A. Maamoun, M. Elbestawi, S. Veldhuis, Influence of Shot Peening on AlSi10Mg Parts Fabricated by Additive Manufacturing, J. Manuf. Mater. Process. 2 (2018) 40.

[390] G. Ziółkowski, E. Chlebus, P. Szymczyk, J. Kurzac, Application of X-ray CT method for discontinuity and porosity detection in 316L stainless steel parts produced with SLM technology, Arch. Civ. Mech. Eng. 14 (2014) 608–614.

[391] D. Gu, Y.-C. Hagedorn, W. Meiners, G. Meng, R.J.S. Batista, K. Wissenbach, R. Poprawe, Densification behavior, microstructure evolution, and wear performance of selective laser melting processed commercially pure titanium, Acta Mater. 60 (2012) 3849–3860.

[392] J. a. Cherry, H.M. Davies, S. Mehmood, N.P. Lavery, S.G.R. Brown, J. Sienz, Investigation into the effect of process parameters on microstructural and physical properties of 316L stainless steel parts by selective laser melting, Int. J. Adv. Manuf. Technol. 76 (2014) 869–879.

[393] S. Tammas-Williams, H. Zhao, F. Léonard, F. Derguti, I. Todd, P.B. Prangnell, XCT analysis of the influence of melt strategies on defect population in Ti-6Al-4V components manufactured by Selective Electron Beam Melting, Mater. Charact. 102 (2015) 47–61.

[394] T. Gustmann, A. Neves, U. Kühn, P. Gargarella, C.S. Kiminami, C. Bolfarini, J. Eckert, S. Pauly, Influence of processing parameters on the fabrication of a Cu-Al-Ni-Mn shape-memory alloy by selective laser melting, Addit. Manuf. 11 (2016) 23–31.

[395] S.L. Campanelli, N. Contuzzi, A. Angelastro, A.D. Ludovico, Capabilities and Performances of the Selective Laser Melting Process, in: M.J. Er (Ed.), New Trends Technol. Devices, Comput. Commun. Ind. Syst., InTech, 2010: p. Chapter 13.

[396] M. Marya, V. Singh, S. Marya, J.Y. Hascoet, Microstructural Development and Technical Challenges in Laser Additive Manufacturing: Case Study with a 316L Industrial Part, Metall. Mater. Trans. B Process Metall. Mater. Process. Sci. 46B (2015) 1654–1665.

[397] S. Dadbakhsh, L. Hao, Effect of Al alloys on selective laser melting behaviour and microstructure of in situ formed particle reinforced composites, J. Alloys Compd. 541 (2012) 328–334.

[398] W.E. King, H.D. Barth, V.M. Castillo, G.F. Gallegos, J.W. Gibbs, D.E. Hahn, C. Kamath, A.M. Rubenchik, Observation of keyhole-mode laser melting in laser powder-bed fusion additive manufacturing, J. Mater. Process. Technol. 214 (2014) 2915–2925.

[399] C. Körner, A. Bauereiß, E. Attar, Fundamental consolidation mechanisms during selective beam melting of powders, Model. Simul. Mater. Sci. Eng. 21 (2013) 1–18.

[400] L. Jinhui, L. Ruidi, Z. Wenxian, F. Liding, Y. Huashan, Study on formation of surface and microstructure of stainless steel part produced by selective laser melting, Mater. Sci. Technol. 26 (2010) 1259–1264.

[401] M. Khajouei-Nezhad, M.H. Paydar, R. Ebrahimi, P. Jenei, P. Nagy, J. Gubicza, Microstructure and mechanical properties of ultrafine-grained aluminum consolidated by high-pressure torsion, Mater. Sci. Eng. A. 682 (2017) 501–508.

[402] P. Li, X. Wang, K.M. Xue, Y. Tian, Y.C. Wu, Microstructure and recrystallization behavior of pure W powder processed by high-pressure torsion, Int. J. Refract. Met. Hard Mater. 54 (2015) 439–444.

[403] J.R. Rice, D.M. Tracey, On the ductile enlargement of voids in triaxial stress fields*, J. Mech. Phys. Solids. 17 (1969) 201–217.

[404] L. Xue, Damage accumulation and fracture initiation in uncracked ductile solids subject to triaxial loading, Int. J. Solids Struct. 44 (2007) 5163–5181.

[405] M. Nakasaki, I. Takasu, H. Utsunomiya, Application of hydrostatic integration parameter for free-forging and rolling, J. Mater. Process. Technol. 177 (2006) 521–524.

[406] A. Wang, P.F. Thomson, P.D. Hodgson, A study of pore closure and welding in hot rolling process, J. Mater. Process. Technol. 60 (1996) 95–102.

[407] M. Saby, P.O. Bouchard, M. Bernacki, Void closure criteria for hot metal forming: A review, J. Manuf. Process. 19 (2015) 239–250.

[408] X.X. Zhang, Z.S. Cui, W. Chen, Y. Li, A criterion for void closure in large ingots during hot forging, J. Mater. Process. Technol. 209 (2009) 1950–1959.

[409] W.W. Wits, S. Carmignato, F. Zanini, T.H.J. Vaneker, Porosity testing methods for the quality assessment of selective laser melted parts, CIRP Ann. - Manuf. Technol. 65 (2016) 201–204.

[410] J. Bidulská, T. Kvačkaj, I. Pokorný, R. Bidulský, M. Actis Grande, Identification of the Critical Pore Sizes in Sintered and Ecaped Aluminium 6XXX Alloy, Arch. Metall. Mater. 58 (2013) 371–375.

[411] I. Maskery, N.T. Aboulkhair, M.R. Corfield, C. Tuck, A.T. Clare, R.K. Leach, R.D. Wildman, I.A. Ashcroft, R.J.M. Hague, Quantification and characterisation of porosity in selectively laser melted Al-Si10-Mg using X-ray computed tomography, Mater. Charact. 111 (2016) 193–204.

[412] M. Valdez, C. Kozuch, E.J. Faierson, I. Jasiuk, Induced porosity in Super Alloy 718 through the laser additive manufacturing process: Microstructure and mechanical properties, J. Alloys Compd. 725 (2017) 757–764.

[413] G. Kasperovich, J. Haubrich, J. Gussone, G. Requena, Correlation between porosity and processing parameters in TiAl6V4 produced by selective laser melting, Mater. Des. 105 (2016) 160–170.

[414] T. Ronneberg, C.M. Davies, P.A. Hooper, Revealing relationships between porosity, microstructure and mechanical properties of laser powder bed fusion 316L stainless steel through heat treatment, Mater. Des. 189 (2020) 108481.

[415] K. Geenen, A. Röttger, W. Theisen, Corrosion behavior of 316L austenitic steel processed by selective laser melting, hot-isostatic pressing, and casting, Mater. Corros. 9999 (2017) 1–12.

[416] A. Röttger, K. Geenen, M. Windmann, F. Binner, W. Theisen, Comparison of microstructure and mechanical properties of 316 L austenitic steel processed by selective laser melting with hot-isostatic pressed and cast material, Mater. Sci. Eng. A. 678 (2016) 365–376.

[417] V.A. Popovich, E. V. Borisov, A.A. Popovich, V.S. Sufiiarov, D. V. Masaylo, L. Alzina, Impact of heat treatment on mechanical behaviour of Inconel 718 processed with tailored microstructure by selective laser melting, Mater. Des. 131 (2017) 12–22.

[418] Y. Kaynak, O. Kitay, Porosity , Surface Quality , Microhardness and Microstructure of Selective Laser Melted 316L Stainless Steel Resulting from Finish Machining, Manuf. Mater. Process. 2 (2018) 1–14.

[419] Y. Yang, Y. Gong, S. Qu, Y. Rong, Y. Sun, M. Cai, Densification , surface morphology , microstructure and mechanical properties of 316L fabricated by hybrid manufacturing, Int. J. Adv. Manuf. Technol. 97 (2018) 2687–2696.

[420] S. Scheriau, Z. Zhang, S. Kleber, R. Pippan, Deformation mechanisms of a modified 316L austenitic steel subjected to high pressure torsion, Mater. Sci. Eng. A. 528 (2011) 2776–2786.

[421] X.H. An, S.D. Wu, Z.F. Zhang, R.B. Figueiredo, N. Gao, T.G. Langdon, Evolution of microstructural homogeneity in copper processed by high-pressure torsion, Scr. Mater. 63 (2010) 560–563.

[422] X.H. An, Q.Y. Lin, S.D. Wu, Z.F. Zhang, R.B. Figueiredo, N. Gao, T.G. Langdon, Significance of stacking fault energy on microstructural evolution in Cu and Cu-Al alloys processed by high-pressure torsion, Philos. Mag. 91 (2011) 3307–3326.

[423] Y. Cao, Y.B. Wang, X.H. An, X.Z. Liao, M. Kawasaki, S.P. Ringer, T.G. Langdon, Y.T. Zhu, Concurrent microstructural evolution of ferrite and austenite in a duplex stainless steel processed by high-pressure torsion, Acta Mater. 63 (2014) 16–29.

[424] S. Mohd Yusuf, Y. Chen, S. Yang, N. Gao, Microstructural evolution and strengthening of selective laser melted 316L stainless steel processed by high-pressure torsion, Mater. Charact. 159 (2020) 110012.

[425] P. Ganesh, R. Giri, R. Kaul, P. Ram Sankar, P. Tiwari, A. Atulkar, R.K. Porwal, R.K. Dayal, L.M. Kukreja, Studies on pitting corrosion and sensitization in laser rapid manufactured specimens of type 316L stainless steel, Mater. Des. 39 (2012) 509–521.

[426] M. El-Tahawy, J. Gubicza, Y. Huang, H. Choi, H. Choe, J.L. Lábár, T.G. Langdon, Evolution of microstructure, phase composition and hardness evolution in 316L stainless steel processed by high-pressure torsion, Mater. Sci. Forum. 879 (2016) 502–507.

[427] M. Kawasaki, R.B. Figueiredo, Y. Huang, T.G. Langdon, Interpretation of hardness evolution in metals processed by high-pressure torsion, J. Mater. Sci. 49 (2014) 6586–6596.

[428] Y.Z. Tian, S.D. Wu, Z.F. Zhang, R.B. Figueiredo, N. Gao, T.G. Langdon, Strain hardening behavior of a two-phase Cu-Ag alloy processed by high-pressure torsion, Scr. Mater. 65 (2011) 477–480.

[429] K. Edalati, T. Fujioka, Z. Horita, Evolution of Mechanical Properties and Microstructures with Equivalent Strain in Pure Fe Processed by High Pressure Torsion, Mater. Trans. 50 (2009) 44–50.

[430] S.M. Yusuf, Y. Chen, S. Yang, N. Gao, Micromechanical Response of Additively Manufactured 316L Stainless Steel Processed by High-Pressure Torsion, Adv. Eng. Mater. 2000052 (2020) 1–12.

[431] T. Ungár, Microstructural parameters from X-ray diffraction peak broadening, Scr. Mater. 51 (2004) 777–781.

[432] G.K. Williamson, R.E. Smallman, III. Dislocation densities in some annealed and cold-worked metals from measurements on the X-ray Debye-Scherrer spectrum, Philos. Mag. 1 (1956) 34–46.

[433] Y.H. Zhao, X.Z. Liao, Z. Jin, R.Z. Valiev, Y.T. Zhu, Microstructures and mechanical properties of ultrafine grained 7075 Al alloy processed by ECAP and their evolutions during annealing, Acta Mater. 52 (2004) 4589–4599.

[434] M. Ferrari, L. Lutterotti, Method for the simultaneous determination stresses and texture by x-ray diffraction of anisotropic residual, J. Appl. Phys. 76 (1994) 7246–7255.

[435] G. Caglioti, A. Paoletti, F.P. Ricci, Choice of collimators for a crystal spectrometer for neutron diffraction, Nucl. Instruments. 3 (1958) 223–228.

[436] C. Yan, L. Hao, A. Hussein, P. Young, J. Huang, W. Zhu, Microstructure and mechanical properties of aluminium alloy cellular lattice structures manufactured by direct metal laser sintering, Mater. Sci. Eng. A. 628 (2015) 238–246.

[437] K.G. Prashanth, S. Scudino, H.J. Klauss, K.B. Surreddi, L. Löber, Z. Wang, A.K. Chaubey, U. Kühn, J. Eckert, Microstructure and mechanical properties of Al-12Si produced by selective laser melting: Effect of heat treatment, Mater. Sci. Eng. A. 590 (2014) 153–160.

[438] F. Trevisan, F. Calignano, M. Lorusso, J. Pakkanen, A. Aversa, E.P. Ambrosio, M. Lombardi, P. Fino, D. Manfredi, On the selective laser melting (SLM) of the AlSi10Mg alloy: Process, microstructure, and mechanical properties, Materials (Basel). 10 (2017).

[439] D. Wang, C. Song, Y. Yang, Y. Bai, Investigation of crystal growth mechanism during selective laser melting and mechanical property characterization of 316L stainless steel parts, Mater. Des. 100 (2016) 291–299.

[440] M. Ziętala, T. Durejko, M. Polański, I. Kunce, T. Płociński, W. Zieliński, M. Łazińska, W. Stępniowski, T. Czujko, K.J. Kurzydłowski, Z. Bojar, The microstructure, mechanical properties and corrosion resistance of 316L stainless steel fabricated using laser engineered net shaping, Mater. Sci. Eng. A. 677 (2016) 1–10.

[441] J.R. Trelewicz, G.P. Halada, O.K. Donaldson, G. Manogharan, Microstructure and Corrosion Resistance of Laser Additively Manufactured 316L Stainless Steel, Jom. 68 (2016) 850–859.

[442] M.A. Melia, H.-D.A. Nguyen, J.M. Rodelas, E.J. Schindelholz, Corrosion Properties of 304L Stainless Steel made by Directed Energy Deposition Additive Manufacturing, Corros. Sci. (2019).

[443] C. Qiu, M. Al Kindi, A.S. Aladawi, I. Al Hatmi, A comprehensive study on microstructure and

tensile behaviour of a selectively laser melted stainless steel, Sci. Rep. (2018) 1–16.

[444] H.Y. Wan, Z.J. Zhou, C.P. Li, G.F. Chen, G.P. Zhang, Effect of scanning strategy on mechanical properties of selective laser melted Inconel 718, Mater. Sci. Eng. A. 753 (2019) 42–48.

[445] U.S. Bertoli, B.E. Macdonald, J.M. Schoenung, Stability of cellular microstructure in laser powder bed fusion of 316L stainless steel, Mater. Sci. Eng. A. 739 (2019) 109–117.

[446] A.T. Polonsky, M.P. Echlin, W.C. Lenthe, R.R. Dehoff, M.M. Kirka, T.M. Pollock, Defects and 3D structural inhomogeneity in electron beam additively manufactured Inconel 718, Mater. Charact. (2018).

[447] A. Leicht, U. Klement, E. Hryha, Effect of build geometry on the microstructural development of 316L parts produced by additive manufacturing, Mater. Charact. (2018).

[448] W. Wu, M. Song, S. Ni, J. Wang, Y. Liu, B. Liu, X. Liao, Dual mechanisms of grain refinement in a FeCoCrNi high-entropy alloy processed by high-pressure torsion, Sci. Rep. 7 (2017) 1–13.

[449] Y. Ma, T.G. Langdon, M. Furukawa, M. Nemoto, An investigation of ductility and microstructural evolution in an Al-3% Mg alloy with submicron grain size, J. Mater. Res. 8 (1993) 2810–2818.

[450] A. Vorhauer, R. Pippan, On the homogeneity of deformation by high pressure torsion, Scr. Mater. 51 (2004) 921–925.

[451] T. Hebesberger, H.P. Stüwe, A. Vorhauer, F. Wetscher, R. Pippan, Structure of Cu deformed by high pressure torsion, Acta Mater. 53 (2005) 393–402.

[452] F. Wetscher, B. Tian, R. Stock, R. Pippan, High pressure torsion of rail steels, Mater. Sci. Forum. 503–504 (2006) 455–460.

[453] R. Pippan, F. Wetscher, M. Hafok, A. Vorhauer, I. Sabirov, The limits of refinement by severe plastic deformation, Adv. Eng. Mater. 8 (2006) 1046–1056.

[454] S. Scheriau, R. Pippan, Influence of grain size on orientation changes during plastic deformation, Mater. Sci. Eng. A. 493 (2008) 48–52. [455] T. Ungár, G. Tichy, J. Gubicza, R.J. Hellmig, Correlation between subgrains and coherently scattering domains, Powder Diffr. 20 (2005) 366–375.

[456] S.V. Muley, A.N. Vidvans, G.P. Chaudhari, S. Udainiya, An assessment of ultra fine grained 316L stainless steel for implant applications, Acta Biomater. 30 (2016) 408–419.

[457] J. Lu, L. Hultman, E. Holmström, K.H. Antonsson, M. Grehk, W. Li, L. Vitos, A. Golpayegani, Stacking fault energies in austenitic stainless steels, Acta Mater. 111 (2016) 39–46.

[458] X.H. An, S.D. Wu, Z.G. Wang, Z.F. Zhang, Significance of stacking fault energy in bulk nanostructured materials: Insights from Cu and its binary alloys as model systems, Prog. Mater. Sci. 101 (2019) 1–45.

[459] D.A. Hughes, N. Hansen, High angle boundaries formed by grain subdivision mechanisms, Acta Mater. 45 (1997) 3871–3886.

[460] J.W. Christian, S. Mahajan, Deformation twinning, Prog. Mater. Sci. 39 (1995) 1–157.

[461] M.A. Meyers, O. Vöhringer, V.A. Lubarda, The onset of twinning in metals: A constitutive description, Acta Mater. 49 (2001) 4025–4039.

[462] W.Z. Han, Z.F. Zhang, S.D. Wu, S.X. Li, Combined effects of crystallographic orientation, stacking fault energy and grain size on deformation twinning in fcc crystals, Philos. Mag. 88 (2008) 3011–3029.

[463] J. Lu, L. Hultman, E. Holmström, K.H. Antonsson, M. Grehk, W. Li, L. Vitos, A. Golpayegani, Stacking fault energies in austenitic stainless steels, Acta Mater. 111 (2016) 39–46.

[464] A. Etienne, B. Radiguet, C. Genevois, J.M. Le Breton, R. Valiev, P. Pareige, Thermal stability of ultrafine-grained austenitic stainless steels, Mater. Sci. Eng. A. 527 (2010) 5805–5810.

[465] P. Chui, K. Sun, Thermal stability of a nanostructured layer on the surface of 316L stainless steel, J. Mater. Res. 29 (2014) 556–560.

[466] Y. Idell, G. Facco, A. Kulovits, M.R. Shankar, J.M.K. Wiezorek, Strengthening of austenitic stainless steel by formation of nanocrystalline γ-phase through severe plastic deformation during two-dimensional linear plane-strain machining, Scr. Mater. 68 (2013) 667–670.

[467] R.E. Schramm, R.P. Reed, Stacking fault energies of seven commercial austenitic stainless steels, Metall. Trans. A. 6 (1975) 1345–1351.

[468] H.M. Otte, The formation of stacking faults in austenite and its relation to martensite, Acta Metall. 5 (1957) 614–627.

[469] N.A. Enikeev, X. Sauvage, M.M. Abramova, M.Y. Murashkin, R.Z. Valiev, High strength state of UFG steel produced by severe plastic deformation, IOP Conf. Ser. Mater. Sci. Eng. 63 (2014) 1–6.

[470] B. Ravi Kumar, S. Sharma, B. Mahato, Formation of ultrafine grained microstructure in the austenitic stainless steel and its impact on tensile properties, Mater. Sci. Eng. A. 528 (2011) 2209–2216.

[471] A.T. Krawczynska, M. Lewandowska, R. Pippan, K.J. Kurzydlowski, The Effect of High Pressure

Torsion on Structural Refinement and Mechanical Properties of an Austenitic Stainless Steel, J. Nanosci. Nanotechnol. 13 (2013) 3246–3249.

[472] D.G. Morris, Strengthening mechanisms in nanocrystalline metals, in: Nanostructured Met. Alloy. Process. Microstruct. Mech. Prop. Appl., Woodhead Publishing Co., 2011: pp. 299–328.

[473] M.J. Starink, S.C. Wang, A model for the yield strength of overaged Al-Zn-Mg-Cu alloys, Acta Mater. 51 (2003) 5131–5150.

[474] S.C. Wang, Z. Zhu, M.J. Starink, Estimation of dislocation densities in cold rolled Al-Mg-Cu-Mn alloys by combination of yield strength data, EBSD and strength models, J. Microsc. 217 (2005) 174–178.

[475] J. Zhang, N. Gao, M.J. Starink, Microstructure development and hardening during high pressure torsion of commercially pure aluminium: Strain reversal experiments and a dislocation based model, Mater. Sci. Eng. A. 528 (2011) 2581–2591.

[476] X.G. Qiao, N. Gao, M.J. Starink, A model of grain refinement and strengthening of Al alloys due to cold severe plastic deformation, Philos. Mag. 92 (2012) 446–470.

[477] H. Halfa, Recent Trends in Producing Ultrafine Grained Steels, J. Miner. Mater. Charact. Eng. 02 (2014) 428–469.

[478] F.R.N. Nabarro, Fifty-year study of the Peierls-Nabarro stress, Mater. Sci. Eng. A. A234-236 (1997) 67–76.

[479] M.V. Karavaeva, M.M. Abramova, N.A. Enikeev, G.I. Raab, R.Z. Valiev, Superior strength of austenitic steel produced by combined processing, including equal-channel angular pressing and rolling, Metals (Basel). 6 (2016).

[480] M.J. Starink, X.G. Qiao, J. Zhang, N. Gao, Predicting grain refinement by cold severe plastic deformation in alloys using volume averaged dislocation generation, Acta Mater. 57 (2009) 5796–5811.

[481] M.J. Starink, X. Cheng, S. Yang, Hardening of pure metals by high-pressure torsion: A physically based model employing volume-averaged defect evolutions, Acta Mater. 61 (2013) 183–192.

[482] J.G. Kim, N.A. Enikeev, J.B. Seol, M.M. Abramova, M. V. Karavaeva, R.Z. Valiev, C.G. Park, H.S. Kim, Superior Strength and Multiple Strengthening Mechanisms in Nanocrystalline TWIP Steel, Sci. Rep. 8 (2018) 1–10.

[483] S. Schmauder, C. Kohler, Atomistic simulations of solid solution strengthening of α-iron, Comput. Mater. Sci. 50 (2011) 1238–1243.

[484] I. Gutierrez-Urrutia, S. Zaefferer, D. Raabe, The effect of grain size and grain orientation on deformation twinning in a Fe-22wt.% Mn-0.6wt.% C TWIP steel, Mater. Sci. Eng. A. 527 (2010) 3552–3560.

[485] I. Gutierrez-Urrutia, D. Raabe, Dislocation and twin substructure evolution during strain hardening of an Fe-22 wt.% Mn-0.6 wt.% C TWIP steel observed by electron channeling contrast imaging, Acta Mater. 59 (2011) 6449–6462.

[486] R.L. Fullman, Measurement of Particle Sizes in Opaque Bodies, Trans. AIME, J. Met. 197 (1953) 447–452.

[487] M.A. Meyers, A. Mishra, D.J. Benson, Mechanical properties of nanocrystalline materials, Prog. Mater. Sci. 51 (2006) 427–556.

[488] J. li Ning, E. Courtois-Manara, L. Kurmanaeva, A. V. Ganeev, R.Z. Valiev, C. Kübel, Y. Ivanisenko, Tensile properties and work hardening behaviors of ultrafine grained carbon steel and pure iron processed by warm high pressure torsion, Mater. Sci. Eng. A. 581 (2013) 8–15.

[489] P. Zhang, S.X. Li, Z.F. Zhang, General relationship between strength and hardness, Mater. Sci. Eng. A. 529 (2011) 62–73.

[490] M.V. Karavaeva, M.A. Nikitina, A.V. Ganeev, R.K. Islamgaliev, High-strength state of ultrafine-grained martensitic steel produced by high pressure torsion, IOP Conf. Ser. Mater. Sci. Eng. 179 (2017) 1–9.

[491] J. Eliasson, R. Sandström, Proof strength values for austenitic stainless steels at elevated temperatures, Steel Res. 71 (2000) 249–254.

[492] K. Kako, E. Kawakami, J. Ohta, M. Mayuzumi, Effects of Various Alloying Elements on Tensile Properties of High-Purity Fe-18Cr-(14-16)Ni Alloys at Room Temperature., Mater Trans. 43 (2002) 155–162.

[493] R.S. Ganji, P. Sai Karthik, K. Bhanu Sankara Rao, K. V. Rajulapati, Strengthening mechanisms in equiatomic ultrafine grained AlCoCrCuFeNi high-entropy alloy studied by micro- and nanoindentation methods, Acta Mater. 125 (2017) 58–68.

[494] G. Nurislamova, X. Sauvage, M. Murashkin, R. Islamgaliev, R. Valiev, Nanostructure and related mechanical properties of an Al-Mg-Si alloy processed by severe plastic deformation, Philos. Mag.

Lett. 88 (2008) 459–466.

[495] W.T. Sun, X.G. Qiao, M.Y. Zheng, Y. He, N. Hu, C. Xu, N. Gao, M.J. Starink, Exceptional grain refinement in a Mg alloy during high pressure torsion due to rare earth containing nanosized precipitates, Mater. Sci. Eng. A. 728 (2018) 115–123.

[496] W.T. Sun, X.G. Qiao, M.Y. Zheng, X.J. Zhao, H.W. Chen, N. Gao, M.J. Starink, Achieving ultra-high hardness of nanostructured Mg-8.2Gd-3.2Y-1.0Zn-0.4Zr alloy produced by a combination of high pressure torsion and ageing treatment, Scr. Mater. 155 (2018) 21–25.

[497] W.T. Sun, X.G. Qiao, M.Y. Zheng, C. Xu, S. Kamado, X.J. Zhao, H.W. Chen, N. Gao, M.J. Starink, Altered ageing behaviour of a nanostructured Mg-8.2Gd-3.8Y-1.0Zn-0.4Zr alloy processed by high pressure torsion, Acta Mater. 151 (2018) 260–270.

[498] S. V. Dobatkin, L.M. Kanutkina, O. V. Rybal’chenko, V.S. Komlev, Phase and structural transformations in corrosion-resistant steels upon high-pressure torsion and heating, Russ. Metall. 2012 (2013) 763–771.

[499] S.M. Yusuf, M. Hoegden, N. Gao, Effect of sample orientation on the microstructure and microhardness of additively manufactured AlSi10Mg processed by high-pressure torsion, Int. J. Adv. Manuf. Technol. (2020) 1–17.

[500] J.R. Donahue, A.B. Lass, J.T. Burns, The interaction of corrosion fatigue and stress-corrosion cracking in a precipitation-hardened martensitic stainless steel, Npj Mater. Degrad. (2017) 1–11.

[501] C.H. Hsu, T.C. Chen, R.T. Huang, L.W. Tsay, Stress corrosion cracking susceptibility of 304L Substrate and 308L weld metal exposed to a salt spray, Materials (Basel). 10 (2017) 1–14.

[502] O.M. Alyousif, R. Nishimura, On the stress corrosion cracking and hydrogen embrittlement behavior of austenitic stainless steels in boiling saturated magnesium chloride solutions, Int. J. Corros. 2012 (2012) 1–11.

[503] R. Parrott, H. Pitts, Chloride stress corrosion cracking in austenitic stainless steel, 2011.

[504] F.K. Yan, G.Z. Liu, N.R. Tao, K. Lu, Strength and ductility of 316L austenitic stainless steel strengthened by nano-scale twin bundles, Acta Mater. 60 (2012) 1059–1071. [505] A.S. Hamada, L.P. Karjalainen, M.C. Somani, Electrochemical corrosion behaviour of a novel submicron-grained austenitic stainless steel in an acidic NaCl solution, Mater. Sci. Eng. A. 431 (2006) 211–217.

[506] M. Kawasaki, J. Il Jang, Micro-mechanical response of an Al-Mg hybrid system synthesized by high-pressure torsion, Materials (Basel). 10 (2017) 1–15.

[507] I.-C. Choi, Y.-J. Kim, B. Ahn, M. Kawasaki, T.G. Langdon, J. Jang, Evolution of plasticity, strain-rate sensitivity and the underlying deformation mechanism in Zn–22% Al during high-pressure torsion, Scr. Mater. 75 (2013) 102–105.

[508] I.C. Choi, D.H. Lee, B. Ahn, K. Durst, M. Kawasaki, T.G. Langdon, J. Il Jang, Enhancement of strain-rate sensitivity and shear yield strength of a magnesium alloy processed by high-pressure torsion, Scr. Mater. 94 (2015) 44–47.

[509] M. Haghshenas, O. Totuk, M. Masoomi, S.M. Thompson, N. Shamsaei, Small-Scale Mechanical Properties of Additively Manufactured Ti-6Al-4V, in: Proc. 28th Annu. Int. Solid Free. Fabr. Symp., 2017: pp. 134–147.

[510] N.T. Aboulkhair, I. Maskery, C. Tuck, I. Ashcroft, N.M. Everitt, On the formation of AlSi10Mg single tracks and layers in selective laser melting: Microstructure and nano-mechanical properties, J. Mater. Process. Technol. 230 (2016) 88–98.

[511] B. Ahn, H.J. Lee, I.C. Choi, M. Kawasaki, J. Il Jang, T.G. Langdon, Micro-Mechanical Behavior of an Exceptionally Strong Metal Matrix Nanocomposite Processed by High-Pressure Torsion, Adv. Eng. Mater. 18 (2016) 1001–1008.

[512] W.C. Oliver, G.M. Pharr, An improved technique for determining hardness and elastic modulus (Young’s modulus), J. Mater. Res. 7 (1992) 1564–1583.

[513] N.Q. Chinh, R.Z. Valiev, X. Sauvage, G. Varga, K. Havancsák, M. Kawasaki, B.B. Straumal, T.G. Langdon, Grain boundary phenomena in an ultrafine-grained Al-Zn alloy with improved mechanical behavior for micro-devices, Adv. Eng. Mater. 16 (2014) 1000–1009.

[514] G.M. Pharr, E.G. Herbert, Y. Gao, The Indentation Size Effect: A Critical Examination of Experimental Observations and Mechanistic Interpretations, Annu. Rev. Mater. Res. 40 (2010) 271–292.

[515] M. Kawasaki, H.J. Lee, I.C. Choi, J. Il Jang, B. Ahn, T.G. Langdon, Evolution of hardness, microstructure, and strain rate sensitivity in a Zn-22% Al eutectoid alloy processed by high-pressure torsion, IOP Conf. Ser. Mater. Sci. Eng. 63 (2014) 1–10.

[516] D.H. Lee, I.C. Choi, M.Y. Seok, J. He, Z. Lu, J.Y. Suh, M. Kawasaki, T.G. Langdon, J. Il Jang, Nanomechanical behavior and structural stability of a nanocrystalline CoCrFeNiMn high-entropy alloy processed by high-pressure torsion, J. Mater. Res. 30 (2015) 2804–2815.

[517] Y. Chen, N. Gao, G. Sha, S.P. Ringer, M.J. Starink, Strengthening of an Al-Cu-Mg alloy processed by high-pressure torsion due to clusters, defects and defect-cluster complexes, Mater. Sci. Eng. A. 627 (2015) 10–20.

[518] Y. Chen, N. Gao, G. Sha, S.P. Ringer, M.J. Starink, Microstructural evolution, strengthening and thermal stability of an ultrafine-grained Al-Cu-Mg alloy, Acta Mater. 109 (2016) 202–212.

[519] I.C. Choi, Y.J. Kim, Y.M. Wang, U. Ramamurty, J. Il Jang, Nanoindentation behavior of nanotwinned Cu: Influence of indenter angle on hardness, strain rate sensitivity and activation volume, Acta Mater. 61 (2013) 7313–7323.

[520] M.J. Mayo, W.D. Nix, A micro-indentation study of superplasticity in Pb, Sn, and Sn-38 wt% Pb, Acta Metall. 36 (1988) 2183–2192.

[521] S. Shim, J. il Jang, G.M. Pharr, Extraction of flow properties of single-crystal silicon carbide by nanoindentation and finite-element simulation, Acta Mater. 56 (2008) 3824–3832.

[522] F. Khodabakhshi, M.H. Farshidianfar, A.P. Gerlich, M. Nosko, V. Trembošová, A. Khajepour, Microstructure, strain-rate sensitivity, work hardening, and fracture behavior of laser additive manufactured austenitic and martensitic stainless steel structures, Mater. Sci. Eng. A. 756 (2019) 545–561.

[523] R.P. Carreker, W.R. Hibbard, Tensile deformation of high-purity copper as a function of temperature, strain rate, and grain size, Acta Metall. 1 (1953) 654–663.

[524] R. Schwaiger, B. Moser, M. Dao, N. Chollacoop, S. Suresh, Some critical experiments on the strain-rate sensitivity of nanocrystalline nickel, Acta Mater. 51 (2003) 5159–5172.

[525] J. May, H.W. Höppel, M. Göken, Strain Rate Sensitivity of Ultrafine Grained FCC- and BCC-Type Metals, Mater. Sci. Forum. 503–504 (2006) 781–786.

[526] Z. Li, T. Voisin, J.T. McKeown, J. Ye, T. Braun, C. Kamath, W.E. King, Y.M. Wang, Tensile properties, strain rate sensitivity, and activation volume of additively manufactured 316L stainless steels, Int. J. Plast. 120 (2019) 395–410.

[527] Y.M. Wang, A. V. Hamza, E. Ma, Temperature-dependent strain rate sensitivity and activation volume of nanocrystalline Ni, Acta Mater. 54 (2006) 2715–2726.

[528] Y.T. Zhu, X.L. Wu, Ductility and plasticity of nanostructured metals: differences and issues, Mater. Today Nano. 2 (2018) 15–20.

[529] Y.T. Zhu, X.Z. Liao, X.L. Wu, Deformation twinning in nanocrystalline materials, Prog. Mater. Sci. 57 (2012) 1–62.

[530] H. Conrad, Plastic deformation kinetics in nanocrystalline FCC metals based on the pile-up of dislocations, Nanotechnology. 18 (2007).

[531] H. Conrad, Grain size dependence of the plastic deformation kinetics in Cu, Mater. Sci. Eng. A. 341 (2003) 216–228.

[532] T. Zhu, J. Li, A. Samanta, H.G. Kim, S. Suresh, Interfacial plasticity governs strain rate sensitivity and ductility in nanostructured metals, Proc. Natl. Acad. Sci. 104 (2007) 3031–3036.

[533] T. Voisin, N.P. Calta, S.A. Khairallah, J.B. Forien, L. Balogh, R.W. Cunningham, A.D. Rollett, Y.M. Wang, Defects-dictated tensile properties of selective laser melted Ti-6Al-4V, Mater. Des. 158 (2018) 113–126.

[534] W. Huo, F. Fang, X. Liu, S. Tan, Z. Xie, J. Jiang, Remarkable strain-rate sensitivity of nanotwinned CoCrFeNi alloys, Appl. Phys. Lett. 114 (2019) 101904-1-101904–4.

[535] V. Yamakov, D. Wolf, S.R. Phillpot, A.K. Mukherjee, H. Gleiter, Dislocation processes in the deformation of nanocrystalline aluminium by molecular-dynamics simulation, Nat. Mater. 1 (2002) 45–48.

[536] H. Van Swygenhoven, Grain Boundaries and Dislocations, Science . 296 (2002) 66–68.

[537] D. Wolf, V. Yamakov, S.R. Phillpot, A. Mukherjee, H. Gleiter, Deformation of nanocrystalline materials by molecular-dynamics simulation: Relationship to experiments?, Acta Mater. 53 (2005) 1–40.

[538] J. Schiøtz, Atomic-scale modeling of plastic deformation of nanocrystalline copper, Scr. Mater. 51 (2004) 837–841.

[539] A.G. Frøseth, P.M. Derlet, H. Van Swygenhoven, Grown-in twin boundaries affecting deformation mechanisms in nc-metals, Appl. Phys. Lett. 85 (2004) 5863–5865.

[540] L. Gil, S. Brühl, L. Jiménez, O. Leon, R. Guevara, M.H. Staia, Corrosion performance of the plasma nitrided 316L stainless steel, Surf. Coatings Technol. 201 (2006) 4424–4429.

[541] A. Di Schino, J.M.J. Kenny, Effects of the grain size on the corrosion behavior of refined AISI 304 austenitic stainless steels, J. Mater. Sci. Lett. 21 (2002) 1631–1634.

[542] Y. Li, F. Wang, Grain size effect on the electrochemical corrosion behavior of surface

nanocrystallized low-carbon steel, Corrosion. 60 (2004) 891–896.

[543] G. Sander, S. Thomas, V. Cruz, M. Jurg, N. Birbilis, X. Gao, M. Brameld, C.R. Hutchinson, On The Corrosion and Metastable Pitting Characteristics of 316L Stainless Steel Produced by Selective Laser Melting, J. Electrochem. Soc. 164 (2017) C250–C257.

[544] N. Zaveri, M. Mahapatra, A. Deceuster, Y. Peng, L. Li, A. Zhou, Corrosion resistance of pulsed laser-treated Ti-6Al-4V implant in simulated biofluids, Electrochim. Acta. 53 (2008) 5022–5032.

[545] ASTM, ASTM G 102-89: Standard Practice for Calculation of Corrosion Rates and Related Information, 1999.

[546] V. Muthukumaran, V. Selladurai, S. Nandhakumar, M. Senthilkumar, Experimental investigation on corrosion and hardness of ion implanted AISI 316L stainless steel, Mater. Des. 31 (2010) 2813–2817.

[547] X. Wang, M. Nie, C.T. Wang, S.C. Wang, N. Gao, Microhardness and corrosion properties of hypoeutectic Al-7Si alloy processed by high-pressure torsion, Mater. Des. 83 (2015) 193–202.

[548] M. Nie, C.T. Wang, M. Qu, N. Gao, J.A. Wharton, T.G. Langdon, The corrosion behaviour of commercial purity titanium processed by high-pressure torsion, J. Mater. Sci. 49 (2014) 2824–2831.

[549] A. Norlin, J. Pan, C. Leygraf, Investigation of interfacial capacitance of Pt, Ti and TiN coated electrodes by electrochemical impedance spectroscopy, Biomol. Eng. 19 (2002) 67–71.

[550] A. Szummer, M. Janik-Czachor, S. Hofmann, Discontinuity of the passivating film at nonmetallic stainless steels, Mater. Sci. Commun. 34 (1993) 181–183.

[551] D.E. Williams, T.F. Mohiuddin, Y.Y. Zhu, Elucidation of a trigger mechanism for pitting corrosion of stainless steels using submicron resolution scanning electrochemical and photoelectrochemical microscopy, J. Electrochem. Soc. 145 (1998) 2664–2672.

[552] J.X. Zou, K.M. Zhang, S.Z. Hao, C. Dong, T. Grosdidier, Mechanisms of hardening, wear and corrosion improvement of 316 L stainless steel by low energy high current pulsed electron beam surface treatment, Thin Solid Films. 519 (2010) 1404–1415.

[553] S. Tamilselvi, R. Murugaraj, N. Rajendran, Electrochemical impedance spectroscopic studies of titanium and its alloys in saline medium, Mater. Corros. 58 (2007) 113–120.

[554] S.L. De Assis, S. Wolynec, I. Costa, Corrosion characterization of titanium alloys by electrochemical techniques, Electrochim. Acta. 51 (2006) 1815–1819.

[555] J.-B. Jorcin, M.E. Orazem, N. Pébère, B. Tribollet, CPE analysis by local electrochemical impedance spectroscopy, Electrochim. Acta. 51 (2006) 1473–1479.

[556] K. Sasaki, G.T. Burstein, The generation of surface roughness during slurry erosion-corrosion and its effect on the pitting potential, Corros. Sci. 38 (1996) 2111–2120.

[557] E. Otero, A. Pardo, M. V. Utrilla, E. Sáenz, J.F. Álvarez, Corrosion behaviour of AISI 304L and 316L stainless steels prepared by powder metallurgy in the presence of sulphuric and phosphoric acid, Corros. Sci. 40 (1998) 1421–1434.

[558] D.R. Gabe, Corrosion and Protection of Sintered Metal Parts, Powder Metall. 20 (1977) 227–231.

[559] Y. Liu, D. Liu, C. You, M. Chen, Effects of grain size on the corrosion resistance of pure magnesium by cooling rate-controlled solidification, Front. Mater. Sci. 9 (2015) 247–253.

[560] M. Rifai, H. Miyamoto, H. Fujiwara, Effects of Strain Energy and Grain Size on Corrosion Resistance of Ultrafine Grained Fe-20 % Cr Steels with Extremely low C and N Fabricated by ECAP, Int. J. Corros. 2015 (2015) 1–9.

[561] N. Birbilis, K.D. Ralston, S. Virtanen, H.L. Fraser, C.H.J. Davies, Grain character influences on corrosion of ECAPed pure magnesium, Corros. Eng. Sci. Technol. 45 (2010) 224–230.

[562] K.D. Ralston, N. Birbilis, C.H.J. Davies, Revealing the relationship between grain size and corrosion rate of metals, Scr. Mater. 63 (2010) 1201–1204.

[563] A. Hemmasian Ettefagh, S. Guo, Electrochemical behavior of AISI316L stainless steel parts produced by laser-based powder bed fusion process and the effect of post annealing process, Addit. Manuf. 22 (2018) 153–156.

[564] X. Ni, D. Kong, W. Wu, L. Zhang, C. Dong, B. He, L. Lu, K. Wu, D. Zhu, Corrosion Behavior of 316L Stainless Steel Fabricated by Selective Laser Melting Under Different Scanning Speeds, J. Mater. Eng. Perform. 27 (2018) 3667–3677.

[565] E. Hug, R. Prasath Babu, I. Monnet, A. Etienne, F. Moisy, V. Pralong, N. Enikeev, M. Abramova, X. Sauvage, B. Radiguet, Impact of the nanostructuration on the corrosion resistance and hardness of irradiated 316 austenitic stainless steels, Appl. Surf. Sci. 392 (2017) 1026–1035.

[566] K. Hajizadeh, H. Maleki-Ghaleh, A. Arabi, Y. Behnamian, E. Aghaie, A. Farrokhi, M.G. Hosseini, M.H. Fathi, Corrosion and biological behavior of nanostructured 316L stainless steel processed by severe plastic deformation, Surf. Interface Anal. 47 (2015) 978–985.

[567] C.T. Kwok, F.T. Cheng, H.C. Man, W.H. Ding, Corrosion characteristics of nanostructured layer on

316L stainless steel fabricated by cavitation-annealing, Mater. Lett. 60 (2006) 2419–2422.

[568] M. Eskandari, M. Yeganeh, M. Motamedi, Investigation in the corrosion behaviour of bulk nanocrystalline 316L austenitic stainless steel in NaCl solution, Micro Nano Lett. 7 (2012) 380–383.

[569] Z.J. Zheng, Y. Gao, Y. Gui, M. Zhu, Corrosion behaviour of nanocrystalline 304 stainless steel prepared by equal channel angular pressing, Corros. Sci. 54 (2012) 60–67.

[570] R.K. Gupta, R.K. Singh Raman, C.C. Koch, Electrochemical characteristics of nano and microcrystalline Fe-Cr alloys, J. Mater. Sci. 47 (2012) 6118–6124.

[571] H. Li, M. Ramezani, M. Li, C. Ma, J. Wang, Tribological performance of selective laser melted 316L stainless steel, Tribiology Int. 128 (2018) 121–129.

[572] H. Li, M. Ramezani, M. Li, C. Ma, J. Wang, Effect of process parameters on tribological performance of 316L stainless steel parts fabricated by selective laser melting, Manuf. Lett. 16 (2018) 36–39.

[573] Y. Zhu, J. Zou, X. Chen, H. Yang, Tribology of selective laser melting processed parts: Stainless steel 316 L under lubricated conditions, Wear. 350–351 (2016) 46–55.

[574] F. Bartolomeu, M. Buciumeanu, E. Pinto, N. Alves, O. Carvalho, F.S. Silva, G. Miranda, 316L stainless steel mechanical and tribological behavior — A comparison between selective laser melting , hot pressing and conventional casting, Addit. Manuf. 16 (2017) 81–89.

[575] L. Valentini, A. Di Schino, J.M. Kenny, Y. Gerbig, H. Haefke, Influence of grain size and film composition on wear resistance of ultra fine grained AISI 304 stainless steel coated with amorphous carbon films, Wear. 253 (2002) 458–464.

[576] S.V. Muley, A.N. Vidvans, G.P. Chaudhari, S. Udainiya, An assessment of ultra fine grained 316L stainless steel for implant applications, Acta Biomater. 30 (2016) 408–419.

[577] J. Sami, C. Mahdi, The influence of surface nanocrystallization on structural, tribological and electrochemical properties of 316 L, AIP Conf. Proc. 1976 (2018) 1–5.

[578] A. Amanov, S.W. Lee, Y.S. Pyun, Low friction and high strength of 316L stainless steel tubing for biomedical applications, Mater. Sci. Eng. C. 71 (2017) 176–185.

[579] S.S. Rezaei-Nejad, A. Abdollah-zadeh, M. Hajian, F. Kargar, R. Seraj, Formation of Nanostructure in AISI 316L Austenitic Stainless Steel by Friction Stir Processing, Procedia Mater. Sci. 11 (2015) 397–402.

[580] Y. Mine, Z. Horita, Y. Murakami, Effect of high-pressure torsion on hydrogen trapping in Fe – 0 . 01 mass % C and type 310S austenitic stainless steel, Acta Mater. 58 (2010) 649–657.

[581] Y. Todaka, Y. Miki, M. Umemoto, C. Wang, K. Tsuchiya, Tensile Property of Submicrocrystalline Pure Fe Produced by HPT-straining, Mater. Sci. Forum. 584–586 (2008) 597–602.

[582] R.Z. Valiev, Y. V. Ivanisenko, E.F. Rauch, B. Baudelet, Structure and deformation behaviour of Armco iron subjected to severe plastic deformation, Acta Mater. 44 (1996) 4705–4712. [583] E.O. Hall, The Deformation and Ageing of Mild Steel: III Discussion of Results, Proc. Phys. Soc. Sect. B. 64 (1951) 747.

[584] N.J. Petch, The cleavage strength of polycrystals, J. Iron Steel Inst. 174 (1953) 25–28.

[585] H. Kato, Y. Todaka, M. Umemoto, K. Morisako, M. Hashimoto, M. Haga, Dry Sliding Wear Properties of Sub-Microcrystalline Ultra-Low Carbon Steel Produced by High-Pressure Torsion Straining, Mater. Trans. 53 (2012) 128–132.

[586] J.F. Archard, Contact and Rubbing of Flat Surfaces, J. Appl. Phys. 24 (1953) 981.

[587] C.T. Wang, N. Gao, M.G. Gee, R.J.K. Wood, T.G. Langdon, Effect of grain size on the micro-tribological behavior of pure titanium processed by high-pressure torsion, Wear. 280–281 (2012) 28–35.

[588] T. Kayaba, K. Hokkirigawa, K. Kato, Analysis of the abrasive wear mechanism by successive observations of wear processes in a scanning electron microscope, Wear. 110 (1986) 419–430.

[589] H. Kato, Y. Todaka, M. Umemoto, M. Haga, Sliding wear behavior of sub-microcrystalline pure iron produced by high-pressure torsion straining, Wear. 336–337 (2015) 58–68.

[590] M.M. Khruschov, Principles of abrasive wear, Wear. 28 (1974) 69–88.

[591] K. Kato, Abrasive wear of metals, Tribol. Int. 30 (1997) 333–338.

[592] K. Kato, Micro-mechanisms of wear - wear modes, Wear. (1992) 277–295.

[593] J.F. Archard, W. Hirst, The Wear of Metals under Unlubricated Conditions, Proc. R. Soc. A. 236 (1956) 397–410.

[594] N.C. Welsh, The Dry Wear of Steels I. The General Pattern of Behaviour, Philos. Trans. R. Soc. London. Ser. A. 257 (1965) 31–70.

[595] T.F.J. Quinn, Review of oxidational wear Part I : The origins of oxidational wear, Tribol. Int. 16 (1983) 257–271.

[596] J. Jiang, F.H. Stott, M.M. Stack, The role of triboparticulates in dry sliding wear, Tribol. Int. 31 (1998) 245–256.

[597] H. Kato, K. Komai, Tribofilm formation and mild wear by tribo-sintering of nanometer-sized oxide particles on rubbing steel surfaces, Wear. 262 (2007) 36–41.

[598] H. Kato, Effects of supply of fine oxide particles onto rubbing steel surfaces on severe – mild wear transition and oxide film formation, Tribol. Int. 41 (2008) 735–742.

[599] T. Roland, D. Retraint, K. Lu, J. Lu, Effect of Surface Nano Crystallization on Tribological Properties of Stainless Steel, Mater. Sci. Forum. 524–525 (2006) 717–722.

[600] W. Qin, J. Kang, J. Li, W. Yue, Y. Liu, D. She, Q. Mao, Y. Li, Tribological behavior of the 316L stainless steel with heterogeneous lamella structure, Materials (Basel). 11 (2018) 1–12.

[601] M. Shen, J. Zheng, X. Meng, X. Li, X. Peng, Influence of Al2O3 particles on the friction and wear behaviors of nitrile rubber against 316L stainless steel, Appl. Phys. Eng. 16 (2015) 151–160.

[602] K. Hokkirigawa, K. Kato, An experimental and theoretical investigation of ploughing , cutting and wedge formation during abrasive wear, Tribol. Int. (1988) 51–57.

[603] I.M. Hutchings, Tribology: Friction and wear of engineering materials, First edit, London, 1992.

[604] A. Triwiyanto, P. Hussain, A. Rahman, M.C. Ismail, The Influence of Nitriding Time of AISI 316L Stainless Steel on Microstructure and Tribological Properties, Asian J. Sci. Res. 6 (2013) 323–330.

[605] H. Kato, Y. Todaka, Microstructure and Wear Properties of High-Pressure Torsion Processed Iron, Mater. Sci. Forum. 890 (2017) 371–374.

[606] A. Bansal, A.K. Sharma, S. Das, P. Kumar, On microstructure and strength properties of microwave welded Inconel 718/ stainless steel (SS-316L), Proc. Inst. Mech. Eng. Part L J. Mater. Des. Appl. 230 (2016) 939–948.

[607] K.I. Mori, N. Bay, L. Fratini, F. Micari, A.E. Tekkaya, Joining by plastic deformation, CIRP Ann. - Manuf. Technol. 62 (2013) 673–694.

[608] J.N. Dupont, S.W. Banovic, A.R. Marder, Microstructural evolution and weldability of dissimilar welds between a super austenitic stainless steel and nickel-based alloys, Weld. J. (Miami, Fla). 82 (2003).

[609] H. Naffakh, M. Shamanian, F. Ashrafizadeh, Dissimilar welding of AISI 310 austenitic stainless steel to nickel-based alloy Inconel 657, J. Mater. Process. Technol. 209 (2009) 3628–3639.

[610] K. Devendranath Ramkumar, S.D. Patel, S. Sri Praveen, D.J. Choudhury, P. Prabaharan, N. Arivazhagan, M.A. Xavior, Influence of filler metals and welding techniques on the structure-property relationships of Inconel 718 and AISI 316L dissimilar weldments, Mater. Des. 62 (2014) 175–188.

[611] P. Kah, M.S.J. Martikainen, Trends in Joining Dissimilar Metals by Welding, Adv. Mater. Sport. Equip. Des. 440 (2014) 269–276.

[612] A. Bandyopadhyay, B. Heer, Additive manufacturing of multi-material structures, Mater. Sci. Eng. R Reports. 129 (2018) 1–16.

[613] M. Kawasaki, T.G. Langdon, Using Severe Plastic Deformation to Fabricate Strong Metal Matrix Composites, Mater. Res. 20 (2017) 46–52.

[614] M. Kawasaki, T.G. Langdon, Formation of Metal Matrix Nanocomposite Synthesized by High-Pressure Torsion via Diffusion Bonding, Mater. Sci. Forum. 879 (2016) 1068–1073.

[615] M. Kawasaki, B. Ahn, H. Lee, A.P. Zhilyaev, T.G. Langdon, Using high-pressure torsion to process an aluminum-magnesium nanocomposite through diffusion bonding, J. Mater. Res. 31 (2016) 88–99.

[616] X. Qiao, X. Li, X. Zhang, Y. Chen, M. Zheng, I.S. Golovin, N. Gao, M.J. Starink, Intermetallics formed at interface of ultrafine grained Al/Mg bi-layered disks processed by high pressure torsion at room temperature, Mater. Lett. 181 (2016) 187–190.

[617] B. Ahn, A.P. Zhilyaev, H.J. Lee, M. Kawasaki, T.G. Langdon, Rapid synthesis of an extra hard metal matrix nanocomposite at ambient temperature, Mater. Sci. Eng. A. 635 (2015) 109–117.

[618] T. Ramkumar, M. Selvakumar, P. Narayanasamy, A.A. Begam, P. Mathavan, A.A. Raj, Studies on the structural property, mechanical relationships and corrosion behaviour of Inconel 718 and SS 316L dissimilar joints by TIG welding without using activated flux, J. Manuf. Process. 30 (2017) 290–298.

[619] B. Baufeld, Mechanical Properties of INCONEL 718 Parts Manufactured by Shaped Metal Deposition (SMD), J. Mater. Eng. Perform. 21 (2011) 1416–1421.

[620] M. Kawasaki, Different models of hardness evolution in ultrafine-grained materials processed by high-pressure torsion, J. Mater. Sci. 49 (2014) 18–34.

[621] Y.Z. Tian, J.J. Li, P. Zhang, S.D. Wu, Z.F. Zhang, M. Kawasaki, T.G. Langdon, Microstructures, strengthening mechanisms and fracture behavior of Cu-Ag alloys processed by high-pressure torsion,

Acta Mater. 60 (2012) 269–281.

[622] S. Bayramoglu, C.H. Gür, I. V. Alexandrov, M.M. Abramova, Characterization of ultra-fine grained steel samples produced by high pressure torsion via magnetic Barkhausen noise analysis, Mater. Sci. Eng. A. 527 (2010) 927–933.

[623] J.T. Hofman, D.F. De Lange, B. Pathiraj, J. Meijer, FEM modeling and experimental verification for dilution control in laser cladding, J. Mater. Process. Technol. 211 (2011) 187–196.

[624] L.E. Murr, E. Martinez, K.N. Amato, S.M. Gaytan, J. Hernandez, D. a. Ramirez, P.W. Shindo, F. Medina, R.B. Wicker, Fabrication of Metal and Alloy Components by Additive Manufacturing: Examples of 3D Materials Science, J. Mater. Res. Technol. 1 (2012) 42–54.

[625] Y.L. Kuo, S. Horikawa, K. Kakehi, The effect of interdendritic ?? phase on the mechanical properties of Alloy 718 built up by additive manufacturing, Mater. Des. 116 (2017) 411–418.

[626] 316/316L Stainless Steel, AK Steel. (2016). https://www.aksteel.com/sites/default/files/2018-01/316316L201706_2.pdf (accessed December 6, 2019).

[627] Haynes International, HAYNES ® 718 alloy, Haynes Int. (2017). http://haynesintl.com/docs/default-source/pdfs/new-alloy-brochures/high-temperature-alloys/brochures/718-brochure.pdf?sfvrsn=3eb829d4_28 (accessed December 6, 2019).

[628] A. Hadadzadeh, C. Baxter, B.S. Amirkhiz, M. Mohammadi, Strengthening mechanisms in direct metal laser sintered AlSi10Mg: Comparison between virgin and recycled powders, Addit. Manuf. 23 (2018) 108–120.

[629] B. Chen, S.K. Moon, X. Yao, G. Bi, J. Shen, J. Umeda, K. Kondoh, Strength and strain hardening of a selective laser melted AlSi10Mg alloy, Scr. Mater. 141 (2017) 45–49.

[630] Y.F. Li, S.T. Hong, H. Choi, H.N. Han, Solid-state dissimilar joining of stainless steel 316L and Inconel 718 alloys by electrically assisted pressure joining, Mater. Charact. 154 (2019) 161–168.

[631] I.E. Locci, C.L. Bowman, T.P. Gabbs, B. Rd, I.E.L. Got, Development of High Temperature Dissimilar Joint Technology for Fission Surface Power Systems, 4th Int. Brazing Solder. Conf. 718 (2009) 165–175.

[632] X.W. Wu, R.S. Chandel, H.P. Seow, H. Li, Wide gap brazing of stainless steel to nickel-based superalloy, J. Mater. Process. Technol. 113 (2001) 215–221.

[633] M.C. Chen, H.C. Hsieh, W. Wu, The evolution of microstructures and mechanical properties during accumulative roll bonding of Al/Mg composite, J. Alloys Compd. 416 (2006) 169–172.

[634] W.T. Sun, X.G. Qiao, M.Y. Zheng, N. Hu, N. Gao, M.J. Starink, Evolution of long-period stacking ordered structure and hardness of Mg-8.2Gd-3.8Y-1.0Zn-0.4Zr alloy during processing by high pressure torsion, Mater. Sci. Eng. A. 738 (2018) 238–252.

[635] J.N. DuPont, J.C. Lippold, S.D. Kiser, Welding Metallurgy and Weldability of Nickel-Base Alloys, Wiley, New Jersey, 2009.

[636] N.R. Tao, K. Lu, Nanoscale structural refinement via deformation twinning in face-centered cubic metals, Scr. Mater. 60 (2009) 1039–1043.

[637] K. Lu, N. Hansen, Structural refinement and deformation mechanisms in nanostructured metals, Scr. Mater. 60 (2009) 1033–1038.

[638] Q. Xue, X.Z. Liao, Y.T. Zhu, G.T. Gray, Formation mechanisms of nanostructures in stainless steel during high-strain-rate severe plastic deformation, Mater. Sci. Eng. A. 410–411 (2005) 252–256.

[639] X.L. Wu, Y.T. Zhu, Inverse grain-size effect on twinning in nanocrystalline Ni, Phys. Rev. Lett. 101 (2008) 1–4.

[640] F.S. Qu, X.G. Liu, F. Xing, K.F. Zhang, High temperature tensile properties of laser butt-welded plate of Inconel 718 superalloy with ultra-fine grains, Trans. Nonferrous Met. Soc. China (English Ed. 22 (2012) 2379–2388.

[641] M. Asadi, D. Guillot, A. Weck, S.R. Hegde, A.K. Koul, T. Sawatzky, H. Saari, Constructing a validated deformation mechanisms map using low temperature creep strain accommodation processes for nickel-base alloy 718, Am. Soc. Mech. Eng. Press. Vessel. Pip. Div. PVP. 2 (2012) 65–73.

[642] A. Lasalmonie, J.L. Strudel, Influence of grain size on the mechanical behaviour of some high strength materials, J. Mater. Sci. 21 (1986) 1837–1852.

[643] A.J. Goodfellow, Strengthening mechanisms in polycrystalline nickel-based superalloys, Mater. Sci. Technol. (United Kingdom). 34 (2018) 1793–1808.

[644] T. Gladman, Precipitation-hardening of metals., Mater. Sci. Technol. 15 (1999) 30–36.

[645] J. De Jaeger, D. Solas, T. Baudin, O. Fandeur, J.H. Schmitt, C. Rey, INCONEL 718 Single and Multipass Modelling of Hot Forging, Superalloys 2012. (2012) 663–672.

[646] Alloy 718 Data Sheet, Maher.Com. (2016) 1–5. https://www.maher.com/media/pdfs/718-

datasheet.pdf (accessed December 10, 2019).

[647] W.T. Sun, C. Xu, X.G. Qiao, M.Y. Zheng, S. Kamado, N. Gao, M.J. Starink, Evolution of microstructure and mechanical properties of an as-cast Mg-8.2Gd-3.8Y-1.0Zn-0.4Zr alloy processed by high pressure torsion, Mater. Sci. Eng. A. 700 (2017) 312–320.

[648] C. Yan, L. Hao, A. Hussein, P. Young, D. Raymont, Advanced lightweight 316L stainless steel cellular lattice structures fabricated via selective laser melting, Mater. Des. 55 (2014) 533–541.

[649] J. Kranz, D. Herzog, C. Emmelmann, Design guidelines for laser additive manufacturing of lightweight structures in TiAl6V4, J. Laser Appl. 27 (2015) S14001.

[650] C. de Formanoir, M. Suard, R. Dendievel, G. Martin, S. Godet, Improving the mechanical efficiency of electron beam melted titanium lattice structures by chemical etching, Addit. Manuf. 11 (2016) 71–76.

[651] L.F. Arenas, F.C. Walsh, C.P. de Leon, 3D-Printing of Redox Flow Batteries for Energy Storage: A Rapid Prototype Laboratory Cell, ECS J. Solid State Sci. Technol. 4 (2015) P3080–P3085.

[652] L.-C. Zhang, H. Attar, Selective Laser Melting of Titanium Alloys and Titanium Matrix Composites for Biomedical Applications : A Review **, Adv. Eng. Mater. 18 (2016) 463–475.

[653] P. Krakhmalev, G. Fredriksson, K. Svensson, I. Yadroitsev, I. Yadroitave, M. Thuvander, R. Peng, Microstructure, Solidification Texture, and Thermal Stability of 316 L Stainless Steel Manufactured by Laser Powder Bed Fusion, Metals (Basel). 8 (2018) 1–18.

[654] Y. Li, K. Chen, N. Tamura, Mechanism of heat affected zone cracking in Ni-based superalloy DZ125L fabricated by laser 3D printing technique, Mater. Des. 150 (2018) 171–181.

[655] L. Huynh, J. Rotella, M.D. Sangid, Fatigue behavior of IN718 microtrusses produced via additive manufacturing, Mater. Des. 105 (2016) 278–289.

[656] M. Fousová, D. Dvorský, A. Michalcová, D. Vojtěch, Changes in the microstructure and mechanical properties of additively manufactured AlSi10Mg alloy after exposure to elevated temperatures, Mater. Charact. 137 (2018) 119–126.

[657] B. Srinivasarao, K. Oh-ishi, T. Ohkubo, T. Mukai, K. Hono, Synthesis of high-strength bimodally grained iron by mechanical alloying and spark plasma sintering, Scr. Mater. 58 (2008) 759–762.

[658] W. Yinmin, C. Mingwei, Z. Fenghua, M. En, High tensile ductility in a nanostructured metal, Nature. 419 (2002) 912.

[659] J.B. Jones, D.E. Cooper, D.I. Wimpenny, G.J. Gibbons, Gateways toward dissimilar multi-material parts, Tech. Pap. - Soc. Manuf. Eng. TP12PUB36 (2012) 1–9. [660] R. Kulagin, Y. Beygelzimer, Y. Ivanisenko, A. Mazilkin, H. Hahn, High Pressure Torsion: From Laminar Flow to Turbulence, IOP Conf. Ser. Mater. Sci. Eng. 194 (2017) 1–6.

[661] R. Kulagin, Y. Beygelzimer, Y. Ivanisenko, A. Mazilkin, B. Straumal, H. Hahn, Instabilities of interfaces between dissimilar metals induced by high pressure torsion, Mater. Lett. 222 (2018) 172–175.

[662] M. Pouryazdan, B.J.P. Kaus, A. Rack, A. Ershov, H. Hahn, Mixing instabilities during shearing of metals, Nat. Commun. 8 (2017) 1–7.

[663] Y. Cao, Y.B. Wang, S.N. Alhajeri, X.Z. Liao, W.L. Zheng, S.P. Ringer, T.G. Langdon, Y.T. Zhu, A visualization of shear strain in processing by high-pressure torsion, J. Mater. Sci. 45 (2010) 765–770.

[664] Y. Cao, M. Kawasaki, Y.B. Wang, S.N. Alhajeri, X.Z. Liao, W.L. Zheng, S.P. Ringer, Y.T. Zhu, T.G. Langdon, Unusual macroscopic shearing patterns observed in metals processed by high-pressure torsion, J. Mater. Sci. 45 (2010) 4545–4553.

[665] Y. Cao, Y.B. Wang, R.B. Figueiredo, L. Chang, X.Z. Liao, M. Kawasaki, W.L. Zheng, S.P. Ringer, T.G. Langdon, Y.T. Zhu, Three-dimensional shear-strain patterns induced by high-pressure torsion and their impact on hardness evolution, Acta Mater. 59 (2011) 3903–3914.

[666] B.Y. Huang, M. Kawasaki, T.G. Langdon, Influence of Anvil Alignment on Shearing Patterns in High-Pressure Torsion **, (2013) 747–755.

[667] Y. Huang, M. Kawasaki, T.G. Langdon, An investigation of flow patterns and hardness distributions using different anvil alignments in high-pressure torsion, J. Mater. Sci. 48 (2013) 4533–4542.

[668] W. Jiang, H. Zhou, Y. Cao, J. Nie, Y. Li, Y. Zhao, M. Kawasaki, T.G. Langdon, Y. Zhu, On the Heterogeneity of Local Shear Strain Induced by High-Pressure Torsion, Adv. Eng. Mater. 22 (2020) 14–16.

[669] R. Kulagin, Y. Beygelzimer, A. Bachmaier, R. Pippan, Y. Estrin, Benefits of pattern formation by severe plastic deformation, Appl. Mater. Today. 15 (2019) 236–241.

[670] K. Edalati, H. Emami, Y. Ikeda, H. Iwaoka, I. Tanaka, E. Akiba, Z. Horita, New nanostructured phases with reversible hydrogen storage capability in immiscible magnesium-zirconium system produced by high-pressure torsion, Acta Mater. 108 (2016) 293–303.

[671] N. Ibrahim, M. Peterlechner, F. Emeis, M. Wegner, S. V. Divinski, G. Wilde, Mechanical alloying

via high-pressure torsion of the immiscible Cu50Ta50 system, Mater. Sci. Eng. A. 685 (2017) 19–30.

[672] O. Bouaziz, H.S. Kim, Y. Estrin, Architecturing of metal-based composites with concurrent nanostructuring: A new paradigm of materials design, Adv. Eng. Mater. 15 (2013) 336–340.

[673] K. Edalati, Z. Horita, Continuous high-pressure torsion, J. Mater. Sci. 45 (2010) 4578–4582.

[674] Y. Harai, Y. Ito, Z. Horita, High-pressure torsion using ring specimens, Scr. Mater. 58 (2008) 469–472.

[675] K. Edalati, Z. Horita, Scaling-up of high pressure torsion using ring shape, Mater. Trans. 50 (2009) 92–95.

[676] R.Z. Valiev, I. Sabirov, A.P. Zhilyaev, T.G. Langdon, Bulk nanostructured metals for innovative applications, Jom. 64 (2012) 1134–1142.

[677] T.G. Langdon, Twenty-five years of ultrafine-grained materials: Achieving exceptional properties through grain refinement, Acta Mater. 61 (2013) 7035–7059.

[678] I. Sabirov, M.Y. Murashkin, R.Z. Valiev, Nanostructured aluminium alloys produced by severe plastic deformation: New horizons in development, Mater. Sci. Eng. A. 560 (2013) 1–24.

[679] L.A. Verhoef, B.W. Budde, C. Chockalingam, B. García Nodar, A.J.M. van Wijk, The effect of additive manufacturing on global energy demand: An assessment using a bottom-up approach, Energy Policy. 112 (2018) 349–360.

[680] Siemens Successfully Tests 3D-Printed Gas Turbine Blades, Power Eng. (2017). https://www.power-eng.com/2017/02/07/siemens-successfully-tests-3d-printed-gas-turbine-blades/#gref (accessed December 15, 2019).

Appendix A [List of Tables]

Appendix A

Table 10-1 Comparison of grain size, phase, and microhardness of various SPD methods for CM 316L SS and other CM austenitic SS in literature, and AM 316L SS in this study.

Appendix B [List of Figures]

Fig. 2-15 Schematic of prototype MM-SLM system by Al Jamal et al. (1) laser nozzle; (2) feeder system; (3) build area; (4) CNC rig; (5) fibre optic cable; (6) Nd:YAG laser; (7) PC controller [210]. Reproduced with permission of the rights holder.

Fig. 2-16 (a) Schematic of a novel MM-SLM machine architecture by Wei et al. [9], (b) example of MM structure made by the novel system. Reproduced with permission of the rights holder.

Fig. 2-17 (a) Schematic of ECAP process, with illustration of shearing effect shown inset of (a), and (b) a cross-section of an ECAP die showing two important internal angles, Φ and Ψ (b) [242]. Reproduced with permission of the rights holder.

Fig. 2-18 The four processing routes of ECAP process [245]. Reproduced with permission of the rights holder.

Fig. 2-19 Schematic of HPT process in a quasi-hydrostatic machine setup [246]. Reproduced with permission of the rights holder.

Fig. 2-20 Hardness variations across diameter of HPT-processed (a) commercial purity Ni [251], (b) 316L SS [252], and (c) that across the radius of HPT-processed Al-Mg-Sc alloy [253]. Reproduced with permission of the rights holder.

Fig. 2-21 (a) Variation of hardness across the radius of HPT-processed Al 6061, EBSD maps showing grain size distribution at the centre and periphery after (b) and (c) 1 revolution, and (d) and (e) after 5 revolutions [255]. Reproduced with permission of the rights holder.

Fig. 2-22 Variation of hardness with equivalent strain in HPT-processed metals: (a) strain hardening without recovery, (b) strain hardening with recovery, and (c) strain softening or weakening [260]. Reproduced with permission of the rights holder.

Fig. 2-23 (a) γ'', needle-like δ, and γ matrix (regions A and B) [311], (b) globular shaped δ [321], (c) MC carbide [336], and (d) Laves phase [336]. Reproduced with permission of the rights holder.

Fig. 2-24 (a) Phase diagram, and (b) solidification path for IN 718 [336]. Reproduced with permission of the rights holder.

Fig. 3-1 (a) 316L SS powder particle morphology, and (b) particle size distribution determined via SEM and ImageJ analysis [374].

Fig. 3-2 (a) IN 718 powder particle morphology, and (b) particle size distribution determined via SEM and ImageJ analysis.

Fig. 3-3 Concept Laser M2 ‘Laser Cusing’ SLM machine.

Fig. 3-4 Schematic of the 316L SS rod built by SLM in this study.

Fig. 3-5 HK PM 250 MM SLM machine developed at the University of Southampton.

Fig. 3-6 (a) Schematic and (b) as-built MM SLM-fabricated 316L SS/IN 718 bar using the ‘discrete material change between layers’ deposition strategy using the HK PM250 SLM machine.

Fig. 3-7 An example of the thin disk divided equally into 316L SS and IN 718 halves for HPT cut from the rectangular bar using wire EDM.

Fig. 3-8 (a) Actual micrograph area, (b) binarised micrograph area ready for analysis.

Appendix B

Fig. 8-1 Microhardness of as-received and HPT-processed disks taken averaged at 8 different locations 3 mm from the centre of the disks following the description in Chapter 3.

Fig. 8-2 Coefficient of friction (COF) and mass loss, m_{loss} for as-received and HPT-processed disks after wear test.

Fig. 8-3 2D analysis of the overall wear track depth of as-received and HPT-processed disk after wear test. Solid line shows sliding direction, dashed line show wear track width.

Fig. 8-4 Average wear depth taken from five different locations along the wear track measured using the surface profilometers. Dashed line indicates the original disk surface.

Fig. 8-5 SEM images of worn track surface for as-received and HPT-processed disks after wear test. Double-arrowed lines indicate sliding direction.

Fig. 8-6 Some wear features on the as-received and HPT-processed disks after wear test. Solid arrow shows micro-cutting, dashed arrows show material adhesion, and areas A, B, and C were subjected to EDX analysis.

Fig. 8-7 Some wear features on the as-received and HPT-processed disks after wear test. Solid arrow shows micro-cutting, dashed arrows show material adhesion, and areas A, B, and C were subjected to EDX analysis.

Fig. 8-8 Microhardness, HV (circle and solid line) and specific wear rate, k_{W} (square and dashed line) vs inverse square root of grain size.

Fig. 9-1 (a) and (b) EDX maps at the interfacial region, (c) IPF colour legend with x-z axis indicating surface-parallel direction, (d) – (f) BSE images showing porosity at respective areas within the interfacial region, and (g) – (h) EBSD maps showing crystallographic orientation for the respective interfacial region areas. All images are from the as-received MM disk.

Fig. 9-2 SEM images taken at surface-parallel of the as-received MM disk showing (a) the interfacial region, (b) sharp FZ boundary, (c) the IN 718 region, (d) columnar cells growing through different melt pools at the IN 718 region (area A in (c)), (e) the 316L region, and (f) various cell morphologies at different melt pools in the 316L SS region (area B in (e)).

Fig. 9-3 TEM; (a) – (f) HAADF-STEM; (g) and (n) images, and corresponding EDX maps; (h) – (m) and (o) – (t) for specific areas at the interfacial region of the as-received MM disk.

Fig. 9-4 SEM; (a) and (b), TEM; (c) and (d), and HAADF-STEM; (e) and (k) images, and corresponding EDX maps; (f) – (j) and (l) – (p) for specific areas at the interfacial region after 1/4 HPT revolution.

Fig. 9-5 SEM; (a), TEM; (b) – (d), and HAADF-STEM; (e) and (l) images, and corresponding EDX maps; (f) – (k) and (m) – (r) for specific areas at the interfacial region after 1 HPT revolution.

Fig. 9-6 SEM; (a), TEM; (b) – (d), and HAADF-STEM; (e) and (l) images and corresponding EDX maps; (f) – (k) and (m) – (r) for specific areas at the interfacial region after 10 HPT revolutions.

Fig. 9-7 XRD spectra taken at (a) the interfacial and (b) IN 718 regions for the as-received and HPT-processed MM disks; (c), (d), and (e) show zoomed-in examples of XRD peaks of the weak (Nb,Ti)C signals from regions I, II, and III of the main XRD spectra.

Appendix C [Published papers]

List of published papers directly related to this PhD project:

[1] S.M. Yusuf and N. Gao (2017) Influence of energy density on metallurgy and properties in metal additive manufacturing, *Materials Science and Technology*, 33, 1269–1289.

[2] S. M. Yusuf, M. Nie, Y. Chen, S. Yang, and N. Gao (2018) Microstructure and corrosion performance of 316L stainless steel fabricated by Selective Laser Melting and processed through high-pressure torsion, *Journal of Alloys and Compounds*, 763, 360–375.

[3] S. M. Yusuf, Y. Chen, S. Yang, and N. Gao, Microstructural evolution and strengthening of selective laser melted 316L stainless steel processed by high-pressure torsion (2019) *Materials Characterization* , 159, 110012.

[4] S. M. Yusuf, Y. Chen, S. Yang, and N. Gao, Micro-mechanical response of additively manufactured 316L stainless steel processed by high-pressure torsion (2020) *Advanced Engineering Materials,* https://doi.org/10.1002/adem.202000052.